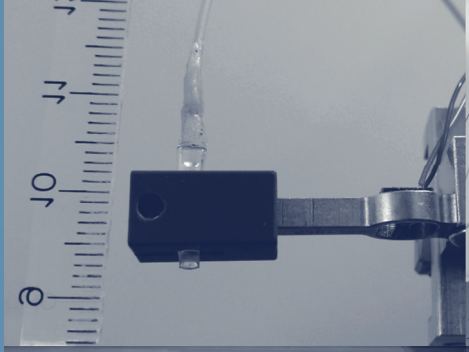
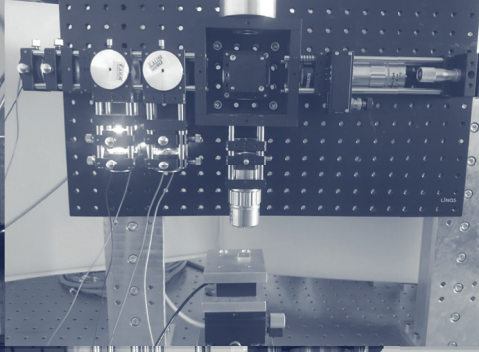


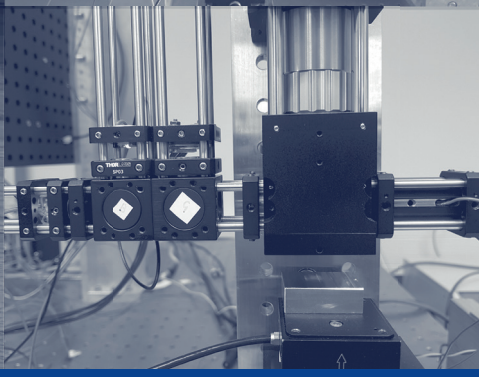

Advanced theory of optical wave propagation and interferometric sensors for topography measurement

Markus C. Schake

kassel
university
press

Markus C. Schake

Advanced theory of optical wave propagation and interferometric sensors for topography measurement

kassel university press

This work has been accepted by Faculty of Electrical Engineering / Computer Science of the University of Kassel as a thesis for acquiring the academic degree of Doktor der Ingenieurwissenschaften (Dr.-Ing.).

Supervisor: Prof. Dr.-Ing. Peter Lehmann
Co-Supervisor: Prof. Dr.-Ing. Tino Hausotte
Defense day: 18. Oktober 2019

https://orcid.org/0000-0002-9883-3494 (Markus C. Schake)

Bibliographic information published by Deutsche Nationalbibliothek
The Deutsche Nationalbibliothek lists this publication in the Deutsche Nationalbibliografie; detailed bibliographic data is available in the Internet at http://dnb.dnb.de.

Zugl.: Kassel, Univ., Diss. 2019
ISBN 978-3-7376-0840-4 (print)
ISBN 978-3-7376-0841-1 (e-book)
DOI: https://dx.doi.org/doi:10.17170/kobra-202007031403

Printed in Germany

Acknowledgments

I want to thank everybody who contributed to the successful completion of this manuscript by ideas, discussions, distracting exhilaration or any other possible means including the mere bearing of my company, throughout the years I have been obsessively occupied with my dissertation.

Special thanks, to my supervisor Prof. Lehmann and my colleagues for supporting my work by sharing their scientific expertise, proofreading of many contributions, sitting through hours of presentations and discussions, and making our department a place I liked to work at and will keep in good memory.

Abstract

The industrial demand in non-contact, perturbation resistant, fast and dynamic topography measurement systems for quality control catalyzes proliferating research in optical metrology. Interferometry enables axial resolution in the nano meter and even sub nano meter range in combination with an adjustable lateral resolution depending on the employed microscope objectives. Therefore, research and development of interferometric devices and the corresponding phase retrieval algorithms are evermore evolving.

This manuscript is organized in three major chapters, considering advances in different fields of interferometry related research. First, presenting advances in teaching and interpretation of non-uniform wave propagation in dissipative media. This manuscript provides a compendium for the application of the non-uniform wave model to standard problems of two beam interference. Especially considering wave propagation at attenuating interfaces and inside dissipative media.

Second, presenting advances in development and applicability of a fiber coupled interferometric system with periodical optical path length modulation employing a long coherent laser illumination. This system employs a miniaturized probe head, which is feasible to perform measurements inside hollow structures or at measuring objects with complex geometry. The present manuscript introduces novel details considering the plane of reference inside the miniaturized fiber probe, the design procedure of a similar probe with low aperture for measurements in an expanded depth of field and correction procedures for systematic phase retrieval deviations related to time discrete Hilbert filters. Also the capability of a 3D-topography measuring system based on the fiber coupled sensor for surface measurements with dynamic focus tracking is presented. An analytic approach for extension of the unambiguity range in multi wavelength interferometry is implemented in a real time digital signal processor and applied for surface measurements and the feasibility of the interferometric point sensor for measurements of rough surfaces is demonstrated with experimental results.

Third, a novel measurement procedure for fast, perturbation resistant, areal surface measurement employing pulsed RGB-illumination and optical path length modulation in the reference arm is introduced. The presented interferometric system employs two interference images in quadrature and a microscopic image in a separate color channel of the recording device to retrieve the phase of the wavefront reflected from the surface. By synchronization of the pulse illumination with the short camera exposure gap between two consecutive images, the total data acquisition time of the interferometer is $< 100\,\mu s$. This causes a high robustness to environmental perturbations and enables topography measurements of objects in lateral motion. The characteristics of the employed interferometers and recording devices, like influence of dispersion effects or color crosstalk are discussed alongside a presentation of topography results illustrating the capabilities of the measuring procedure.

Contents

Chapter 1

State of the art in optical surface metrology

Optical surface metrology is a fast developing field of research. The industrial needs for fast and non destructive, inline quality control require precise optical instruments offering high lateral and height resolution, which yield reliable results in the presence of vibrations or other perturbations. Tactile measurement systems like the atomic force microscope and the stylus instrument, are limited by their slow measurement speed. Also the tactile probe may cause damage to the surface under investigation or the thin cantilevers used for probing might break [1,2]. Since optical measurement systems are contact free, they allow the sampling of much bigger areas in shorter time, while maintaining a high resolution. Therefore, numerous techniques for optical surface measurement have emerged and are constantly developed and improved.

The highly relevant optical surface measurement techniques, which are commonly used in commercial applications, can be clustered depending on their physical principle of surface reconstruction into systems based on focus variation microscopy, confocal microscopy, wavefront sensors, fringe projection, deflectometry methods and interferometers. Figure 1.1 provides an overview of the common industrial and scientific applications of these techniques.

Fringe projection and deflectometry

Fringe projection methods are based on the projection of a fringe pattern on the surface under investigation. The projected pattern is commonly created by a projector, but the interference fringes of optical gratings or interferometers are also used for the fringe pattern illumination. The surface of the measuring object is reconstructed, by evaluation of the phase shifts, the surface structure causes in the projected fringe pattern. Therefore,

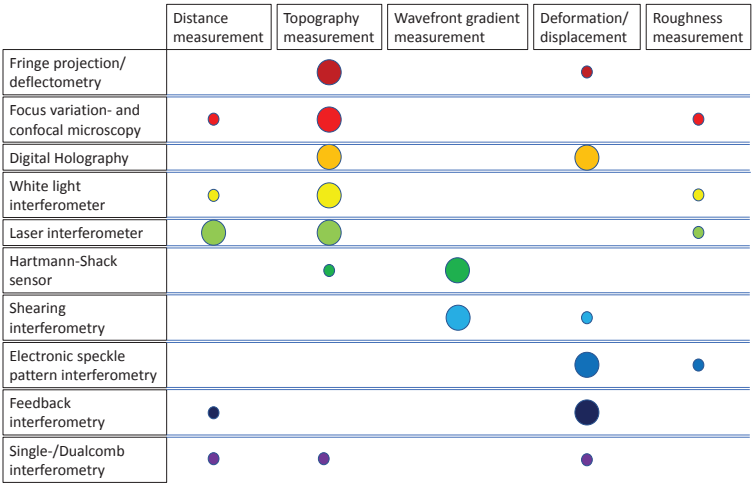

Figure 1.1: Common applications of the introduced optical surface measurement techniques. Big circles indicate the main field of application with industrial relevance, small circles indicate less common or evolving applications of scientific interest.

the phase retrieval algorithms used for fringe projection methods are very similar to those applied in phase shifting interferometry. In interferometry the phase demodulation is often conducted in the Fourier domain or by means of the Hilbert Transformation. To increase the robustness against vibrations and other environmental perturbations single shot methods for the fringe projection based surface profiling, using colored fringes and a color camera, are proposed [3–5]. A related technique especially applied to measure specular surfaces is deflectometry. In deflectometry the topography information is restored from deformations in the recorded reflection of a known projected pattern.

Focus variation- and confocal microscopy

Focus variation microscopy and confocal microscopy are both based on the conduction of a depth scan through the imaging systems focus region and determine the measuring objects surface height by the identification of the best focus for each pixel. In confocal microscopy a small aperture or a pinhole array like a multi-pinhole-disc or Nipkow-disc is placed in the optical path. Therefore, only light from an axially and laterally restricted spatial region is reaching the optical sensor and thus the spatial resolution of the system is increased and speckle effects are reduced in comparison with the focus variation microscopy. A common type of confocal microscopes are confocal chromatic sensors, which

employ the wavelength specific longitudinal chromatic aberration and a spectrum analyzer to determine the measuring object distance to the probes reference plane, omitting the need of mechanically moving the probe in a depth scan. The application of a focal-distance-modulated fiber-coupled confocal point sensor for coordinate measuring systems is demonstrated by [6]. In conventional confocal microscopy the sensitivity of the intensity response to path length changes is reduced in the vicinity of the focal plane due to its vanishing slope. Introducing a focal-distance modulation enables the evaluation of the modulated signal's higher harmonics by a lock-in amplifier to yield a better linear characteristic for position tracking [6]. By the introduction of a spatial light modulator for structured illumination (SIM) or the use of stimulated emission depletion (STED) microscopy in the confocal microscope, it is even possible to break the diffraction barrier of far-field optical imaging, as it has been presented in multiple contributions on super resolution microscopy in the recent past [7–9]. The STED is based on fluorescence whereas SIM is label-free.

Hartmann-Shack sensors

Wave front sensors like the Hartmann-Shack (HS) sensor are used to reconstruct the measuring object's surface from the wavefront gradient of a wave, which either transmitted or was reflected by the measuring object. The system is referenced to a known surface. In case of the Hartmann-Shack sensor a microlens array is placed in front of the optical detector, eg. a CCD or CMOS array. Depending on the local tilt of the incoming wave front, the spot created by the microlens array is shifted in its position on the sensor compared to the reference case. This procedure is for example used as a one-shot measurement in the inspection of aspheric lenses [10]. The unambiguity range of HS sensors is high compared to interferometers employing a single wavelength for phase retrieval. The application of a HS sensor to support surface unwrapping of interferometric measurement data is studied in [11]. The HS sensor may also be applied to study the beam propagation parameters of laser radiation [12–14].

Interferometers

Interferometric sensors are based on the superposition of coherent or partially coherent waves, which originate from the same light source and are divided into different optical paths, until they are recombined in front of the detector. The optical path length difference of the interfering waves is reconstructed from the interferogram and yields the measurement result by interpreting it with respect to the experimental setup. Numerous interferometric measurement systems exist, which are applied to length measurement, form testing, surface profiling, material sciences and other applications. Common measurement techniques based on interferometry are digital holography, feedback interferometry,

femto-second-laser interferometry, fiber coupled laser interferometry, shearing interferometry, speckle pattern interferometry and white light interferometry. The state of the art in digital holography, feedback interferometry, femto-second-laser interferometry, shearing interferometry and speckle pattern interferometry will be shortly outlined here while fiber coupled laser interferometry and white light interferometry are thoroughly treated, since they are in the scope of this work.

Digital holography

Holographic interferometry, is based on the idea to reconstruct the complex field of the object wave from the recorded interferogram of the object wave with a known reference wave. Before the digital recording of images by means of CCD or CMOS arrays was available, holograms were recorded on photographic plates. The term hologram refers to the interferometric image that emerges if light of a coherent source is split up in a reference and an object path and these waves are superimposed on a recording screen. By illuminating the hologram with the reference wave, an observer facing the hologram from its backside will see the virtual image of the object, the hologram was recorded with. In digital holography the complex object wave is reconstructed from the recorded hologram by means of analytic or numerical signal processing requiring the knowledge of the complex reference wave. If the object wave passed an imaging system prior to its recording, it is back propagated using optical imaging theory to reconstruct the original object image [15]. Recent contributions on digital holography deal with the reconstruction of the object wave by Fourier transform and constrained optimization problems. In phase shifting digital holography the reference path of the interferometer is periodically modulated in its length or stepwise incremented, and a stack of holograms is recorded. By applying a generalized lock-in algorithm, which involves Fourier domain filtering, or using a N-step algorithm the phase of the complex object wave is retrieved. This application was recently proposed by Zhu et al. [16] featuring a generalized lock-in algorithm, which is adaptable to arbitrary actor modulation functions. To achieve high measurement rates single shot digital holography procedures were introduced. They may feature tilted reference planes to overlay a carrier fringe pattern on the measuring objects interferogram or require a certain tilt of the object itself. The phase reconstruction from these single shot holograms can be performed in terms of classic spectral domain filtering methods. However, when the object's relative tilt to the reference plane is small and the spectral components of the carrier fringes overlap with the low frequency components in the Fourier domain, spectral domain filtering methods do not yield feasible results. To overcome this obstacle, Khare et al. introduced a procedure to obtain the complex object field from the hologram by solving a constrained optimization problem. Based on the recorded hologram and the complex reference field a least square optimization problem is iteratively solved, considering a smoothing condition, to reconstruct the complex object field, which is than back propagated to the image plane [17, 18].

Feedback interferometry

Feedback interferometry is generally based on the principle, that light, which emerged from the laser cavity, reenters it after being reflected from the measuring object and its interaction in the cavity changes the laser's operating parameters like terminal voltage, output power or frequency [19]. By Measuring these changes the characteristics of the measured object can be reconstructed [20]. Recent contributions are dealing with the applicability of feedback interferometry in optical surface roughness measurement [21] and a speckle-insensitive fringe detection method for displacement reconstruction or velocimetry applications [22]. In the latter case, the optical output power of the self-mixing laser interferometer is periodically modulated due to the measurement objects displacement, while the signal is disturbed by amplitude modulation caused by speckles. The resulting signals are similar to those observed in fiber coupled interferometric sensors with optical path length modulation. The amplitude modulation due to speckle effects, causes deviations in the displacement reconstruction, if it is performed in the time domain. Thus, in [22] the signal phase is retrieved by using an analytic signal resulting from Hilbert transformation of the sampled data in the frequency domain.

Single-/Dualcomb interferometry

The development of femtosecond pulsed lasers, which generate extremely short light pulses in the femto- to picosecond range has led to a variety of interferometric measurement applications. A single pulse in the time domain forms a continuous spectrum in the frequency domain. If a train of coherent pulses is generated with a fixed repetition frequency, as the femtosecond pulsed laser does, it forms a discrete spectrum in the frequency domain, where the frequency resolution is given by the repetition frequency. If the pulse train is considered to be infinite long, its spectrum would be a frequency comb, where each tooth is separated from the next by the repetition frequency [23]. The femtosecond pulsed laser serves as a spectrally broadband light source with extremely short pulsed illumination. Therefore, it is applicable to investigate very fast displacements in the sub-nanosecond time scale, using it as a stroboscopic light source to virtually freeze the motion. This application is used in [24], where the performance of a pulsed laser in terms of displacement noise is compared to that of a frequency stabilized continuous wave laser. Jin et al. propose the use of a femtosecond pulsed laser to build a Fizeau-type spectral domain interferometer [25]. It uses the broad spectrum of the pulse to acquire multiple interference signals in the frequency domain, implementing a virtual phase shift in the wavelength dependent interferogram through its discrete spectral components without mechanical motion. The interferogram is recorded by a spectrum analyzer, its intensity is modulated over the wavelength. The phase slope depends on the optical path difference between the measurement object and the reference surface. If the measurement arm contains a stratified medium with multiple reflective layers, multiple interferograms with path

length difference dependent phase slope are superimposed. By Fourier transformation of the interference spectrum the path length differences belonging to the respective layers can be retrieved. Therefore, the proposed setup is applicable for thickness measurements of silicon wafers.

Another technique which emerged from the research revolving around femtosecond pulsed laser interferometry is dual comb interferometry. It requires two frequency comb sources, with slightly differing repetition frequencies. At least one of the frequency comb sources, is probing the measurement object. This can be a transparent sample in a Mach-Zehnder configuration or a measurement surface in a Michelson type interferometer. In front of the detector, the frequency combs are combined. Each comb mode of the measurement frequency comb will beat with each comb mode of the reference comb, when they are superimposed. The electric fields of the respective frequency combs can be described as the superposition of plane monochromatic waves, where each comb tooth represents a discrete frequency. The electric field of the measurement comb contains the complex amplitude information of the measurement object in form of an attenuation and phase shift term. The recorded interferogram results from the electric fields cross-correlation, between the measurement and reference comb. Thus, if the electric fields cross-correlation is calculated, the cosine modulation of the resulting interferogram is no longer in the range of the optical frequencies, as it is for the discrete electric field components of the single combs, but is down scaled to the range of the pulsed lasers repetition frequency. By this the material or surface dependent complex amplitude information of the measurement combs electric field is also shifted to this lower frequency range, where it is accessible for sampling. By Fourier analysis of the recorded interferogram the complex amplitude information of the sample can be retrieved [23]. The principle of dual comb interferometry can be applied for absolute distance measurements of distances in the range of multiple meters as demonstrated in [26]. The refresh rate of dual comb interferometers is predominantly limited by the comb sources repetition rates, because a certain amount of pulses needs to be sampled to receive the optical spectrum. Dual comb interferometers, based on modelocked laser technology require two modelocked lasers as comb sources, which can typically achieve pulse repetition rates in the MHz range. An alternative is given by the use of electrooptic comb generators. A single laser provides the input to the comb generators, which are composed of a chain of electrooptic modulators. These electrooptic comb generators can achieve repetition rates in the GHz range and therefore, the refresh rate of a dual comb interferometer using this technique can be significantly increased [27].

Shearing interferometry

The shearing interferometer is a device used in beam and wavefront characterization, phase measurement and optical shop testing. The basic principle of the shearing interferometer is to duplicate the incident wavefront, introducing an optical path length difference to the duplicate and recording the interference pattern between the original and displaced

wavefront. The optical path length difference is commonly introduced by placing a plane parallel plate in a 45° angle in the light path, where the incident wavefront is reflected at the front and back interface of the plate introducing a lateral shear between them. Optical gratings are also used to introduce the shear. In this case the incident wave passes the grating and an order selection mask is used to only transmit the plus and minus first diffraction orders. The wave fronts of the first diffraction orders are overlapping with a lateral displacement to each other and form the shearing interferogram [28]. If a collimated beam featuring a plane wavefront is incident on the wedged shear plate, the interferogram of the sheared wave fronts shows equidistantly spaced fringes perpendicular to the shear. A deformed wavefront causes variations in the fringe spacing and orientation. By comparison of the recorded interferogram to the interferogram of a collimated beam the wave front gradient is retrieved, enabling the restoration of the incident wavefront from the shearing interferogram. Similar to deflectometers and Hartmann-Shack sensors shearing interferometry retrieves the wavefront gradient, which may be used for topography measurements. A lateral and rotational shearing phase-shifting interferometer is proposed by [29] to perform single shot phase measurements. The setup features polarizing beam splitters and a phase grating, to multiplex the wave fronts and enable independent phase shifts around each diffraction order. Therefore, multiple interferograms with a different shift are recorded simultaneously and phase shifting algorithms can be applied for phase reconstruction. A common-path wavefront diagnosis system based on a cross grating lateral shearing interferometer is proposed in [30]. The setup employs a cross grating in combination with an order selection mask to select the positive and negative first diffraction order in horizontal and vertical direction. From the resulting shearing interferogram of the four diffraction orders the wavefront under test is retrieved using Fourier transform and Zernike polynomial fitting methods. The three-wave shearing interferometer proposed by [31] is using a spatial light modulator to realize an adaptive, one dimensional grating to introduce the shear. The positive and negative first diffraction order, as well as the zero diffraction order contribute to the shearing interferogram. The spatial light modulator can introduce a phase shift to the shearing interferogram and a generalized five step phase shifting algorithm for the three-wave shearing interferogram is proposed for phase retrieval. In [4] the use of a shearing interferometer as a source of structured illumination is discussed. A plane parallel shear plate is mounted on an actuator in the illumination path. The shearing interferogram is used to project a fringe pattern on the measurement object. A phase shift can be introduced to the fringe pattern by moving the shear plate in the illumination path and the surface structure is retrieved using fringe projection algorithms.

Electronic speckle pattern interferometry

A method to investigate static and dynamic displacements of structures with rough surfaces is given by the electronic speckle pattern interferometry (ESPI). When laser light is diffusely reflected from a rough surface, the wave fronts form a random but surface

specific intensity distribution called a speckle pattern. In electronic speckle pattern interferometry the speckle image of the measurement surface is superimposed with a reference beam on the detector, thus forming a speckle interferogram. If the object is deformed its random but specific speckle interferogram will change depending on the surface deformation. By subtracting two recorded speckle interferograms captured at different time and different object deformation states so called correlation fringes appear in the difference image. These correlation fringes refer to the local surface deformation between the two moments in time. The reference beam can be used to introduce a specified phase shift to the speckle interferogram, thus shifting the correlation fringes and enabling the use of phase shifting interferometry algorithms for phase recovery [15, 32]. The accurate reconstruction of surface deformation or vibration motion by means of electronic speckle pattern interferometry is an active field of research. Recent contributions suggested approaches to retrieve accurate phase information by utilizing surface optimization methods to save computation time or achieve higher spatial resolution [32, 33]. A combination of spatial and temporal phase unwrapping methods is proposed to improve surface reconstruction [34]. An experimental setup is proposed, that uses polarization filters in the ESPI to achieve the simultaneous recording of four differently phase shifted interferograms, to implement a phase shifting interferometry based one-shot phase retrieval [35]. Speckle pattern techniques are also applied for optical roughness measurements, in [36] the advantages of using an optical vortex illumination to create the speckle pattern in determination of the mean roughness are discussed.

1.1 Laser interferometers with optical path length modulation and corresponding phase retrieval methods

One of the scopes of this dissertation is a fiber coupled laser interferometer with periodical optical path length modulation, which is developed in the department of optical metrology at the university of Kassel and is reported in multiple contributions [1, 37–47]. To adequately position the advances achieved in this field among the contemporary research the state of the art in interferometric sensors with optical path length modulation and corresponding methods for phase retrieval is outlined here.

A valuable feature of interferometric point sensors is their potential for miniaturization. Employing fiber components and gradient index (GRIN) lenses it is possible to create a very small and flexible probe head in a common path interferometer configuration. The interferometric probe is configured as a common path or Fizeau-type interferometer. The edge of a cleaved fiber is attached to a focusing or collimating gradient index lens. The fiber's end facet serves as the reference plane in the common path interferometer and the GRIN lens is focusing or collimating the measurement beam on the object. These probes

have very small diameter of approximately 3 mm and are suitable for in-hole measurements and similar applications. Fiber optical probes of this type are reported in combination with a Michelson interferometer and broadband illumination sources in [37, 48–50]. Their application in laser interferometry is reported in [1, 38–40, 43–47, 51]. Different possible probe configurations are discussed in [46]. In [52] a laser interferometer in a fiber coupled Michelson configuration is proposed, where the measurement and reference arm each end in their respective fiber coupled probes. A similar configuration is reported in [53], which employs high numerical aperture fibers to reduce speckle effects. Compared to the common path configurations, these fiber coupled Michelson interferometers show the disadvantage, that the interference of light from the measurement and reference path, does not immediately take place in the fiber probe head, but the light travels separated through the respective fibers until combined in front of the detector. Thus, mechanical disturbances in the measuring and reference fiber cause phase changes in the recorded interferogram. Nakata and Watanabe [54] propose a fiber coupled common path laser interferometer, which employs a photonic crystal polarizer as the reference plain, resulting in different polarization directions of the reference and the probing beam. Employing additional polarization optics and phase retarders in front of the detector, the setup enables the recording of four interferometric images, each shifted by $\frac{\pi}{2}$ in phase to apply phase shifting interferometry (PSI) algorithms for surface topography retrieval. In comparison to the simple fiber probes, this allows a higher acquisition rate of measurement data but also makes the probe more bulky and complex. This dissertation contributes to the further development and characterization of the miniaturized fiber probe by experimental validation of the reference plane location at the fiber end and the development of a low aperture fiber probe with extended working distance and depth of field (DOF).

A common obstacle in surface topography measurements employing laser interferometers is the limited unambiguity range. Using a single wavelength λ, the unambiguity is limited to an interval of $\pm\frac{\lambda}{4}$. Extending the unambiguity of laser interferometers is an active field of research and multiple approaches have been proposed in literature. Analytic approaches, employing the combination of two different wavelengths to use the extended ambiguity range of the resulting longer synthetic wavelength are reported in [51, 55, 56]. Jennewein et al. [51] present the combination of laser sources, that differ in their wavelength only by some nanometers and therefore achieve a very long synthetic wavelength. The interferograms of different wavelength are separated using diffraction gratings. A similar approach, employing a fiber coupled interferometer with electrooptic path length modulation and four different wavelengths is presented in [57]. De Groot proposes an analytical approach of signal evaluation in a two wavelength system [56], which is related to the exact fraction theory of Michelson and Benoit, but yields a fully analytic solution, increasing the unambiguity range without the necessity of sampling additional information. The increase of unambiguity range using this method is dependent on the ratio of used wavelengths. In comparison to the exact fraction approach, fringe order information is discarded to achieve higher robustness in fringe order determination and sustain an analytic solution. In [55] a similar approach is presented and extended by the use of the

shorter synthetic wavelength to increase the accuracy in phase retrieval. Falaggis [58–60] and Decker et al. [61] contribute approaches, which employ the full set of information related to the exact or also called excess fraction method. Falaggis presents an adaption of the exact fraction method to yield the full extension of the unambiguity range, based on an analytic solution and uses redundant phase information to increase the robustness of the method. Decker et al. identify the fringe orders by solving a numerical residual search problem employing a least square approach. In [62] the surface profile dependent pixel position of a specific fringe order related intensity distribution is used to extend the unambiguity of step height measurements on plane surfaces with steep edges. Yang et al. [63] report the combination of a low coherence source with a laser source to achieve unambiguous surface measurement. The setup employs a low coherence phase-crossing technique for fringe order determination and uses the additional phase information of the laser source for accurate determination of the fractional fringes. Therefore, in comparison with the signal evaluation based approaches for unambiguity extension mentioned above, it achieves ambiguity free absolute height measurement. In this dissertation, carrying on the work presented in [56] a fully analytic, signal evaluation based extension of the unambiguity range is proposed. Hindering constraints of the previous work are overcome and a successful experimental implementation of the algorithm is presented [42].

An increasingly important application of interferometric sensors are optical roughness measurements, since the contact free procedure is potentially faster and minimizes the risk of causing surface damage during the measurement. Chand [64] and Vorburger [2] compare classic tactile stylus measurements to optical coherence tomography (OCT) or scanning white light interferometry (SWLI), phase shifting interferometry (PSI) and confocal microscopy. The reported results indicate, that optical methods can yield comparable roughness values to the tactile methods depending on the numerical aperture of the optical device, its unambiguity range, the slope steepness on the sample and further parameters. Since OCT methods like SWLI are capable of performing unambiguous measurements they are predominately used in optical roughness measurements and industrial systems based on this technique are available. Caber [65] reports the advantage of the unambiguous measurement of SWLI systems in roughness determination and Kim et al. [66] suggest the usage of the fringe contrast, in SWLI roughness measurement, to identify surface areas of high slope or low reflectance, where the fringe contrast is below a threshold value close to the noise level. The identified areas are marked and set blank and their surface profile is retrieved by interpolation from the potentially valid neighboring points. In [67, 68] Bodendorfer et al. contribute results on the applicability of speckle interferometry for qualitative and quantitative roughness measurement. According to their results the surface roughness can not be estimated quantitatively by employing one single speckle related surface parameter, because surfaces of the same roughness, but different form may lead to different roughness measurement results if speckle interferometry is employed. Therefore, if no apriori knowledge of the surface form is available multivariate analysis has to be employed to retrieve the roughness information from the speckle pattern. In the course of this dissertation, the experimental application of the miniaturized

fiber probe laser interferometer with periodical optical path length modulation for surface roughness measurements according to ISO 4287 and ISO 11562 is presented. Also, the use of a second laser wavelength in surface roughness measurement to reduce the influence and occurrence of phase jumps caused by ambiguity issues and low signal quality is proposed [41].

The periodical optical path length modulation of either the reference or measurement path of the interferometer is a central feature, which enables the application of carrier fringe based Lock-In approaches and PSI methods for surface phase retrieval. In [69] Sasaki and Okazaki describe the basic idea of using a sinusoidal modulation in the reference path to create a temporal carrier fringe pattern. Surface phase changes occurring at a much slower rate than the modulation frequency are converted to a phase shift in the carrier fringe pattern. Multiple periods of the carrier fringe pattern are recorded and used for surface phase retrieval by applying discrete Fourier transform (DFT) based Lock-In detection algorithms or feasible alternatives. The DFT Lock-In approach is used and described in [43–47]. For the temporal carrier fringe based approach, the oscillation frequency of the actuator limits the measurement rate, since interferometric data has to be sampled over multiple periods of carrier fringes to receive robust phase retrieval. Thus, the introduction of the periodical path length modulation not by mechanical motion but by modulation of the laser diode current [70] and therefore the wavelength or using an electro-optic modulator (EOM) [71] poses interesting alternatives to achieve higher measurement rates. However, by actuating the reference mirror of a fiber coupled interferometer mechanically Hagemeier et al. [72] achieved an actuator oscillation frequency of 58 kHz. The classic Lock-In algorithm is designed for a linear phase modulation. However, in experimental setups, most basic and accessible path length modulators cause a sinusoidal phase modulation. Zhu et al. [73] proposed a generalization of the Lock-In method, adapting it to the non-linear phase modulation to enhance its performance. In [74] a variation of the Lock-In approach is presented, which employs the Fourier expansion of rectangular waves for filtering to recover the sine and cosine component of the carrier modulated interference signal for quadrature based phase retrieval. A widely used alternative to Lock-In detection in phase retrieval are linear phase shifting techniques. Most linear phase shifting techniques are based on the recording of multiple interferometric images, each differing by a constant and known phase shift. N-step phase shifting algorithms, $N \in [2, 3, \cdots]$ can be designed in the frequency domain and applied as discrete convolution filters in the time domain [75]. Generalizations of the phase shifting algorithms are proposed, which are based on Carre algorithm [28] and work with a constant, unknown phase shift, but require the recording of at least four images [76]. Based on the Gram-Schmidt orthogonalization algorithm, a PSI phase retrieval method employing only two interferometric images with unknown arbitrary phase shift is proposed in [77]. This dissertation involves the implementation of embedded Lock-In detection and a discrete PSI Hilbert filter in an ARM based microprocessor environment for real time surface height retrieval applications. The real time implementation enables additional measurement features like dynamic focus tracking and thus increases the dynamic measurement range of the fiber probe setup.

A functional 3D-surface topography measurement device employing three perpendicular moving linear axis is presented, performing on the fly height measurements based on the fast embedded algorithms.

1.2 Low coherence-, polarizing- and RGB-interferometry systems for topography measurement

Another scope of this dissertation is the development of an RGB-interferometer system with pulsed LED illumination for perturbation resistant, areal surface measurements. The RGB-Linnik-interferometer setup and a novel phase retrieval approach are reported in [78]. A quadrature based Michelson interferometer setup employing pulsed RGB-illumination and periodical optical path length modulation is reported in [11, 79]. To adequately position the advances achieved in this field among the contemporary research the state of the art in optical coherence tomography (OCT) also referred to as scanning white light interferometry (SWLI) or coherence scanning interferometry (CSI), phase shifting interferometry (PSI), spectral interferometry (SI) and the influence of colored illumination and color cameras on these techniques is outlined here.

Time domain OCT, CSI or SWLI are standard procedures in unambiguous optical surface phase retrieval, which have been reported in numerous contributions and are applied in commercial surface topography measuring devices. The basic implementation of SWLI involves a low coherent light source and the recording of an image stack of the correlogram, while a depth scan is performed. The recorded images are used for envelope or phase evaluation procedures for surface topography retrieval. Basic applications of these techniques, considering also the possible influences of dispersion effects are reported in [80–85]. In [86] a phase-crossing algorithm is proposed to identify the zero optical path length difference position, where the measurement and reference arm are balanced. To apply this technique the phase development for two separate wavelength channels needs to be recorded while performing the depth scan. Detection of the crossing point of the wrapped phase profiles, near the envelope peak position enables precise determination of the balancing point and therefore, unambiguous surface height retrieval. A detailed analysis of signal modeling in low coherence interference microscopy, explaining the origin of common surface detection errors in the vicinity of steep edges, like the batwing effect is given by Xie [87]. To enhance signal quality an automated best focus determination procedure employing a focused laser beam is reported in [88]. After the focus position is adjusted, the optical path length difference for highest interference fringe contrast is determined by a depth scan. Due to the possibility of unambiguous measurement white light interferometers are an interesting alternative to tactile measurement systems when the topography of rough surfaces shall be measured. Pavlicek and Hybel [89] report about measurement uncertainty caused by

noise in the interferogram for SWLI applications on rough surfaces. Coherence scanning interferometry can be applied for refractive index determination of thin films, as reported by Yoshino et al. [90]. Information of the thin film thickness and refractive index are retrieved from the distorted depth scan correlogram of the surface with the thin film and a reference measurement without the thin film. A common obstacle in scanning white light interferometry is given by the long data acquisition time related to the depth scan. The long acquisition time makes the SWLI vulnerable to environmental disturbances, especially mechanical vibrations, which may distort the recorded correlogram in a way that no surface retrieval is possible. To achieve vibration resistance Tereschenko et al. [91] propose the combination of a depth scanning white light interferometer with a laser interferometer measuring the vibration perturbations and using these for correction of the SWLI signal. In [92] a dual low coherence scanning interferometer is introduced, which employs an additional reference arm with an optical path length difference offset to reduce the depth scan range and therefore acquisition time in measuring large step heights. By adding a reference arm, there is additional occurrence of positions, where the optical path length difference (OPLD) of beam pairs from the respective light paths becomes zero and therefore, multiple correlograms can be recorded with a smaller scanning range.

To overcome the high data acquisition time of the time domain OCT or SWLI respectively, the spectral domain OCT or spectral interferometry was introduced. For this technique, the surface information of the investigated object is retrieved from the optical interference spectrum, which is acquired in a single-shot manner employing multichannel spectrometers as recording devices. If one arm of the interferometer contains a dispersive element, the setup can only be balanced for one certain wave number, thus causing a modulation of the spectral intensity over the wave number from which the surface structure is retrieved. Pavlicek and Häusler [93] propose a fiber coupled white light interferometer based on this principle. In [94] Papastathopoulos et al. describe a spectral interferometer in combination with confocal filtering. Employing a diffractive optical element in addition to the microscope objective, the focus position varies as a function of wavelength, which leads to a decoupling of the sensors depth range from the numerical aperture of the microscope objective. The confocal filtering stops light from outside the focal plane and thus maintains a chirp free spectrally resolved interferogram with a constant frequency in the spectrally modulated intensity distribution used in the phase retrieval procedure.

To enable the observation of measuring objects, which move by a fast but periodic oscillation, stroboscopic SWLI may be applied. A pulsed illumination is synchronized to the motion frequency and thus allows the recording of the moving object at a certain point of its motion period in a quasi static manner. A transfer standard for traceable, dynamic calibration of stroboscopic SWLI systems is proposed in [95].

To overcome the limitations of high sampling time in SWLI and the usually small unambiguity range of PSI, multiple approaches based on the use of a color camera either 3-chip-CCD or Bayer pattern, carrier fringes or polarization optics have been proposed. To overcome the limitation of fringe-contour map and moirè topography in determining

the sign of retrieved phase, Takeda [85] proposed a single shot monochrome image carrier fringe approach based on Fourier transformation. The carrier fringes are used to separate the phase information in the spectral domain such that by application of frequency selective filtering and inverse Fourier transformation the phase information is retrieved. Similar to Hilbert transformation based approaches the obtained phase is indeterminate to an integer multiple of 2π and the carrier fringes are required to be the predominant source of phase modulation to yield feasible results.

Katsuichi Kitagawa [96, 97] proposed a single-shot interferometric approach using an interferometer with a reference mirror tilted with respect to the measuring object, three color LED illumination and a color camera. In this setup the three color interferograms are recorded simultaneously during one camera frame and the Local Model Fitting (LMF) method is applied for phase retrieval. To apply the LMF algorithm the fringe frequency in the interference images needs to be estimated requiring rather plane measuring object surfaces. Then the phase is estimated by a least square approach. To increase the unambiguity range, the phase values of all three color channels are combined applying the method of exact fractions [56]. The method appears to be suitable for step height measurements with extended unambiguity range and on plane surface objects, but its applicability seems to be restricted in case of continuous surface height variations with a gradient similar to that of the tilted reference mirror. In further contributions, the requirement of carrier fringes introduced by the tilted reference mirror is overcome and replaced by the use of a global model fitting algorithm, which retrieves the wavelength specific offset and modulation depth parameters of the two beam interference equation as well as the pixel dependent phase by solving an optimization problem [98, 99]. However, the approach contains the constraint that the intensity offset and modulation depth of the interference signal are constant throughout the field of view, which restricts the method to homogenous surfaces.

Another carrier fringe based approach is proposed by Srivastava et al. [100]. A Michelson interferometer with tilted reference mirror is used to record three color interferograms simultaneously with a Bayer pattern CCD assuming that the carrier fringes introduced by the tilted reference mirror are the predominant source of fringe modulation. The Hilbert Transformation is applied to the periodical signal to create the analytic signal referring to each interferogram and from this immediately retrieve the phase by employing the inverse tangent transformation. The unambiguity range is increased by using the synthetic wavelength approach [42, 56]. Since the approach is based on carrier fringes it is constricted by the same limitations as mentioned before [96, 97]. Pförtner et al. [101] apply a RGB-laser illumination in a PSI setup to increase the unambiguity range without additional recording of images compared to the mono color application. The phase is retrieved using a 5-step PSI algorithm, thus requiring the recording of five interferometric images in all color channels of the used three-chip CCD camera. Similar to the paper of Kitagawa [98] the surface profile is retrieved with extended unambiguity range by application of the exact fraction method to the wrapped phase values of the respective

color channels. Pförtner and Schwider report, that the crosstalk error is negligible for the three-chip CCD, but the color specific phase-dispersion has to be considered for successful fringe order determination by the exact fraction method.

Koliopoulos [102] proposes a simultaneous phase shift interferometer, employing four CCD detectors, a laser light source and optical elements for polarization specific phase retardation to record four phase shifted interferometric images simultaneously. These images are in quadrature or out of phase to each other respectively and allow immediate phase retrieval using a 4-step PSI algorithm. Millerd et al. [103] describe the application of a pixelated phase mask in front of a CCD detector combined with perpendicularly polarized reference and measurement beam. This enables the adjustment of a pixel specific phase shift on the detector, depending on the pixelated mask. The application of a 4-step PSI algorithm for phase retrieval using a $[0°, 90°, 180°, 270°]$ phase mask is presented with experimental results [103]. Safrani and Abdulhalim [104] propose a Linnik interferometer setup combining the use of two-wavelength interferometry with parallel PSI, recording the interferograms of two color channels with three phase-masked CCD cameras simultaneously. Polarization of the illuminating light enables the three phase-masked CCD-Cameras to record the two color interferograms each with an adjustable phase retardation of an integer multiple of $\pi/2$. In this way the necessary information for the application of a 3-step PSI algorithm for phase retrieval is recorded within a single shot. The single phase information of the respective color channels are then combined employing two-wavelength interferometry procedures to unwrap the 3D-surface with the extended unambiguity of the synthetic wavelength. In [105] the combination of a $[0°, 45°, 90°, 135°]$ phase mask and a CMOS Bayer pattern camera is proposed. Four images of the respective polarization are simultaneously recorded in the three separate color channels. The phase is retrieved employing a 4-step algorithm and the unambiguity range is extended employing the synthetic wavelength. However, a cell of 4×4 pixels is required for the data recording, which results in a single topography value, thus reducing the effective lateral resolution of the camera chip.

Suodong Ma et al. [106] propose the use of a three-Chip color CCD in a SWLI setup, to achieve the full camera chip resolution for each color without the influence of interpolated intensity values as in the case of Bayern pattern cameras and to maintain the color information in the interferograms for a precise determination of the position of zero optical path difference. To determine the surface height precisely the chromatic aberration of the color channels is considered and an optimization problem related to the dispersion error in the phase of the three color channels is solved, which reaches a minimum at zero optical path difference. Buchta et al. [107] investigated the dependence of artificially composed white light correlograms on the used LED light sources. A white light illumination composed of red, green and blue LED sources, shows a broader envelope in the correlogram, but contains side orders, which cause a sharper distinction of the zeroth fringe order maximum. Experimental results are presented using the customized white light illumination, and a Bayern-pattern camera to record SWLI signals in three color

channels simultaneously and retrieving the phase employing a phase crossing algorithm searching for the position of zero optical path length difference similar to Ma et al. [106]. An approach based on spectrally resolved white light interferometry is proposed by Zhu and Wang [108]. A frequency comb illumination generated by a Fabry-Perot etalon is used in combination with a white light source to generate a frequency comb illumination of discrete equidistant wave numbers. A Mirau interference objective and an adjustable slit in combination with a blazed grating are used to disperse the overlapping multicolor interferograms spatially separated on a CCD detector. By this an arbitrary number of independent interferograms for each separate wave number is recorded simultaneously, limited by the available size of the CCD-Chip. By evaluating the phase change of a single point in the separated interferograms exploiting the known discrete wavelength difference the retrieval of an absolute height value is performed. A drawback of this single shot method is the small field of view, that is limited in one dimension according to the slit width, causing the field of view to be shaped like a narrow rectangle.

This dissertation considers a novel approach for phase retrieval based on parameter estimation in the two beam interference equation. A 3-Chip color CCD camera is used to record two interference images of red and green illumination, respectively, and one microscopic image with blue illumination. Based on these recorded images the unknown parameters in the two-beam interference equation are determined and the wrapped surface phase is retrieved by using the inverse cosine function. By pulsing the illuminating LEDs synchronized to a moving mirror in the reference path the sign of the wrapped cosine function is retrieved and the 3D-surface topography is reconstructed. The approach is similar to those introduced in references [98, 99], but the parameters are restored from a different basis of recorded images. In addition, the intensity offset of the interferometric images is not assumed to be constant throughout the field of view, but obtained for each pixel individually by measurement. Another advantage of the proposed method in comparison with references [96–100, 104], is that by pulsing the illumination, the actual recording time of the interference images takes only a small interval of the camera integration time, enabling the time for image recording being independent of the camera exposure time and frame rate [78]. Furthermore, a dispersion resistant dual-shot quadrature method employing a Michelson interferometer configuration and a color camera is introduced. Using the oscillating reference mirror and synchronizing the pulse illumination to the camera exposure gap, a very short acquisition time is achieved. The method enables simple analytic phase retrieval and may be recognized as a quasi single-shot measurement considering low frequency perturbations. It is more suitable for experimental applications, since it is robust against the aberration errors reported in [78]. Yet, the retrieved phase is indeterminate to an integer multiple of 2π and surface unwrapping has to be performed. The proposed measurement procedure is feasible for perturbation resistant topography measurements and capable of retrieving the topography of measuring objects in lateral motion, as it is presented by experimental results [11, 79].

Chapter 2

Theory of wave propagation and interference

The propagation of electromagnetic waves through interfaces of different materials is a mandatory component of education in the field of physics and optical engineering. It is commonly treated in the context of Snell's Law, Fresnel coefficients and material dispersion relation. The case of non-attenuating media is well covered by standard textbooks and comprehensively taught in courses and lectures. Also a variety of undergraduate lab experiments exist to visualize the effects described by the common equations [109–114]. The case of wave propagation through attenuating interfaces has mostly been treated in scientific literature not neccessarily comprehensive to undergraduate students. The contributions of Canning [115–117] deal with the issue of the appearance of a complex angle in the notations commonly used in literature and introduce a derivation of Fresnel equations based on the phase- attenuation vector notation where no complex angles occur. However, the form of his derivation is mainly based on Stratton's book [114] and superficially differs from the derivations commonly used in textbooks and lectures for the treatment of the loss free case [110–112]. Between 2003 and 2015 multiple contributions on the matter of wave propagation in attenuating media were released in the American- and European Journal of Physics [118–121]. They deal with wave propagation and evanescent waves in absorbing media [120], polarization characteristics of electromagnetic waves in dissipative media [121], summation and transfer matrix methods in stratified media [118] and the suggestion of an advanced lab experiment dealing with the Fresnel coefficients of metallic coatings with complex refractive index [119]. All of these contributions share some common issues. While defining the wave vector the non-uniform nature of the wave in the attenuating medium is not discussed. It may even be assumed, that the wave vector is introduced in terms of a uniform propagating wave, which would be unfeasible to derive Snell's law and the dispersion relation in the attenuating media. However, later in these contributions a formula for the complex form of Snell's law or the dispersion relation in complex angle notation is used. This implies, that the wave vector is defined for the non-

uniform wave in complex angle notation, since otherwise the used formula could not be derived. For someone not familiar with the notations of the non-uniform wave vector and it's commonly applied implicit use in complex angle notation the appearance of complex angles in Snell's Law is not comprehensible and the question arises, why it is possible to use the standard Fresnel equations for the attenuating interface, just by replacing the real valued refractive index with a complex one and accept complex angles.

The contributions of F. Capasso et al. [122–125] deal with the reflection and refraction of light at attenuating and anisotropic metasurfaces. These contributions include the postulation of a generalized form of Snell's law, derived on the basis of Fermat's principle. Since the uniform wave vector is employed in the derivation, the boundary conditions for the electric field's tangential components at the metasurface interface can not be satisfied. Metallic antenna structures cause a phase gradient along the interface, which by consideration of the meta surface interface as a single layer interface precludes the conservation of translational invariance. This is resolved by the introduction of an additional „*phase matching*“ term in the wave vector conservation equation to account for the phase shift introduced by the attenuating interface. This measure is explained by stating „*...that due to the lack of translational invariance along the interface the tangential wavevector of the incident photon is not conserved; the interface contributes an additional "phase matching" term equal to the phase gradient,...* “ [122](p.1703). However, by consideration of the respective metasurface segments, metallic antennas and free space respectively, this may be omitted. The transmission characteristic of the single antennas may be described by complex Fresnel coefficients employing the non-uniform wave model. Thereby a local phase shift is assigned to each antenna. Employing Huygens principle, the meta surface interface may be assumed as the origin of elemental waves with position dependent phase offset. Thus the antenna array may be modeled as a phase grid. Simulations of 4 periods of a phase grid consisting of 8 antennas, as described in the experimental section of [124] where each antenna is represented by a single elemental wave with respective phase shift, showed good agreement with the presented simulation and measurement results.

Thus, the generalized form of Snell's law postulated by Capasso et al. may also be derived employing complex Fresnel coefficients based on the non uniform wave model [126, 127] to describe the phase shift introduced by the antennas and considering the far field interference of the resulting phase grid. By this the assumption of missing translational invariance along the interface may be omitted. Thereby, the non-uniform wave model and the interference equation provide the theoretic background to derive the generalized form of Snell's law proposed in [122, 123, 125] maintaining compliance to Maxwell's equations.

The origin of these common issues is revealed by comparing the literature used in these articles, all refer to the book of Born [110] and also partly refer to [111, 112, 114]. These books are standard literature on the topic and all of them share the described issues. The implicit use of the non-uniform wave vector in complex angle notation has passed on in educational purposes over decades. The intention of this section is to introduce a comprehensible and compact overview of the basics of wave propagation in non-attenuating

and dissipative media. The uniform and non-uniform wave model are introduced and the derived laws for wave propagation are finally applied in the derivation of two beam interference. The careful explanation and separation between certain notations is commonly omitted in standard literature to achieve brevity. The educational issues and implications on scientific research are indicated in [128], which also contains a comparison of recent results for the determination of effective propagation constants at attenuating interfaces. The careful treatment of wave propagation and interference in this section is dedicated to improve teaching and understanding of wave propagation, especially in consideration of attenuating interfaces.

2.1 Uniform plane wave equation

Based on Maxwell's equations a differential equation is found, which describes the propagation characteristics of the electric field $\vec{E}_m(x,y,z,t)$ of a plane wave, referred to as wave equation. This differential equation is solved by trigonometric functions describing plane, harmonic waves.

Following the electric field's wave equation of an elliptically polarized, uniform, harmonic, plane wave propagating in an optical isotropic, attenuating medium m with real valued magnetic permeability is given in cartesian coordinates [110, 111, 129–134].

$$\begin{aligned}\vec{E}_m(x,y,z,t) &= \frac{1}{2}\left(\underline{\vec{E}}_{0m} e^{j\left(\begin{bmatrix}\underline{k}_{xm}\\ \underline{k}_{ym}\\ \underline{k}_{zm}\end{bmatrix}\cdot\begin{bmatrix}x\\ y\\ z\end{bmatrix}-\omega_0 t\right)} + \underline{\vec{E}}^{*}_{0m} e^{-j\left(\begin{bmatrix}\underline{k}^{*}_{xm}\\ \underline{k}^{*}_{ym}\\ \underline{k}^{*}_{zm}\end{bmatrix}\cdot\begin{bmatrix}x\\ y\\ z\end{bmatrix}-\omega_0 t\right)}\right)\\ &= \Re\left\{\underline{\vec{E}}_{0m} e^{j\left(\begin{bmatrix}\underline{k}_{xm}\\ \underline{k}_{ym}\\ \underline{k}_{zm}\end{bmatrix}\cdot\begin{bmatrix}x\\ y\\ z\end{bmatrix}-\omega_0 t\right)}\right\}\\ &= \Re\left\{\underline{\vec{E}}_{0m} e^{j((\Re\{\underline{k}_m\}+j\Im\{\underline{k}_m\})\vec{u}_{km}\cdot\vec{r}-\omega_0 t)}\right\}\end{aligned} \tag{2.1}$$

The magnetic field is expressed analog to the electric field in equation (2.2).

$$\vec{H}_m(x,y,z,t) = \Re\left\{\underline{\vec{H}}_{0m} e^{j((\Re\{\underline{k}_m\}+j\Im\{\underline{k}_m\})\vec{u}_{km}\cdot\vec{r}-\omega_0 t)}\right\} \tag{2.2}$$

In equation (2.1) the vector

$$\underline{\vec{E}}_{0m} = \begin{bmatrix} E_{xm}e^{j\phi_{xm}}\\ E_{ym}e^{j\phi_{ym}}\\ E_{zm}e^{j\phi_{zm}}\end{bmatrix}, \tag{2.3}$$

which is referred to as Jones vector, describes the complex amplitude of the electromagnetic wave in the m-th medium. The absolute values $E_{xm},\ E_{ym},\ E_{zm}$ and phases $\phi_{xm},\ \phi_{ym},\ \phi_{zm}$ of this vector's elements, determine the wave's polarization [111, 131].

The complex uniform wave vector in equation (2.4) determines the wave's direction of propagation and spatial phase evolution in the m-th medium.

$$\vec{\underline{k}}_m = \begin{bmatrix} \underline{k}_{xm} \\ \underline{k}_{ym} \\ \underline{k}_{zm} \end{bmatrix} = \left(\Re\left\{\underline{k}_m\right\} + j\Im\left\{\underline{k}_m\right\}\right)\vec{u}_{km} = \left(\alpha_{0m} + j\beta_{0m}\right)\vec{u}_{km} \tag{2.4}$$

In this equation α_{0m} and β_{0m} are the so called intrinsic propagation constants of the m-th medium [135]. This section considers a uniform, plane wave, whose planes of constant amplitude and planes of constant phase propagate parallel in the same direction, the unit vector $\vec{u}_{km}$ describing the wave's propagation direction is the same for the real and imaginary part of $\vec{\underline{k}}_m$. The unit vector describing the propagation direction of the uniform, plane wave is given by equation (2.5).

$$\vec{u}_{km} = \frac{\Re\left\{\vec{\underline{k}}_m\right\}}{|\Re\left\{\vec{\underline{k}}_m\right\}|} = \frac{\Im\left\{\vec{\underline{k}}_m\right\}}{|\Im\left\{\vec{\underline{k}}_m\right\}|}. \tag{2.5}$$

The unit vector for the uniform, plane wave's propagation direction from equation (2.5) $\vec{u}_{km}$ will be used in this work, whenever the uniform, plane wave model is considered. In equation (2.1) the term $\vec{r} = \begin{bmatrix} x & y & z \end{bmatrix}^{\mathrm{T}}$ refers to the position vector in cartesian coordinates.

The electrical field $\vec{E}_m(x, y, z, t)$ according to equation (2.1) is a real valued physical magnitude. Because the expression in terms of sin() and cos() functions is impractical for numerous field calculations the wave is commonly expressed in Euler's form as real part of the complex wave function $\vec{\underline{E}}_m(x, y, z, t)$. The complex wave function is also referred to as phasor expression. Commonly an abbreviated form is used, in which the separation of the real part or the addition of the complex conjugate is not explicitly depicted. Still it has to be considered, that the vector of the physical electric field is always real. In its abbreviated form equation (2.1) is given by the complex wave function as:

$$\begin{aligned} \vec{E}_m(x, y, z, t) &= \frac{1}{2}\left(\vec{\underline{E}}_m(x, y, z, t) + \vec{\underline{E}}^*_m(x, y, z, t)\right) \\ &= \Re\left\{\vec{\underline{E}}_m(x, y, z, t)\right\} \end{aligned} \tag{2.6}$$

The electric flux density, magnetic flux density, magnetic field and polarization are also real valued, physical quantities. For numerous calculations concerning these quantities also the complex phasor expression is used. Equation (2.7) summarizes the relations

between the mentioned physical quantities and their complex phasor expressions [130,131].

$$\begin{aligned}
&\text{Electric field } \vec{E}_m(x,y,z,t) = \Re\left\{\underline{\vec{E}}_m(x,y,z,t)\right\}\\
&\text{Electric flux density } \vec{D}_m(x,y,z,t) = \Re\left\{\underline{\vec{D}}_m(x,y,z,t)\right\}\\
&\text{Magnetic field } \vec{H}_m(x,y,z,t) = \Re\left\{\underline{\vec{H}}_m(x,y,z,t)\right\}\\
&\text{Magnetic flux density } \vec{B}_m(x,y,z,t) = \Re\left\{\underline{\vec{B}}_m(x,y,z,t)\right\}\\
&\text{Electric polarization } \vec{P}_m(x,y,z,t) = \Re\left\{\underline{\vec{P}}_m(x,y,z,t)\right\}
\end{aligned} \tag{2.7}$$

2.2 Non-uniform plane wave equation

For a plane wave the areas of constant phase are given by planes. If the plane wave is uniform, the amplitude is also constant on the planes of constant phase. For the case of a non-uniform plane wave the amplitude is not constant on the constant phase planes and the planes of constant phase, which can also be referred to as wave fronts, do not coincide to the planes of constant amplitude [136]. In literature uniform waves are also referred to as homogenous and non-uniform waves as inhomogeneous waves [115, 127, 128, 135, 137, 138]. Figure 2.1 shows an example of the special case of a uniform plane wave in a non-attenuating medium incident on the interface to an attenuating medium in which it propagates as a non-uniform wave with coplanar propagation and attenuation direction vectors. Usually, when the propagation behavior of plane waves at the interface of lossy media is considered, the non-uniform or as it is also referred to inhomogeneous wave model is used. This model is commonly expressed in the phase and attenuation vector representation, based on the notation used in [135]. It describes the non-uniform wave vector as the sum of an arbitrary real vector pointing towards the phase propagation direction and a purely imaginary vector pointing towards the direction of attenuation. For the case of coplanar direction vectors for phase and attenuation vector the non-uniform wave vector is:

$$\begin{aligned}
\underline{\vec{k}}_m^{(\mathrm{nu})} &= \vec{\alpha}_m + j\vec{\beta}_m\\
&= \alpha_m\left(\cos(\xi_m+\rho_m)\vec{u}_1 + \sin(\xi_m+\rho_m)\vec{u}_2\right) + j\beta_m\left(\cos(\xi_m)\vec{u}_1 + \sin(\xi_m)\vec{u}_2\right)
\end{aligned} \tag{2.8}$$

Where $\alpha_m,\ \beta_m \in \mathbb{R}$ are the effective propagation and attenuation constants in the m-th medium as referred to in [127]. $\vec{u}_1 \perp \vec{u}_2$ are the perpendicular unit vectors spanning the plane of incidence and $(\xi_m+\rho_m), \xi_m \in \mathbb{R}$ are the real valued angles $\vec{\alpha}_m$ and $\vec{\beta}_m$ enclose with the vector $\vec{u}_1$ normal to the considered interface. There is another commonly used representation of the non-uniform wave model referred to as the complex angle notation. The complex angle notation describes the non-uniform wave vector as the product of the intrinsic propagation constants with a complex unit vector. For the case of coplanar

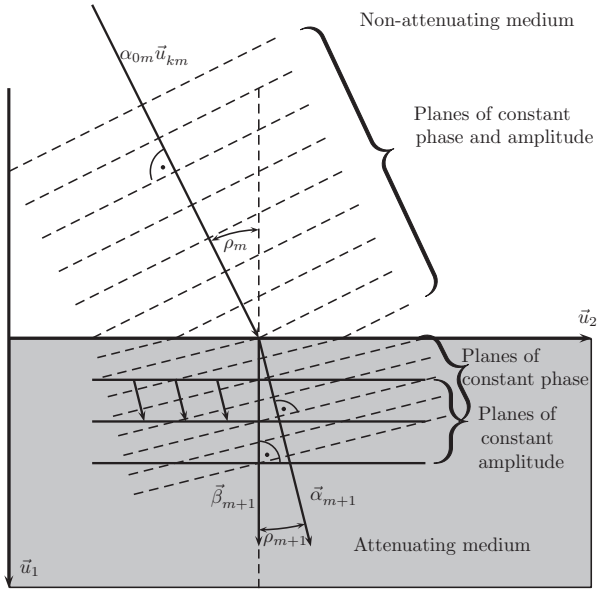

Figure 2.1: Special case of a uniform incident wave with real valued unit direction vector $\vec{u}_{km}$, causing coplanar propagation and attenuation vectors in the attenuating medium and $\cos\angle(\vec{\beta}_{m+1}, \vec{u}_1)$=1 and therefore the angle enclosed between $\vec{\beta}_{m+1}$, $\vec{u}_1$ is $\xi_{m+1} = 0$. The reflected wave in the first medium is not depicted.

direction vectors for phase and attenuation vector, it is given by:

$$\begin{aligned} \vec{\underline{k}}_m^{(\mathrm{nu})} &= (\alpha_{0m} + j\beta_{0m})\, \vec{\underline{u}}_{km}^{\mathrm{uni}} \\ &= (\alpha_{0m} + j\beta_{0m})\, (\cos(\underline{\theta}_m)\vec{u}_1 + \sin(\underline{\theta}_m)\vec{u}_2)\,. \end{aligned} \tag{2.9}$$

Here $\alpha_{0m},\ \beta_{0m} \in \mathbb{R}$ are the intrinsic propagation constants in the m-th medium as referred to in [127], $\vec{u}_1 \perp \vec{u}_2$ are the perpendicular unit vectors spanning the plane of incidence and $\underline{\theta}_m = \theta_{Rm} + j\theta_{Im}$ is the complex angle that the complex unit vector $\vec{\underline{u}}_{km}^{\mathrm{uni}}$, which satisfies $\vec{\underline{u}}_{km}^{\mathrm{uni}} \cdot \vec{\underline{u}}_{km}^{\mathrm{uni}} = 1$, encloses with the vector $\vec{u}_1$ normal to the considered interface. A detailed study considering the advantages of the respective notations and their application to determine the effective propagation constants in attenuating media is presented in [128]. This contribution emerged from theoretical investigations, independent of the scope of this dissertation and resolved educational issues in the treatment of wave propagation at attenuating interfaces. It is quite common in standard literature that the non-uniform wave model is used implicitly in its complex angle notation without mentioning it.

By the notation of (2.8) the non-uniform wave model representation of the electric and magnetic field of an elliptically polarized harmonic plane wave propagating in an isotropic, attenuating medium are given by (2.10) and (2.11).

$$\vec{\underline{E}}_m(x,y,z,t) = \vec{\underline{E}}_{0m} e^{j\left(\vec{\underline{k}}_m^{(\mathrm{nu})} \cdot \vec{r} - \omega_0 t\right)} \tag{2.10}$$

$$\vec{\underline{H}}_m(x,y,z,t) = \vec{\underline{H}}_{0m} e^{j\left(\vec{\underline{k}}_m^{(\mathrm{nu})} \cdot \vec{r} - \omega_0 t\right)} \tag{2.11}$$

Here, $\underline{E}_{0m}$, $\underline{H}_{0m}$ define the electric and magnetic field's amplitude and polarization in the m-th medium, $\vec{r}$ is the positional vector in carthesian coordinates, ω_0 represents the angular frequency and $t \in \mathbb{R} > 0$ denotes the time. By comparison of the phase attenuation vector notation and the complex angle notation some conclusions are presented [128]. Considering the use of correct parameters in terms of the effective and intrinsic propagation constants in both models, they offer an algebraic and numerically equal representation of the complex wave vector of the non-uniform wave model. Yet each of these notations offers specific advantages. The phase attenuation vector representation (2.8) describes the complex wave vector separated in real and imaginary part using the real valued effective propagation constants, real valued angles and real valued unit direction vectors. Given this, it is possible to depict the propagation direction of the wave split up in constant phase and amplitude planes, which might be interpreted as the wave fronts of the real and imaginary part as depicted in figure 2.1.

2.3 Wave polarization

Independent of the wave model the plane wave's polarization is specified by its complex amplitude $\vec{\underline{E}}_{0m}$ given in (2.3), which is referred to as Jones vector for the electric or $\vec{\underline{H}}_{0m}$ for the magnetic field, respectively. In the most general case arbitrary values of amplitude $E_{xm}, E_{ym}, E_{zm} \in \mathbb{R}$ and phase $\phi_{xm}, \phi_{ym}, \phi_{zm} \in \mathbb{R}$ can occur, which would cause the field vector to rotate on an ellipse. Therefore, this case is called elliptic polarization. A special case of the elliptically polarized wave is the linearly polarized wave. It exhibits the special characteristic, that the phase difference between the phase of the orthogonal field components depending on the propagation direction $|\phi_{xm} - \phi_{ym}|$, $|\phi_{xm} - \phi_{zm}|$ or $|\phi_{ym} - \phi_{zm}|$ are either in phase $|\Delta\phi| \in \{0, 2\pi, 4\pi, \cdots\}$ or shifted by 180° referring to $|\Delta\phi| \in \{\pi, 3\pi, 5\pi, \cdots\}$ [111]. Since each elliptically polarized wave can be described as the superposition of linearly polarized waves, linearly polarized waves can be used in considerations concerning the propagation characteristics of waves at optical interfaces without any loss of generality [111]. As outlined in the beginning of this section, the polarization has no dependence on the wave vector and therefore, it does not matter if the uniform or non-uniform wave model is applied. Although, the graphical depiction of the linearly polarized wave is less complex for the case of non-attenuating media.

For a graphical example an inclining, linearly polarized, uniform, harmonic, plane wave propagating in an isotropic, non-attenuating medium in complex phasor expression $\underline{\vec{E}}_m(x,y,z,t)$ with $\phi_{xm}, \phi_{ym}, \phi_{zm} = 0$ is assumed.

$$\begin{aligned}\underline{\vec{E}}_m(x,y,z,t) &= \begin{bmatrix} E_{xm} \\ E_{ym} \\ E_{zm} \end{bmatrix} e^{j\left(\vec{k}_m \cdot \vec{r} - \omega_0 t\right)} \\ &= \begin{bmatrix} E_{xm} \\ E_{ym} \\ E_{zm} \end{bmatrix} e^{j(k_{xm}x + k_{ym}y + k_{zm}z - \omega_0 t)}\end{aligned} \tag{2.12}$$

The wave is described in a right handed, cartesian coordinate system. The coordinate system is chosen such, that the propagation vector of the wavefront $\vec{k}_m = \begin{bmatrix} k_{xm} \\ k_{ym} \\ k_{zm} \end{bmatrix}$ lies in the x-y-plane as the plane of incidence. Thus the inclining wave does not propagate towards z-direction and therefore $k_{zm} = 0$ equals zero. The considered optical boundary surface is given by the x-z-plane.

Using the principle of superposition, the inclining wave is split up into a s-polarized (TE-polarized) component with $\underline{\vec{E}}_{0m}$ perpendicular to the plane of incidence and a p-polarized (TM-polarized) component with $\underline{\vec{E}}_{0m}$ parallel to the plane of incidence. The polarization is determined by the orientation of the electric field vector $\vec{E}_{0m} = \begin{bmatrix} E_{xm} \\ E_{ym} \\ E_{zm} \end{bmatrix}$ to the plane of incidence [111, 133]. Considering the coordinate system chosen above the s-polarized wave in figure 2.2 is described by equation (2.13).

$$\underline{\vec{E}}_{sm}(x,y,z,t) = \begin{bmatrix} 0 \\ 0 \\ E_{zm} \end{bmatrix} e^{j(k_{xm}x + k_{ym}y - \omega_0 t)} \tag{2.13}$$

As depicted in figure 2.2 the absolute value of the electric field component in z-direction equals the amplitude of the s-polarized electric field $E_{zm} = E_{sm}$. The p-polarized wave according to figure 2.3 is described by equation (2.14).

$$\underline{\vec{E}}_{pm}(x,y,z,t) = \begin{bmatrix} E_{xm} \\ E_{ym} \\ 0 \end{bmatrix} e^{j(k_{xm}x + k_{ym}y - \omega_0 t)} \tag{2.14}$$

As depicted in figure 2.3 the amplitude of the field components in x- and y-direction $E_{xm} = E_{pm}\cos(\theta_m)$ and $E_{ym} = E_{pm}\sin(\theta_m)$ can be determined employing trigonometric functions. The figures 2.2 and 2.3 show that the incident wave is reflected and transmitted at the boundary surface in the x-z-plane. In that process the electric and magnetic field components of the incident wave have to satisfy boundary conditions, which arise from Maxwell's equations [111, 133].

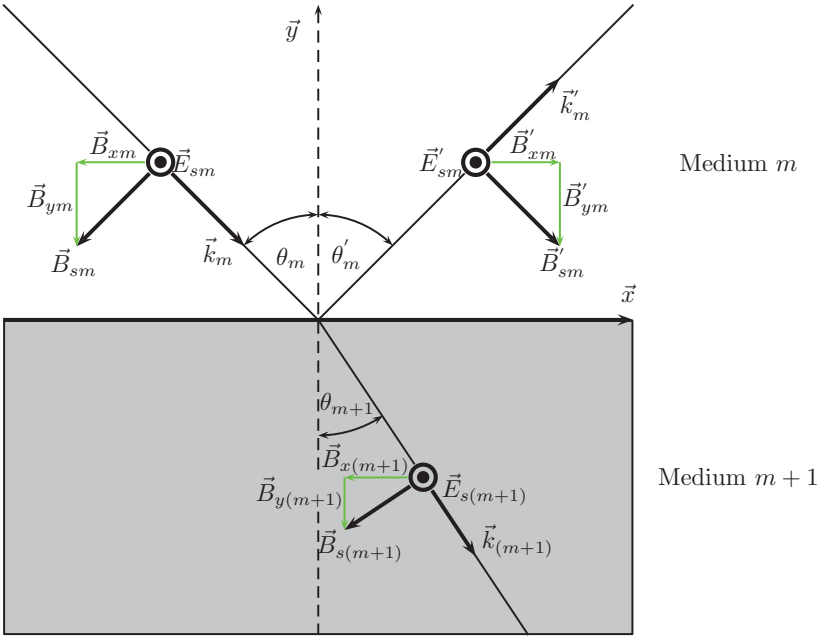

Figure 2.2: Propagation characteristic of an electromagnetic wave, polarized perpendicular to the x-y-plane of incidence (TE-polarized) at an optical interface [111].

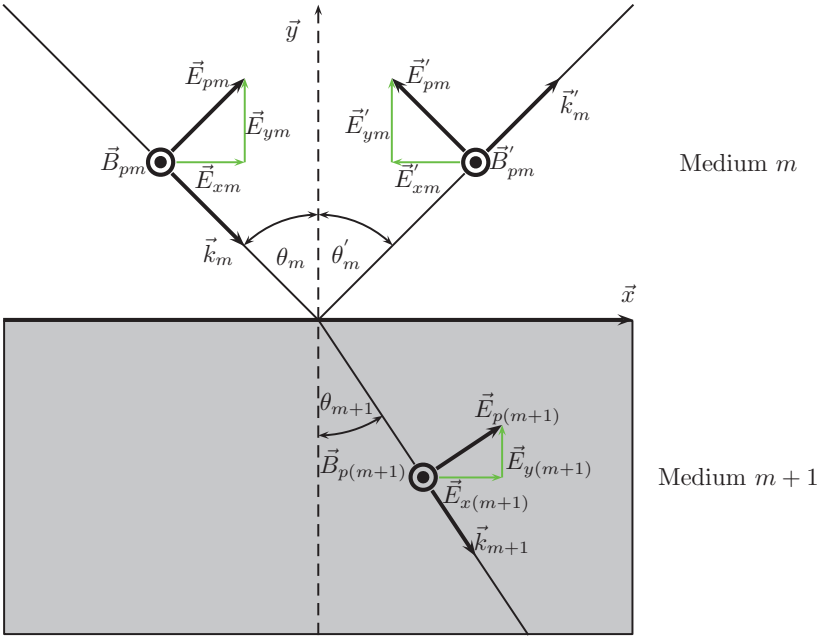

Figure 2.3: Propagation characteristic of an electromagnetic wave, polarized parallel to the x-y-plane of incidence (TM-polarized) at an optical interface [111].

2.4 Maxwell's equations

The classical theory of electromagnetic fields is mostly based on a set of four partial differential equations, known as Maxwell's equations. They are fundamental for the derivation of the boundary conditions at the interface of two media and are shortly introduced in this section [110–112].

The first Maxwell equation, which corresponds to Gauss's law for the electric field, yields a boundary condition for the components of the electric flux density perpendicular to the boundary surface D_{ym}. It states that electric charge Q or charge density ρ is the source of the electric field.

$$\vec{\nabla} \cdot \vec{D} = \rho \tag{2.15}$$

The second Maxwell equation, which corresponds to Gauss's law for the magnetic field, yields a boundary condition for the components of the magnetic flux density perpendicular to the boundary surface B_{ym}. It states that there are no magnetic charges or magnetic monopoles.

$$\vec{\nabla} \cdot \vec{B} = 0 \tag{2.16}$$

The third Maxwell equation, which corresponds to Faraday's law of induction, yields a boundary condition for the components of the electric field parallel to the boundary surface, which are either E_{xm} or E_{zm} depending on polarization. It states that a time varying magnetic field induces an electric field.

$$\vec{\nabla} \times \vec{E} = -\frac{\partial}{\partial t}\vec{B} \tag{2.17}$$

The fourth Maxwell equation, which corresponds to the extended form of Ampere's circuital law, yields a boundary condition for the components of the magnetic field parallel to the boundary surface, which are either H_{xm} or H_{zm} depending on polarization. It states that an electric current or a time varying electric field induces a magnetic field.

$$\vec{\nabla} \times \vec{B} = \mu_0 \mu_m^{'} \left(\epsilon_0 \epsilon_m^{'} \frac{\partial}{\partial t}\vec{E} + \sigma_m \vec{E} \right) \tag{2.18}$$

These equations are also commonly used in their integral forms, which are introduced in the respective sections. Also, the definition of the electric charge density ρ, the electric permittivity $\epsilon_0 \epsilon_m^{'}$, the magnetic permeability $\mu_0 \mu_m^{'}$ and the electric conductivity σ_m are introduced in detail in the following sections. The relation between the electric and magnetic field $\vec{E}$, $\vec{H}$ and the respective flux density $\vec{D}$, $\vec{B}$ is introduced in equation (2.48) (p. 42) for non-attenuating media.

2.5 Boundary conditions of the electric and magnetic field components parallel to the interface

This section is dedicated to the derivation of the boundary conditions for the tangential components of arbitrary electric and magnetic fields propagating through a boundary surface. The derivation of these boundary conditions is based on Maxwell's equations and contains no assumption about the wave model chosen for representation of the electric or magnetic field. To achieve an easy comprehensible graphical depiction a uniform, harmonic plane wave of incidence, polarized parallel to the plane of incidence and propagating in an isotropic, non-attenuating material is depicted in figure 2.3. The p-polarized wave

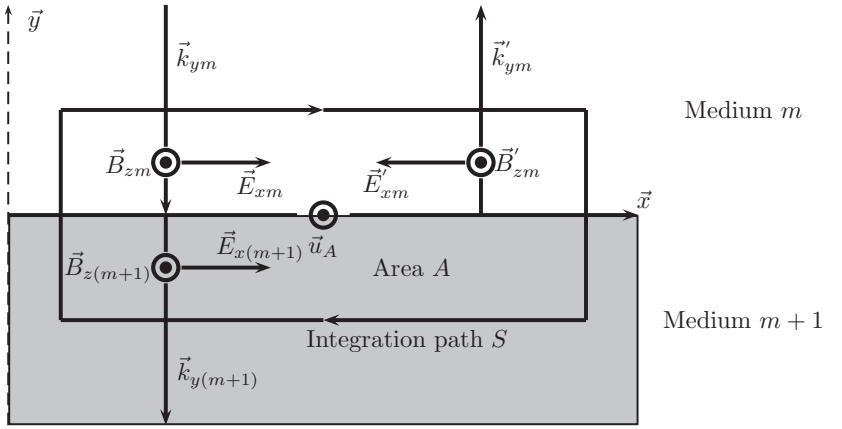

Figure 2.4: Integration path on the plane of incidence for the p-polarized wave to illustrate the continuity conditions of the electric field's tangential components at the boundary surface of the interface. Only the perpendicular components of the wave vector and the tangential components of the electric field are depicted, since the perpendicular electric field components $\vec{E}_y$ do not contribute to the line integral.

of incidence depicted in figure 2.4 contains an electrical field component $\vec{E}_{xm}$, which is oriented parallel to the boundary surface in the x-z-plane. This tangential component of the electric field is orthogonal to the y-component of the wavefronts direction vector $\vec{k}_{ym}$.

The third Maxwell equation (Faraday's Law of Induction) in its differential form is given by equation (2.17). It states, that a variation in the magnetic flux density causes an electric vortex field [111]. To obtain the continuity conditions for the electric field components parallel to the boundary surface, equation (2.17) is used to determine the surface integral over the area enclosed by the integration path S in the x-y-plane. In figure 2.4 the area of

integration and its enclosing integration path S are depicted. The unit vector $\vec{u}_A$ of the integration surface is oriented parallel to the boundary surface in z-direction. Therefore, the integration surface immerges into both media. By applying Stoke's theorem the surface integral over the curl of the electric field on the left hand side of equation (2.17) can be expressed as a line integral over the frame S enclosing the integration surface [111]. Thus, the integral form of Maxwell's third equation results in equation (2.19).

$$\oint_S \vec{E} \cdot d\vec{s} = -\iint_A \frac{\partial}{\partial t}\vec{B} \cdot d\vec{A} \tag{2.19}$$

The left hand side of equation (2.19) can be expressed as the sum of two simple line Integrals [133].

$$\int \vec{E}^{(m)} \cdot d\vec{x} - \int \vec{E}^{(m+1)} \cdot d\vec{x} = \vec{x} \cdot (\vec{E}^{(m)} - \vec{E}^{(m+1)}) \tag{2.20}$$

Where $\vec{E}^{(m)} = \sum \vec{E}_m$ represents the sum of the electric field's components in the medium characterized by the refractive index n_m and $\vec{E}^{(m+1)} = \sum \vec{E}_{(m+1)}$ represents the sum of the electric field's components in the medium characterized by the refractive index n_{m+1}. The unit vector $\vec{x}$ describes the direction of integration for the case depicted in figure 2.4, considering an infinitesimal width of the integration surface in the y-direction. As shown on the right hand side of equation (2.20) the solution of the line integral is given as the scalar product of the integration path $\vec{x}$ with the sum of field components in the respective medium. Since the scalar product causes a projection of the field vector on the integration path, which is oriented parallel to the boundary surface, this implicitly contains the confinement of the boundary condition to the tangential field components.

The field components $\vec{E}_y$ of the p-polarized wave (see figure 2.3) may be neglected, since they do not contribute to the line integral for the considered integration path. Under the assumption of an infinitesimal width of the integration surface in y-direction orthogonal to the boundary surface, the surface integral over the magnetic flux density on the right hand side of equation (2.19) converges to zero. Inserting this assumption in equation (2.20), yields the continuity of the electric field components parallel to the boundary surface.

$$\vec{x} \cdot (\vec{E}^{(m)} - \vec{E}^{(m+1)}) = 0 \tag{2.21}$$

Introducing the unit vector $\vec{u}_{bs} = \vec{y}$, which is the normal vector of the boundary surface pointing towards y-direction by the conventions of figure 2.4, equation (2.21) can be rewritten in terms of a vector product. This is useful since it covers the confinement to tangential components for both, TE- and TM-polarized electric fields [114, 115].

$$\begin{aligned}
&\vec{x} = -(\vec{u}_A \times \vec{u}_{bs}) \\
&(\vec{u}_A \times \vec{u}_{bs}) \cdot (\vec{E}^{(m+1)} - \vec{E}^{(m)}) = 0 \\
&\text{Using the identity: } (\vec{a} \times \vec{b}) \cdot \vec{c} = (\vec{b} \times \vec{c}) \cdot \vec{a} = (\vec{c} \times \vec{a}) \cdot \vec{b} \\
&(\vec{u}_{bs} \times (\vec{E}^{(m+1)} - \vec{E}^{(m)})) \cdot \vec{u}_A = 0 \\
&\vec{u}_{bs} \times (\vec{E}^{(m+1)} - \vec{E}^{(m)}) = 0
\end{aligned} \tag{2.22}$$

In equation (2.22) the scalar product with the integration path $\vec{x}$ from equation (2.21) is no longer visible, but since (2.22) equals (2.21) it is still including it. Thus, the equations (2.21) and (2.22) apply to any arbitrary electrical field vector $\vec{E}$ independent of polarization and generally state the continuity of the electric field's tangential components. Therefore, any valid solution of the wave equation used to describe the electric field's propagation at a boundary surface has to satisfy equation (2.22).

By analogue consideration of the magnetic field components parallel to the boundary surface $\vec{H} = \mu_m \cdot \vec{B}$ the fourth Maxwell equation (2.18), which is correlated to the extended form of Ampere's circuital law, is used to show their continuity. Thereby μ_m denotes the real valued permeability $\mu_m = \mu_0 \cdot \mu_m^{'}$, which connects the magnetic field with the magnetic flux density. Under consideration of a conducting boundary surface with electric conductivity σ_m, equation (2.23) describes the integral form of the fourth Maxwell equation [111]. The direction of integration is oriented at the situation depicted in figure 2.4. Therefore the vector normal to the surface $\widetilde{A}$ is oriented parallel to the boundary surface in negative x-direction and the integration surface is enclosed by the integration path $\widetilde{S}$.

$$\oint_{\widetilde{S}} \vec{H} \cdot d\vec{\widetilde{s}} = \epsilon_0 \epsilon_m^{'} \iint_{\widetilde{A}} \frac{\partial}{\partial t} \vec{E} \cdot d\vec{\widetilde{A}} + \iint_{\widetilde{A}} \sigma_m \vec{E} \cdot d\vec{\widetilde{A}} \tag{2.23}$$

In equation (2.23) the constant $\epsilon_m^{'}$ denotes the real part of the relative electric permittivity. By considering the case of an infinitesimal surface of integration the continuity condition for the magnetic field components parallel to the boundary surface results.

$$\vec{z} \cdot (\vec{H}^{(m)} - \vec{H}^{(m+1)}) = 0 \tag{2.24}$$

As already shown for the parallel components of the electric field, equation (2.24) can be expressed as a vector product using the unit vector normal to the boundary surface $\vec{u}_{bs}$.

$$\vec{u}_{bs} \times (\vec{H}_m^{(m+1)} - \vec{H}_m^{(m)}) = 0 \tag{2.25}$$

The boundary conditions for the parallel components of the electric field in equation (2.21),(2.22) and magnetic field in equation (2.24),(2.25) have to be satisfied by the uniform as well as the non-uniform wave model since no assumptions were made during the derivation concerning the form of the wave vector.

2.6 Boundary conditions of the electric and magnetic flux density components orthogonal to the interface

This section is dedicated to the derivation of the boundary conditions for the orthogonal components of arbitrary electric and magnetic fields propagating through a boundary surface. The derivation of these boundary conditions is based on Maxwell's equations and contains no assumption about the wave model chosen for representation of the electric or magnetic field. To achieve an easy comprehensible graphical depiction a uniform, harmonic plane wave of incidence, which is polarized parallel to the plane of incidence and propagating in an isotropic, non-attenuating material is depicted in figure 2.3 (see p. 30). The p-polarized wave of incidence depicted in figure 2.5 contains an electric flux

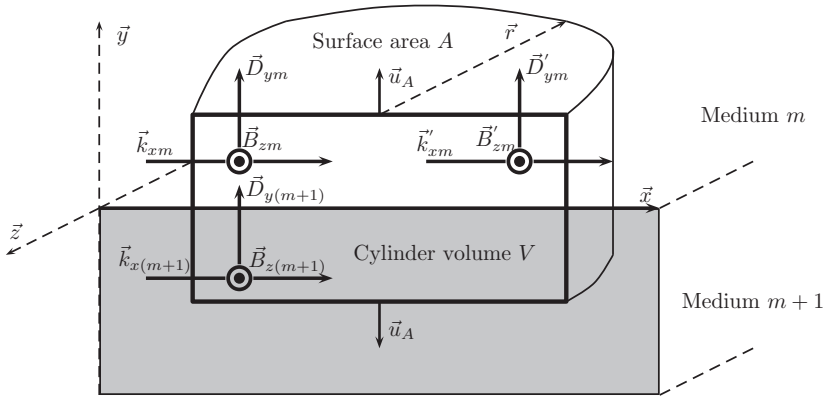

Figure 2.5: Cylindrical integration volume in the plane of incidence of the p-polarized wave, used to check whether the continuity conditions of the electric flux density components orthogonal to the boundary surface are satisfied.

density component $\vec{D}_{ym}$, which is directed orthogonal to the boundary surface in the x-z-plane. This orthogonal component of the electric flux density is also perpendicular to the x-component of the direction vector of the wavefront $\vec{k}_{xm}$.

The first Maxwell equation, Gauss's law for the electric field, is given in its differential form by equation (2.15) (see p. 31).

It states, that the electric charge density ρ is the source of the electric field [111]. For a charge free space it can be concluded, that the divergence of the electric flux density equals zero $\vec{\nabla} \cdot \vec{D} = 0$. To obtain the continuity conditions for the electric flux density components orthogonal to the boundary surface the volume integral over the enclosed cylindrical volume V is determined using equation (2.15). Figure 2.5 shows the volume of integration with its enclosing surface A. The vector $\vec{u}_A$ normal to the cylinder surface, is oriented perpendicular to the boundary surface in y-direction on the top side of the cylinder. Therefore, the cylinder volume immerses into both media. Gauss's divergence theorem states, that the surface integral over a closed surface, which is penetrated by a vector field, equals the volume integral over the divergence of this vector field integrated over the enclosed volume [134]. By applying Gauss's divergence theorem to equation (2.15), the integral form of the first Maxwell equation given in (2.26) results.

$$\oiint_A \vec{D} \cdot d\vec{A} = \iiint_V \rho \, dV \tag{2.26}$$

The p-polarized wave's electric flux density components $\vec{D}_x$ parallel to the boundary surface, pierce through the curved surface area of the cylinder and therefore, do not contribute to the surface integral. The surface integral over the electric flux density components $\vec{D}_y$ orthogonal to the boundary surface is therefore proportional to the circular top and bottom side of the cylinder, this yields equation (2.27).

$$\oiint_A \vec{D} \cdot d\vec{A} = \pi r^2 \vec{u}_A \cdot (\vec{D}^{(m)} - \vec{D}^{(m+1)}) \tag{2.27}$$

Where $\vec{D}^{(m)}$ denotes the sum of the electric flux density components in the medium with refractive index n_m and $\vec{D}^{(m+1)}$ denotes the sum of the electric flux density components in the medium with refractive index n_{m+1}. Here again as already described in section 2.5 the integration results in a scalar product of the field components with a unit vector. The arbitrary vectors of the electric flux density $\vec{D}$ are projected on the integration surfaces normal vector $\vec{u}_A$, which is orthogonal to the boundary surface, and therefore implicates the confinement of the boundary conditions described in equation (2.28) to the orthogonal field components. Assuming that the boundary surface is free of charges and the cylinder height is infinitesimal, the charge density ρ enclosed in the cylinder volume equals zero $\rho = 0$. Thus, the volume integral on the right hand side of equation (2.26) also converges to zero. From applying this constraint and the result from equation (2.27) to equation (2.26) results the continuity condition for the orthogonal components of the electric flux density.

$$\pi r^2 \vec{u}_A \cdot (\vec{D}^{(m)} - \vec{D}^{(m+1)}) = 0 \tag{2.28}$$

Analogue the second Maxwell equation 2.16, Gauss's law for the magnetic field, can be used to demonstrate the continuity of the magnetic flux density components orthogonal to the boundary surface $\vec{B}_y$ of a s-polarized wave as shown in figure 2.2 (see p. 29). To do so the volume integral over the divergence of the magnetic flux density is used. The

integration volume is chosen as a cylinder, as depicted in figure 2.5, immersing into both media. The integral form of the second Maxwell equation is given in equation (2.29).

$$\oiint_A \vec{B} \cdot d\vec{A} = 0 \tag{2.29}$$

The surface integral over the magnetic flux density in equation (2.29) always equals zero, since the magnetic field is solenoidal. If the case of an infinitesimal height of the cylinder is considered and the surface integral on the left hand side of equation (2.29) is solved, the continuity conditions for the magnetic flux density components orthogonal to the boundary surface result immediately.

$$\pi r^2 \vec{u}_A \cdot (\vec{B}^{(m)} - \vec{B}^{(m+1)}) = 0 \tag{2.30}$$

2.7 Maxwell's equations and the dispersion relation of the non-uniform plane wave

Maxwell's equations are valid independent of the considered wave model. They actually can be used to check the validity of the wave model. If the wave model's wave vector, electric and magnetic field do not solve Maxwell's equations the model would be unfeasible to describe the wave propagation. Maxwell's first curl equation is given in (2.17) (see p. 31) and (2.31).

$$\vec{\nabla} \times \underline{\vec{E}}_m + \mu_m \frac{d}{dt} \underline{\vec{H}}_m = 0 \tag{2.31}$$

Maxwell's second curl equation is given in (2.18) (see p. 31) and (2.32).

$$\vec{\nabla} \times \underline{\vec{H}}_m - \epsilon_0 \epsilon_m^{'} \frac{d}{dt} \underline{\vec{E}}_m = \sigma_m \underline{\vec{E}}_m \tag{2.32}$$

In (2.32) the parameter $\sigma_m \in \mathbb{R}$ describes the material dependent electrical conductivity. Using the non-uniform wave model specified by (2.8), (2.10) and (2.11) in Maxwell's first curl equation (2.31) and calculating the rotation of the electric and the time derivative of the magnetic field results in equation (2.33).

$$\begin{aligned} & j \left(\vec{\alpha}_m + j \vec{\beta}_m \right) \times \underline{\vec{E}}_m - j \omega_0 \mu_m \underline{\vec{H}}_m = 0 \\ \Rightarrow \underline{\vec{H}}_m &= \frac{1}{\omega_0 \mu_m} \underline{\vec{k}}_m^{(\mathrm{nu})} \times \underline{\vec{E}}_m \end{aligned} \tag{2.33}$$

This provides the phasor representations of the magnetic field's dependence on the electric field for a non-uniform, plane wave in compliance with Cannings contributions [115–117]. Using the non-uniform wave model specified by (2.8), (2.10) and (2.11) (see p. 27) in Maxwell's second curl equation (2.32) and calculating the rotation of the magnetic and the time derivative of the electric field results in equation (2.34).

$$\begin{aligned} & j \left(\vec{\alpha}_m + j \vec{\beta}_m \right) \times \underline{\vec{H}}_m = -j \omega_0 \epsilon_0 \epsilon_m^{'} \underline{\vec{E}}_m + \sigma_m \underline{\vec{E}}_m \\ \Rightarrow & \underline{\vec{k}}_m^{(\mathrm{nu})} \times \underline{\vec{H}}_m = -\omega_0 \epsilon_0 \left(\epsilon_m^{'} + j \frac{\sigma_m}{\omega_0 \epsilon_0} \right) \underline{\vec{E}}_m \\ \Rightarrow & \underline{\vec{E}}_m = \frac{-1}{\omega_0 \underline{\epsilon}_m} \underline{\vec{k}}_m^{(\mathrm{nu})} \times \underline{\vec{H}}_m \end{aligned} \tag{2.34}$$

Here $\underline{\epsilon}_m = \epsilon_0 \left(\epsilon_m^{'} + j \epsilon_m^{''} \right)$ denotes the complex electric permittivity. For more information concerning its time and frequency domain notations see section 2.12. To find the relation describing the material dependence of the wave vector a second representation of equation (2.34) is required. This is found by applying the rotation operator to both sides of equation (2.33) and employing the vector triple product expansion

$\vec{a} \times \left(\vec{b} \times \vec{c}\right) = \left(\vec{a} \cdot \vec{c}\right)\vec{b} - \left(\vec{a} \cdot \vec{b}\right)\vec{c}$ [131, p. 15]. The details of this transformation are presented in [115]. The result is:

$$\begin{aligned} \underline{\vec{E}}_m &= -\omega_0 \mu_m \frac{\left(\vec{\alpha}_m + j\vec{\beta}_m\right) \times \underline{\vec{H}}_m}{\left[\alpha_m^2 - \beta_m^2 + 2j\alpha_m\beta_m \cos\left(\rho_m\right)\right]} \\ \Rightarrow \underline{\vec{E}}_m &= -\omega_0 \mu_m \frac{\vec{\underline{k}}_m^{(\mathrm{nu})} \times \underline{\vec{H}}_m}{\vec{\underline{k}}_m^{(\mathrm{nu})} \cdot \vec{\underline{k}}_m^{(\mathrm{nu})}} \end{aligned} \tag{2.35}$$

In (2.35) ρ_m is the angle enclosed between the wave vector's real and imaginary part. By comparing the coefficients of (2.34) and (2.35) the dispersion relation of the complex non-uniform wave vector is derived using the phase attenuation vector notation with effective propagation constants.

$$\begin{aligned} \omega_0^2 \mu_m \underline{\epsilon}_m &= \vec{\underline{k}}_m^{(\mathrm{nu})} \cdot \vec{\underline{k}}_m^{(\mathrm{nu})} \\ \Rightarrow \omega_0^2 \mu_m \underline{\epsilon}_m &= \alpha_m^2 - \beta_m^2 + 2j\alpha_m\beta_m \cos\left(\rho_m\right) \end{aligned} \tag{2.36}$$

The derivation of (2.36) is also presented in [135]. The dispersion relation of the non-uniform wave is used in the determination of the effective propagation constants α_m and β_m. Common approaches for this procedure are discussed and compared in [128].

Equations (2.34) and (2.35) are general results from Maxwell's equations and therefore, also account for the uniform wave model. However, if the uniform wave vector from equation (2.4) is employed the dispersion relation of the uniform wave results.

$$\begin{aligned} \omega_0^2 \mu_m \underline{\epsilon}_m &= \vec{\underline{k}}_m \cdot \vec{\underline{k}}_m \\ \Rightarrow \omega_0^2 \mu_m \underline{\epsilon}_m &= \alpha_{0m}^2 - \beta_{0m}^2 + 2j\alpha_{0m}\beta_{0m} \end{aligned} \tag{2.37}$$

This is solely dependent on the intrinsic propagation constants. The dispersion relation in equation (2.37) also results if the complex angle notation of the wave vector of the non-uniform wave is employed in (2.34) and (2.35). This may cause confusion, but is a reasonable result since the complex angle notation of the non-uniform wave vector is also dependent on the intrinsic propagation constants, which contain no information about the actual wavefront propagation. It is easy to confuse the uniform wave vector and the complex angle notation of the non-uniform wave vector when only considering the dispersion relation, but it is important to distinguish between them, since they yield different results in the deviation of Snell's law. More details concerning the non-uniform wave vector in complex angle notation are given in [128]. The general information contained in equation (2.36) and (2.37) is that the intrinsic propagation constants are fully determined by the parameters of the medium and the wave's frequency [135]. The effective propagation constants are not fully determined by this, but also depend on the propagation direction.

2.8 Snell's Law for the non-uniform wave model

The boundary condition of continuous propagation for the tangential field components, introduced in equation (2.22) and revisited in a more general notation in (2.57) and (2.58) (see p. 46) through the interface between two different media leads to the constraint that the wave vectors also have to propagate continuously through the interface. Thus, satisfying

$$\underline{\vec{k}}_m^{(\mathrm{nu})} \cdot \vec{r}_\parallel = \underline{\vec{k}}_m^{(\mathrm{nu})'} \cdot \vec{r}_\parallel + c_m^{'} = \underline{\vec{k}}_{m+1}^{(\mathrm{nu})} \cdot \vec{r}_\parallel + c_{m+1} \tag{2.38}$$

with $\vec{r}_\parallel$ lying in the boundary surface spanned by the direction vectors $\vec{u}_2$ and $\vec{u}_3$ in figure 2.1 pointing to an arbitrary point on the boundary surface and $c_m^{'},\ c_{m+1} \in \mathbb{R}$ are real constants depending on the position of the coordinate system's origin [110–112, 115, 137]. Assuming that the coordinate system's origin is chosen such that $c_m^{'} = c_{m+1} = 0$, introducing the normal vector of the boundary surface $\vec{u}_{bs} = -\vec{u}_1$ and using the identity $\vec{r}_\parallel = -\vec{u}_{bs} \times \left(\vec{u}_{bs} \times \vec{r}_\parallel\right)$ which is valid on the interface [115], (2.38) can be formulated by:

$$\underline{\vec{k}}_m^{(\mathrm{nu})} \times \vec{u}_{bs} = \underline{\vec{k}}_{m+1}^{(\mathrm{nu})} \times \vec{u}_{bs} \tag{2.39}$$

Substituting the non-uniform wave vector by its phase attenuation vector representation according to equation (2.8) and considering that the cross product $\vec{u}_1 \times \vec{u}_{bs} = 0$ results in:

$$\begin{aligned} &(\alpha_m \sin(\xi_m + \rho_m)\vec{u}_2 + j\beta_m \sin(\xi_m)\vec{u}_2) \times \vec{u}_{bs} \\ &= (\alpha_{m+1} \sin(\xi_{m+1} + \rho_{m+1})\vec{u}_2 + j\beta_{m+1} \sin(\xi_{m+1})\vec{u}_2) \times \vec{u}_{bs} \end{aligned} \tag{2.40}$$

Since $\vec{u}_2 \times \vec{u}_{bs} = \vec{u}_3$ on both sides of equation (2.40) the direction vector is eliminated. Thus, Snell's law of refraction for the non-uniform wave model with coplanar propagation vectors results.

$$\alpha_m \sin(\xi_m + \rho_m) + j\beta_m \sin(\xi_m) = \alpha_{m+1} \sin(\xi_{m+1} + \rho_{m+1}) + j\beta_{m+1} \sin(\xi_{m+1}) \tag{2.41}$$

Substituting the non-uniform wave vector by its complex angle representation according to equation (2.9) and considering that the cross product $\vec{u}_1 \times \vec{u}_{bs} = 0$ results in Snell's law of refraction for the non-uniform wave model with coplanar propagation vectors in complex angle notation (2.42).

$$(\alpha_{0m} + j\beta_{0m}) \sin(\underline{\theta}_m) = \left(\alpha_{0(m+1)} + j\beta_{0(m+1)}\right) \sin(\underline{\theta}_{m+1}) \tag{2.42}$$

Equations (2.41) and (2.42) are both valid representations of Snell's law in the non-uniform wave model. More details concerning the interpretability of these notations are given in [128]. In the special case, that the m-th medium is loss free $\beta_m = 0$ and $\xi_m = 0$, as depicted in figure 2.1 Snell's law takes the following form.

$$\alpha_m \sin(\rho_m) = \alpha_{m+1} \sin(\xi_{m+1} + \rho_{m+1}) + j\beta_{m+1} \sin(\xi_{m+1}) \tag{2.43}$$

Substituting the uniform wave vector from equation (2.4) in equation (2.39), which generally describes Snell's law as a vector product independent of the wave model, results in:

$$\begin{aligned} &(\alpha_{0m} + j\beta_{0m})\,\vec{u}_{km} \times \vec{u}_{bs} = \left(\alpha_{0(m+1)} + j\beta_{0(m+1)}\right)\vec{u}_{k(m+1)} \times \vec{u}_{bs} \\ \Rightarrow\; &(\alpha_{0m} + j\beta_{0m})\sin(\rho_m) = \left(\alpha_{0(m+1)} + j\beta_{0(m+1)}\right)\sin(\rho_{(m+1)}) \end{aligned} \tag{2.44}$$

Considering the special case, that the m-th medium is loss free $\beta_{0m} = 0$, as depicted in figure 2.1, equation (2.44) takes the following form.

$$\alpha_{0m}\sin(\rho_m) \stackrel{!}{=} \left(\alpha_{0(m+1)} + j\beta_{0(m+1)}\right)\sin(\rho_{(m+1)}) \tag{2.45}$$

Obviously, applying the uniform wave model, there is no valid solution for equation (2.45), besides the special case $\rho_{(m+1)} = 0$, if the m-th medium is loss free and the (m+1)-th medium is attenuating $\beta_{0(m+1)} \neq 0$. In common literature like [110–112, 114] the problem occurring in equation (2.44) is commonly omitted by switching to the non-uniform wave model in its complex angle notation without introducing the correct wave vector or mentioning this. Thus, the derivation of Snell's law at interfaces to attenuating media requires the application of the non-uniform wave model. The derivations presented in [110–112, 114] are inconsistent, but the presented results are correct.

2.9 Fresnel's equation in non-attenuating media

By the law of reflection (2.46) and Snell's law of refraction (2.47), which are described in detail in [111,130,133], the propagation properties of the wave vectors $\vec{k}_m, \vec{k}_m^{'}, \vec{k}_{(m+1)}$ of the incident, reflected and transmitted, linearly polarized, harmonic, uniform plane wave in isotropic, loss free media are given in their complex phasor expression as $\underline{\vec{E}}_m, \underline{\vec{E}}_m^{'}, \underline{\vec{E}}_{(m+1)}$. By the law of reflection (2.46), the law of refraction (2.47), the frequency condition $\omega_m = \omega_m^{'} = \omega_{(m+1)}$ and the boundary conditions derived in the above section for the tangential components of the electric and magnetic field (2.21), (2.24) and the orthogonal components of the electric and magnetic flux density (2.28), (2.30), the reflection and transmission properties of the wave of incidence can be completely described [111, 130, 133].

$$\theta_m = \theta_m^{'} \tag{2.46}$$

$$n_m \sin(\theta_m) = n_{(m+1)} \sin(\theta_{(m+1)}) \tag{2.47}$$

The equations, which characterize the behavior of the propagation direction and amplitude of the wave during reflection and transmission are called Fresnel's equations and are motivated here for the case of a linearly polarized, harmonic, uniform plane wave, propagating in an isotropic, loss free medium.

Besides the already mentioned relations, material specific equations are required, which describe the connection between permittivity, permeability and refractive index as well as the connection between electric and magnetic field components. These material equations can get sophisticated if they shall apply for universal materials, but in the assumed case of loss free, isotropic materials they have a simple formulation. The relevant material equations are summarized in equation (2.48) according to [130, 132].

$$\begin{array}{ll}
\vec{D} = \epsilon_0 \epsilon_m^{'} \vec{E} = \epsilon_m \vec{E} & \text{Permittivity} \\
\vec{B} = \mu_0 \mu_m^{'} \vec{H} = \mu_m \vec{H} & \text{Permeability} \\
c_0 = \frac{1}{\sqrt{\epsilon_0 \mu_0}} & \text{Light velocity in vacuum} \\
c = \frac{1}{\sqrt{\epsilon_m \mu_m}} = \frac{c_0}{\sqrt{\epsilon_m^{'} \mu_m^{'}}} = \frac{c_0}{\underline{n}_m} & \text{Light velocity in matter} \\
n_m = \sqrt{\epsilon_m^{'} \mu_m^{'}} \approx \sqrt{\epsilon_m^{'}}|_{(\mu_m^{'} \approx 1)} & \text{Maxwell-Relation} \\
E = Bc & \text{Absolute relation el. field to mag. flux density} \\
\vec{E} = \vec{B} \times \vec{c} & \text{Vector relation el. field to mag. flux density} \\
E = \sqrt{\frac{\mu_m}{\epsilon_m}} H & \text{Absolute relation el. field to mag. field} \\
\vec{E} = \vec{H} \times \sqrt{\frac{\mu_m}{\epsilon_m}} \vec{k} & \text{Vector relation el. field to mag. field}
\end{array} \tag{2.48}$$

The derivation of Fresnel's equations is described in [111, 129–131, 133, 134, 139] and will be summarized here.

2.9.1 Reflection and transmission of TE-light polarized perpendicular to the plane of incidence

In this section the reflection and transmission coefficients for an inclining, transverse electric (TE) polarized, harmonic, uniform plane wave propagating in an isotropic non-attenuating medium are derived.
The reflection coefficient is defined as $\left(\frac{E_m^{'}}{E_m}\right)_{\perp}$.
The transmission coefficient is defined as $\left(\frac{E_{(m+1)}}{E_m}\right)_{\perp}$. Therefore, the task is to determine the reflected $\vec{\underline{E}}_m^{'}(x,y,z,t)$ and transmitted $\vec{\underline{E}}_{(m+1)}(x,y,z,t)$ wave, based on the known wave of incidence given in equation (2.13) (see p. 28) and depicted in figure 2.2. Thus, a linear equation system containing two equations in dependence of the unknown waves is required. Those equations result from the boundary conditions for the electric and magnetic field components parallel to the boundary surface given in equation (2.21) and (2.24). As depicted in figure 2.2 the TE-polarized wave of incidence does only include an electric field component parallel to the boundary surface in z-direction, $\underline{E}_m(x,y,z,t) = E_{zm} \cdot e^{j(k_{xm} \cdot x + k_{ym} \cdot y - \omega_0 t)}$. This is employed in equation (2.21) to yield the first conditional equation from the boundary conditions of the electric fields tangential components.

$$\underline{E}_m(x, y = 0, z, t) + \underline{E}_m^{'}(x, y = 0, z, t) = \underline{E}_{(m+1)}(x, y = 0, z, t) \tag{2.49}$$

In equation (2.49) the y-component is assumed to be zero $y = 0$, since the boundary surface lies in the x-z-plane and the boundary conditions apply only inside the boundary surface. Considering the continuity of the wave vector's x-components $k_{xm} = k_{xm}^{'} = k_{x(m+1)} \mid_{y=0}$, derived in equation (2.21) for the electric field components parallel to the boundary surface, the propagation of the wave in the x-y-plane with $z = 0$ and the frequency condition $\omega_m = \omega_m^{'} = \omega_{(m+1)}$, the complex exponential functions of the inclining, reflected and transmitted wave all have the same value in the x-z-plane and compensate each other. The same applies for the arguments of the cosine terms, if the wave functions are written in their real field expression. Using this, equation (2.49) can be expressed as the sum of the absolute electric field components.

$$E_m + E_m^{'} = E_{(m+1)} \tag{2.50}$$

The second conditional equation results from the continuity of the magnetic field's parallel components given in equation (2.24). Analog to the electric field it is sufficient to consider the absolute value of the magnetic field's tangential components, since the complex phase terms compensate each other in the boundary surface. Referring to figure 2.2 the continuity conditions for the magnetic field's components parallel to the boundary surface are described by equation (2.51) [111].

$$\begin{aligned} &\left(\vec{H}_m + \vec{H}_m^{'}\right) \cdot \vec{x} = \vec{H}_{(m+1)} \cdot \vec{x} \\ &- H_m \cos(\theta_m) + H_m^{'} \cos(\theta_m^{'}) = -H_{(m+1)} \cos(\theta_{(m+1)}) \end{aligned} \tag{2.51}$$

Considering the relation between electric and magnetic field from equation (2.48), equation (2.51) is expressed in terms of the electric field components $E_m,\ E_m^{'},\ E_{(m+1)}$. Since the electric and magnetic field are linked by the cross product $\vec{E} = \vec{H} \times \sqrt{\frac{\mu_m}{\epsilon_m}}\vec{k}$, it can be concluded that the electric field components derived from the magnetic field's tangential components point towards the same direction as $\vec{E}_m,\ \vec{E}_m^{'},\ \vec{E}_{(m+1)}$. Thus, the second conditional equation for the electric field results from the boundary conditions of the magnetic field's parallel components.

$$\frac{n_m}{\mu_m}\left(E_m - E_m^{'}\right)\cos(\theta_m) = \frac{n_{(m+1)}}{\mu_{(m+1)}}E_{(m+1)}\cos(\theta_{(m+1)}) \tag{2.52}$$

By solving the linear equation system consisting of equation (2.50) and (2.52) the desired amplitude ratio of the incident and reflected or transmitted wave results. These equations are called Fresnel's equations for the s-polarized wave [111].

$$\begin{aligned}\left(\frac{E_m^{'}}{E_m}\right)_{\perp} &= \frac{\frac{n_m}{\mu_m}\cos(\theta_m) - \frac{n_{(m+1)}}{\mu_{(m+1)}}\cos(\theta_{(m+1)})}{\frac{n_m}{\mu_m}\cos(\theta_m) + \frac{n_{(m+1)}}{\mu_{(m+1)}}\cos(\theta_{(m+1)})} \\ \left(\frac{E_{(m+1)}}{E_m}\right)_{\perp} &= \frac{2\frac{n_m}{\mu_m}\cos(\theta_m)}{\frac{n_m}{\mu_m}\cos(\theta_m) + \frac{n_{(m+1)}}{\mu_{(m+1)}}\cos(\theta_{(m+1)})}\end{aligned} \tag{2.53}$$

In dielectric media, where the permeability is given by $\mu_m \approx \mu_{(m+1)} \approx \mu_0$, equation (2.53) can be simplified.

2.9.2 Reflection and transmission of TM-light polarized parallel to the plane of incidence

In this section the reflection- and transmission coefficients for an inclining, transverse magnetic (TM) polarized, homogenous, harmonic, plane wave propagating in an isotropic non-attenuating medium are derived.
The reflection coefficient is defined as $\left(\frac{E_m^{'}}{E_m}\right)_{\parallel}$.
The transmission coefficient is defined as $\left(\frac{E_{(m+1)}}{E_m}\right)_{\parallel}$.

Therefore, the task is to determine the reflected $\underline{\vec{E}}_m^{'}(x,y,z,t)$ and transmitted $\underline{\vec{E}}_{(m+1)}(x,y,z,t)$ wave based on the known incident wave given in equation (2.14). Thus, a linear equation system containing two equations in dependence of the unknown waves is required. Those equations result from the boundary conditions for the electric and magnetic field components parallel to the boundary surface given in equation (2.21) and (2.24). As shown in figure 2.3 the inclining, electromagnetic wave $\underline{\vec{E}}_m(x,y,z,t)$ includes an electric field component $E_{xm} = E_m \cdot \cos(\theta_m)$ oriented tangential to the boundary surface and a component $E_{ym} = E_m \cdot \sin(\theta_m)$ oriented perpendicular to the boundary surface.

As introduced in section 2.9.1 it is suitable to consider the absolute value of the electric or magnetic field amplitudes, since for complex notation the complex exponential functions and for real notation the cosine functions compensate each other on the boundary surface. Applying these simplifications, motivated in more detail in section 2.9.1, the first conditional equation is formulated using the boundary conditions for the electric fields tangential components from equation (2.21) with the notations of figure 2.3.

$$\begin{aligned} \left(\vec{E}_m + \vec{E}_m^{'}\right) \cdot \vec{x} &= \vec{E}_{(m+1)} \cdot \vec{x} \\ \left(E_m - E_m^{'}\right) \cos(\theta_m^{'}) &= E_{(m+1)} \cos(\theta_{(m+1)}) \end{aligned} \tag{2.54}$$

The boundary conditions for the magnetic field's tangential components, yield the second conditional equation analogous to section 2.9.1.

$$\begin{aligned} H_m + H_m^{'} &= H_{(m+1)} \\ \frac{n_m}{\mu_m}(E_m + E_m^{'}) &= \frac{n_{(m+1)}}{\mu_{(m+1)}} E_{(m+1)} \end{aligned} \tag{2.55}$$

By solving the linear equation system consisting of equation (2.54) and (2.55) the desired amplitude ratio of the inclining and reflected or transmitted wave results. These equations are called Fresnel's equations for the p-polarized wave [111].

$$\begin{aligned} \left(\frac{E_m^{'}}{E_m}\right)_{\parallel} &= \frac{\frac{n_{(m+1)}}{\mu_{(m+1)}} \cos(\theta_m) - \frac{n_m}{\mu_m} \cos(\theta_{(m+1)})}{\frac{n_{(m+1)}}{\mu_{(m+1)}} \cos(\theta_m) + \frac{n_m}{\mu_m} \cos(\theta_{(m+1)})} \\ \left(\frac{E_{(m+1)}}{E_m}\right)_{\parallel} &= \frac{2\frac{n_m}{\mu_m} \cos(\theta_m)}{\frac{n_{(m+1)}}{\mu_{(m+1)}} \cos(\theta_m) + \frac{n_m}{\mu_m} \cos(\theta_{(m+1)})} \end{aligned} \tag{2.56}$$

For dielectric media with permeability $\mu_m \approx \mu_{(m+1)} \approx \mu_0$, equation (2.56) can be simplified.

2.10 Fresnel equations for lossy media in complex phasor expression

The basic linear equation system from which the Fresnel coefficients result is given by the boundary conditions of the electric and magnetic field components parallel to the interface (2.57) and (2.58), which are immediate results of Maxwell's first (2.31) and second (2.32) curl equation [110, 112, 114, 115]. The boundary conditions for the electric field's components parallel to the interface are given in two common representations with respect to their polarization by (2.57), using the coordinate system introduced above in figure 2.1.

$$\begin{aligned} &\text{TE: } \vec{u}_3 \cdot (\underline{\vec{E}}^{(m)} - \underline{\vec{E}}^{(m+1)}) = 0 \quad \text{TM: } \vec{u}_2 \cdot (\underline{\vec{E}}^{(m)} - \underline{\vec{E}}^{(m+1)}) = 0 \\ &\text{TE or TM: } \vec{u}_1 \times (\underline{\vec{E}}^{(m+1)} - \underline{\vec{E}}^{(m)}) = 0 \end{aligned} \tag{2.57}$$

In (2.57) $\underline{\vec{E}}^{(m)}$, $\underline{\vec{E}}^{(m+1)}$ represent the sum of the electric field components in the m-th or (m+1)-th medium and $\vec{u}_1$ is the boundary surface's unit vector as depicted in figure 2.1. The boundary conditions for the magnetic field's components parallel to the interface are given in two common representations with respect to their polarization by (2.58).

$$\begin{aligned} &\text{TE: } \vec{u}_2 \cdot (\underline{\vec{H}}^{(m)} - \underline{\vec{H}}^{(m+1)}) = 0 \quad \text{TM: } \vec{u}_3 \cdot (\underline{\vec{H}}^{(m)} - \underline{\vec{H}}^{(m+1)}) = 0 \\ &\text{TE or TM: } \vec{u}_1 \times (\underline{\vec{H}}^{(m+1)} - \underline{\vec{H}}^{(m)}) = 0 \end{aligned} \tag{2.58}$$

In (2.58) $\underline{\vec{H}}^{(m)}$, $\underline{\vec{H}}^{(m+1)}$ represent the sum of the magnetic field components in the m-th and (m+1)-th medium, respectively. In the non-uniform, plane wave model the complex wave vector's real and imaginary part may point towards different directional vectors as shown in eq. (2.8). However, the direction of the electric or magnetic field of the elliptically polarized, non-uniform, harmonic, plane wave propagating in an isotropic, attenuating medium given in (2.10) or (2.11) is characterized by a single unit direction vector, which can be described as the superposition of multiple linearly polarized field vectors. Therefore, in the derivation of Fresnel coefficients only the case of linearly polarized TE- or TM-light is considered without loss of generality, since all other polarizations can be derived from this by superposition. The directional vectors of the electric and magnetic field's real and imaginary part components point towards the same direction, since the imaginary part in this case describes the time dependent oscillation of the field along this direction.

Fresnel coefficients for TM-polarization

For the case of the linearly polarized, non-uniform TM-wave considered here the magnetic field's direction vector $\vec{u}_{H_m}$ is perpendicular to the plane of incidence. Therefore, the mag-

netic field's amplitude is only oscillating in one direction, while its phase is still dependent on the non-uniform, coplanar wave vector. Figure 2.6 depicts the situation using the wave vector $\vec{\underline{k}}_m^{(\mathrm{nu})}$ according to equation (2.8) consisting of $\vec{\alpha}_m$, $\vec{\beta}_m$, and unit vectors for the direction of the magnetic field vector $\vec{u}_{H_m}$ and electric field vector $\vec{u}^1_{E_m}$, $\vec{u}^2_{E_m}$. Considering

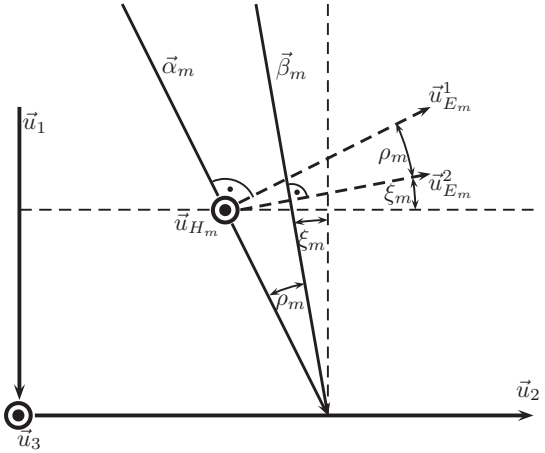

Figure 2.6: Direction vectors of the incident, coplanar, wave vector, electric and magnetic field vector for an arbitrary, TM-polarized non-uniform plane wave.

this, the first conditional equation is found by employing the boundary conditions for the magnetic field's components parallel to the boundary surface given in (2.58).

$$\begin{aligned} \left(\vec{\underline{H}}_m + \vec{\underline{H}}_m^{'}\right) \cdot \vec{u}_3 &= \vec{\underline{H}}_{m+1} \cdot \vec{u}_3 \\ \underline{H}_m + \underline{H}_m^{'} &= \underline{H}_{m+1} \end{aligned} \tag{2.59}$$

Here, $\underline{H}_m^{'}$ denotes the reflected magnetic field in the m-th medium and $\underline{H}_{m+1}$ is the transmitted field in the m+1-th medium. Since the direction vectors of $\vec{\underline{H}}_m$, $\vec{\underline{H}}_m^{'}$ and $\vec{\underline{H}}_{m+1}$, for the case of the TM-polarized wave are parallel to the vector $\vec{u}_3$ the boundary condition for the magnetic field components parallel to the interface takes the simple scalar form in the second line of equation (2.59).

The second conditional equation is derived by employing eq. (2.57) for the boundary conditions of the electric field's components parallel to the boundary surface. The unit vectors $\vec{u}^1_{E_m}$ and $\vec{u}^2_{E_m}$ are introduced to describe the directional vectors of the electric field's components. By superposition of these components the direction vector of the complex

electric field vector is described, which is polarized parallel to the plane of incidence. Therefore, the second conditional equation is given by:

$$\left(\vec{\underline{E}}_m + \vec{\underline{E}}_m^{'}\right) \cdot \vec{u}_2 = \vec{\underline{E}}_{m+1} \cdot \vec{u}_2 \tag{2.60}$$

To use (2.60) for determination of the Fresnel coefficients for the magnetic field it is necessary to express the electric field in terms of the magnetic field. Since the non-uniform wave model is applied, (2.35) has to be used. Therefore, the dependence of the electric on the magnetic field is given by:

$$\vec{\underline{E}}_m = -\omega_0 \mu_m \frac{\vec{\underline{k}}_m^{(\mathrm{nu})} \times \vec{\underline{H}}_m}{\vec{\underline{k}}_m^{(\mathrm{nu})} \cdot \vec{\underline{k}}_m^{(\mathrm{nu})}} \tag{2.61}$$

Next the special property of the TM-polarized wave, the quasi uniform magnetic field vector is exploited. Since the magnetic field of the TM-polarized wave only points towards $\vec{u}_3$-direction perpendicular to the plane of incidence the magnetic field vector for this special case takes the form:

$$\vec{\underline{H}}_m = \underline{H}_m \vec{u}_{H_m} \tag{2.62}$$

Using this in (2.61) results in (2.63).

$$\begin{aligned} \vec{\underline{E}}_m &= -\omega_0 \mu_m \underline{H}_m \frac{\left(\vec{\alpha}_m \times \vec{u}_{H_m} + j\vec{\beta}_m \times \vec{u}_{H_m}\right)}{\vec{\underline{k}}_m^{(\mathrm{nu})} \cdot \vec{\underline{k}}_m^{(\mathrm{nu})}} \\ &= \omega_0 \mu_m \underline{H}_m \frac{\left(\alpha_m \vec{u}^1_{\underline{E}_m} + j\beta_m \vec{u}^2_{\underline{E}_m}\right)}{\vec{\underline{k}}_m^{(\mathrm{nu})} \cdot \vec{\underline{k}}_m^{(\mathrm{nu})}} \end{aligned} \tag{2.63}$$

This is put into (2.60) to get the second conditional equation in dependency of the magnetic field:

$$\begin{aligned} &\omega_0 \mu_m \underline{H}_m \frac{\left(\alpha_m \vec{u}^1_{\underline{E}_m} \cdot \vec{u}_2 + j\beta_m \vec{u}^2_{\underline{E}_m} \cdot \vec{u}_2\right)}{\vec{\underline{k}}_m^{(\mathrm{nu})} \cdot \vec{\underline{k}}_m^{(\mathrm{nu})}} \\ &+\omega_0 \mu_m \underline{H}_m^{'} \frac{\left(\alpha_m \vec{u}^1_{\underline{E}'_m} \cdot \vec{u}_2 + j\beta_m \vec{u}^2_{\underline{E}'_m} \cdot \vec{u}_2\right)}{\vec{\underline{k}}_m^{(\mathrm{nu})'} \cdot \vec{\underline{k}}_m^{(\mathrm{nu})'}} \\ &=\omega_0 \mu_{m+1} \underline{H}_{m+1} \frac{\left(\alpha_{m+1} \vec{u}^1_{\underline{E}_{m+1}} \cdot \vec{u}_2 + j\vec{\beta}_{m+1} \vec{u}^2_{\underline{E}_{m+1}} \cdot \vec{u}_2\right)}{\vec{\underline{k}}_{m+1}^{(\mathrm{nu})} \cdot \vec{\underline{k}}_{m+1}^{(\mathrm{nu})}} \end{aligned} \tag{2.64}$$

Using the notations introduced in figure 2.6 the scalar products of the electric field's direction vectors and the unit vector in u_2-direction can be solved. As a result the electric field's direction vectors $\vec{u}^2_{\underline{E}_m}$, $\vec{u}^2_{\underline{E}_{m+1}}$, $\vec{u}^2_{\underline{E}'_m}$ enclose the angles ξ_m, ξ_{m+1}, $\xi_m^{'}$ with the u_2-axis, respectively, and the electric field's direction vectors $\vec{u}^1_{\underline{E}_m}$, $\vec{u}^1_{\underline{E}_{m+1}}$, $\vec{u}^1_{\underline{E}'_m}$ and the

u_2-axis include the angles $\xi_m + \rho_m,\ \xi_{m+1} + \rho_{m+1},\ \xi_m^{'} + \rho_m^{'}$, respectively. The dispersion relation of the non-uniform wave in (2.36) indicates that in the isotropic m-th medium $\vec{\underline{k}}_m^{(\mathrm{nu})} \cdot \vec{\underline{k}}_m^{(\mathrm{nu})} = \vec{\underline{k}}_m^{(\mathrm{nu})'} \cdot \vec{\underline{k}}_m^{(\mathrm{nu})'}$, which is also shown by the continuity conditions of the wave vectors at the interface in the derivation of Snell's law (2.38). Using these conditions (2.64) can be formulated in a simple scalar form:

$$\begin{aligned} &\mu_m \left(\underline{H}_m - \underline{H}_m^{'}\right) \frac{\left(\alpha_m \cos\left(\xi_m + \rho_m\right) + j\beta_m \cos\left(\xi_m\right)\right)}{\vec{\underline{k}}_m^{(\mathrm{nu})} \cdot \vec{\underline{k}}_m^{(\mathrm{nu})}} \\ =&\mu_{m+1} \underline{H}_{m+1} \frac{\left(\alpha_{m+1} \cos\left(\xi_{m+1} + \rho_{m+1}\right) + j\beta_{m+1} \cos\left(\xi_{m+1}\right)\right)}{\vec{\underline{k}}_{m+1}^{(\mathrm{nu})} \cdot \vec{\underline{k}}_{m+1}^{(\mathrm{nu})}} \end{aligned} \tag{2.65}$$

By solving the linear equation system given by (2.59) and (2.65) the following reflection and transmission coefficients result.

$$\left(\frac{\underline{H}_m^{'}}{\underline{H}_m}\right)_{\parallel} = \frac{\mu_m \frac{(\alpha_m \cos(\xi_m+\rho_m)+j\beta_m \cos(\xi_m))}{\vec{\underline{k}}_m^{(\mathrm{nu})} \cdot \vec{\underline{k}}_m^{(\mathrm{nu})}} - \mu_{m+1} \frac{(\alpha_{m+1} \cos(\xi_{m+1}+\rho_{m+1})+j\beta_{m+1} \cos(\xi_{m+1}))}{\vec{\underline{k}}_{m+1}^{(\mathrm{nu})} \cdot \vec{\underline{k}}_{m+1}^{(\mathrm{nu})}}}{\mu_m \frac{(\alpha_m \cos(\xi_m+\rho_m)+j\beta_m \cos(\xi_m))}{\vec{\underline{k}}_m^{(\mathrm{nu})} \cdot \vec{\underline{k}}_m^{(\mathrm{nu})}} + \mu_{m+1} \frac{(\alpha_{m+1} \cos(\xi_{m+1}+\rho_{m+1})+j\beta_{m+1} \cos(\xi_{m+1}))}{\vec{\underline{k}}_{m+1}^{(\mathrm{nu})} \cdot \vec{\underline{k}}_{m+1}^{(\mathrm{nu})}}} \tag{2.66}$$

$$\left(\frac{\underline{H}_{m+1}}{\underline{H}_m}\right)_{\parallel} = \frac{2\mu_m \frac{(\alpha_m \cos(\xi_m+\rho_m)+j\beta_m \cos(\xi_m))}{\vec{\underline{k}}_m^{(\mathrm{nu})} \cdot \vec{\underline{k}}_m^{(\mathrm{nu})}}}{\mu_m \frac{(\alpha_m \cos(\xi_m+\rho_m)+j\beta_m \cos(\xi_m))}{\vec{\underline{k}}_m^{(\mathrm{nu})} \cdot \vec{\underline{k}}_m^{(\mathrm{nu})}} + \mu_{m+1} \frac{(\alpha_{m+1} \cos(\xi_{m+1}+\rho_{m+1})+j\beta_{m+1} \cos(\xi_{m+1}))}{\vec{\underline{k}}_{m+1}^{(\mathrm{nu})} \cdot \vec{\underline{k}}_{m+1}^{(\mathrm{nu})}}} \tag{2.67}$$

These Fresnel coefficients are equal to those presented in [110,115,126,127,140,141]. The derivation of the TE-Fresnel coefficients is completely analog employing the boundary conditions for the electric field of a TE-polarized wave. They are derived in detail in [128]. The corresponding coefficients for the electric field of the TM-polarized wave result in the same simple manner as for the loss free case, since the Fresnel coefficients depend on the field vector's absolute value and only contain information about the amplitude ratio and not about the propagation direction. The propagation direction results from the effective propagation constants. Taking the absolute value of equation (2.34) and using the dispersion relation for the non-uniform plane wave from equation (2.36) results in:

$$\begin{aligned} \underline{E}_m &= \frac{1}{\omega_0 \underline{\epsilon}_m} |\vec{\underline{k}}_m^{(\mathrm{nu})} \times \vec{\underline{H}}_m| \\ &= \frac{1}{\omega_0 \underline{\epsilon}_m} |\vec{\underline{k}}_m^{(\mathrm{nu})}| |\vec{\underline{H}}_m| \sin\left(90^\circ\right) \\ &= \frac{1}{\omega_0 \underline{\epsilon}_m} \underline{H}_m \sqrt{\vec{\underline{k}}_m^{(\mathrm{nu})} \cdot \vec{\underline{k}}_m^{(\mathrm{nu})}} \\ &= \underline{H}_m \sqrt{\frac{\mu_m}{\underline{\epsilon}_m}} \end{aligned} \tag{2.68}$$

The angle enclosed between the coplanar real valued direction vectors of the non-uniform wave vector $\vec{\underline{k}}_m^{(\mathrm{nu})}$ and the magnetic field vector $\vec{\underline{H}}_m$ is supposed to be 90° for the TM-wave,

since $\underline{\vec{k}}_m^{(\mathrm{nu})}$ lies in the plane of incidence and $\underline{\vec{H}}_m$ is perpendicular to the plane of incidence, as shown in figure 2.6. By substituting (2.68) into (2.66) and (2.67), the corresponding Fresnel coefficients for the electric field result.

To calculate the Fresnel coefficients of the non-uniform wave with coplanar phase and attenuation vectors in phase-attenuation vector notation, the intrinsic propagation constants $\alpha_{0m},\ \alpha_{0m+1},\ \beta_{0m},\ \beta_{0m+1}$ and the effective propagation constants $\alpha_m,\ \alpha_{m+1},\ \beta_m,\ \beta_{m+1}$ are required. The intrinsic propagation constants are directly linked to the complex refractive index by the dispersion relation. The effective propagation constants are the real and imaginary part of the complex non-uniform wave vector and include it's material dependence, but also the direction of propagation separated in phase and amplitude evolution. The contribution [128] deals with the determination of these propagation constants. In literature [110, 126, 141] the Fresnel coefficients are derived in terms of the complex angle representation (2.9) of the non-uniform wave model, which is more compact and only requires knowledge about the intrinsic propagation constants. The numerical value obtained for the Fresnel coefficients is identical to that obtained by employing the phase-attenuation vector notation. A comparison of the Fresnel coefficients of the electric field components of a TE-polarized wave in phase-attenuation vector and complex angle notation is presented in [128].

2.11 Interference equations employing the non-uniform wave model

In this section the basic principle of interference will be recapped and the influence of the results of Fresnel equations on the equilibrium in energy flux density in common interferometric settings will be outlined. The introduction of two beam interference is based on [110] with an expansion covering non-uniform wave vectors.

For a given pair of two temporally and spatially coherent, elliptic polarized, non-uniform, harmonic, plane waves propagating in an isotropic, attenuating medium described in cartesian coordinates according to equation (2.10) (see p. 27) the wave equations are given in equation (2.69).

$$\begin{aligned}\vec{E}_{1m}(\vec{r},t) &= \frac{1}{2}\left(\underline{\vec{E}}_{01m}e^{j(\underline{\vec{k}}_m^{(\mathrm{nu})}\cdot\vec{r}-\omega_0 t+\phi_{1m})} + \underline{\vec{E}}_{01m}^{*}e^{-j(\underline{\vec{k}}_m^{(\mathrm{nu})*}\cdot\vec{r}-\omega_0 t+\phi_{1m})}\right)\\ \vec{E}_{2m}(\vec{r},t) &= \frac{1}{2}\left(\underline{\vec{E}}_{02m}e^{j(\underline{\vec{k}}_m^{(\mathrm{nu})}\cdot\vec{r}-\omega_0 t+\phi_{2m})} + \underline{\vec{E}}_{02m}^{*}e^{-j(\underline{\vec{k}}_m^{(\mathrm{nu})*}\cdot\vec{r}-\omega_0 t+\phi_{2m})}\right)\end{aligned} \tag{2.69}$$

Since the waves are temporally and spatially coherent, which is required for obtaining interference, their propagation is described by the same wave vector $\underline{\vec{k}}_m^{(\mathrm{nu})}$ and they have the same frequency ω_0. Furthermore, both waves should be equally polarized, which requires the phase terms of the complex amplitudes of the vectors $\underline{\vec{E}}_{01m},\ \underline{\vec{E}}_{02m}$ namely ϕ_x, ϕ_y, ϕ_z to be equal. Therefore, they differ only in their amplitudes $\underline{\vec{E}}_{01m},\ \underline{\vec{E}}_{02m}$ and the phase offsets $\phi_{1m},\ \phi_{2m}$, which are linearly dependent on the optical path length difference of the waves.

In equation (2.70) the complex wave vector $\underline{\vec{k}}_m^{(\mathrm{nu})}$ from equation (2.8) (see p. 25) is separated into its phase shifting real part describing the wavefront propagation and its damping imaginary part.

$$\begin{aligned}\vec{E}_{1m}(\vec{r},t) &= \frac{1}{2}e^{-\left(\vec{\beta}_m\cdot\vec{r}\right)}\left(\underline{\vec{E}}_{01m}e^{j(\vec{\alpha}_m\cdot\vec{r}-\omega_0 t+\phi_{1m})} + \underline{\vec{E}}_{01m}^{*}e^{-j(\vec{\alpha}_m\cdot\vec{r}-\omega_0 t+\phi_{1m})}\right)\\ \vec{E}_{2m}(\vec{r},t) &= \frac{1}{2}e^{-\left(\vec{\beta}_m\cdot\vec{r}\right)}\left(\underline{\vec{E}}_{02m}e^{j(\vec{\alpha}_m\cdot\vec{r}-\omega_0 t+\phi_{2m})} + \underline{\vec{E}}_{02m}^{*}e^{-j(\vec{\alpha}_m\cdot\vec{r}-\omega_0 t+\phi_{2m})}\right)\end{aligned} \tag{2.70}$$

To shorten notations equation (2.70) is rewritten in dependency of the fucntions $\mathrm{b}(\vec{r}) \in \mathbb{R}$ and $\mathrm{a}(\vec{r},t) \in \mathbb{R}$ where $\mathrm{b}(\vec{r}) = \vec{\beta}_m \cdot \vec{r}$ describes the position dependent damping of the propagating wave in the attenuating medium and $\mathrm{a}(\vec{r},t) = \vec{\alpha}_m \cdot \vec{r} - \omega_0 t$ the position and time dependent phase of the propagating wave fronts. Using the given substitutions $\mathrm{b}(\vec{r})$ and $\mathrm{a}(\vec{r},t)$ equation (2.71) results.

$$\begin{aligned}\vec{E}_{1m}(\vec{r},t) &= \frac{1}{2}e^{-\mathrm{b}(\vec{r})}\left(\underline{\vec{E}}_{01m}e^{j(\mathrm{a}(\vec{r},t)+\phi_{1m})} + \underline{\vec{E}}_{01m}^{*}e^{-j(\mathrm{a}(\vec{r},t)+\phi_{1m})}\right)\\ \vec{E}_{2m}(\vec{r},t) &= \frac{1}{2}e^{-\mathrm{b}(\vec{r})}\left(\underline{\vec{E}}_{02m}e^{j(\mathrm{a}(\vec{r},t)+\phi_{2m})} + \underline{\vec{E}}_{02m}^{*}e^{-j(\mathrm{a}(\vec{r},t)+\phi_{2m})}\right)\end{aligned} \tag{2.71}$$

The superposition of the interfering electric fields in equation (2.71) yields:

$$\begin{aligned}\vec{E}_m(\vec{r},t) &= \vec{E}_{1m}(\vec{r},t) + \vec{E}_{2m}(\vec{r},t)\\ \vec{E}_m(\vec{r},t) &= \frac{1}{2}e^{-\mathrm{b}(\vec{r})}\left(\left(\vec{\underline{E}}_{01m}e^{j\phi_{1m}} + \vec{\underline{E}}_{02m}e^{j\phi_{2m}}\right)e^{\mathrm{ja}(\vec{r},t)} + \left(\vec{\underline{E}}^{*}_{01m}e^{-j\phi_{1m}} + \vec{\underline{E}}^{*}_{02m}e^{-j\phi_{2m}}\right)e^{-\mathrm{ja}(\vec{r},t)}\right)\end{aligned} \tag{2.72}$$

Since the electric fields of light waves oscillate with very high frequency in the range of hundreds of Terahertz, the field amplitude itself is not accessible for direct measurement. Instead the irradiance, the average amount of radiant flux impining on a unit surface area in a unit time interval is investigated. The irradiance is also referred to as radiant flux density, energy flux density or intensity [110, 111, 131, 139].

The energy flux density I_m is defined as the absolute magnitude of the time average of the poynting vector [110, 111, 139].

$$I_m = \left|\left\langle \vec{S}_m(\vec{r},t)\right\rangle\right| = \left|\frac{1}{T}\int_{t-\frac{T}{2}}^{t+\frac{T}{2}} \vec{S}_m(\vec{r},t)dt\right| \tag{2.73}$$

Where T denotes the periodic time, which is connected to the wave's angular frequency by $\omega_0 = 2\pi/T$. The time varying position dependent poynting vector $\vec{S}_m(\vec{r},t)$ is a result of Maxwell's equations. Its magnitude is a measure of energy flux density and its direction in isotropic media points towards the propagation of light. The poynting vector is defined as the vector product of the electric field $\vec{E}_m(\vec{r},t)$ and the magnetic field $\vec{H}_m(\vec{r},t)$ [110, 111, 131, 139].

$$\vec{S}_m(\vec{r},t) = \vec{E}_m(\vec{r},t) \times \vec{H}_m(\vec{r},t) \tag{2.74}$$

Using equation (2.74) equation (2.73) can be written as [135, p. 424], [110, p. 35]:

$$\vec{I}_m = \left\langle \vec{S}_m(\vec{r},t)\right\rangle = \frac{1}{T}\int_{t-\frac{T}{2}}^{t+\frac{T}{2}} \vec{E}_m(\vec{r},t) \times \vec{H}_m(\vec{r},t)dt \tag{2.75}$$

$$= \frac{1}{2}\Re\left\{\vec{\underline{E}}_m(\vec{r},t) \times \vec{\underline{H}}^{*}_m(\vec{r},t)\right\} \tag{2.76}$$

These equations show, that the time average of the poynting vector can be either calculated by solving an integral over the vector product of the real fields (2.75), or by using the complex phasor notation to express the fields (2.76) and considering only the real part of their vector product [110]. Both methods are commonly used in literature to introduce the energy flux density.

By using the results of maxwell equations to show the transversality of the field, the magnetic field can be expressed in terms of the electric field, electric permittivity and

magnetic permeability as shown in equation (2.33) [110] (Born p. 24).

$$\begin{aligned}\underline{\vec{H}}_m(\vec{r},t) &= \frac{1}{\omega_0\mu_m}\vec{\underline{k}}_m^{(\mathrm{nu})} \times \underline{\vec{E}}_m(\vec{r},t) \\ \vec{H}_m(\vec{r},t) &= \Re\left\{\frac{1}{\omega_0\mu_m}\vec{\underline{k}}_m^{(\mathrm{nu})} \times \underline{\vec{E}}_m(\vec{r},t)\right\} \\ &= \frac{1}{\omega_0\mu_m}\left(\vec{\alpha}_m \times \Re\left\{\underline{\vec{E}}_m(\vec{r},t)\right\} + \vec{\beta}_m \times \Re\left\{j\underline{\vec{E}}_m(\vec{r},t)\right\}\right)\end{aligned} \tag{2.77}$$

In equation (2.77) $\vec{\alpha}_m$ and $\vec{\beta}_m$ denote the real valued vectors of the effective propagation constants introduced in section 2.2 and $\mu_m = \mu_0\mu_m^{'}$ the real valued magnetic permeability.

For the deviation of the poynting vector in dependence of the electric field only TE-polarization is considered. The poynting vector may be derived in dependence of the magnetic field in an analog manner for TM-polarization [135]. Inserting equation (2.77) into equation (2.75), (2.76) and using the vector triple product expansion $\vec{a}\times(\vec{b}\times\vec{c}) = \vec{b}(\vec{a}\cdot\vec{c}) - \vec{c}(\vec{a}\cdot\vec{b})$ yields [131](p. 15):

Time averaged poynting vector in real field expression:

$$\begin{aligned}\left\langle \vec{S}_m(\vec{r},t)\right\rangle &= \frac{1}{T}\int_{t-\frac{T}{2}}^{t+\frac{T}{2}} \vec{E}_m(\vec{r},t) \times \frac{1}{\omega_0\mu_m}\left(\vec{\alpha}_m \times \Re\left\{\underline{\vec{E}}_m(\vec{r},t)\right\} + \vec{\beta}_m \times \Re\left\{j\underline{\vec{E}}_m(\vec{r},t)\right\}\right) dt \\ &= \frac{1}{\omega_0\mu_m}\frac{1}{T}\int_{t-\frac{T}{2}}^{t+\frac{T}{2}} \vec{\alpha}_m \cdot \left(\vec{E}_m(\vec{r},t)\cdot\vec{E}_m(\vec{r},t)\right) + \vec{\beta}_m \cdot \left(\vec{E}_m(\vec{r},t)\cdot\Re\left\{\underline{\vec{E}}_m(\vec{r},t)e^{j\frac{\pi}{2}}\right\}\right) dt\end{aligned} \tag{2.78}$$

Time averaged poynting vector in complex phasor expression:

$$\begin{aligned}\left\langle \vec{S}_m(\vec{r},t)\right\rangle &= \frac{1}{2}\frac{1}{\omega_0\mu_m}\Re\left\{\underline{\vec{E}}_m(\vec{r},t) \times \left(\vec{\underline{k}}_m^{(\mathrm{nu})*} \times \underline{\vec{E}}_m(\vec{r},t)^*\right)\right\} \\ &= \frac{1}{2}\frac{1}{\omega_0\mu_m}\Re\left\{\underline{\vec{E}}_m(\vec{r},t) \times \left(\vec{\alpha}_m \times \underline{\vec{E}}_m(\vec{r},t)^*\right) + \underline{\vec{E}}_m(\vec{r},t) \times \left(-j\vec{\beta}_m \times \underline{\vec{E}}_m(\vec{r},t)^*\right)\right\} \\ &= \frac{1}{2}\frac{1}{\omega_0\mu_m}\Re\left\{\vec{\alpha}_m \cdot \left(\underline{\vec{E}}_m(\vec{r},t)\cdot\underline{\vec{E}}_m(\vec{r},t)^*\right) + \vec{\beta}_m \cdot \left(\underline{\vec{E}}_m(\vec{r},t)\cdot\underline{\vec{E}}_m(\vec{r},t)^* e^{-j\frac{\pi}{2}}\right)\right\}\end{aligned} \tag{2.79}$$

To receive (2.78) and (2.79) the TE-polarization property $\vec{E}_m(\vec{r},t)\cdot\vec{\alpha}_m = \vec{E}_m(\vec{r},t)\cdot\vec{\beta}_m = 0$ is employed. Both approaches for the calculation of the time averaged poynting vector in equation (2.78) and (2.79) yield the same result.

2.11.1 Time averaged poynting vector in real field expression

The real field approach for the time average of the poynting vector from equation (2.78) is an immediate result of the high optical frequencies in the Terahertz range. Since the

time variant position dependent energy flux density denoted by $\vec{S}_m(\vec{r},t)$ is not accessible by direct measurement its mean value $\left\langle \vec{S}_m(\vec{r},t) \right\rangle$ is measured instead. Employing the Staschenko identity (5.2) on (2.78) results in (2.80).

$$\begin{aligned}\left\langle \vec{S}_m(\vec{r},t) \right\rangle &= \frac{1}{\omega_0\mu_m}\frac{1}{T}\int_{t-\frac{T}{2}}^{t+\frac{T}{2}} \vec{\alpha}_m\cdot\left(\vec{E}_m(\vec{r},t)\cdot\vec{E}_m(\vec{r},t)\right)+\vec{\beta}_m\cdot\left(\vec{E}_m(\vec{r},t)\cdot\Re\left\{\underline{\vec{E}}_m(\vec{r},t)e^{j\frac{\pi}{2}}\right\}\right)dt \\ &= \frac{1}{\omega_0\mu_m}\left(\vec{\alpha}_m\frac{1}{T}\int_{t-\frac{T}{2}}^{t+\frac{T}{2}}\left(\vec{E}_m(\vec{r},t)\cdot\vec{E}_m(\vec{r},t)\right)dt\right. \\ &\left.+\vec{\beta}_m\cos(\frac{\pi}{2})\frac{1}{T}\int_{t-\frac{T}{2}}^{t+\frac{T}{2}}\left(\vec{E}_m(\vec{r},t)\cdot\vec{E}_m(\vec{r},t)\right)dt\right) \\ &= \frac{1}{\omega_0\mu_m}\vec{\alpha}_m\frac{1}{T}\int_{t-\frac{T}{2}}^{t+\frac{T}{2}}\left(\vec{E}_m(\vec{r},t)\cdot\vec{E}_m(\vec{r},t)\right)dt\end{aligned} \tag{2.80}$$

Equation (2.80) explains how to calculate the energy flux density based on real electric fields, considered as a temporally and spatially coherent, TE-polarized, non-uniform, harmonic, plane wave propagating in an isotropic, attenuating medium. A more extended calculation using the complex conjugate expression for the real fields can be found in the appendix 5 in equation (5.1). By the application of the Staschenko identity in (2.80) it is shown, that no energy is propagating in the direction of the imaginary attenuation vector $\vec{\beta}_m$. Although the non-uniform wave model is employed the poynting vector shows that energy transfer only occurs in the direction of wavefront propagation described by the effective propagation constant $\vec{\alpha}_m$. To determine I_m equation (2.72) has to be squared.

$$\begin{aligned}&\vec{E}_m(\vec{r},t)^2 \\ =&\frac{1}{4}e^{-2\mathrm{b}(\vec{r})}\left[\left(\underline{\vec{E}}_{01m}e^{j\phi_{1m}}+\underline{\vec{E}}_{02m}e^{j\phi_{2m}}\right)^2 e^{2j\mathrm{a}(\vec{r},t)}+\left(\underline{\vec{E}}^*_{01m}e^{-j\phi_{1m}}+\underline{\vec{E}}^*_{02m}e^{-j\phi_{2m}}\right)^2 e^{-2j\mathrm{a}(\vec{r},t)}\right] \\ +&\frac{1}{4}e^{-2\mathrm{b}(\vec{r})}\left[2\left(\underline{\vec{E}}_{01m}e^{j\phi_{1m}}+\underline{\vec{E}}_{02m}e^{j\phi_{2m}}\right)\cdot\left(\underline{\vec{E}}^*_{01m}e^{-j\phi_{1m}}+\underline{\vec{E}}^*_{02m}e^{-j\phi_{2m}}\right)\right]\end{aligned} \tag{2.81}$$

Next the result of equation (2.81) is applied to equation (2.80) and the mean value integral is resolved. Since the mean value integral of the complex exponential functions over a full period $\left\langle e^{2j\mathrm{a}(\vec{r},t)}\right\rangle$ equals zero [111, 131], equation (2.80) simplifies to (2.82).

$$\left\langle \vec{S}_m(\vec{r},t) \right\rangle = \frac{1}{\omega_0\mu_m}\vec{\alpha}_m\frac{1}{2}e^{-2\mathrm{b}(\vec{r})}\left(\underline{\vec{E}}_{01m}e^{j\phi_{1m}}+\underline{\vec{E}}_{02m}e^{j\phi_{2m}}\right)\cdot\left(\underline{\vec{E}}^*_{01m}e^{-j\phi_{1m}}+\underline{\vec{E}}^*_{02m}e^{-j\phi_{2m}}\right) \tag{2.82}$$

Assuming equally polarized interfering waves as mentioned above the scalar product $\vec{a}\cdot\vec{b}=ab\cos(\theta)$ of the complex vectors in equation (2.82) yields (2.83).

$$\begin{aligned}\left\langle \vec{S}_m(\vec{r},t) \right\rangle = \frac{1}{\omega_0\mu_m}\vec{\alpha}_m\frac{1}{2}e^{-2\mathrm{b}(\vec{r})}&\left(E^2_{01m}+E^2_{02m}+E_{01m}E_{02m}\cos(\theta)e^{j(\phi_{1m}-\phi_{2m})}\right. \\ &\left.+E_{01m}E_{02m}\cos(\theta)e^{-j(\phi_{1m}-\phi_{2m})}\right)\end{aligned} \tag{2.83}$$

In equation (2.83) $\cos(\theta)$ is the cosine of the angle enclosed by the field vector amplitudes $\vec{E}_{01m}$ and $\vec{E}_{02m}$. Under the given assumption of equally polarized waves the unit vectors of the interfering fields point in the same direction and $\theta = 0$. This yields:

$$\left\langle \vec{S}_m(\vec{r},t) \right\rangle = \frac{1}{2}\frac{1}{\omega_0\mu_m}\vec{\alpha}_m e^{-2\mathrm{b}(\vec{r})}\left(E_{01m}^2 + E_{02m}^2 + 2E_{01m}E_{02m}\cos(\phi_{1m}-\phi_{2m})\right) \tag{2.84}$$

Finally equation (2.85) results for the energy flux density I_m using equation (2.73) on the single field components.

$$\begin{aligned} I_m &= \left|\left\langle \vec{S}_m(\vec{r},t) \right\rangle\right| = \frac{1}{\omega_0\mu_m}|\vec{\alpha}_m|\frac{1}{2}e^{-2\mathrm{b}(\vec{r})}\left(E_{01m}^2 + E_{02m}^2 + 2\sqrt{E_{01m}^2E_{02m}^2}\cos(\phi_{1m}-\phi_{2m})\right) \\ &= I_{1m} + I_{2m} + 2\sqrt{I_{1m}I_{2m}}\cos(\phi_{1m}-\phi_{2m}) \end{aligned} \tag{2.85}$$

Equation (2.85) describes the energy flux density of two interfering, temporally and spatially coherent, TE-polarized, non-uniform, harmonic, plane waves propagating in an isotropic, attenuating medium described in cartesian coordinates. In literature, the case of the poynting vector for the non-uniform plane wave in attenuating media is covered in [135], but without consideration of the real field expression and using a different notation of the complex electric field vector and wave vector. The poynting vector in dissipative media is more commonly expressed in terms of the uniform wave model [138,142,143]. Employing the uniform wave vector defined in equation (2.4) in equation (2.78) and (2.79) results in the poynting vector of a uniform, harmonic, plane wave propagating in an isotropic, attenuating medium.

$$\begin{aligned} I_m^{(\mathrm{uf})} &= \left|\left\langle \vec{S}_m^{(\mathrm{uf})}(\vec{r},t) \right\rangle\right| \\ &= \frac{\alpha_{0m}}{\omega_0\mu_m}\frac{1}{2}e^{-2\beta_{0m}\vec{u}_{km}\cdot\vec{r}}\left(E_{01m}^2 + E_{02m}^2 + 2\sqrt{E_{01m}^2E_{02m}^2}\cos(\phi_{1m}-\phi_{2m})\right) \\ &= \frac{|\underline{k}_m|\cos(\gamma_{\eta m})}{\omega_0\mu_m}\frac{1}{2}e^{-2\beta_{0m}\vec{u}_{km}\cdot\vec{r}}\left(E_{01m}^2 + E_{02m}^2 + 2\sqrt{E_{01m}^2E_{02m}^2}\cos(\phi_{1m}-\phi_{2m})\right) \\ &= \frac{\cos(\gamma_{\eta m})}{|\underline{\eta}_m|}\frac{1}{2}e^{-2\beta_{0m}\vec{u}_{km}\cdot\vec{r}}\left(E_{01m}^2 + E_{02m}^2 + 2\sqrt{E_{01m}^2E_{02m}^2}\cos(\phi_{1m}-\phi_{2m})\right) \end{aligned} \tag{2.86}$$

In equation (2.86) $\underline{\eta}_m = \sqrt{\frac{\underline{\epsilon}_m}{\mu_m}}$ is the complex intrinsic impedance and $\gamma_{\eta m}$ the angle enclosed by α_{0m} and β_{0m} in the complex plane described by the argument of the complex uniform wave vector. The main difference between the poynting vector in the uniform and non-uniform wave model is, that the more general non-uniform wave model representation depends on the effective propagation constants $\vec{\alpha}_m$, $\vec{\beta}_m$, while the uniform representation depends on the intrinsic parameters α_{0m}, β_{0m}. Since in section 2.8 it is shown, that the wave propagation in dissipative media in the general case of arbitrary propagation

direction requires the application of the non-uniform wave model, equation (2.86) is very limited in its applicability.

For loss free media equation (2.85) simplifies to equation (2.87) which is commonly depicted in lectures and text books concerning optics [110, 111, 130, 131].

$$I_m = \frac{1}{\eta_m}\frac{1}{2}\left(E_{01m}^2 + E_{02m}^2 + 2\sqrt{E_{01m}^2 E_{02m}^2}\cos(\phi_{1m} - \phi_{2m})\right) \tag{2.87}$$

2.11.2 Time averaged poynting vector in complex phasor expression

The phasor approach for the time average of the poynting vector in equation (2.79) offers an easier calculation and yields the same algebraic solution as equation (2.84).

Considering the result presented in equation (2.79) the complex poynting vector is given by [110, 135] (Adler p. 424):

$$\begin{aligned}\underline{\vec{S}}_m(\vec{r},t) &= \frac{1}{2}\frac{1}{\omega_0\mu_m}\left(\vec{\alpha}_m\cdot\left(\underline{\vec{E}}_m(\vec{r},t)\cdot\underline{\vec{E}}_m(\vec{r},t)^*\right) - j\vec{\beta}_m\cdot\left(\underline{\vec{E}}_m(\vec{r},t)\cdot\underline{\vec{E}}_m(\vec{r},t)^*\right)\right)\\ &= \frac{1}{2}\frac{1}{\omega_0\mu_m}\left(\vec{\alpha}_m - j\vec{\beta}_m\right)\left(\underline{\vec{E}}_m(\vec{r},t)\cdot\underline{\vec{E}}_m(\vec{r},t)^*\right)\end{aligned} \tag{2.88}$$

To compare the results with Adler et al. [135] the differences in the definition of the complex electric field vector in equation (2.10) and equation (8.2) (Adler p. 321, 403) has to be considered. Employing the substitution $\vec{k}_m^{(\mathrm{nu})} = j\overline{\vec{\gamma}}$ or $\overline{\vec{\gamma}} = -j\vec{k}_m^{(\mathrm{nu})}$ for the complex non-uniform wave vector and considering $\vec{\alpha}_m = -\boldsymbol{\beta}$ and $\vec{\beta}_m = \boldsymbol{\alpha}$ for the effective propagation constants yields comparability with the result presented in [135], when the poynting vector is derived using equation (2.76). Equation (2.88) yields the conclusion that only reactive power flows along the planes of constant phase perpendicular to the wavefront propagation direction $\vec{\alpha}_m$ and only real power flows along the planes of constant amplitude perpendicular to the attenuation direction vector $\vec{\beta}_m$ [135]. This is equivalent to the behavior explained in section 2.11.1 that real energy propagates along the direction of wavefront propagation $\vec{\alpha}_m$ and only reactive energy propagates along the direction of the attenuation vector $\vec{\beta}_m$. Taking the real part of equation (2.88) yields equation (2.89).

$$\left\langle \vec{S}_m(\vec{r},t)\right\rangle = \frac{1}{2}\frac{1}{\omega_0\mu_m}\Re\left\{\left(\vec{\alpha}_m - j\vec{\beta}_m\right)\left(\underline{\vec{E}}_m(\vec{r},t)\cdot\underline{\vec{E}}_m(\vec{r},t)^*\right)\right\} \tag{2.89}$$

Obviously the product of the electric field with its complex conjugate $\underline{\vec{E}}_m(\vec{r},t)\cdot\underline{\vec{E}}_m(\vec{r},t)^*$ will yield a real valued result. Thus, the real part is obtained by simply omitting the imaginary part $j\vec{\beta}_m$. By inserting the complex vectors of the electric field in equation (2.89) and applying the assumptions for the interfering fields used in section 2.11.1, which

are TE-polarized fields and therefore the angle θ enclosed between $\vec{\underline{E}}_{01m}$ and $\vec{\underline{E}}_{02m}$ is zero, equation (2.90) results.

$$
\begin{aligned}
&\left\langle \vec{S}_m(\vec{r},t) \right\rangle \\
&= \frac{1}{2}\frac{1}{\omega_0\mu_m}\vec{\alpha}_m e^{-2\mathrm{b}(\vec{r})}\left(\left(\vec{\underline{E}}_{01m}e^{j\phi_{1m}}+\vec{\underline{E}}_{02m}e^{j\phi_{2m}}\right)e^{\mathrm{ja}(\vec{r},t)}\left(\vec{\underline{E}}^{*}_{01m}e^{-j\phi_{1m}}+\vec{\underline{E}}^{*}_{02m}e^{-j\phi_{2m}}\right)e^{-\mathrm{ja}(\vec{r},t)}\right) \\
&= \frac{1}{2}\frac{1}{\omega_0\mu_m}\vec{\alpha}_m e^{-2\mathrm{b}(\vec{r})}\left(E^2_{01m}+E^2_{02m}+E_{01m}E_{02m}\cos(\theta)e^{j(\phi_{1m}-\phi_{2m})}+E_{01m}E_{02m}\cos(\theta)e^{-j(\phi_{1m}-\phi_{2m})}\right) \\
&= \frac{1}{2}\frac{1}{\omega_0\mu_m}\vec{\alpha}_m e^{-2\mathrm{b}(\vec{r})}\left(E^2_{01m}+E^2_{02m}+2E_{01m}E_{02m}\cos(\theta)\cos(\phi_{1m}-\phi_{2m})\right) \\
&= \frac{1}{2}\frac{1}{\omega_0\mu_m}\vec{\alpha}_m e^{-2\mathrm{b}(\vec{r})}\left(E^2_{01m}+E^2_{02m}+2E_{01m}E_{02m}\cos(\phi_{1m}-\phi_{2m})\right)
\end{aligned}
\tag{2.90}
$$

Comparing equations (2.90) and (2.84) demonstrates, that the complex phasor expression of the electric fields can be used for calculations concerning interfering electrical fields.

2.11.3 Interference conditions of the common path interferometer

In this section the interference equation for a common path interferometer is derived, considering a TE-polarized, non-uniform, harmonic, plane wave propagating in an optical isotropic, attenuating medium with real valued magnetic permeability. Thus, the results of section 2.2, 2.10 and 2.11.2 for the non-uniform wave model are employed. Figure 2.7

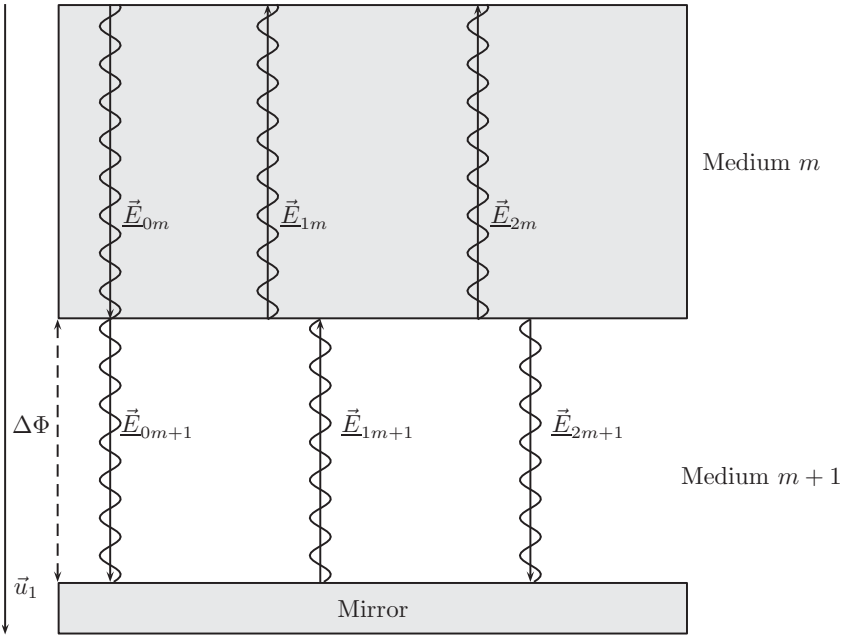

Figure 2.7: Schematic depiction of the relevant electric field components to derive the two beam interference equation for a common path interferometer consisting of the interface between two media and a reflective measuring object. The depicted electric field components all overlap in one single point, but are depicted laterally distributed for better overview.

depicts the electric field components involved in the two beam interference of a common path interferometer. The phasor $\underline{\vec{E}}_{0m}$ indicates the complex electric field of the incident wave. The respective field components are calculated by multiplication of the reflection and transmission coefficients of the non-uniform TE-polarized wave derived in [128]. The mirror is considered to have 100% reflectivity, thus the respective field components are

defined in equation (2.91) to (2.94).

$$\underline{E}_{01m} = \underline{E}_{00m} \left(\frac{\underline{E}_{01m}}{\underline{E}_{00m}} \right)_{\perp} \tag{2.91}$$

$$\underline{E}_{02m} = \underline{E}_{00m} \left(\frac{\underline{E}_{00m+1}}{\underline{E}_{00m}} \right)_{\perp} \left(\frac{\underline{E}_{02m}}{\underline{E}_{01m+1}} \right)_{\perp} e^{j2\Delta\Phi} \tag{2.92}$$

$$\underline{E}_{00m+1} = \underline{E}_{00m} \left(\frac{\underline{E}_{00m+1}}{\underline{E}_{00m}} \right)_{\perp} \tag{2.93}$$

$$\underline{E}_{02m+1} = \underline{E}_{00m} \left(\frac{\underline{E}_{00m+1}}{\underline{E}_{00m}} \right)_{\perp} \left(\frac{\underline{E}_{02m+1}}{\underline{E}_{01m+1}} \right)_{\perp} e^{j2\Delta\Phi} \tag{2.94}$$

The influence of terms of higher order which may occur by considering multiple reflection between the measuring object and the reference interface is neglected here. The consequences of this simplifying assumption are shortly discussed at the end of this section. In equation (2.91)-(2.94) $\left(\frac{\underline{E}_{01m}}{\underline{E}_{00m}}\right)_{\perp}$ is the reflection coefficient from medium m to $m+1$, $\left(\frac{\underline{E}_{00m+1}}{\underline{E}_{00m}}\right)_{\perp}$ is the transmission coefficient from medium m to $m+1$, $\left(\frac{\underline{E}_{02m}}{\underline{E}_{01m+1}}\right)_{\perp}$ is the transmission coefficient from medium $m+1$ to m and $\left(\frac{\underline{E}_{02m+1}}{\underline{E}_{01m+1}}\right)_{\perp}$ is the reflection coefficient from medium $m+1$ to m. These coefficients are calculated in dependency of the effective propagation constants as the Fresnel coefficients for TE-polarization in the non-uniform wave model in an attenuating medium derived in [128]. For the case of TM-polarization the coefficients given in equation (2.66) and (2.67) would be considered instead. The term $e^{j2\Delta\Phi}$ indicates the optical path length difference the respective waves have traveled with respect to the interface before interference occurs. Considering the equation for the reflection coefficients of the non-uniform TE-wave in [128] as well as the reflection coefficients for the non-uniform TM-wave in (2.66) shows, that the reflection coefficients referring to a reflection at the interface m to $m+1$ and $m+1$ to m are equal in their absolute value but differ in their sign. Thus, $\left(\frac{\underline{E}_{01m}}{\underline{E}_{00m}}\right)_{\perp} = -\left(\frac{\underline{E}_{02m+1}}{\underline{E}_{01m+1}}\right)_{\perp}$ is used in equation (2.94). Employing the complex poynting vector according to equation (2.88) on the interfering pairs of waves $\left(\vec{\underline{E}}_{1m}, \vec{\underline{E}}_{2m}\right)$ and $\left(\vec{\underline{E}}_{0m+1}, \vec{\underline{E}}_{2m+1}\right)$ and the reflection and transmission coefficients according to equation (2.91)-(2.94) results in equation (2.95) and

(2.96).

$$
\begin{aligned}
&\underline{\vec{S}}_m(\vec{r},t)\\
&=\frac{1}{2}\frac{1}{\omega_0\mu_m}e^{-2\vec{\beta}_m\cdot\vec{r}}\left(\underline{E}_{01m}+\underline{E}_{02m}\right)\left(\underline{E}^*_{01m}+\underline{E}^*_{02m}\right)\left(\vec{\alpha}_m-j\vec{\beta}_m\right)\\
&=\frac{1}{2}\frac{1}{\omega_0\mu_m}e^{-2\vec{\beta}_m\cdot\vec{r}}\left(\underline{E}_{00m}\left(\frac{\underline{E}_{01m}}{\underline{E}_{00m}}\right)_\perp+\underline{E}_{00m}\left(\frac{\underline{E}_{00m+1}}{\underline{E}_{00m}}\right)_\perp\left(\frac{\underline{E}_{02m}}{\underline{E}_{01m+1}}\right)_\perp e^{j2\Delta\Phi}\right)\\
&\cdot\left(\left(\underline{E}^*_{00m}\left(\frac{\underline{E}_{01m}}{\underline{E}_{00m}}\right)^*_\perp+\underline{E}^*_{00m}\left(\frac{\underline{E}_{00m+1}}{\underline{E}_{00m}}\right)^*_\perp\left(\frac{\underline{E}_{02m}}{\underline{E}_{01m+1}}\right)^*_\perp e^{-j2\Delta\Phi}\right)\right)\left(\vec{\alpha}_m-j\vec{\beta}_m\right)\\
&\underline{\vec{S}}_{m+1}(\vec{r},t)\\
&=\frac{1}{2}\frac{1}{\omega_0\mu_{m+1}}e^{-2\vec{\beta}_{m+1}\cdot\vec{r}}\left(\underline{E}_{00m+1}+\underline{E}_{02m+1}\right)\left(\underline{E}^*_{00m+1}+\underline{E}^*_{02m+1}\right)\left(\vec{\alpha}_{m+1}-j\vec{\beta}_{m+1}\right)\\
&=\frac{1}{2}\frac{1}{\omega_0\mu_{m+1}}e^{-2\vec{\beta}_{m+1}\cdot\vec{r}}\left(\underline{E}_{00m}\left(\frac{\underline{E}_{00m+1}}{\underline{E}_{00m}}\right)_\perp+(-1)\underline{E}_{00m}\left(\frac{\underline{E}_{00m+1}}{\underline{E}_{00m}}\right)_\perp\left(\frac{\underline{E}_{01m}}{\underline{E}_{00m}}\right)_\perp e^{j2\Delta\Phi}\right)\\
&\cdot\left(\underline{E}^*_{00m}\left(\frac{\underline{E}_{00m+1}}{\underline{E}_{00m}}\right)^*_\perp+(-1)\underline{E}^*_{00m}\left(\frac{\underline{E}_{00m+1}}{\underline{E}_{00m}}\right)^*_\perp\left(\frac{\underline{E}_{01m}}{\underline{E}_{00m}}\right)^*_\perp e^{-j2\Delta\Phi}\right)\left(\vec{\alpha}_{m+1}-j\vec{\beta}_{m+1}\right)
\end{aligned}
\tag{2.95}
$$

(2.96)

For further considerations the reflection and transmission coefficients in equation (2.95) and (2.96) are written in Euler notation as $\left(\frac{\underline{E}_{01m}}{\underline{E}_{00m}}\right)_\perp=R^m_{m+1}e^{j\Phi_{R^m_{m+1}}}$, $\left(\frac{\underline{E}_{00m+1}}{\underline{E}_{00m}}\right)_\perp=T^m_{m+1}e^{j\Phi_{T^m_{m+1}}}$ and $\left(\frac{\underline{E}_{02m}}{\underline{E}_{01m+1}}\right)_\perp=T^{m+1}_m e^{j\Phi_{T^{m+1}_m}}$.

$$
\begin{aligned}
&\underline{\vec{S}}_m(\vec{r},t)\\
&=\frac{1}{2}\frac{1}{\omega_0\mu_m}e^{-2\vec{\beta}_m\cdot\vec{r}}\left(E^2_{01m}+E^2_{02m}+\right.\\
&\left.E^2_{00m}R^m_{m+1}T^m_{m+1}T^{m+1}_m\cos\left(2\Delta\Phi+\Phi_{R^m_{m+1}}+\Phi_{T^m_{m+1}}+\Phi_{T^{m+1}_m}\right)\right)\left(\vec{\alpha}_m-j\vec{\beta}_m\right)
\end{aligned}
\tag{2.97}
$$

$$
\begin{aligned}
&\underline{\vec{S}}_{m+1}(\vec{r},t)\\
&=\frac{1}{2}\frac{1}{\omega_0\mu_{m+1}}e^{-2\vec{\beta}_{m+1}\cdot\vec{r}}\left(E^2_{00m+1}+E^2_{02m+1}+\right.\\
&\left.E^2_{00m}R^m_{m+1}T^m_{m+1}T^m_{m+1}\cos\left(2\Delta\Phi-\pi+\Phi_{R^m_{m+1}}+\Phi_{T^m_{m+1}}+\Phi_{T^m_{m+1}}\right)\right)\left(\vec{\alpha}_{m+1}-j\vec{\beta}_{m+1}\right)
\end{aligned}
\tag{2.98}
$$

The interference of $\left(\underline{\vec{E}}_{1m},\underline{\vec{E}}_{2m}\right)$ is observed by a detector, while the interference of $\left(\underline{\vec{E}}_{0m+1},\underline{\vec{E}}_{2m+1}\right)$ occurs between the reference plane and the measuring object. If the path length difference $\Delta\Phi$ varies, the observed interferogram will change between constructive and destructive interference. Since the sum of real and reactive energy in the system, which is indicated by the absolute value of the complex poynting vectors of the interfering waves in equation (2.97) and (2.98), is required to be constant to satisfy energy

conservation, the phase and amplitude of these interference pairs need to be coupled. Only the cosine terms vary in dependence of the optical path difference. Thus, it is sufficient to consider these terms to show energy conservation for the common path interferometer employing the non-uniform wave model. Since these terms determine the modulation depth of the interferogram they will be abbreviated $\underline{\vec{M}}_m$ and $\underline{\vec{M}}_{m+1}$. The common constant coefficients of the amplitude and phase offset $\frac{1}{2\omega_0}E_{00m}^2 R_{m+1}^m T_{m+1}^m$ and $\Phi_{R_{m+1}^m} + \Phi_{T_{m+1}^m}$ are omitted.

$$\underline{\vec{M}}_m = \frac{1}{\mu_m} e^{-2\vec{\beta}_m \cdot \vec{r}} T_m^{m+1} \cos\left(2\Delta\Phi + \Phi_{T_m^{m+1}}\right) \left(\vec{\alpha}_m - j\vec{\beta}_m\right) \tag{2.99}$$

$$\underline{\vec{M}}_{m+1} = \frac{1}{\mu_{m+1}} e^{-2\vec{\beta}_{m+1} \cdot \vec{r}} T_{m+1}^m \cos\left(2\Delta\Phi - \pi + \Phi_{T_{m+1}^m}\right) \left(\vec{\alpha}_{m+1} - j\vec{\beta}_{m+1}\right) \tag{2.100}$$

To show energy conservation considering electromagnetic fields Poynting's theorem [110] is employed. Since the volume element around the interface contains two potentially attenuating media, energy transfer to the medium by absorption effects has to be considered. The Poynting theorem for a complex Poynting vector in its integral form is given in equation (2.101). The terms $\underline{\hat{R}}$, $\underline{R}$ represent energy transfer by absorption and are physically interpreted as the electric power density resulting of the product of the current density and the electric field in the conducting medium and other radiation losses [112]. The difference between $\underline{\hat{R}}$ and $\underline{R}$ is caused by omitting the coefficients of the amplitude and phase offset mentioned above.

$$\begin{aligned} \underline{\hat{R}} &= \oiint_A \underline{\vec{S}} \cdot \vec{u}_A dA \\ &= \left(\underline{S}_m + \underline{S}_{m+1}\right) \\ \Rightarrow \underline{R} &= \left(\underline{M}_m + \underline{M}_{m+1}\right) \end{aligned} \tag{2.101}$$

In equation (2.101) A indicates an arbitrarily formed closed surface surrounding the volume element with the Poynting vectors, dA is an infinitesimal small surface element oriented in the direction $\vec{u}_A$. Since the surface is arbitrarily formed, it is assumed that the Poynting vector and the surface direction vector are parallel. This is reasonable, since the energy conservation considers the absolute sum of energy entering and leaving the volume element independent of the detailed propagation direction. In [128] the transmission coefficients for a TE-wave are derived as follows:

$$\underline{T}_{m+1}^m = \frac{2\left(\frac{\alpha_m}{\mu_m}\cos\left(\xi_m + \rho_m\right) + j\frac{\beta_m}{\mu_m}\cos(\xi_m)\right)}{\left(\frac{\alpha_m}{\mu_m}\cos\left(\xi_m + \rho_m\right) + j\frac{\beta_m}{\mu_m}\cos(\xi_m)\right) + \left(\frac{\alpha_{m+1}}{\mu_{m+1}}\cos\left(\xi_{m+1} + \rho_{m+1}\right) + j\frac{\beta_{m+1}}{\mu_{m+1}}\cos(\xi_{m+1})\right)}$$

$$\underline{T}_m^{m+1} = \frac{2\left(\frac{\alpha_{m+1}}{\mu_{m+1}}\cos\left(\xi_{m+1} + \rho_{m+1}\right) + j\frac{\beta_{m+1}}{\mu_{m+1}}\cos(\xi_{m+1})\right)}{\left(\frac{\alpha_m}{\mu_m}\cos\left(\xi_m + \rho_m\right) + j\frac{\beta_m}{\mu_m}\cos(\xi_m)\right) + \left(\frac{\alpha_{m+1}}{\mu_{m+1}}\cos\left(\xi_{m+1} + \rho_{m+1}\right) + j\frac{\beta_{m+1}}{\mu_{m+1}}\cos(\xi_{m+1})\right)} \tag{2.102}$$

Considering perpendicular incidence $\xi_m = \rho_m = \xi_{m+1} = \rho_{m+1} = 0$ and abbreviating the denominators in equation (2.102) by D the absolute value and phase of the transmission coefficients is given by:

$$\begin{aligned} T_{m+1}^{m} &= \frac{\frac{2}{\mu_m}\left(\alpha_m^2+\beta_m^2\right)^{\frac{1}{2}}}{|D|}, \qquad \Phi_{T_{m+1}^{m}} = \tan^{-1}\left(\frac{\beta_m}{\alpha_m}\right) \\ T_{m}^{m+1} &= \frac{\frac{2}{\mu_{m+1}}\left(\alpha_{m+1}^2+\beta_{m+1}^2\right)^{\frac{1}{2}}}{|D|}, \qquad \Phi_{T_{m}^{m+1}} = \tan^{-1}\left(\frac{\beta_{m+1}}{\alpha_{m+1}}\right) \end{aligned} \tag{2.103}$$

Employing (2.99), (2.100) and (2.103) in equation (2.101) yields:

$$\begin{aligned} &\frac{1}{\mu_m}\frac{\frac{2}{\mu_{m+1}}\left(\alpha_{m+1}^2+\beta_{m+1}^2\right)^{\frac{1}{2}}}{|D|}e^{-2\vec{\beta}_m\cdot\vec{r}}\cos\left(2\Delta\Phi+\Phi_{T_m^{m+1}}\right)(\alpha_m - j\beta_m) \\ &+\frac{1}{\mu_{m+1}}\frac{\frac{2}{\mu_m}\left(\alpha_m^2+\beta_m^2\right)^{\frac{1}{2}}}{|D|}e^{-2\vec{\beta}_{m+1}\cdot\vec{r}}\cos\left(2\Delta\Phi-\pi+\Phi_{T_{m+1}^{m}}\right)(\alpha_{m+1} - j\beta_{m+1}) = \underline{R} \end{aligned} \tag{2.104}$$

Writing the scalar form of the non-uniform wave vectors in polar coordinates results in:

$$\begin{aligned} &\frac{2}{\mu_m\mu_{m+1}}\frac{\left(\alpha_{m+1}^2+\beta_{m+1}^2\right)^{\frac{1}{2}}\left(\alpha_m^2+\beta_m^2\right)^{\frac{1}{2}}}{|D|}e^{-2\vec{\beta}_m\cdot\vec{r}}\cos\left(2\Delta\Phi+\Phi_{T_m^{m+1}}\right)e^{-j\Phi_{T_{m+1}^{m}}} \\ &+\frac{2}{\mu_m\mu_{m+1}}\frac{\left(\alpha_{m+1}^2+\beta_{m+1}^2\right)^{\frac{1}{2}}\left(\alpha_m^2+\beta_m^2\right)^{\frac{1}{2}}}{|D|}e^{-2\vec{\beta}_{m+1}\cdot\vec{r}}\cos\left(2\Delta\Phi-\pi+\Phi_{T_{m+1}^{m}}\right)e^{-j\Phi_{T_m^{m+1}}} = \underline{R} \end{aligned} \tag{2.105}$$

Dividing both sides of equation (2.105) by the common, constant coefficient in front of the exponential functions yields:

$$e^{-2\vec{\beta}_m\cdot\vec{r}}\cos\left(2\Delta\Phi+\Phi_{T_m^{m+1}}\right)e^{-j\Phi_{T_{m+1}^{m}}} + e^{-2\vec{\beta}_{m+1}\cdot\vec{r}}\cos\left(2\Delta\Phi-\pi+\Phi_{T_{m+1}^{m}}\right)e^{-j\Phi_{T_m^{m+1}}} = \underline{\tilde{R}} \tag{2.106}$$

Writing the phase terms in the trigonometric function representation and applying addition theorems from equation (2.107),

$$\begin{aligned} \sin(x)\sin(y) &= \frac{1}{2}\left(\cos(x-y)-\cos(x+y)\right) \\ \cos(x)\cos(y) &= \frac{1}{2}\left(\cos(x-y)+\cos(x+y)\right) \\ \sin(x)\cos(y) &= \frac{1}{2}\left(\sin(x-y)+\sin(x+y)\right) \end{aligned} \tag{2.107}$$

results in:

$$
\begin{aligned}
&e^{-2\vec{\beta}_m\cdot\vec{r}}\cos\left(2\Delta\Phi+\Phi_{T_m^{m+1}}\right)\left(\cos(\Phi_{T_{m+1}^m})-j\sin(\Phi_{T_{m+1}^m})\right)\\
&+e^{-2\vec{\beta}_{m+1}\cdot\vec{r}}\cos\left(2\Delta\Phi-\pi+\Phi_{T_{m+1}^m}\right)\left(\cos(\Phi_{T_m^{m+1}})-j\sin(\Phi_{T_m^{m+1}})\right)=\underline{\tilde{R}}
\end{aligned}
$$

$$
\begin{aligned}
\Leftrightarrow &e^{-2\vec{\beta}_m\cdot\vec{r}}\left[\frac{1}{2}\left(\cos(2\Delta\Phi+\Phi_{T_m^{m+1}}-\Phi_{T_{m+1}^m})+\cos(2\Delta\Phi+\Phi_{T_m^{m+1}}+\Phi_{T_{m+1}^m})\right)\right.\\
&\left.-j\frac{1}{2}\left(\sin(\Phi_{T_{m+1}^m}-2\Delta\Phi-\Phi_{T_m^{m+1}})+\sin(\Phi_{T_{m+1}^m}+2\Delta\Phi+\Phi_{T_m^{m+1}})\right)\right]\\
&+e^{-2\vec{\beta}_{m+1}\cdot\vec{r}}\left[\frac{1}{2}\left(\cos(2\Delta\Phi-\pi+\Phi_{T_{m+1}^m}-\Phi_{T_m^{m+1}})+\cos(2\Delta\Phi-\pi+\Phi_{T_{m+1}^m}+\Phi_{T_m^{m+1}})\right)\right.\\
&\left.-j\frac{1}{2}\left(\sin(\Phi_{T_m^{m+1}}-2\Delta\Phi+\pi-\Phi_{T_{m+1}^m})+\sin(\Phi_{T_m^{m+1}}+2\Delta\Phi-\pi+\Phi_{T_{m+1}^m})\right)\right]=\underline{\tilde{R}}
\end{aligned}
$$

$$
\begin{aligned}
\Leftrightarrow &e^{-2\vec{\beta}_m\cdot\vec{r}}\left[\frac{1}{2}\left(\cos(2\Delta\Phi+\Phi_{T_m^{m+1}}-\Phi_{T_{m+1}^m})+\cos(2\Delta\Phi+\Phi_{T_m^{m+1}}+\Phi_{T_{m+1}^m})\right)\right.\\
&\left.-j\frac{1}{2}\left(-\sin(2\Delta\Phi+\Phi_{T_m^{m+1}}-\Phi_{T_{m+1}^m})+\sin(2\Delta\Phi+\Phi_{T_m^{m+1}}+\Phi_{T_{m+1}^m})\right)\right]\\
&+e^{-2\vec{\beta}_{m+1}\cdot\vec{r}}\left[\frac{1}{2}\left(-\cos(2\Delta\Phi+\Phi_{T_{m+1}^m}-\Phi_{T_m^{m+1}})-\cos(2\Delta\Phi+\Phi_{T_{m+1}^m}+\Phi_{T_m^{m+1}})\right)\right.\\
&\left.-j\frac{1}{2}\left(\sin(2\Delta\Phi+\Phi_{T_{m+1}^m}-\Phi_{T_m^{m+1}})-\sin(2\Delta\Phi+\Phi_{T_{m+1}^m}+\Phi_{T_m^{m+1}})\right)\right]=\underline{\tilde{R}}
\end{aligned}
\tag{2.108}
$$

If the special case $\vec{r}=0$ is considered on the interface, equation (2.108) simplifies to:

$$
\begin{aligned}
&\frac{1}{2}\left(\cos(2\Delta\Phi+\Phi_{T_m^{m+1}}-\Phi_{T_{m+1}^m})-\cos(2\Delta\Phi+\Phi_{T_{m+1}^m}-\Phi_{T_m^{m+1}})\right)\\
&-j\frac{1}{2}\left(\sin(2\Delta\Phi+\Phi_{T_{m+1}^m}-\Phi_{T_m^{m+1}})-\sin(2\Delta\Phi+\Phi_{T_m^{m+1}}-\Phi_{T_{m+1}^m})\right)=\underline{\tilde{R}}
\end{aligned}
\tag{2.109}
$$

The absolute value of equation (2.109) corresponds to the energy transferred to the medium in order to introduce the phase shift $|\Phi_{T_m^{m+1}}-\Phi_{T_{m+1}^m}|$ between the coupled interfering pairs of waves:

$$
|\underline{\tilde{R}}|=\frac{1}{2}\sqrt{2-2\cos\left(2\left(\Phi_{T_m^{m+1}}-\Phi_{T_{m+1}^m}\right)\right)}
\tag{2.110}
$$

The result of the Poynting theorem applied to the interfering pairs of waves in a common path interferometer in (2.108) shows that their phase is coupled and in the vicinity of attenuating media is shifted by $\pi+(\Phi_{T_m^{m+1}}-\Phi_{T_{m+1}^m})$, although the amplitude of the modulation depth is equal for both interfering pairs of waves at the interface with $\vec{r}=0$. Thus,

energy is not solely alternating between the interference modes, but also exchanged with the medium in the form of absorption or radiation. Therefore, the difference in equation (2.110) corresponds to the energy absorbed or radiated by the medium to achieve the respective phase shift. The exponentially decaying functions $e^{-2\vec{\beta}_m \cdot \vec{r}}$ and $e^{-2\vec{\beta}_{m+1} \cdot \vec{r}}$ model the energy transfer due to absorption in dependence of penetration depth $\vec{r}$. Equation (2.108) and (2.109) demonstrate that in the case of dissipative media real and reactive energy have to be considered to preserve energy conservation independent of the total optical path length difference $\Delta\Phi$.

As mentioned above, the influence of higher order reflections, which may occur in the cavity between the common path interferometer's reference plane and the measuring object depicted in figure 2.7, are not considered in the derivation of equation (2.110). This is reasonable for the theoretic consideration of energy conservation in the two beam interference case presented above, because the additional transmitted and reflected waves originate from multiple reflections in the resonator formed between the reference plane and the measuring object which functions as an energy storage. The energy budget of the multiple beam interference would have to include the resonator and is more complex. However, since the superposed waves do not disturb each other, the original two beam interference pair is untouched by the occurrence of multiple reflections and energy conservation has to be satisfied also when considered isolated. The additional reflections will influence the observed interference effects as perturbations which are not covered by the two beam interference. They contribute to the energy budget of multiple beam interference, but not to the theoretical two beam interference energy budget. The extend to which the experimentally observed interference will deviate from the two beam model depends on the reflection and transmission coefficients of the resonator interfaces.

If the simple case of non-attenuating media is considered $\beta_m = \beta_{m+1} = 0$ and $\Phi_{T^m_{m+1}} = \Phi_{T^{m+1}_m} = 0$, it immediately results from equation (2.108) that energy is exchanged without losses between the coupled interfering pairs of waves and the absorbed energy is $|\underline{\tilde{R}}| = 0$. By this the energy conservation of two beam interference in a common path interferometer is fully described in the case of attenuating and loss free media. The energy conservation at other interferometric setups, such as the Michelson interferometer is performed in an analog manner.

2.12 Complex electric permittivity

In the time domain, the connection between the electric flux density $\vec{D}(t)$ and an exciting electric field $\vec{E}(t)$ in dependence of the causal susceptibility

$$\chi(t) = \alpha(t)\theta(t) \text{ with } \theta(t) = \begin{cases} 1, & t \geq 0 \\ 0, & t < 0 \end{cases} \tag{2.111}$$

is given by the following equation [144, 145].

$$\vec{D}(t) = \epsilon_0 \left(\vec{E}(t) + \int_{-\infty}^{\infty} \chi(t-\tau)\vec{E}(\tau)d\tau \right) \tag{2.112}$$

To obtain a complex representation of the susceptibility $\underline{\chi}(\omega)$ describing its dispersion characteristics in the frequency domain, the Fourier Transformation is applied to both sides of equation (2.112). Exploiting the convolution theorem results in:

$$\begin{aligned} \mathbb{F}\left\{\vec{D}(t)\right\} &= \epsilon_0 \left(\mathbb{F}\left\{\vec{E}(t)\right\} + \mathbb{F}\left\{\chi(t)\right\} \mathbb{F}\left\{\vec{E}(t)\right\} \right) \\ &= \epsilon_0 \mathbb{F}\left\{\vec{E}(t)\right\} \cdot (1 + \mathbb{F}\left\{\chi(t)\right\}) \end{aligned} \tag{2.113}$$

Next, the Fourier transform $\mathbb{F}\{\chi(t)\}$ of the causal function $\chi(t)$ is examined in more detail. In the time domain the susceptibility is expressed as the product $\chi(t) = \alpha(t)\theta(t)$, consisting of the signal $\alpha(t)$ and the step function $\theta(t)$. Multiplication with the step function indicates causality of the signal.

The causality of the susceptibility shows, that no polarization of the medium is possible before the exciting field is applied. The time domain multiplication in $\chi(t)$ is expressed as a convolution in the Fourier domain by application of the convolution theorem.

$$\begin{aligned} &\mathbb{F}\{\chi(t)\} = \frac{1}{2\pi} \int_{-\infty}^{\infty} \mathbb{F}\{\alpha(t)\}(\acute{\omega}) \cdot \mathbb{F}\{\theta(t)\}(\omega - \acute{\omega}) d\acute{\omega} \\ &\text{with } \mathbb{F}\{\alpha(t)\}(\acute{\omega}) = A(\acute{\omega}) \text{ und } \mathbb{F}\{\theta(t)\}(\omega - \acute{\omega}) = \pi\delta(\omega - \acute{\omega}) + \frac{1}{j(\omega - \acute{\omega})} \\ &\mathbb{F}\{\chi(t)\} = \frac{1}{2\pi} \int_{-\infty}^{\infty} A(\acute{\omega}) \cdot \left(\pi\delta(\omega - \acute{\omega}) + \frac{1}{j(\omega - \acute{\omega})} \right) d\acute{\omega} \end{aligned} \tag{2.114}$$

In equation (2.111), the causality of the susceptibility is expressed by multiplication of $\alpha(t)$ with the step function. The multiplication with the step function does not cause any changes to the signal in the time domain. Thus, also the spectrum in the frequency domain is unchanged and has to satisfy $\mathbb{F}\{\chi(t)\} = \mathbb{F}\{\alpha(t)\} = A(\omega)$. In equation (2.114) $\delta(\omega - \acute{\omega})$ denotes the Dirac delta function. Solving the integral yields:

$$A(\omega) = \frac{1}{2}A(\omega) + \frac{1}{2\pi j} \fint_{-\infty}^{\infty} \frac{A(\acute{\omega})}{(\omega - \acute{\omega})} d\acute{\omega} \tag{2.115}$$

Due to its singularity in $\omega = \acute{\omega}$, the integral in equation (2.115) is treated as a Cauchy principal value integral. Employing Cauchy's integral theorem, it is possible to determine the value of such an integral by integrating over a closed path in a plane around the singularity [146]. Separating real and imaginary part in equation (2.115) yields:

$$\begin{aligned} \Re\{\mathbb{F}\{\chi(t)\}\} = \Re\{A(\omega)\} = \mathbb{H}^{-1}\{\Im\{A(\omega)\}\} = \frac{1}{\pi}\fint_{-\infty}^{\infty} \frac{\Im\{A(\acute{\omega}\})}{(\omega - \acute{\omega})} d\acute{\omega} \\ \Im\{\mathbb{F}\{\chi(t)\}\} = \Im\{A(\omega)\} = \mathbb{H}\{\Re\{A(\omega)\}\} = -\frac{1}{\pi}\fint_{-\infty}^{\infty} \frac{\Re\{A(\acute{\omega}\})}{(\omega - \acute{\omega})} d\acute{\omega} \end{aligned} \tag{2.116}$$

According to equation (2.116) the imaginary part of a Fourier transformed causal signal is given as the Hilbert transform $\mathbb{H}\{\Re\{A(\omega)\}\}$ of the real part and vice versa. This relation shows, that causality in the time domain results in a Kramer-Kronig relation or Hilbert transformation pair in the frequency domain [144,145,147]. The Hilbert transform describes a phase shift in the frequency domain by multiplication with $\underline{H}(\omega) = -j \cdot \text{sign}(\omega)$. For this the sign function is defined as $\text{sign}(\omega) = \begin{cases} 1, & \omega > 0 \\ 0, & \omega = 0 \\ -1, & \omega < 0 \end{cases}$. The Hilbert transform causes a phase shift of $+j = e^{j\frac{\pi}{2}}$ for all $\omega < 0$ and a phase shift of $-j = e^{-j\frac{\pi}{2}}$ for all $\omega > 0$ [148]. Thus, the susceptibility in the frequency domain is generally described as a complex variable given in equation (2.117).

$$\mathbb{F}\{\chi(t)\} = \underline{\chi}(\omega) = \chi^{'} - j\text{sign}(\omega)\chi^{''} \tag{2.117}$$

Employing the definition of the relative permittivity $\epsilon_m^{'} + j\epsilon_m^{''} = 1 + \underline{\chi}$ and using $\mathbb{F}\{\chi(t)\}$ equation (2.113) is written as:

$$\begin{aligned} \mathbb{F}\left\{\vec{D}(t)\right\} &= \epsilon_0 \mathbb{F}\left\{\vec{E}(t)\right\} \cdot \left(\epsilon_m^{'} - j\text{sign}(\omega)\epsilon_m^{''}\right) \\ \mathbb{F}\{\epsilon(t)\} &= \underline{\epsilon}_m(\omega) = \epsilon_0(\epsilon_m^{'} - j\text{sign}(\omega)\epsilon_m^{''}) \end{aligned} \tag{2.118}$$

The electric field is described by the wave equation of a linearly polarized, harmonic, plane wave propagating in an isotropic, attenuating medium referring to equation (2.10), but assuming linear polarization and employing the notations introduced in equation (2.70) for the non-uniform wave vector.

$$\vec{E}_m(\vec{r}, t) = \vec{E}_{0m} e^{-\left(\vec{\beta}_m \cdot \vec{r}\right)} \cos(\vec{\alpha}_m \cdot \vec{r} - \omega_0 t) \tag{2.119}$$

Equation (2.119) contains the compact real expression of the wave function. Corresponding to equation (2.118), the time domain Fourier transformed wave function is required, which is given by:

$$\mathbb{F}\left\{\vec{E}_m(\vec{r}, t)\right\} = \frac{\vec{E}_{0m} e^{-\left(\vec{\beta}_m \cdot \vec{r}\right)}}{2} \left(\delta(\omega + \omega_0) + \delta(\omega - \omega_0)\right) \tag{2.120}$$

Inserting in equation (2.118) yields:

$$\begin{aligned}\mathbb{F}\left\{\vec{D}(t)\right\} &= \frac{\vec{E}_{0m}e^{-\left(\vec{\beta}_m\cdot\vec{r}\right)}}{2}\left(\delta(\omega+\omega_0)+\delta(\omega-\omega_0)\right)\cdot\epsilon_0\left(\epsilon_m^{'}-j\text{sign}(\omega)\epsilon_m^{''}\right)\\ &= \frac{\vec{E}_{0m}e^{-\left(\vec{\beta}_m\cdot\vec{r}\right)}}{2}\epsilon_0\left[\left(\delta(\omega+\omega_0)+\delta(\omega-\omega_0)\right)\cdot\epsilon_m^{'}+\left(\delta(\omega+\omega_0)-\delta(\omega-\omega_0)\right)\cdot j\epsilon_m^{''}\right]\end{aligned} \tag{2.121}$$

By inverse transformation of equation (2.121) back to the time domain, the real expression of the electric current density in dependence of the components of the complex susceptibility or permittivity results:

$$\begin{aligned}\vec{D}(t) &= \mathbb{F}^{-1}\left\{\mathbb{F}\left\{\vec{E}_m(\vec{r},t)\right\}\cdot\underline{\epsilon}_m(\omega)\right\}\\ &= \vec{E}_{0m}e^{-\left(\vec{\beta}_m\cdot\vec{r}\right)}\cdot\epsilon_0\cdot\left(\epsilon_m^{'}\cdot\cos(\vec{\alpha}_m\cdot\vec{r}-\omega_0 t)+\epsilon_m^{''}\cdot\sin(\vec{\alpha}_m\cdot\vec{r}-\omega_0 t)\right)\end{aligned} \tag{2.122}$$

The electric current density in an attenuating medium is therefore composed of two oscillations, which are phase shifted by 90°. One oscillation component oscillates in phase with the exciting field. The off phase oscillation is caused by energy transfer between the wave and ions in the medium and corresponds to absorption [145].

There is an alternative algebraic approach to calculate the current density in attenuating media. The approach is based on the phasor expression of the electric field and does not offer a clear physical interpretation as equation (2.112). However, the calculation effort is strongly reduced and results in the same solution than equation (2.122). Since the alternative approach yields an abbreviated notation of equation (2.112), which is difficult to understand without knowing the earlier described theory based on the time domain model, the abbreviated notation is shortly introduced here.

$$\vec{D}(t) = \Re\left\{\underline{\vec{E}}_m(\vec{r},t)\cdot\underline{\epsilon}_m(\omega)\right\} \tag{2.123}$$

Equation (2.123) shows the abbreviated form of (2.112). The linearly polarized, non-uniform, harmonic, plane wave in an isotropic medium is given in its complex phasor expression, introduced in equation (2.124).

$$\underline{\vec{E}}_m(\vec{r},t) = \vec{E}_{0m}e^{-\left(\vec{\beta}_m\cdot\vec{r}\right)}\cdot e^{j(\vec{\alpha}_m\cdot\vec{r}-\omega_0 t)} \tag{2.124}$$

Insertion and multiplication in equation (2.123) yields:

$$\begin{aligned}\vec{D}(t) &= \Re\left\{\vec{E}_{0m}e^{-\left(\vec{\beta}_m\cdot\vec{r}\right)}\cdot e^{j(\vec{\alpha}_m\cdot\vec{r}-\omega_0 t)}\cdot\epsilon_0(\epsilon_m^{'}-j\text{sign}(\omega)\epsilon_m^{''})\right\}\\ &= \Re\left\{\vec{E}_{0m}e^{-\left(\vec{\beta}_m\cdot\vec{r}\right)}\cdot(\cos(\vec{\alpha}_m\cdot\vec{r}-\omega_0 t)+j\sin(\vec{\alpha}_m\cdot\vec{r}-\omega_0 t))\cdot\epsilon_0(\epsilon_m^{'}-j\text{sign}(\omega)\epsilon_m^{''})\right\}\\ &= \vec{E}_{0m}e^{-\left(\vec{\beta}_m\cdot\vec{r}\right)}\cdot\epsilon_0\cdot\left(\epsilon_m^{'}\cos(\vec{\alpha}_m\cdot\vec{r}-\omega_0 t)+\text{sign}(\omega)\epsilon_m^{''}\sin(\vec{\alpha}_m\cdot\vec{r}-\omega_0 t)\right)\\ &= \vec{E}_{0m}e^{-\left(\vec{\beta}_m\cdot\vec{r}\right)}\cdot\epsilon_0\cdot\left(\epsilon_m^{'}\cos(\vec{\alpha}_m\cdot\vec{r}-\omega_0 t)+\epsilon_m^{''}\sin(\vec{\alpha}_m\cdot\vec{r}-\omega_0 t)\right)\ \ \forall\omega>0\end{aligned} \tag{2.125}$$

For all positive frequencies $\omega > 0$, equation (2.123) yields the same result as equation (2.112). Thus, the correlation between electric flux density and the electric field in an attenuating medium is given in its abbreviated form by equation (2.123). This abbreviated form may be confusing, since in equation (2.123) the wave's complex phasor expression in the time domain is multiplied by the complex permittivity in the frequency domain.

Chapter 3

Fiber coupled dual wavelength common path laser interferometer with periodical optical path length modulation

The fiber coupled interferometric point sensor for micro- and nano metrology, which is reported in [1,37–47], is schematically depicted in figure 3.1 a). The setup consists of two laser diodes (LD) emitting infrared light at 1310 nm and 1550 nm and two photo diodes (PD), which in pairs are connected to an optical coupler. Mixing of the incoming and wavelength specific separation of the outgoing light is performed by a wavelength division multiplexer (WDM). Part of the illuminating laser light is reflected at the boundary surface of the cleaved single mode fiber, which is adjusted in a glass ferrule with some distance to a gradient index (GRIN) lens forming the miniaturized probe head. The light reflected at the fiber end face serves as the reference wave in the common path interferometer setup, which is theoretically treated in 2.11.3. Transmitting light is focused by the GRIN lens on the measurement object, reflected and scattered at its surface and coupled back into the fiber. Thus, the reference and measurement wave are superposed at the fiber's end surface and interference occurs. The interfering light is guided in the single mode fiber, split up in its wavelength components by the WDM and recorded at the PDs. Because interference occurs starting from the fiber's boundary surface, mechanical stress or vibration of the fiber does not have an immediate impact on the phase measurement, since the reference and measurement wave are simultaneously affected. The probe head depicted in figure 3.1 b) is mounted to a piezo driven bending beam. Expansion and contraction of the piezo element cause the bending beam to periodically oscillate perpendicular to the measured surface. Thus, a periodical optical path length modulation resulting in a phase modulation is introduced to the recorded interference signal, enabling the application of carrier fringe based lock-in detection algorithms for phase evaluation as mentioned in sec-

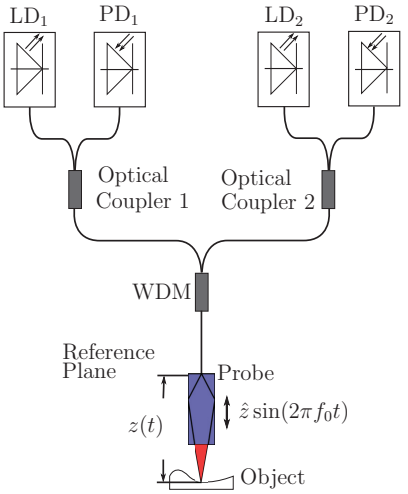

(a)

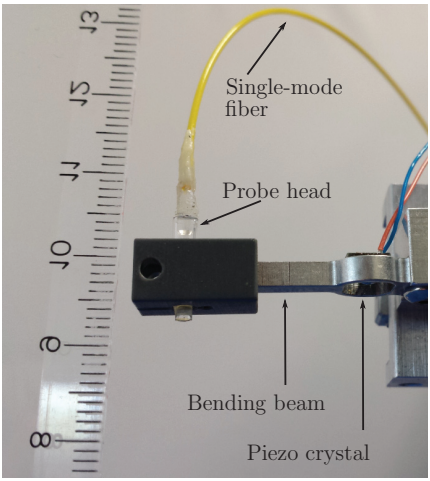

(b)

Figure 3.1: a) Schematic drawing of the dual wavelength common path interferometer setup, b) closeup of the probe head with piezo actuator.

tion 1.1. According to equation (2.85) the recorded interference signal intensity $I_k(t)$ of the k-th wavelength is modeled by the relation in equation (3.1), where I_{1k}, I_{2k} denote the intensity of the measurement and reference path, λ_k is the respective laser wavelength, $\hat{z}$ is the amplitude of the bending beam oscillation, f_0 is the bending beam oscillation frequency and $z(t)$ is the optical path length difference between the measurement and reference wave, which corresponds to the surface topography under investigation.

$$\begin{aligned} I_k(t) &= I_{1k} + I_{2k} + 2\sqrt{I_{1k}I_{2k}}\cos\left(\frac{4\pi}{\lambda_k}\left[\hat{z}\sin\left(2\pi f_0 t\right) + z(t)\right]\right) \\ &= I_{1k} + I_{2k} + 2\sqrt{I_{1k}I_{2k}}\cos\left(\frac{4\pi}{\lambda_k}\hat{z}\sin\left(2\pi f_0 t\right) + \phi_k(t)\right) \end{aligned} \tag{3.1}$$

The topography related phase $\phi_k(t) = \frac{4\pi}{\lambda_k} z(t)$ is commonly retrieved from the interferogram in equation (3.1) by employing Fourier transformation based frequency domain filtering, lock-in detection algorithms or phase shifting interferometry (PSI) approaches as referred to in section 1.1. The employed setup uses a real time implementation of a carrier fringe based lock-in detection algorithm on a microcontroller board, which retrieves the unwrapped phase from the recorded interferogram.

3.1 Identification of the reference plane location in a common path interferometer

The interferometric probe head of the point sensor setup is assembled of the fiber end surface adjusted to a focusing GRIN lens in a glass ferrule. The width of the air gap between the fiber end and the GRIN lens influences the imaging behavior and the numerical aperture of the probe. The probe assembly and transfer matrix based imaging simulations are considered in [44,46]. In total there are three interfaces of changing refractive index in the probe, which cause the reflection of a wave. The first is the boundary surface between the fiber end and the air gap, the second is air GRIN lens and the third the GRIN lens air interface. Due to the high temporal coherence of the distributed feedback laser source, all these interfaces may serve as reference planes. However, the recorded interferogram does not show disturbances due to multiple interference signals. Thus, the reflection from the reference plane is supposed to be of much higher intensity than those reflections from the other interfaces.

To identify the location of the reference plane the strong dependency of the measured optical path length difference with respect to wavelength changes is employed. The optical path length difference dependent phase term $\phi_k(t)$ in equation (3.1) is related to the optical path length difference as given by equation (3.2), where k denotes the index of the employed wavelength.

$$z_k(\phi_k(t), \lambda_k(t)) = \phi_k(t)\frac{\lambda_k(t)}{4\pi} \tag{3.2}$$

Assuming there are no mechanical influences such that $\frac{d\phi_k(t)}{dt} = 0$, the phase is constant and applying the law of propagation of uncertainty, considering the change in wavelength $\frac{d\lambda_k(t)}{dt}\Delta t = \Delta\lambda_k$ yields equation (3.3).

$$\begin{aligned}\Delta z_k(\phi_k(t), \lambda_k(t)) &= \phi_k(t)\frac{\Delta\lambda_k}{4\pi} \\ &= \frac{\Delta\lambda_k}{\lambda_k} z_k(\phi_k(t), \lambda_k(t))\end{aligned} \tag{3.3}$$

For the common path interferometer setup depicted in figure 3.1 the absolute optical path length difference $z_k(\phi_k(t), \lambda_k(t))$ is in the mm to cm range, depending on where the reference plane is assumed to lie, while the wavelength is in the µm range. Thus, a wavelength difference $\Delta\lambda_k$ is scaled with a factor of approximately 100 to 1000, resulting in a well measurable change in the optical path length difference.

To identify the position of the reference plane an experimental setup assembled in a master degree project at the measurement technology department [149] is employed. In this setup the illuminating laser diode is mounted in a metallic housing, attached to an active Peltier cooler. Thus, the laser diode temperature is adjustable between 283 K and 293 K, with a precision of approximately 0.1 K. The DFB Laser diode has a center wavelength of

$\lambda_1 = 1310\,\text{nm}$ and is specified by the supplier to have a wavelength drift over temperature of $\Delta\lambda_1/\Delta T = 0.1\,\text{nm/K}$. The interferometric probe is mounted at the oscillating bending beam as depicted in figure 3.1 b) and placed in its focal distance above a plane mirror as the measuring object on an actively damped table. Besides the periodical optical path length modulation by the piezo actuator to generate the carrier fringes, there is no mechanical motion applied to the setup. The distance between the measuring object and the potential reference planes is estimated using a caliper gauge, which offers a precision of approximately 0.1 mm. Thus, the distance between the fiber end and the measuring object is assumed to be $\overline{AD} \approx 10.5\,\text{mm}$, the distance between GRIN lens entrance plane and object $\overline{BD} \approx 5.0\,\text{mm}$ and the distance between the exit plane of the GRIN lens and the object $\overline{CD} \approx 0.7\,\text{mm}$. Additionally, the effective wavelength of the laser beam inside the GRIN lens material with a refractive index of 1.616 specified at a wavelength of 1550 nm has to be considered [150]. Thus, the corrected distance values are $\tilde{\overline{AD}} \approx 13.1\,\text{mm}$, $\tilde{\overline{BD}} \approx 7.7\,\text{mm}$ and $\overline{CD} \approx 0.7\,\text{mm}$. To receive precise results also the effect of the effective wavelength due to the NA of the probe, which is in the range of $\text{NA} \in [0.4, 0.5]$ corresponding to an acceptance angle in air of $\alpha \approx \sin^{-1}(\text{NA})$ would have to be considered. This causes an increased effective wavelength of approximately $\lambda_{\text{k,eff}} \approx \frac{\lambda_k}{\cos(\alpha/2)}$ on the distance $\overline{CD}$, but since the given measurements are only good estimates, the small influence of this effect is not considered here. The distances are illustrated in figure 3.2 a). In the experiment, the

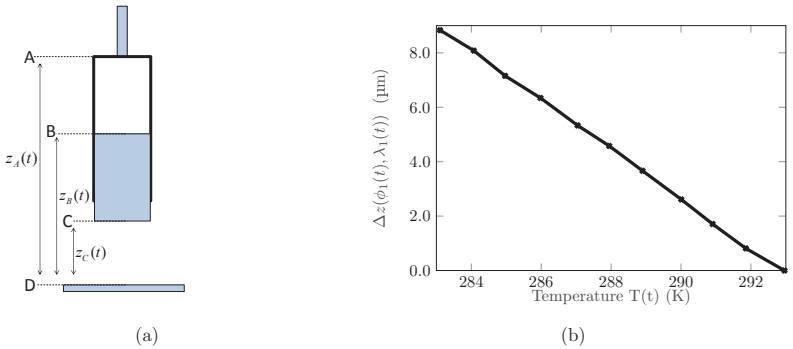

(a) (b)

Figure 3.2: a) Schematic drawing of the potential planes of reference in the fiber optical probe. Single mode fiber end plane A, entrance plane of the GRIN lens B, exit plane of the GRIN lens C, plane of the measuring object D., b) Optical path length difference caused by the temperature dependent change in wavelength.

temperature of the laser diode is gradually decreased form 293 K to 283 K in steps of 1 K, while the optical path length difference in dependence of the corresponding wavelength change, $\Delta z_k(\phi_k(t), \lambda_k(t))$ according to equation (3.3), is recorded. When the wavelength changes a different multiple of wave cycles fits into the optical path length difference and

thus the phase of the interference signal changes although no mechanical motion occurs. This change of the optical path length difference is depicted in figure 3.2 b). The raw data of height and temperature values is taken from [149]. The measurement data shows that the relation between the temperature change and the optical path length difference is almost linear. Nonlinearities may be caused by temperature fluctuations due to the oscillation behavior of the temperature controller as described in [149] or by environmental perturbations. The mean slope is $\frac{d\Delta z_k(\phi_k(t),\lambda_k(t))}{dT(t)} \approx 883\,\mathrm{nm/K}$. Assuming the reference plane to lie at position A in figure 3.2 a), yields $\Delta\lambda_1/\Delta T \approx 0.09\,\mathrm{nm/K}$ employing equation (3.3). This is with a relative deviation of 10% the closest result compared to the specified value of wavelength temperature drift. Since the temperature controller shows a deviation of similar size and the tolerance in the specification of the supplier is unknown, the result appears plausible. Thus, the fiber end surface is concluded to be the most likely dominant reference surface in the fiber probe. The original intention of the master thesis project [149] was to determine the temperature dependent wavelength instability $\Delta\lambda_k$ by a comparative measurement conducted at two different temperatures $T(t_0) = T_1$ and $T(t_1) = T_2$, so that the absolute distance to the reference plane $z_k(\phi_k(t), \lambda_k(t))$ would not be required. Measuring a specified, known height difference $\overline{P_1P_2}$ introduced by a precision positioner at two different temperatures the wavelength change $\Delta\lambda_k$, according to equation (3.2) and (3.3) is calculated by:

$$
\begin{aligned}
&z_{k,\overline{P_1P_2}}(T_1) = \phi_{k,\overline{P_1P_2}}\frac{\lambda_{k,T_1}}{4\pi}\\
&z_{k,\overline{P_1P_2}}(T_2) = \phi_{k,\overline{P_1P_2}}\frac{\lambda_{k,T_2}}{4\pi}\\
&\text{Subtracting the measured distances and employing (3.3) yields:}\\
&z_{k,\overline{P_1P_2}}(T_1) - z_{k,\overline{P_1P_2}}(T_2) = \frac{z_{k,\overline{P_1P_2}}(T_1)}{\lambda_{k,T_1}}\Delta\lambda_k\\
&z_{k,\overline{P_1P_2}}(T_1) - z_{k,\overline{P_1P_2}}(T_2) = \frac{z_{k,\overline{P_1P_2}}(T_2)}{\lambda_{k,T_2}}\Delta\lambda_k
\end{aligned}
\tag{3.4}
$$

As explained above, the distance due to mechanic path length changes ϕ_k is assumed to be independent of the temperature, and the measured virtual change in path length is related to the wavelength difference, which is the foundation of equation (3.4). To determine $z_{k,\overline{P_1P_2}}(T_1)$, $z_{k,\overline{P_1P_2}}(T_2)$ in equation (3.4) it is assumed that the wavelength λ_k, is constant during the measurement at a constant temperature and the phase change $\phi_{k,\overline{P_1P_2}}$ is caused by the mechanical motion of a precise axis like a piezo driven stage. However, due to the limited depth of field of the used interferometric fiber coupled probe the measurement range is limited to approximately 100 µm. Measuring the path length difference of $\overline{P_1P_2} = 100\,\mu\mathrm{m}$ at temperature $T_1 = 10\,\mathrm{K}$ and $T_2 = 20\,\mathrm{K}$, assuming a wavelength change of $\Delta\lambda_k = 1\,\mathrm{nm}$ would result in a height change of approximately 100 nm employing equation (3.4). Since the height resolution of the interferometric sensor is approximately 1 nm this difference could be well resolved. However, the temperature controller showed a waviness of approximately 0.1 K, which due to the strong scaling with

the total optical path length difference caused measurement uncertainties of a similar size. Thus, the comparative measurements of optical path length difference at different temperatures did not yield reasonable results. Repeating the experiment with a lower NA probe enabling a higher measurement range and a more precise temperature controller would enable the precise characterization of wavelength change and also absolute height measurement. The results recorded with the experimental setup described above are not feasible to receive a precise characterization of the wavelength change in dependence of the temperature or to conduct precise absolute height measurements. However, they are used to identify the position of the reference plane of the common path interferometer and indicate the strong dependence of the setup to temperature changes, which has to be considered in long term measurements.

3.2 Low aperture, fiber coupled, interferometric probe for focus tracking

A promising application of the fiber coupled interferometric point sensor is the topography measurement of 3D-objects like glass lenses, since the reflection coefficient of the air-glass interface at the measuring object is in the same order of magnitude than that of the silicon-air reference plane and the lateral measuring field can be adapted depending on the range of the linear stages used for scanning the surface. However, due to the rather high NA of the measuring probe, the depth of field of the measuring sensor is limited. The depth response of the fiber coupled interferometric point sensor is modeled as that of a confocal interference microscope featuring a small aperture in the illumination and imaging path, which is studied in detail in [151]. The confocal behavior is assumed due to the small aperture of the illuminating fiber, which yields a good approximation of a point source for spatially coherent illumination similar to the confocal microscope. The application of single mode fibers to substitute the conventional pinhole in a confocal microscope is described by [152–154] and found to be feasible. A mayor difference to the case considered in [151] is the assumption of a monochromatic laser light source, which simplifies the calculation of the intensity depth response by avoiding integration of intensities for distinct spectral components, which would be required in case of a broadband illumination. Also, since a guided laser beam is used for illumination, the pupil function describing the intensity distribution in the GRIN lenses entrance pupil is assumed to be gaussian. As discussed in [46] the gaussian beam model is feasible to describe the beam shape of the fiber coupled point sensor. The assumption of a gaussian beam shape in combination with the application of single mode fibers is also mentioned in [152]. Since no structured surfaces shall be considered in the depth response simulation of the point sensor, the reference and measurement object are assumed to be perfectly plane mirrors. Diffraction restrictions due to optical resolution are not considered. Thus, the integration over the electric fields inside the airy disc, commonly modeled by a Bessel function, may

be skipped. Employing these modifications to the intensity model of the confocal interference microscope in equation (6.42) in [151] results in the adapted model presented in equation (3.5).

$$\begin{aligned} \underline{E}_{\text{mea}}(\Delta z) &= 2\int_0^{\theta_{max}} P(\theta_e) E_0 e^{jk\cos\theta_e(z_0+\Delta z)} d\theta_e \\ \underline{E}_{\text{ref}}(\Delta z) &= 2\int_0^{\theta_{max}} P(\theta_e) E_0 e^{jkz_0} d\theta_e \\ I(\Delta z) &= |\underline{E}_{\text{mea}}(\Delta z)^2 + \underline{E}_{\text{ref}}(\Delta z)^2|^2 \end{aligned} \tag{3.5}$$

In equation (3.5) $\theta_{max} = \sin^{-1}(\text{NA})$ denotes the maximum angle of incidence due to the numerical aperture of the GRIN lens, $P(\theta_e) = e^{-\left(\frac{\theta_e^2}{2\sigma^2}\right)}$ is the gaussian shaped pupil function modeling the electric field amplitude distribution of the incident laser beam in the GRIN lense's Fourier plane, E_0 is the electric field amplitude, z_0 the constant optical path length in the reference and measurement arm and Δz the optical path length difference in the measurement arm due to the depth scan. Then, $I(\Delta z)$ contains the intensity distribution of the depth response assuming confocal behavior and a spatially coherent illumination. Figure 3.3 a) depicts the simulated depth response of the confocal

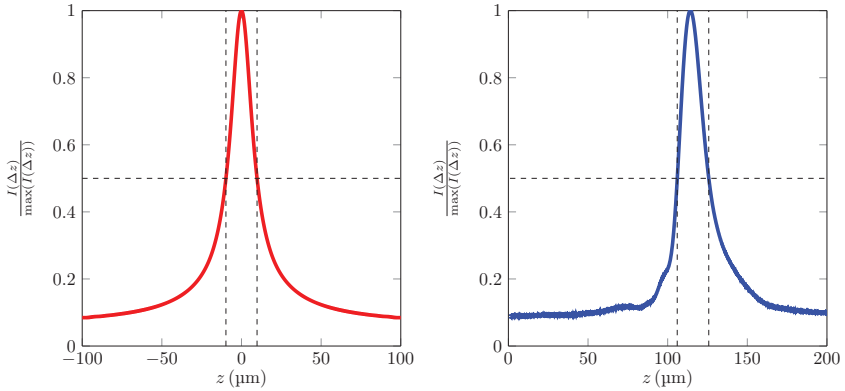

Figure 3.3: a) Simulated intensity depth response of the confocal interferometric point sensor assuming NA = 0.42, $\lambda_0 = 1310\,\text{nm}$, $\sigma = \frac{\theta_{max}}{3.4}$ and $\text{FWHM}_{\text{sim}} \approx 20\,\mu\text{m}$, b) measured intensity depth response of the confocal interferometric point sensor with $v = 0.02\,\frac{\text{mm}}{\text{s}}$, a sampling rate of 800 Hz and $\text{FWHM}_{\text{meas}} \approx 20\,\mu\text{m}$.

interferometric probe assuming a numerical aperture NA = 0.42 and pupil function characterized by $\sigma = \frac{\theta_{max}}{3.4}$. The simulated depth response shows a full width at half maximum

of $\mathrm{FWHM}_{\mathrm{sim}} \approx 20\,\mu\mathrm{m}$. This result is in good agreement with an intensity measurement performed with the interferometric point sensor. The sensor is moved by a distance of $200\,\mu\mathrm{m}$ employing a linear stage with a velocity of $0.02\,\frac{\mathrm{mm}}{\mathrm{s}}$. The start position is chosen below the focus point close to the object and than the distance to the measuring object is increased while passing the focus and recording the offset component of the intensity. The measurement result is depicted in figure 3.3 b), and shows a full width at half maximum $\mathrm{FWHM}_{\mathrm{meas}} \approx 20\,\mu\mathrm{m}$, which is in good agreement with the simulation. However, the measured intensity depth response is not fully symmetric, which might be caused by multiple beam interference effects in the sub-focal region. These are mentioned in [46], but not considered in the simulation. Also, the surface of the measuring object might be slightly tilted or show other imperfections compared to the model. The comparison of the simulation and measurement results indicates that the assumption of a confocal behavior of the interferometric point sensor is feasible. The confocal characteristic of a similar fiber coupled point sensor has also been reported by observations considering the transverse response of the probe in terms of an improvement in resolution in [155]. The intensity depth response in figure 3.3 shows that the intensity and thus the modulation depth and signal to noise ratio of the recorded interference signals significantly decrease when defocusing occurs. This motivates the implementation of a focus tracking system maintaining

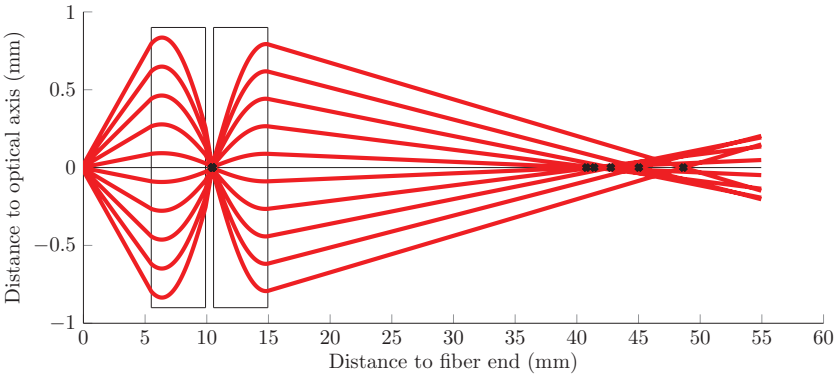

Figure 3.4: Transfer matrix based simulation of the beam propagation in a two GRIN lens configuration to achieve a fiber coupled sensor with high measuring range.

the position of the measuring probe with respect to the surface, while it is scanned. To not lose height resolution a second interferometric sensor with low numerical aperture and thus, high measuring range is employed as the reference sensor. The reference sensor should also be assembled as a fiber coupled sensor to maintain the mounting flexibility. Simulations of beam paths employing the transfer matrix method used in [46, 156] were carried out to determine a feasible optics design. These simulations indicate that the

combination of two GRIN lenses is suitable to achieve a probe with a potential measuring range of multiple millimeters. Figure 3.4 depicts the beam path simulation result for a combination of two gradient index lenses characterized by a pitch of $p_{\mathrm{GRIN}} = 0.25$, length $l_{\mathrm{GRIN}} = 4.4\,\mathrm{mm}$ and diameter $d_{\mathrm{GRIN}} = 1.8\,\mathrm{mm}$. The position of the GRIN lenses are indicated by the black rectangles, the beam path inside the lenses is iteratively determined using the aforementioned transfer matrix approach. The first GRIN lens is positioned in a distance of 5.5 mm with respect to the fiber end face. This distance is chosen such that considering the NA of the single mode fiber, which is assumed to be $\mathrm{NA}_{\mathrm{fiber}} \approx 0.14$ specified by the manufacturer the entrance pupil of the GRIN lens is almost fully illuminated. The distance between the GRIN lenses is chosen to be 0.65 mm for the simulation. The imaging behavior of the system is very sensitive to this distance, a displacement of 0.01 mm already shifts the respective focus point by several mm, thus active adjustment of the probe is required. To adequately use the positioning range of the z-linear stage a measuring range of $10\,\mathrm{mm} - 20\,\mathrm{mm}$ is required for the reference sensor. The transfer matrix simulation shows that it is possible to design a probe with low NA and an extended focal region considering the different focal positions for different angles of incidence, i.e. spherical aberration. Employing the angle between the outer beam path and the optical axis the numerical aperture of the simulated probe would be $\mathrm{NA}_{\mathrm{Sim}} \approx 0.017$, thus the surface tilt for the reference measurement is supposed to be $< 1°$. The depth response of

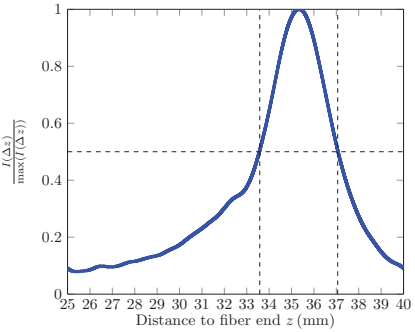

(a)

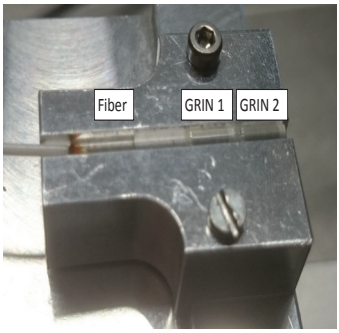

(b)

Figure 3.5: a) Measured intensity depth response of the confocal, interferometric, reference point sensor with $v = 0.2\,\frac{\mathrm{mm}}{\mathrm{s}}$, a sampling rate of 800 Hz and $\mathrm{FWHM}_{\mathrm{ref}} \approx 3.5\,\mathrm{mm}$. b) Photograph of the assembled, fiber coupled reference probe consisting of the fiber end surface and two GRIN lenses.

the reference probe is measured, via moving the measuring object 15 mm away from the reference probe, starting at a distance of 25 mm relative to the fiber end and stopping at 40 mm. The velocity of the motion is $v = 0.2\,\frac{\mathrm{mm}}{\mathrm{s}}$ and the sampling rate i.e. the oscillation frequency of the bending beam is 800 Hz. The recorded intensity depth response of

the reference probe is depicted in figure 3.5 a). The overall shape of the depth response resembles that of the measuring probe depicted in figure 3.3 b), which is plausible since the reference probe also has a small pinhole in the illumination path and thus should show confocal behavior. Due to the much smaller NA of the reference probe its focal region and measuring range is much more extended than that of the measuring probe. Although the full width at half maximum of the intensity depth response is approximately $\mathrm{FWHM}_{\mathrm{ref}} \approx 3.5\,\mathrm{mm}$, height measurement is possible throughout a range of $\Delta z > 20\,\mathrm{mm}$. This is caused by the high robustness of the employed lock-in detection algorithm for phase retrieval, which can handle rather weak signal amplitudes and signal-to-noise ratio. Comparing the simulated beam propagation in figure 3.4 to the measured depth response in figure 3.5 a) shows deviations with respect to the expected position of the intensity peak. However, as mentioned above the simulation already showed that misalignments of the GRIN lenses in the range of 0.01 mm would change the focus position by several mm. Considering this, the achieved result is within the expected tolerance. Figure 3.5 b) shows a photograph of the assembled fiber coupled reference probe. The low NA reference sensor with its high measuring range is feasible to track the position of the measuring probe and thus will be applied for focus tracking to increase the overall measuring range of the system. The detailed arrangement is introduced in section 3.4.

3.3 Phase retrieval algorithms for real time implementation

One of the major features of the fiber coupled interferometric point sensor considered in this chapter is its periodical optical path length modulation. The oscillation of the probe only affects the optical path length difference in the measuring path of the common path interferometer, modulating the interference signal and thus causing topography related changes in the optical path length to appear as phase shifts in the modulated signal in the time domain as expressed in equation (3.1) (see p. 70). In the frequency domain the modulation shifts the low frequency topography related phase information to the higher modulation frequency, thus enabling the application of carrier fringe based phase retrieval approaches by spectral filtering like the lock-in algorithm. The modulated interference

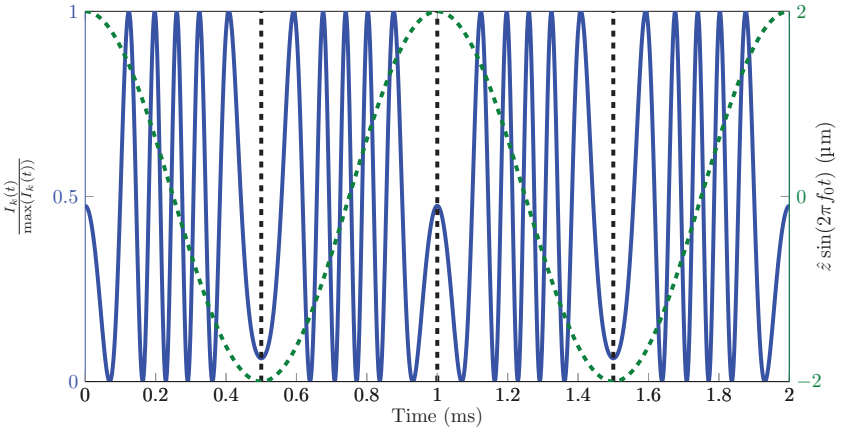

Figure 3.6: Simulated actor movement (green, dashed), simulated interference signal (blue, solid), turning points location (black, dashed)

signal from equation (3.1) is depicted in figure 3.6, together with the actor movement. The wavelength is assumed to be $\lambda_k = 1550\,\text{nm}$, resulting in $\frac{4\hat{z}}{\lambda_k} \approx 5.2$ periods of the interference signal for one half cycle of the actor oscillation for an amplitude $\hat{z} = 2\,\mu\text{m}$. At the turning points of the actor movement, which are marked by dashed black lines in figure 3.6 the sign of the phase evolution $\frac{d\phi_k(t)}{dt}$ is inverted, thus interrupting the almost harmonic sinusoidal phase evolution. Also within one actor slope, the changing velocity of the bending beam causes a frequency modulation, which increases close to the turning points.

3.3.1 Lock-in detection algorithm

A basic and well-established approach for phase retrieval from the signal shown in figure 3.6, is given by the lock-in detection algorithm. This approach is described in detail and illustrated for the purpose of phase retrieval with the fiber coupled interferometric point sensor with periodical optical path length modulation in [44]. It was successfully applied for phase retrieval in [41, 42, 44–47] and showed high robustness with respect to the modulation amplitude of the the interference signal. To apply the lock-in algorithm, the section of the interference signal corresponding to the almost linear section of actor movement around the center of each slope is recorded. The actor amplitude is chosen to be $> \lambda_k$ such that this section contains multiple periods of the interference signal. The sample interval on the slope may be chosen arbitrarily as long as it does not overlap with the turning points of the actuator movement and contains at least two interference fringes. Then the dominant frequency of the recorded interferogram is determined employing a discrete Fourier transform (DFT). For consecutive phase retrieval, the real- and imaginary part of the complex spectrum of the respective interferograms are determined by a DFT algorithm for the dominant frequency component only and the inverse tangent function is used to calculate the phase value within an unambiguity interval $\phi_k \in [-\pi, \pi]$ [44].

$$\underline{H}_{m_0} = \frac{1}{N} \sum_{n=0}^{N-1} h_n e^{-j2\pi \frac{m_0 n}{N}} \tag{3.6}$$

The DFT formula to calculate the complex spectrum for the dominant frequency component at index m_0 is formulated in equation (3.6). Therein $\underline{H}_{m_0} = \underline{H}(m_0 \Delta f)$ is the complex spectral component of the Fourier transformed signal at index m_0, N is the total number of samples recorded at each respective slope interval and $h_n = h(n\Delta t)$ are the discrete sample points of the intensity $I_k(t)$. The single frequency component DFT in equation (3.6) is also referred to as the lock-in detection. It combines a narrow frequency filter for the dominant signal frequency component at frequency index m_0 with an averaging in the time domain, by summing up the weighted samples $h(n\Delta t)$. Thus, disturbances occurring at other frequencies in the spectral domain are filtered and white signal noise in the time domain may also average out. This causes the high robustness of the lock-in detection algorithm with respect to periodic and also randomly distributed perturbations, affecting the interferograms amplitude and not its phase. However, a drawback of the lock-in detection algorithm is given in its comparable low phase data rate, since N samples of the intensity are required to calculate one phase value and in the setting with the oscillating bending beam, the data rate is limited to one phase value per half cycle of the actor. In section 3.2 the advantage of focus tracking during measurements with the fiber coupled point sensor is motivated. This focus tracking application requires the on the fly real time determination of the surface topography under investigation to dynamically maintain the position of the measuring probe with respect to the measuring surface. Thus, the phase values, which are directly proportional to the surface height values have to be computed on a real time system like a digital signal processor (DSP). Otherwise, the focus position

could not be maintained during measurement and either the measurement would have to be paused or bad positioning and collisions may occur. To reduce the overall system cost a low priced DSP, the STM32F4 Discovery Board is employed to conduct the 3D-topography measurements. The computational power of this device is feasible to implement the on the fly phase retrieval algorithm. However, processing time has to be treated as a limited resource, motivating the consideration of the algorithmic implementations of phase retrieval methods presented in this section, which in combination with more potent DSP or FPGA systems would yield very high phase data rates. The output rate of topography data is, due to the limited unambiguity range of the laser interferometer, also directly related to the maximum possible scanning speed of the point sensor. The ambiguity of the phase values limits the maximum height difference between to neighboring sample points on the measuring object to $\pm\frac{\lambda_k}{4}$, if a single wavelength is considered for the measurement. Thus, if the measuring object shows a steep slope, a higher phase data rate enables the unambiguous measurement at a higher scanning speed. This relation has also been considered in [157]. The computational effort per phase value of the different considered methods is compared by the number of floating point operations required. Referring to [158] basic floating point operations like addition, subtraction, multiplication and division require a similar amount of processing cycles on modern processing units when implemented in C. By counting the number of floating point operations required to calculate a phase value the different approaches for phase retrieval on the digital signal processor are compared. In case of the lock-in detection algorithm according to equation (3.6) N additions and N multiplications are required to calculate both, the real and imaginary part of the complex spectral component.

An interesting alternative to the phase retrieval employing the lock-in detection algorithm is given by time discrete Hilbert filters and quadrature filters, which are described in [75,148]. Hilbert transformation as a phase retrieval approach to achieve higher phase data rate is discussed in [44, 46, 157] and has already been shown to yield feasible topography results. However, there are two characteristic, systematic errors commonly observed in the surface phase profiles retrieved by employing the Hilbert Transform, which are considered in the following section in detail, also suggesting a possible correction.

3.3.2 Time discrete Hilbert filters

The Hilbert transformation in the time domain causes the application of a $\frac{\pi}{2}$ phase shift by multiplication of an arbitrary spectral distribution $\underline{H}(\omega)$ with the transfer function $\underline{G}(\omega)$ in the frequency domain:

$$\begin{aligned}\underline{G}(\omega)\underline{H}(\omega) &= -j\mathrm{sign}(\omega)\underline{H}(\omega)\\ &= e^{-j\frac{\pi}{2}}\mathrm{sign}(\omega)\underline{H}(\omega)\end{aligned} \tag{3.7}$$

Here sign(ω) denotes the sign function in dependence of the frequency.

$$\underline{G}(\omega) = \begin{cases} +j \ \forall \ \omega < 0 \\ 0 \ \ \forall \ \omega = 0 \\ -j \ \forall \ \omega > 0 \end{cases} \tag{3.8}$$

Resulting in a phase shift of $+\frac{\pi}{2}$ for all $\omega < 0$ and $-\frac{\pi}{2}$ for all $\omega > 0$. The frequency domain representation of the Fourier transform of the continuous time domain Hilbert transformation according to equation 3.7 may also be considered as a convolution of the arbitrary signal $h(t)$ with $g(t)$ in the time domain. To determine the time domain representation of $\underline{G}(\omega)$ the following transformation pair is used.

$$\begin{aligned} &\frac{1}{2}\text{sign}(t) \circ\!\!-\!\!\bullet -\frac{j}{\omega} \\ \Rightarrow \ &\text{sign}(t) \circ\!\!-\!\!\bullet \frac{2}{j\omega} \end{aligned} \tag{3.9}$$

To find the desired transformation pair the duality of the Fourier transformation is employed, which states that if the transformation pair $x(t) \circ\!\!-\!\!\bullet \underline{X}(\omega)$ exists, there also exists the dual transformation pair $\underline{X}(t) \circ\!\!-\!\!\bullet 2\pi x(-\omega)$ [159]. Thus, equation (3.9) implicates the existence of the required transformation pair.

$$\begin{aligned} &\frac{2}{jt} \circ\!\!-\!\!\bullet 2\pi\text{sign}(-\omega) \\ \Rightarrow \ &\frac{1}{j\pi t} \circ\!\!-\!\!\bullet \text{sign}(-\omega) \\ \Rightarrow \ &\frac{1}{\pi t} \circ\!\!-\!\!\bullet -j\text{sign}(\omega) \end{aligned} \tag{3.10}$$

Therefore, the continuous Hilbert transformation is described in the time domain as the convolution $\underline{G}(\omega)\underline{H}(\omega) \bullet\!\!-\!\!\circ \ g(t) * h(t)$ with $g(t) = \frac{1}{\pi t}$.

In the following section the discrete approximation of the Hilbert transformation for practical implementation is introduced. Assuming the Hilbert filter $g(m)$ is composed of $2M + 1$ discrete coefficients $m \in \mathbb{Z}$ for $-M \leq m \leq M$ and N samples of the signal $h(n)$ are acquired $n \in \mathbb{N}$ for $0 \leq n \leq N - 1$, with the sampling interval Δt. The discrete Hilbert transformation serves the same purpose as the continuous Hilbert transformation and shall approximate the transfer function in (3.8). The frequency-dependent transfer function $\underline{G}(k)$ is visualized as its z-transform on the unit circle in figure 3.7 a), the index $-K < k < K$ refers to the discrete frequencies separated by $\Delta f = \frac{1}{N\Delta t}$. The index $k = K$ is associated with the maximum frequency $\omega_{\max} = 2\pi f_{\max}$ where $f_{\max} = \frac{f_s}{2}$ is half the sample frequency and thus the highest frequency satisfying the sample theorem. When the transfer function is analyzed over the unit circle in the z-plane the position $\phi = 0$ is associated to $\omega = 0$ and $\phi = \pi$ to $\omega = \omega_{\max}$. The upper half of the unit circle $0 < \phi < \pi$ represents $0 < \omega < \omega_{\max}$ and the lower half $0 > \phi > -\pi$ represents $0 > -\omega > -\omega_{\max}$.

„The spectrum of a signal is defined as the value of its z-transform on the unit circle in the z-plane [148].“ In the z-plane the spectrum of the signal $g(m)$ is written as $\underline{G}(e^{j\phi})$, where ϕ represents the angle of the vector from the origin to the respective point on the unit circle. A sequence of finite length can also be represented by its discrete Fourier transform:

$$\underline{G}(k) = \frac{1}{2M+1} \sum_{m=-M}^{M} g(m) e^{j2\pi \frac{mk}{2M+1}} \tag{3.11}$$

From figure 3.7 a) also the relation of the transfer function $\underline{G}(\omega)$ in the frequency do-

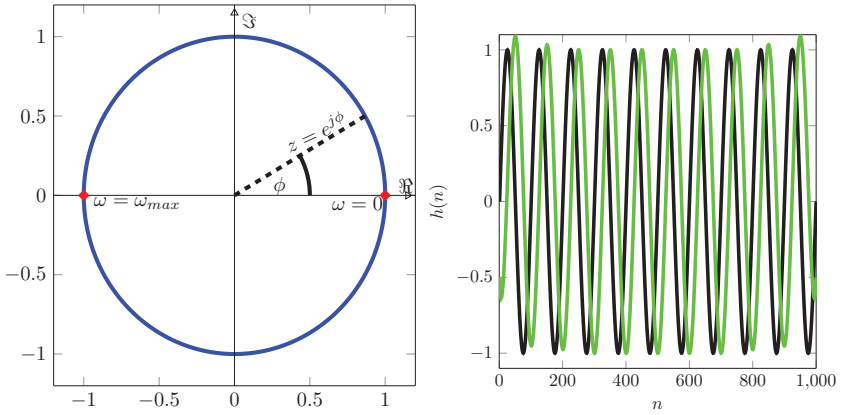

(a) (b)

Figure 3.7: a) Representation of a signal spectrum on the unit circle in the z-plane. b) Sampled sinusoidal signal of $N = 1000$ sample points (black line), phase shifted signal resulting from the time domain convolution of the sinusoidal signal with the time discrete Hilbert transformer $g(m)$ with $M = 226$ (green line).

main to the transfer function $\underline{G}(z)$ in polar coordinates (z-plane) is withdrawn. Mapping the complex transfer function $\underline{G}(\omega)$ to the complex plane in dependence of the complex variable $z = e^{j\phi}$ results in the transfer function in equation (3.12).

$$\underline{G}(z) = \begin{cases} -j \ \forall \ 0 < \phi < \pi \\ +j \ \forall \ \pi < \phi < 2\pi \end{cases} \tag{3.12}$$

The transfer function in equation (3.8) and (3.12) is that of an ideal Hilbert transformer represented in the spectral domain over the frequency and in the z-plane over the unit circle respectively. Applying the inverse z-transformation to $\underline{G}(z)$ the coefficients of the time discrete Hilbert filter $g(m)$ will result. The analytic description of the inverse z-transformation employing contour integrals is given in equation (3.13) as considered in

[148].

$$g(m) = \frac{1}{2\pi j} \oint \underline{G}(z) \cdot z^{(m-1)} dz \tag{3.13}$$

By substitution of $z = e^{j\phi}$ the contour integral in equation (3.13) is changed into a line integral. The differential is therefore substituted by $dz = je^{j\phi}d\phi$.

$$\begin{aligned} g(m) &= \frac{1}{2\pi j} \left(\int_0^{\pi} -je^{j\phi(m-1)} je^{j\phi} d\phi + \int_{\pi}^{2\pi} je^{j\phi(m-1)} je^{j\phi} d\phi \right) \\ &= -\frac{1}{2\pi} \left(\left[\frac{e^{j\phi m}}{m} \right]_0^{\pi} - \left[\frac{e^{j\phi m}}{m} \right]_{\pi}^{2\pi} \right) \\ &= -\frac{1}{2\pi m} \left(\left(e^{j\pi m} - 1 \right) - \left(e^{j2\pi m} - e^{j\pi m} \right) \right) \\ &= \frac{1}{2\pi m} \left(\cos(m\pi) - 1 - \cos(m2\pi) + \cos(m\pi) \right) \\ &= \frac{1 - \cos(m\pi)}{m\pi} \end{aligned} \tag{3.14}$$

The function $g(m)$ in equation (3.14) is employed to calculate the discrete time domain coefficients of the Hilbert filter for a window size of $m \in \mathbb{Z}$ for $-M \leq m \leq M$. Thus, by convolution $\tilde{h}(n) = g(m) * h(n)$ of the time discrete filter function $g(m)$ with the sampled signal $h(n)$ the $\frac{\pi}{2}$ phase shifted signal $\tilde{h}(n)$ results.

$$\tilde{h}(n) = \sum_{m=-M}^{M} \frac{1 - \cos(m\pi)}{m\pi} \cdot h(n-m) \quad \forall\, 0 \leq n \leq N-1 \tag{3.15}$$

In figure 3.7 b) $h(n) = \sin(2\pi \frac{10n}{N})$ and the corresponding signal $\tilde{h}(n)$ are illustrated as an example for $N = 1000$ and $M = 226$. On the intervals $[0, M]$ and $[N - M, M]$ close to the edges of the sampled signal the amplitude of the phase shifted signal is not correct. This is due to the Hilbert filter not being fully loaded with sampling data. To generate valid results the filter has to be fully loaded with sample data. Thus, by convolving it with a signal errors will occur in the described intervals caused by a lack of sample data. According to equation (3.15) the retrieval of each phase value requires $2M + 1$ additions and multiplications. Thus, compared to the computation effort of the lock-in detection approach, the discrete Hilbert filter is more efficient per phase value as long as $M \leq \frac{2N-1}{2}$.

3.3.3 Characteristic deviations of discrete Hilbert filters

The ideal Hilbert transformer is a non-causal infinite impulse response (IIR) filter. The discrete Hilbert filter, whose coefficients are given in equation (3.14), is an approximation of the ideal Hilbert transformer by a finite impulse response (FIR) filter of the length $2M + 1$ [160]. Compared to the ideal transformer with an infinite number of coefficients,

the FIR filter appears to be windowed by multiplication with a rectangular window function in the time domain. Thus, its transfer function in the frequency domain is convoluted with a sinc-function causing deviations to the transfer behavior of the ideal Hilbert transformer. The absolute value of the transfer function of a time discrete Hilbert filter $|\underline{G}(\omega)| = |\mathbb{F}\{g(m)\}|$ with $M = 32$ and $M = 128$ is depicted in figure 3.8 a). It is visible,

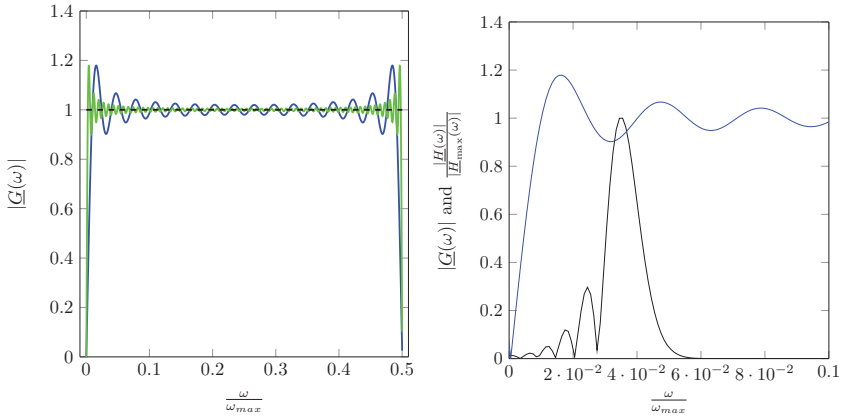

Figure 3.8: a) Absolute value of the spectrum of the time discrete Hilbert filter $g(m)$ in the frequency domain for $M = 32$ (blue line) and $M = 128$ (green line) in comparison to the absolute value transfer function of an ideal Hilbert transformer (black dashed line). b) Absolute value of the spectrum of the time discrete Hilbert filter $g(m)$ in the frequency domain for $M = 32$ (blue line) and spectrum of the sampled interference signal $h(t)$ from figure 3.6 corresponding to the actor movement using a Blackman window (black line).

that the FIR Hilbert filters show a sinc-like oscillation in their absolute value transfer function. With an increasing number of filter coefficients the step function characteristic of the ideal transformer is better approximated. However, the Gibbs phenomenon is observed causing an overshooting at the edges. The convolution of a sampled signal in the time domain with the FIR Hilbert filter may also be considered as a multiplication of its transfer function in the frequency domain with the Fourier transformed signal $g(t) * h(t) \circ\!\!-\!\!\bullet \underline{G}(\omega)\underline{H}(\omega)$. Thus, the non constant absolute value transfer function of the FIR Hilbert filter is multiplied with the discrete spectrum of the sampled signal. In this process, the waviness of the Hilbert filter's transfer function will cause different amplification or weighting of the signal's spectral components at different frequencies. This leads to a systematic deviation in the amplitude of the imaginary part of the reconstructed analytic signal and thus also to a deviation in retrieved phase values. The implications of these systematic deviations considering signals of the fiber coupled point sensor as shown

in figure 3.6 will be outlined here. Figure 3.8 b) shows the spectral distribution of the sampled interference signal, using a Blackman window (black line), corresponding to a half period of the actor movement depicted in figure 3.6 and described in equation (3.1). Due to the frequency modulation in the signal its spectrum is broad and contains side lobes. Thus, by calculating $\underline{G}(\omega)\underline{H}(\omega)$ the spectral components are differently weighted due to the waviness of the non ideal Hilbert transformer. This results in an error in the determined analytic signal and the phase retrieved from it. Furthermore, it is noteworthy that the amplification error is also dependent on the signal frequency determined in relation to the spectral function of the Hilbert transformer. If the signal frequency changes and the lobes in the spectrum move to a different position also the amplitude of the imaginary part of the analytic signal is affected. This even occurs if a perfectly sinusoidal function is considered. The relative position of the discrete spectrum of the sine function to the filter spectrum determines the amplification error. Together with the deviations caused by missing signal information at the window edges described earlier, the waviness of the absolute value transfer function of the non-ideal Hilbert filter are the predominant sources of deviations employing time discrete Hilbert transformation filters.

3.3.4 Signal resampling to reduce systematic deviations in discrete Hilbert transformation

The interferogram of the fiber coupled point sensor is characterized by the sinusoidal actor movement, resulting in the frequency modulated interference signal over time shown in figure 3.6. Since the interferogram is sampled temporally equidistant, the spatial sample density increases around the areas of slower actor movement and the sample points are not equally spaced. In [46,157] the option of resampling the temporally equidistant signal into a spatially equidistant signal is discussed. An analytic procedure to calculate the indices $n_{\Delta s}$ of the discrete sample points of the spatially equidistant signal based on the temporally equidistant signal assuming a periodic sine or cosine actor movement $\hat{z}\sin(2\pi f_0 n\Delta t)$ as in equation (3.1) is introduced in [157] and represented by equation (3.16).

$$n_{\Delta s} = \text{round}\left(\frac{N}{2\pi}\arccos\left(1-\frac{2n}{N_{\Delta s}}\right)\right) \tag{3.16}$$

Therein, $n_{\Delta s}$ refers to the indices of the spatially equidistant sample points in the original temporally equidistant sampled signal $h(n)$, N is the number of sample points in the temporally equidistant signal, n is the sample index of the temporally equidistant sample points in the discrete signal $h(n)$ and $N_{\Delta s}$ is the number of spatially equidistant sample points. By the resampling algorithm a subset of indices $n_{\Delta s} \subseteq n \in \{0,\cdots,N-1\}$ is chosen among the set of indices in the temporally equidistant signal, such that by $h(n_{\Delta s})$ the spatially equidistant signal with a total number of $N_{\Delta s} \leq N$ samples is described. To achieve proper results in the case of strongly nonlinear actor movement, as in the considered case of sinusoidal actor movement, $N_{\Delta s} << N$ should be chosen. However, the sampling theorem has to be considered to find a feasible value of $N_{\Delta s}$. After determination of

the spatially equidistant sample indices, the spatially equidistant signal $h(n_{\Delta s})$ is linearly interpolated to match the number of original sample points N with $\tilde{n}_{\Delta s} \in \{0, \cdots, N-1\}$. After interpolation the final set of spatially equidistant sample points $h(\tilde{n}_{\Delta s})$ results. Considering the interference equation (3.1), the resampling linearizes the nonlinear part of the periodical optical path length modulation by substituting $\hat{z} \sin(2\pi f_0 n \Delta t) = \hat{z} - \tilde{n}_{\Delta s} \cdot \Delta s$, which is the basis of the derivation of the resampling algorithm in [157]. Thus the phase evolution $\phi(t)$, which is nonlinear in the case of temporally equidistant sampling and causes the frequency modulation becomes linear resulting in a constant frequency in the resampled interference signal.

To illustrate the resampling procedure, the temporally equidistant sampled signal $h(n)$ of half an actor period with $N = 256$ is compared to the resampled signal $h(\tilde{n}_{\Delta s})$, which was resampled using $N_{\Delta s} = 128$ in figure 3.9 a). Figure 3.9 b) shows the spectrum of the

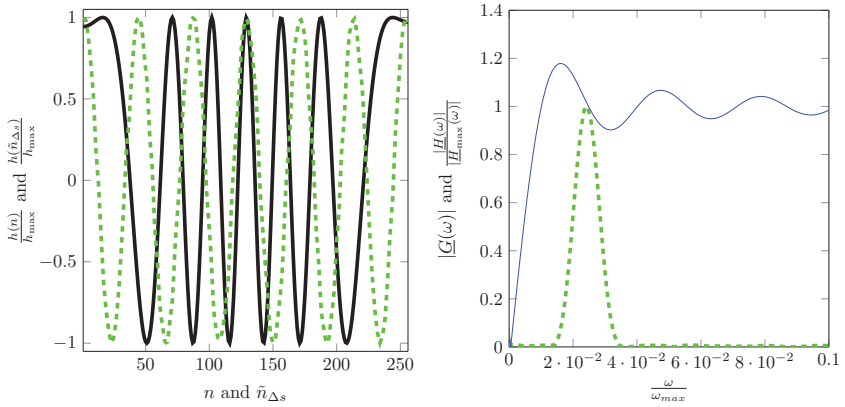

Figure 3.9: a) Temporally equidistant sampled interference signal $h(n)$ corresponding to half an actor period (black solid line), spatially equidistant resampled signal $h(\tilde{n}_{\Delta s})$ (green dashed line). b) Absolute value spectrum of the time discrete Hilbert filter $g(m)$ in the frequency domain for $M = 32$ (blue line) and spectrum of the resampled interference signal $h(\tilde{n}_{\Delta s})$ using a Blackman window (dashed green line).

spatially equidistant resampled signal $h(\tilde{n}_{\Delta s})$ after windowing with a Blackman window (green dashed line). In comparison to the spectrum of the temporally equidistant signal $h(n)$ in figure 3.8 b) no side lobes occur in the spectrum of the spatially equidistant resampled signal, indicating the successful linearization of the phase evolution and thus the cancellation of the frequency modulation. Therefore, the characteristic error in the signal phase retrieved from the analytic signal is expected to be smaller for the resampled signal.

If a plane mirror is used as the measuring object with the fiber coupled point sensor, no movement is applied to the object and environmental perturbations are neglected, the phase of the interference signal is solely modulated by the periodic actor movement. By recording the interference signal for one actor half cycle as considered in the simulation in figure 3.9 a), the Lock-In detection algorithm discussed in section 3.3.1 would yield a single phase value retrieved from the recorded interferogram. However, employing the discrete Hilbert filter discussed in this section the analytic signal is reconstructed, and a phase value for each sample point is retrieved, resulting in a profile of the actor movement. The sampled signal $h(n)$ and its corresponding resampled signal $h(\tilde{n}_{\Delta s})$ according to figure 3.9 are used in a simulation to calculate the analytic signal by convolving them with the time discrete Hilbert filter $g(m)$. From this the phase information containing the actor movement is retrieved. Assuming a wavelength $\lambda_1 = 1310\,\mathrm{nm}$, an actor amplitude $\hat{z} = 2\,\mu\mathrm{m}$, actor frequency $f_0 = 1\,\mathrm{kHz}$, a sample number $N = 512$ and Hilbert filter width with $M = 32$, the actor movement $z_A(n\Delta t)$ is retrieved from the phase. The difference of the reconstructed actor movement $z_A(n\Delta t)$ to the original actor movement $\hat{z}\sin(2\pi f_0 n\Delta t)$ used in the simulation of the interference signal, is compared for the temporally and spatially equidistant sampled signals respectively in figure 3.10. The phase deviations caused

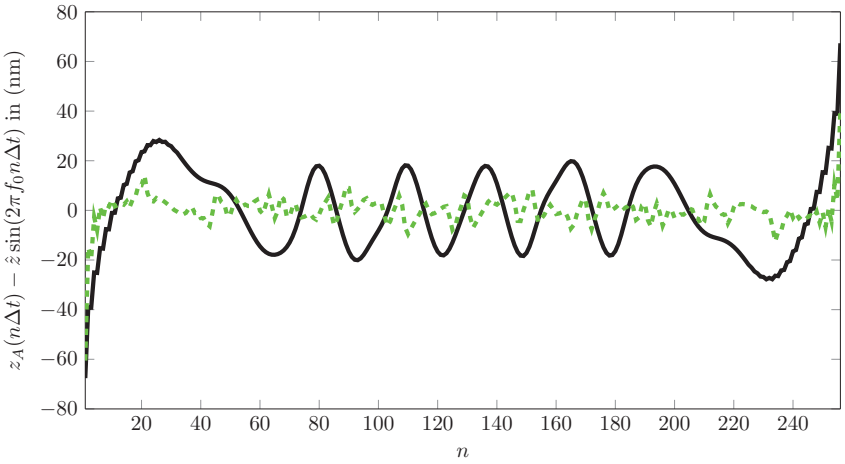

Figure 3.10: Difference of the reconstructed actor movement $z_A(n\Delta t)$ to the original actor movement $\hat{z}\sin(2\pi f_0 n\Delta t)$ for the temporally equidistant signal (black solid line), and for the resampled spatially equidistant signal (green dashed line).

by lacking signal information at the edges of the signal, where the time discrete filter of length $2M + 1$ is not fully loaded are similar in both, the temporally equidistant and the resampled spatially equidistant signal. However, the temporally equidistant sampled

signal shows the characteristic phase error caused by the waviness of the absolute value transfer function of the not ideal Hilbert filter as explained in section 3.3.3. For the spatially equidistant resampled signal this characteristic deviation is effectively reduced. Systematic errors in the determination of the imaginary part of the analytic signal employing Hilbert transform approaches were already pointed out in [38]. However, in that contribution the deviations were analyzed referring to the amplitude errors of the analytic signal in the time domain. The underlying phenomena in the frequency domain pointed out in section 3.3.3 were not considered. In [38] the amplitude error in the analytic signal is corrected in the time domain, by offset and tilt compensation of the analytic signal thus reducing the phase deviation, but maintaining its characteristic periodic form. Also, the correction of the imaginary part of the analytic signal in the time domain may be difficult if it is subject to additional amplitude modulations. Thus, the resampling approach in combination with the discrete Hilbert filter offers advantages.

3.3.5 Frequency selective quadrature filters

In [161] Hilbert filters and further quadrature filters based on [75] are considered as convolution filters in the time domain to retrieve the envelope of a white light interference signal from the analytic signal. The employed quadrature filters are composed of sine and cosine functions in the frequency domain, they are specifically adjusted to the spectrum of the sampled signal. If properly designed, they emulate the transfer behavior of an ideal Hilbert filter for a narrow frequency band centered around the dominant frequency of the sampled signal and suppressing side lobes. Thus, they combine the Hilbert transformation with a frequency filtering in the spectral domain, making the filters more robust against frequency modulations, but also limiting their functionality to the design frequency. The design process of these filters is discussed in detail in [75, 161]. Since the basic function of these quadrature filters is to generate an analytic signal from the sampled input signal they may as well be used for phase retrieval. If frequency modulated signals like in figure 3.9 are processed by such quadrature filters, the amplitude errors in the imaginary part of the resulting analytic signal may also be reduced by resampling of the frequency modulated signal. This is especially true for the case of low order quadrature filters, which are rather broadband in the frequency domain and do not offer a sufficient suppression of side lobes. Considerable advantages of the quadrature filters presented in [75] are their straight forward design in the frequency domain and their customizable frequency selective transfer function. As the time discrete Hilbert filters they are applicable as convolution filters in the time domain and yield a phase value for each discrete sample point. Their calculation efficiency per phase value is equivalent to that of the discrete Hilbert filter. However, these quadrature filters usually require less filter coefficients M.

3.4 Focus-tracking system

The fiber coupled interferometric point sensor according to figure 3.1 together with the reference probe depicted in figure 3.5 and the real-time signal evaluation implemented on a DSP board is employed in a 3D-topography measuring system with focus tracking. The setup consists of three linear stages, two dedicated to the x-y-scanning and positioning of the measuring object with respect to the probe and one for the focus tracking in z-direction. The reference probe is mounted above the measuring probe and not affected by the movement of the tracking axis. The oscillation of the polished upper surface of the measuring probe's bending beam modulates the interference signal of the reference probe. Thus, the measuring probe records the topography changes on the measuring

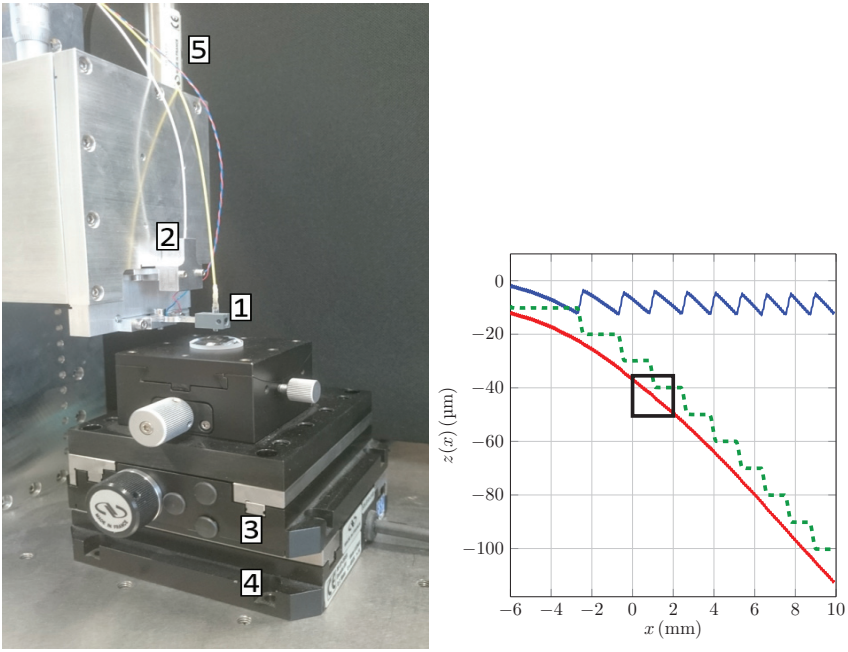

(a) (b)

Figure 3.11: a) 1: Interferometric measuring probe, 2: Interferometric reference probe, 3: x-scanning axis, 4: y-scanning axis, 5: z-tracking axis b) Height profile $z_m(x)$ of the measuring probe (blue line), height profile $z_r(x)$ of the reference probe (green dashed line), combined height profile $z_m(x) - z_r(x)$ (red line).

object and also the changes in the optical path length difference (OPLD) due to focus tracking, while the reference probe measures the OPLD of the tracking movements only. By subtraction of the reference interferometer height profile from the height profile of the measuring interferometer the actual topography of the measuring object results. Since both interferometers have the same depth resolution in the z-direction the quality of the topography measurement is almost unaffected. Figure 3.11 a) shows the setup composed of the interferometric point sensors and the linear stages. The phase information of the topography is retrieved in real time during the measurement procedure by a lock-in detection algorithm implemented on a DSP board. Output lines of the signal processor board are directly connected to the input pins of the axis controller, which runs a real time application. When a topography measurement is started the DSP locks the relative OPLD z_0 at the starting time as the reference position of the measuring probe, which should be maintained. If the difference $\Delta z = z(t) - z_0$ between the current OPLD $z(t)$ and z_0 reaches a threshold Δz_{Thr} the z-tracking axis is triggered to maintain the absolute distance to the measuring object. As explained in section 3.3.1 the topography data rate of the setup is limited to two phase values per actor period, when employing the lock-in algorithm. Thus, assuming an actor frequency of 1 kHz, which is well achievable using the piezo actor bending beam, the OPLD $z(t)$ is refreshed at a rate of 2 kHz. The clock period of the real time system running on the axis controller „XPS-Q8 “ is specified to be 10 kHz. Therefore, a correction of the focus position of the setup would theoretically be possible within a time interval of 0.5 ms. However, the experiments show that the actual response time of the z-positioner including accelerating, moving and stopping the z-axis is much slower. Depending on the size of Δz_{Thr}, which due to the small depth of field presented in figure 3.3 is in the µm range, the completion of the tracking movement took about 500 ms. Since the common scanning speed of the interferometric point sensor is in the range of $v \in [0.1, 2]\,\frac{\mathrm{mm}}{\mathrm{s}}$ the comparably slow focus tracking does not allow to react to fast topography changes as they occur on rough surfaces. However, the focus tracking is useful when measuring extended surface parts of objects featuring a continuous tilt or curvature, like lenses. To test the capabilities of the focus tracking a 16 mm × 0.4 mm surface section of the sinusoidal standard „531“ fabricated by Rubert & Co. Ltd., is placed slightly tilted with respect to the measuring probe and the surface topography is recorded with the focus tracking setup. The sinusoidal standard is specified by a period of 100 µm and an amplitude of 500 nm. In figure 3.11 b) the topography results $z_m(x, y)$ and $z_r(x, y)$ of the measuring and reference sensor as well as the combined topography $z_m(x, y) - z_r(x, y)$ are depicted for one line scan. The scan velocity is $v = 2\frac{\mathrm{mm}}{\mathrm{s}}$, the actor frequency $f_0 = 1\,\mathrm{kHz}$ and 4 lines with a distance of 0.1 mm to each other are scanned in a meandering pattern. The focus tracking threshold is adjusted to be $\Delta z_{\mathrm{Thr}} = 10\,\mu\mathrm{m}$, such that if the distance to the locked focus position z_0 becomes bigger than that threshold a correction movement of the z-axis occurs. The tracking motion causes the sawtooth like pattern in the height profile recorded by the measuring probe (blue line) and the step like pattern recorded by the reference probe (green line) in figure 3.11 b). By subtraction $z_m(x, y) - z_r(x, y)$ of the measuring and reference profile the combined height profile (red line) results, which represents the actual topography of the tilted sine standard. In figure 3.12 the topogra-

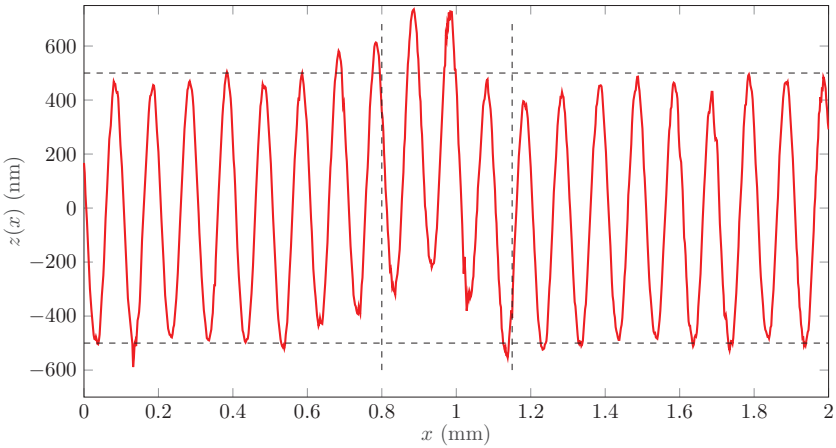

Figure 3.12: Zoomed section of the combined height profile $z_m(x) - z_r(x)$ related to the black rectangle in figure 3.11 b). Tilt is removed from the sinusoidal surface profile by subtracting the local straight line fitted to the height data on the interval $x \in [0, 2]$ mm by linear regression.

phy region enclosed by the black rectangle in figure 3.11 b) is depicted. A straight line fitted to the height data on the interval $x \in [0, 2]$ mm by linear regression is subtracted to remove the tilt from the sinusoidal surface profile, such that the periodic structure may be examined in more detail. The sinusoidal structure of the measurement standard is well resolved. The amplitude of 500 nm is determined correctly overall, with some minor deviations. Also 10 periods per mm are recorded, confirming the specified 100 µm periodicity of the standard. The peaks of the sinusoidal structure appear to be somewhat serrated. This is caused by the rather low number of 100 data points per period and the strong mismatching in the dimensions of the abscissa and ordinate. If the ordinate is squeezed the structure looks almost perfectly sinusoidal. A recurring phenomena has to be pointed out, which is visible in the intervals where the focus tracking movement occurs. In figure 3.12 this region is enclosed by two vertical dashed lines on the interval $x \in [0.8, 1.15]$ mm. Apparently a deviation of ≈ 200 nm occurs between the height measurement of the measuring and reference interferometer during the tracking motion. However, since there is no stationary, step like offset introduced to the combined topography the focus tracking distance Δz_{Thr} appears to be measured correctly by both sensors. The locally constrained occurence of the deviation in the regions of tracking motion implies, that it may be related to the axis acceleration process or another influence only present during dynamic motion of the system. Deviations of similar magnitude are observable in each focus tracking interval. Part of this deviation may be caused by a difference in the central wavelength of

the laser sources. Employing equation (3.3), the height deviation of $\approx 200\,\mathrm{nm}$ on the distance of $10\,\mu\mathrm{m}$ would correspond to a wavelength difference $\Delta\lambda \approx 26\,\mathrm{nm}$. The distributed feedback laser sources are specified with a peak wavelength of $\lambda_{\mathrm{peak}} = 1310\,\mathrm{nm} \pm 15\,\mathrm{nm}$ by the distributor. However, a deviation in wavelength is unsuitable to explain the dynamic behavior, since it would result in a stationary offset after each tracking move. Also the strong amplitude modulation occurring in the interference signal during the focus tracking movement may contribute to this deviation. Comparative measurements of the amplitude modulation in the interferogram of the wavelength $\lambda_1 = 1310\,\mathrm{nm}$ and $\lambda_2 = 1550\,\mathrm{nm}$ show, that the amplitude modulation of the measuring probe is wavelength specific. The imaging by the GRIN lenses causes chromatic aberration effects, resulting in a different focal position for the respective wavelengths. Therefore, if the system is focused for λ_1 it is defocused for λ_2. Due to the confocal behavior of the probes, discussed in section 3.2, the amplitude modulation is stronger for the focused wavelength and may cause deviations in the phase retrieval process. However, the lock-in detection algorithm is quite robust against this perturbation and should cancel out most of it. Further sources of phase measurement deviations are given by the averaging effect of the extended illuminated area on the measuring object. In focal position the diameter of the illuminating Gaussian intensity profile is, depending on the probes numerical aperture, about $2\,\mu\mathrm{m}$ [46, 155]. In the case of defocusing the illuminated surface area is increased. The scanning speed may also contribute to the generation of phase errors. If the rate of phase evolution of the surface reaches similar dimensions as that of the actor movement, the carrier fringe pattern is distorted and the phase retrieval process will yield perturbed results. In case of measurements, which take multiple seconds, also a potential influence of drifting wavelength in the respective laser sources has to be considered. As outlined in section 3.1 very small variations $< 0.1\,\mathrm{nm}$ in the lasers peak wavelength may cause remarkable height deviations. In the case of the reference sensor this effect is even stronger due to the larger total optical path length difference between the reference plane and the measuring object. The impact of the different sources of deviation on the measurement results presented in figure 3.12 is analyzed by simulations with a comparable virtual measuring object. The results obtained from these indicate that the wavelength mismatching is probably the predominant source of deviations between the results of the reference and measuring interferometers. However, comparative measurements of a distance change of $1\,\mathrm{mm}$, applied by moving the z-positioner and assuming the wavelength $\lambda_1 = 1310\,\mathrm{nm}$, for both laser sources of the reference and measuring probe respectively, revealed the peak wavelength of the laser diodes to be $\lambda_1 \approx 1315\,\mathrm{nm}$ and $\lambda_2 \approx 1547\,\mathrm{nm}$. Thus, the mismatching in the assumed and actual wavelength is almost equal in the measuring and reference system and should not cause strong deviations. Another possible cause for the deviations is given by the mechanical impact of the fiber coupled probe itself on the measurement, when mechanical motion is applied. If the fiber is subject to mechanical stretch or strain it applies a force on the bending beam, thus influencing the optical path difference. When a focus tracking movement is conducted, the measuring probe and the attached fiber are moved. The resulting force on the tip of the bending beam might cause a deviation in the measured optical path length difference. This is not recognized by the reference interferometer, which is

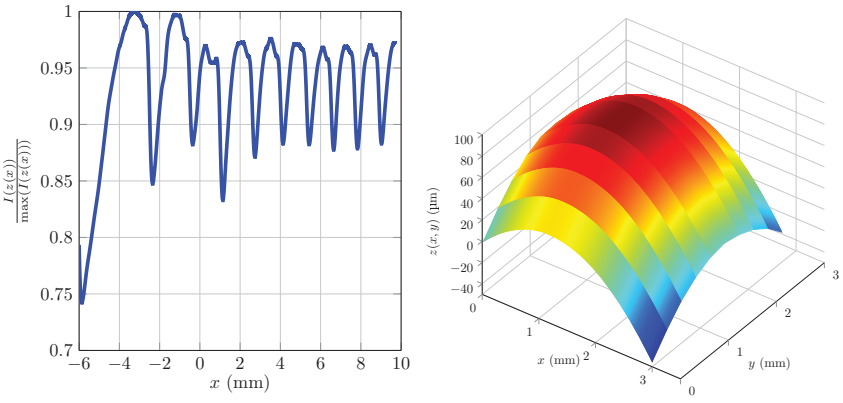

(a) (b)

Figure 3.13: a) Relative intensity distribution $\frac{I(z(x))}{\max(I(z(x)))}$, after reduction of the high frequent intensity modulation due to the sinusoidal surface structure by low pass filtering to visualize the impact of the focus tracking motions. b) 3 mm × 3 mm surface section of a plano-concave lens measured with the focus tracking system.

focused on the center of the bending beam. Comparative focus tracking measurements with different tracking distances Δz_{Thr}, different scanning speed v and different surface profiles showed similar deviations, which tended to be smaller with decreasing scanning speed and tracking distance. This supports the idea of a mechanical impact of the fiber on the measurement. A feasible explanation might be provided by Abbe's comparator principle, which is illustrated for the considered measurement setup in figure 3.14. Under ideal conditions, the probes would be aligned in-line to each other. In case of in-line alignment a change in height Δh_1 at the tip of the measuring probe causes an equal change Δh_2 at the position of the reference probe. However, if the measuring probe is not in-line and tilted by the angle α with respect to the reference probe during motion, the height change at the measuring probes tip Δh_1 will result in a different height change Δh_2. The first order deviation $\Delta h_1 - \Delta h_2$ depends on the Abbe-offset x_2 and is described by the following equation [163].

$$\Delta h_1 - \Delta h_2 = x_2 \sin(\alpha) \tag{3.17}$$

A tilt between the probes may be caused by misalignment of the mechanical tracking axis and α may also vary when a force is applied to the tip of the bending beam. During the focus tracking motion, strain in the fiber, which is attached to the measuring probe might cause a variation in the tilt angle and thus result in the dynamic deviation described above. The Abbe-offset between the focus points of the probes is $x_2 \approx 10\,\mathrm{mm}$. Using this in equation (3.17) yields a measurement deviation of $\Delta h_1 - \Delta h_2 \approx 50\,\mathrm{nm}/1''$. Overall, the

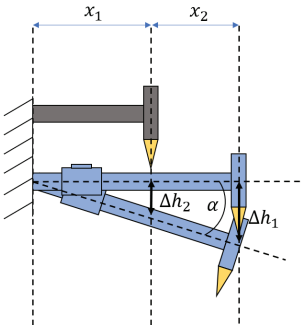

Figure 3.14: Illustration of a first order measurement deviation caused by violation of Abbe's comparator principle in the interferometric system in figure 3.11 a). The Abbe-offset between the interferometer probes is indicated by x_2, which occurs if the sensors are not aligned according to the Abbe's comparator principle [162] and α is the angle of tilt between the probes.

deviations are small compared to the high dynamic range of the system with activated focus tracking and it is likely that all of the aforementioned sources of deviations contribute to the observation presented in figure 3.12. The immediate impact of the focus tracking on the intensity is depicted in figure 3.13 a). To point out the influence of the focus tracking steps, the high frequent intensity modulations caused by the sinusoidal surface structure is filtered out. The diagram shows, that the relative intensity $\frac{I(z(x))}{\max(I(z(x)))}$ of the starting position is maintained and thus the measuring probe stays focused although an overall height distance of over 100 µm is scanned as shown in figure 3.11 b), which is higher than the probes depth of field, as depicted in figure 3.3 b). Finally figure 3.13 b) shows the reconstructed surface topography of a 3 mm × 3 mm surface section of a plano-concave lens, which was measured with the focus tracking system at a speed of $v = 0.2\,\frac{\text{mm}}{\text{s}}$ and a data rate of $f_0 = 800\,\text{Hz}$. Assuming a numerical aperture of the measuring probe of NA = 0.42 as motivated in section 3.2, the acceptance angle of the probe spans the interval $\theta \in [-\theta_{\max}, \theta_{\max}]$ with $\theta_{\max} \approx 24.8°$. Therefore, the reflection coefficient of the glass surface $\left(\frac{E_m'}{E_m}\right)_\perp$ calculated by equation (2.53) assuming $n_{\text{glass}} \approx 1.5$, ranges from 20% to 23% on the plane center area of the lens. For such materials with high transmission the focus tracking is useful, because it can maintain a higher signal quality. Especially considering the increasing slope of the low reflecting glass surface in case of the plano-concave lens, the signal quality would rapidly decrease to be insufficient for phase retrieval without focus tracking. For the depicted section of the lens, 10 lines were scanned in a meandering pattern and the position locks of the scanning axis were used to arrange the height values in the measuring field. The focus tracking motion is already compensated in figure 3.13 b). The compensation by subtracting the reference probe measurement

results from the measuring probe profile worked almost flawless for the presented case. The measurement results and perturbation analysis in this section indicate the potential of the focus tracking setup to enable high dynamic range measurements on measuring objects with a rather plane surface structure.

3.5 Analytic extension of the unambiguity range in dual wavelength interferometry

The unambiguity range of a single wavelength interferometer with wavelength λ_k and the corresponding phase $\phi_k \in [-\pi, \pi]$ is limited to $\pm\frac{\lambda_k}{4}$. By application of the synthetic wavelength $\Lambda = \frac{\lambda_1 \lambda_2}{|\lambda_1 - \lambda_2|}$ and the corresponding phase $\Phi \in [-\pi, \pi]$ in dual wavelength interferometry, the unambiguity is extended to $\pm\frac{\Lambda}{4}$ [28]. As outlined in the state of the art section, the extension of the unambiguity range in laser interferometry is an active field of research and multiple contributions were published in recent years [42,51,55,56,58–61]. The analytic approach for the extension of the unambiguity range in dual wavelength interferometry summarized here is mainly based on the contribution of Peter de Groot [56] and the exact fraction method developed by Michelson and Benoit [110]. The theory of the analytic approach and the extensions to [56] by introduction of a Δ-system are discussed and explained in detail in [42]. The basic proof of principle by experimental results is also shown in [42]. However, employing chopped phase measurements of a sloped depth standard instead of measurements at an actual step standard. The extension of the unambiguity range employing the algorithm in the Δ-system with an extended domain of definition is a simple analytic procedure. It will work properly for any difference phase tuple $\left(\Delta\acute{\Phi}, \Delta\acute{\phi}_k\right)$ as long as the interference signal and the corresponding phase values are not disturbed. The requirements for the successful application of exact fraction based unambiguity range extension algorithms considering the signal quality are discussed in [79].

$$\acute{\phi}_k(n) \in [-\pi, \pi] = \phi_k(n) - \phi_{k0} \; k \in \{1, 2\} \tag{3.18}$$

$$\Delta\acute{\phi}_k(n) \in [-\pi, \pi] = \acute{\phi}_k(n) - \acute{\phi}_k(n-1) \; k \in \{1, 2\} \tag{3.19}$$

$$\Delta\acute{\Phi}(n) \in [-\pi, \pi] = \Delta\acute{\phi}_1(n) - \Delta\acute{\phi}_2(n) \tag{3.20}$$

The components of the difference phase tuple $\left(\Delta\acute{\Phi}, \Delta\acute{\phi}_k\right)$ are defined in equation (3.18) to (3.20) [42]. Therein n denotes the index of the time discrete samples, k is the wavelength index and ϕ_{k0} is the phase value of the k-th wavelength for $n = 0$. To investigate the behavior of the algorithm at measuring objects featuring real step like structures, where typical deviations like the batwing effect [87] may occur, measurements on the vertical standard VS with a nominal step height of 2 µm fabricated by „SiMetricS“ were performed. This step height does not require the extended unambiguity range of the algorithm presented

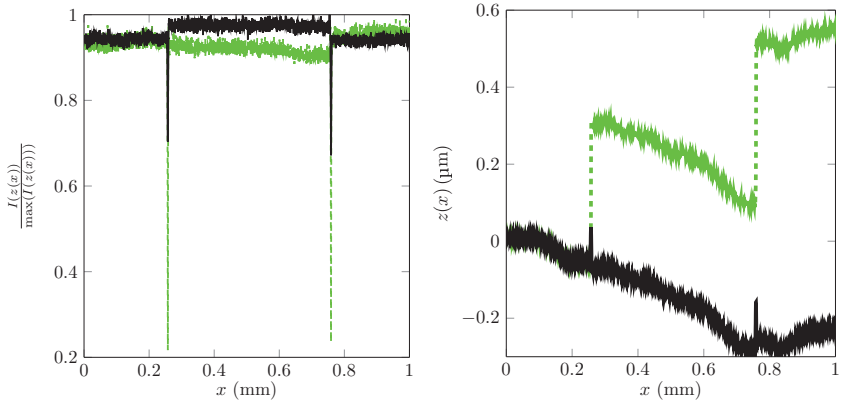

Figure 3.15: Measurement results at the step standard of 2 µm nominal height: a) Normalized intensity in the step region for wavelength $\lambda_1 = 1310\,\text{nm}$ (black line) and $\lambda_2 = 1550\,\text{nm}$ (green dashed line). b) Single wavelength height profile in the step region for wavelength $\lambda_1 = 1310\,\text{nm}$ (black line) and $\lambda_2 = 1550\,\text{nm}$ (green dashed line)

in [42, 56]. However, it is suitable to investigate the influence of perturbations related to the appearance of steep edges, relative to the $\approx 2\,\mu\text{m}$ spot size of the optical probe on the measuring object [46]. The optical surface measurement was performed with the fiber coupled interferometric point sensor according to figure 3.1, employing a scanning speed $v = 0.2\,\frac{\text{mm}}{\text{s}}$ and a data rate of $f_0 = 800\,\text{Hz}$. In figure 3.15 a) the normalized intensity along the lateral dimension of the step profile $\frac{I(z(x))}{\max(I(z(x)))}$ is depicted. At the edges of the structure located approximately at $x \approx 0.22\,\text{mm}$ and $x \approx 0.76\,\text{mm}$ a significant drop in the intensity is observed, which is stronger for the wavelength $\lambda_2 = 1550\,\text{nm}$. This is most probable due to the height-to-wavelength-ratio (HWR) describing the relation between the step height and the effective wavelength [87, 151]. The HWR is related to the interference behavior of light from the distinct levels of the step. Due to the diameter of the illuminating gaussian beam on the measuring object, light from the upper and lower plateau of the step is coupled into the fiber probe simultaneously while passing the step and interferes. To achieve feasible measurement results, the effect of the emission bandwidth of the light source and the influence of the focusing optics on the effective illumination wavelength are considered. Since the DFB laser sources are almost monochromatic, temporal coherence effects may be neglected, when calculating the effective wavelength $\lambda_{k\text{eff}}$, based on the nominal wavelengths λ_k. The effect of the NA on the effective wavelength due to spatial coherence effects is also assumed to be small, since the NA ≈ 0.42 of the probe is not too big and the gaussian pupil function $P(\theta_e)$ according to equation (3.5)

would also have to be considered as a weighting function when calculating the effective wavelength by integration over the entrance angles. To check the assumed small deviation from the nominal wavelength a calibration measurement is performed, moving the measuring probe 10 µm perpendicularly to the surface of a plane mirror by the focus tracking z-positioner and comparing the measured to the nominal distance change. To reduce the influence of positioner errors 6 steps were measured and averaged for each wavelength. The precision of the step height measurement is characterized by a standard deviation of $\sigma_{\text{step}} \approx 80\,\text{nm}$ corresponding to a relative standard deviation of $\sigma_{\text{step,rel}} \approx 0.8\,\%$. From this calibration a measured effective wavelength of $\lambda_{1\text{eff}} \approx 1317\,\text{nm}$ and $\lambda_{2\text{eff}} \approx 1551\,\text{nm}$ results. Compared to the wavelength calibration conducted with the low aperture reference probe in section 3.4 these results show a plausible increase in the effective wavelength for the higher NA probe as expected. However, due to the relative standard deviation in the step height measurements of $\sigma_{\text{step,rel}} \approx 0.8\,\%$, which propagates as an uncertainty to the determined effective wavelengths this effect might be coincidental. Employing the measured effective wavelengths $\text{HWR}_{\lambda 1} = 1.52$ and $\text{HWR}_{\lambda 2} = 1.29$ results. The interesting part of the HWR is its modulo. A modulo of the HWR $\text{mod}(\text{HWR}) \in \{0, 0.5\}$ indicates that the interfering waves from the upper and lower level of the step are in phase and constructive interference occurs, while $\text{mod}(\text{HWR}) \in \{0.25, 0.75\}$ indicates destructive interference. The latter case of destructive interference is related to the appearance of the batwing effect, since it decreases the signal intensity and thus causes deviations in phase retrieval. The correlation of the HWR and the batwing effect in white light interferometry is discussed in [87, 151]. Applying the implications of the HWR to figure 3.15 a) yields a plausible explanation for the strong decrease in signal intensity at the step edges observed for wavelength $\lambda_{2\text{eff}} \approx 1551\,\text{nm}$ (green dashed line). In figure 3.15 b), the influence of the perturbing interference effects at the step on the retrieved signal phase for the single wavelengths is depicted. The height profile of $\lambda_{1\text{eff}} \approx 1317\,\text{nm}$ (black line) shows minor deviations due to the lateral averaging over the step, because the phase values from both levels of the step are similar considering the unambiguity interval of $\pm\frac{\lambda_k}{4}$. In case of the second wavelength $\lambda_{2\text{eff}} \approx 1551\,\text{nm}$ phase jumps occur, since the phase values in the unambiguity interval centered on the upper and lower level of the step respectively do not align. Additionally, due to the drop in signal intensity the phase values of $\lambda_{2\text{eff}}$ may be disturbed stronger in the vicinity of the step. However, neither of the single wavelength measurements yields the correct step height, because of their limited unambiguity range. To correctly resolve the step height the basic synthetic wavelength approach [28], based on $\Lambda = \frac{\lambda_1 \lambda_2}{|\lambda_1 - \lambda_2|} \approx 8.46\,\mu\text{m}$, is employed and compared to the results of the extended algorithm introduced in [42]. The height profiles received for the two different algorithms are compared to a tactile reference measurement of the step height standard performed by the stylus instrument MarSurf GD26, which is also employed as a tactile reference instrument in [155]. The MarSurf GD26 is calibrated abiding by EN ISO 3274. The results of the synthetic wavelength algorithm (red dashed line), the extended unambiguity range algorithm (blue line) and the tactile reference measurement (black line) are plotted in figure 3.16 a). The tactile reference measurement shows the expected form of the 2 µm step standard. In case of the synthetic wavelength algorithm, the step height appears to be retrieved

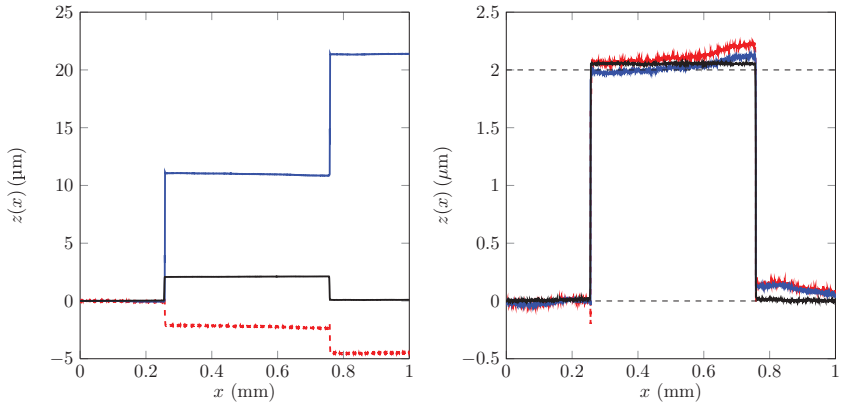

Figure 3.16: Measurement results at the step height standard of 2 µm nominal height: a) Height profiles in the step region considering the full interference signal, including the disturbed intensity values at the edges, basic dual wavelength algorithm $z\left(\Phi(x)\right)$ (red dashed line), extended unambiguity algorithm $z\left(\Delta\acute{\Phi}(x), \Delta\acute{\phi}_1(x)\right)$ (blue line) [42], tactile reference measurement from stylus instrument MarSurf GD26 (black line). b) Height profiles in the step region neglecting the disturbed signal components near the edges, based on the application of a threshold value to the normalized intensity in figure 3.15, basic dual wavelength algorithm $z\left(\Phi(x)\right)$ (red dashed line), extended unambiguity algorithm $z\left(\Delta\acute{\Phi}(x), \Delta\acute{\phi}_1(x)\right)$ (blue line) [42], tactile reference measurement from stylus instrument MarSurf GD26 (black line).

correctly, however, the orientation of the height development is not correct for the first step and batwing like overshoots occur close to the edges of the steps. These are difficult to see in the figure due to the ordinate scaling. In case of the extended unambiguity range algorithm the step height is determined with very high deviations to the reference, the height development orientation is incorrect in case of the second step, but the batwing like overshoots close to the edges are not observable. Considering the synthetic wavelength algorithm first, the deviations are probably related to the HWR, because $\mathrm{HWR}_\Lambda \approx 0.24$. Thus, the phase values retrieved from the synthetic wavelength at the lower and upper level of the step do not align. This is reasonable since in the case of this experiment the synthetic phase Φ is not obtained by direct measurement, but calculated as the phase difference of the single wavelength phases as introduced in equation (3.20) and [42,44,56]. The single wavelength result of λ_2 shows the HWR related misalignment of phase values between the step levels and thus also the phase of the synthetic wavelength is disturbed.

The averaging effect, which distorted both single wavelength phase values in the vicinity of the steps, therefore also distorts the phase of the synthetic wavelength and causes the observed overshooting and undershooting effects near the edges. However, since the phase difference between consecutive phase values in the Δ-system $\Delta\acute{\Phi}(n)$ stays within the unambiguity interval of the synthetic wavelength the step height is overall correctly retrieved. The extended unambiguity algorithm based on the phase tuple $\left(\Delta\acute{\Phi}(x), \Delta\acute{\phi}_1(x)\right)$ involves a fringe order estimation of the synthetic as well as the single wavelength fringe order. The details of this algorithm are described in [42]. The fringe order estimation is sensitive to disturbances in the phase of the synthetic and single wavelength. Due to the perturbations introduced by the averaging effect and the amplitude modulations at the steps, incorrect fringe order estimations of the synthetic wavelengths fringe order occur and result in the high deviations observed in figure 3.16 a).

A valuable consideration to improve the height measurement results for both algorithms is to cut the perturbed phase values in the vicinity of the steps based on a quality threshold value, like for the relative intensity $\frac{I(z(x))}{\max(I(z(x)))}$ in figure 3.15 a). To achieve the results presented in figure 3.16 b) a threshold value of $\frac{I(z(x))}{\max(I(z(x)))} \geq 0.8$ is applied to select the valid phase data for the height retrieval. Employing this procedure the surface height results of both, the synthetic wavelength approach (red dashed line) with standard deviation $\sigma_{\text{syn}} \approx 8.7\,\text{nm}$ and the extended unambiguity algorithm (blue line) $\sigma_{\text{ext}} \approx 2.0\,\text{nm}$ are in good agreement with the tactile reference measurement (black line) $\sigma_{\text{ref}} \approx 2.3\,\text{nm}$. The standard deviations are related to the surface height deviations determined on a 1.5 mm long plane section of the step height standard after removing the waviness. The dashed black line indicates the nominal height of the standard and shows, that the stylus instrument determined the step height a little too high. It measures a step height of $\approx 2.03\,\mu\text{m}$, while the standard is specified with a nominal height of $2.0\,\mu\text{m} \pm 25\,\text{nm}$ by the distributor. The deviations between the optical measurements and the tactile measurement in figure 3.16 b) are probably caused by vibrations of the scanning axes, temperature drifts or other environmental perturbations. Comparing the synthetic wavelength approach and the extended unambiguity algorithm the latter one yields the better results in accordance to the tactile reference measurement and nominal surface height. It also features a smaller standard deviation, since the height values within the estimated fringe orders are determined from the phase data of one single wavelength only and not from the difference of the independent single wavelength phase data as in the case of the synthetic wavelength approach. Thus, the experimental results presented here confirm the applicability of the algorithm introduced in [42] to real step structures with perpendicular edges, considering adequate measures for compensation of phase distortions at the step edges.

3.6 Applicability of the fiber coupled laser interferometer for roughness measurements

The applicability of contact free, interferometric methods for roughness measurements is an active field of research. Multiple contributions considering the use of interferometric setups for roughness measurements and comparing the optical measurement results to tactile measurements were published [2, 41, 64, 65, 67, 68]. The standards for tactile roughness measurements are given by ISO 4287 [164] and ISO 11562 [165]. A common obstacle in the application of laser interferometers for the measurement of rough surfaces are the occurring speckle patterns, which are enabling techniques like the speckle pattern interferometry, but also disturb the fringe pattern in phase evaluating interferometric approaches. Considering the fiber coupled interferometric probe with periodical optical path length modulation depicted in figure 3.1, its confocal properties are advantageous in canceling out speckle perturbations. The small fiber core diameter in the reference plane acts as a pinhole and blocks the extended speckle pattern from reaching the photodiode detector. Thus, the fiber coupled laser interferometer probe is applicable to surface roughness measurements. The point-wise data acquisition of the fiber coupled interferometric probe while scanning the measuring surface is equivalent to the data acquisition when using tactile stylus methods, and thus the ISO standards are also applicable to the surface measurement results generated by the interferometric probe. Comparative measurements of the fiber coupled interferometric point sensor with periodical optical path length modulation introduced in the beginning of this chapter and a tactile stylus instrument on roughness standards are published in [41]. The measured roughness standards featured nominal R_a and R_z values of $R_a = 483\,\mathrm{nm}$, $R_z = 3290\,\mathrm{nm}$ (standard 626) and $R_a = 1650\,\mathrm{nm}$ $R_z = 7960\,\mathrm{nm}$ (standard 6633), respectively. Comparative measurements showed higher deviations between tactile and optical measurement for the standard with higher R_a and R_z values. A detailed analysis of the sources of these deviations identified phase jumps, similar to those occurring at the edges of the step standard in section 3.5, to be a major source of distortions in the retrieved surface profile. To improve the surface profile results an algorithmic approach employing the redundant phase information of a dual wavelength recording of the surface structure, to correct phase jump related height errors referred to as „Ghost Steps“ is provided in [41]. The application of the algorithm to the recorded surface data yields a remarkable improvement in reducing the deviations between the optical and the tactile measurements. In case of small surface roughness $R_a < \frac{\lambda}{4}$ and $R_z < \frac{\lambda}{4}$ phase jumps and unambiguity issues should not occur. The limiting characteristic of the performance in terms of correct surface reconstruction is then given by the lateral optical resolution of the interferometric probe in dependence of the illuminating gaussian beam diameter. Measurements at the superfine roughness standard $R_a = 25\,\mathrm{nm}$, $R_z = 150\,\mathrm{nm}$ KNT 4070/03 [166] presented in figure 3.17 show an excellent congruence of the optical and tactile surface measurement. The roughness measurements are performed abiding by ISO 4287 [164] and ISO 11562 [165], employing a cut off wave-

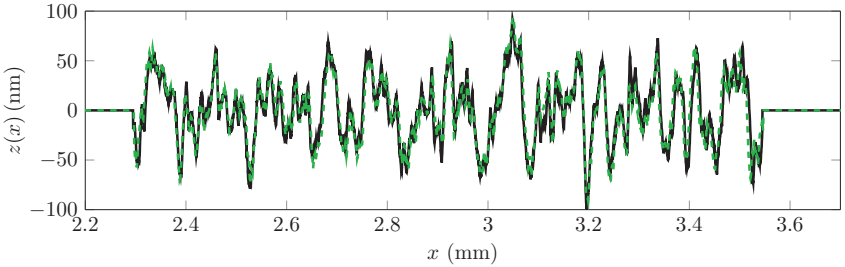

Figure 3.17: Comparative roughness measurement of the super fine roughness standard KNT 4070/03 [166] with nominal $R_a = 25\,\text{nm}$, $R_z = 150\,\text{nm}$. Measurement with tactile stylus instrument (black line) $R_{a,\text{ref}} = 27.0\,\text{nm}$, $R_{z,\text{ref}} = 146.4\,\text{nm}$, measurement with the fiber coupled interferometric probe (green dashed line) $R_{a,\text{opt}} = 26.9\,\text{nm}$, $R_{z,\text{opt}} = 141.5\,\text{nm}$.

length $\lambda_c = 0.25\,\text{mm}$ and sampling a lateral testing interval $l_t \geq 6\lambda_c$ from which the evaluation length $l = 5\lambda_c$ is retrieved after filtering. The tactile reference measurement is performed employing a stylus instrument. The reference surface profile depicted in figure 3.17 (black line), is provided by the distributor HALLE Präzisions-Kalibriernormale GmbH [166]. The optical surface measurement (green dashed line) is performed with the fiber coupled interferometric point sensor employing a scanning speed $v = 1\,\frac{\text{mm}}{\text{s}}$ and a data rate of $f_0 = 800\,\text{Hz}$. The retrieved roughness average $R_{a,\text{opt}} = 26.9\,\text{nm}$ is in good agreement to the nominal R_a value. The relative deviation between the optically determined average height $R_{a,\text{opt}}$ and the nominal R_a value is $\frac{R_{a,\text{opt}} - R_a}{R_a} \approx 7.6\,\%$. However, the relative deviation $\frac{R_{a,\text{ref}} - R_a}{R_a} \approx 8\,\%$ is of similar size. The relative deviation between the optically determined average maximum height $R_{z,\text{opt}} = 141.5\,\text{nm}$ and the nominal R_z value is $\frac{R_{z,\text{opt}} - R_z}{R_z} \approx 5.6\,\%$. The relative deviation $\frac{R_{z,\text{ref}} - R_z}{R_z} \approx 2.4\,\%$ is smaller. The tactile stylus instrument abides by DIN EN ISO 3274. It employs a stylus tip with a radius of $2\,\mu\text{m}$. Comparing the stylus tip radius to the diameter of the illuminating gaussian beam $\approx 2\,\mu\text{m}$ of the optical sensor [46, 155], shows that the lateral resolution of the systems is similar. Due to the curvature of the stylus tip, its actual contact surface on the standard might even be smaller than the gaussian beam diameter. Implications considering the lateral resolution of confocal optical sensors in comparison with tactile measurement systems are discussed in [155]. The underestimate of the R_z value by both sensors is probably related to a lack of lateral resolution, causing an averaging over a fine peak in the rough surface and thus, the deviation from the nominal R_z value. This hypothesis is supported by the rough surface's power-density spectrum, which is depicted in figure 3.18 with respect to the structure size distribution of the superfine roughness standard. The lateral distance between two sample points is $\Delta x_{\text{opt}} = 1.25\,\mu\text{m}$ for the interferometric probe and $\Delta x_{\text{ref}} = 0.4\,\mu\text{m}$ for the stylus instrument limiting the minimal structure size considered

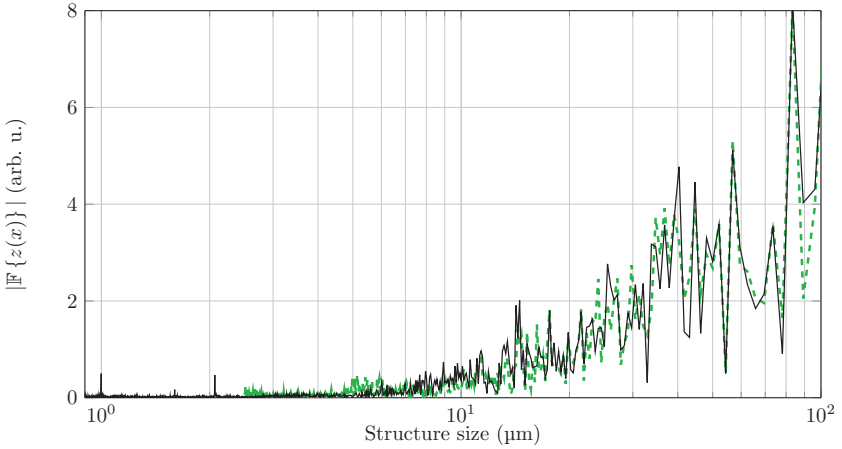

Figure 3.18: Power-density spectra of the rough surface profiles depicted in figure 3.17 for the stylus instrument (black line) and the interferometric probe (green dashed line).

in the spectral distribution by the sampling theorem. The power-density spectrum of the stylus instrument (black line) shows peaks at a structure size of 2.1 µm and 1.0 µm. These fine structures are not covered by the power-density distribution of the surface measured by the interferometric point sensor (green dashed line). Considering a structure size > 10.0 µm the power-density spectra of the sensors are in good agreement. In summary the comparative measurements of optical and tactile probes presented in [41] and figure 3.17 indicate that the fiber coupled interferometric point sensor with periodical optical path length modulation shows the potential to be a feasible supplement or substitution to tactile stylus instruments for surface roughness measurement. In case of superfine roughness structures it shows almost no disadvantage compared to the tactile method, but features a contact free measurement at higher scanning speed. Considering surfaces with higher roughness as in [41] phase jumps and unambiguity issues cause stronger deviations to the tactile reference measurements, but algorithmic approaches employing redundant phase data from a second wavelength channel may compensate for these perturbations and yield roughness measurement results with acceptable uncertainty.

Chapter 4

RGB-interferometry with pulsed LED illumination

Two novel approaches for surface phase retrieval employing a perturbation resistant RGB interferometer with pulsed LED illumination and oscillating reference mirror using a single color camera for fast image acquisition are introduced in this section. A Linnik interferometer setup employing a 3-Chip CCD camera for image acquisition and using parameter identification in the two beam interference equation for surface phase retrieval similar to the approach of Kitagawa [98, 99] is reported in [78]. Since dispersion effects show strong influence on the parameter identification approach, the phase retrieval algorithm is replaced by a quadrature based approach. The feasibility of the quadrature based phase retrieval is demonstrated by measurements in a Michelson interferometer setup, employing a Bayer pattern CMOS camera for image acquisition. Surface measurement results of the Michelson interferometer setup covering a variety of surface standards are reported in [11, 79]. The experimental setups and mentionable results from previous contributions [11, 78, 79] are summarized in section 4.1 and 4.2 for the Linnik- and Michelson interferometer respectively. Section 4.3 considers the influence of longitudinal chromatic aberration in the Michelson interferometer setup and section 4.4 deals with the offset intensity distribution from the microscopic images. In section 4.5 the effect of color crosstalk is discussed and section 4.6 introduces measurement results obtained from measuring objects in lateral motion.

4.1 RGB-Linnik-Interferometer for parameter identification based phase retrieval

The perturbation resistant RGB-Linnik-interferometer with pulsed LED illumination is schematically depicted in figure 4.1 and a photograph of the instrument is shown in figure 4.2. A comprised description of related research articles as well as a detailed explanation of the employed phase retrieval procedure and experimental results are presented in [78].

The Linnik type interferometer employs two 10× magnifying objectives, a collimated

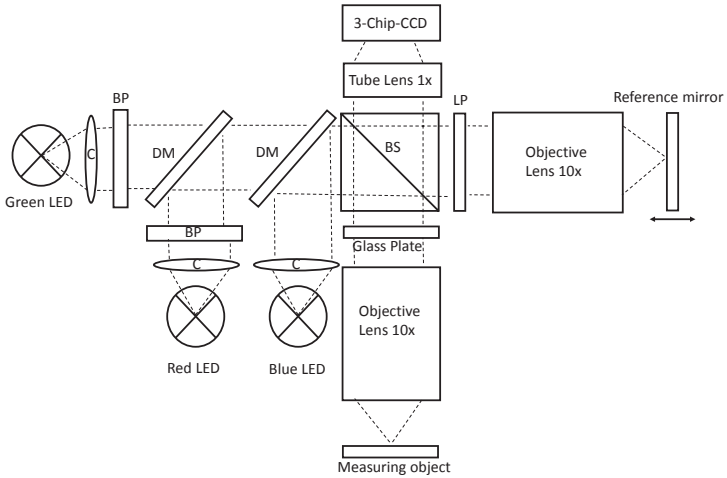

Figure 4.1: Schematic of the Linnik interferometer, collimator (C), bandpass filter (BP), dichroic mirror (DM), beam splitter (BS), absorption long pass filter (LP).

RGB-LED illumination and an oscillating reference mirror. Interferometric bandpass filters may be placed in front of the red and green LED to increase the temporal coherence length in the respective interferograms. A characteristic feature of the setup is the long pass filter in the reference arm, which absorbs the blue light. A 3-Chip-CCD camera is employed to simultaneously record two interferograms in the red and green color channel, respectively, and one microscopic image of the measuring surface in the blue color channel. Since the red and green LED are pulsed, the actual illumination time depending on the pulse width is in the single digit µs range and covers a small interval of the much greater total camera exposure time. The red and green LED are pulsed consecutively with a small pulse gap $\Delta\tau$ between the respective pulses. This enables the adjustment of a specific optical path length difference between the red and green interferogram, synchronizing

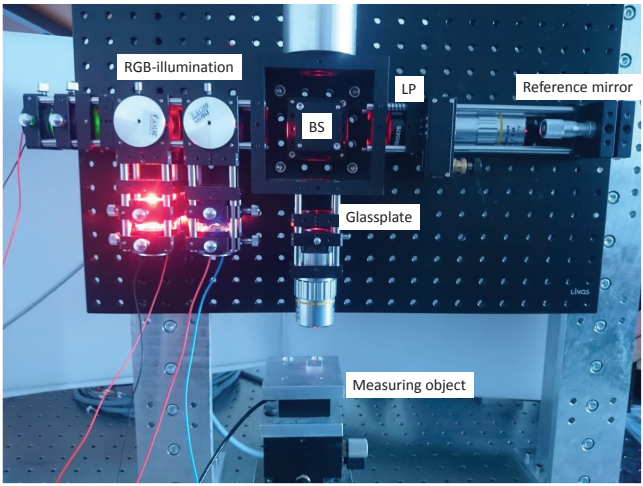

Figure 4.2: Photograph of the Linnik interferometer setup, with RGB-Illumination, Mitutoyo M-Plan-APO 10x microscope objectives in the reference and measurement path, beam splitter (BS) cube, and a tube lens in the camera path.

the pulses with the reference mirror oscillation. During the camera exposure time, the two phase shifted interferograms and the offset intensity distribution of the measuring object in the blue color channel are recorded, supplying the required information for surface phase retrieval by the parameter identification method proposed in [78]. The parameter identification procedure employed for phase retrieval is based on the two beam interference equation in the uniform wave model according to equation (2.86). For more convenient use employing the measurement data equation (2.86) is rearranged, separated in the offset intensity distributions of the measurement and reference arm $A_k(x, y)$ and $B_k(x, y)$, respectively, with $C_k(x, y, h_k)$ accounting for the complex degree of coherence in equation (4.1) [78]:

$$I_k(x,y) = A_k(x,y) + B_k(x,y) + 2\sqrt{A_k(x,y)B_k(x,y)}|C_k(x,y,h_k)| \cos\left(\frac{4\pi}{\lambda_k}h_k(x,y) + \phi_k\right) \tag{4.1}$$

In Eq. (4.1), x and y denote the pixel index, $I_k(x, y)$ denotes the recorded interferogram of the k-th color channel $k \in \{1, 2\}$, λ_k denotes the wavelength, $h_k(x, y)$ is the wrapped surface height and ϕ_k is a known, adjustable phase offset between the interferograms applied by the reference mirror movement. The microscopic image in the blue color channel is described by Eq. (4.2).

$$I_{blue}(x,y) = A_{blue}(x,y) \tag{4.2}$$

To determine the wrapped surface height $h_k(x, y)$, the unknown parameters $A_k(x, y)$, $B_k(x, y)$, $C_k(x, y)$ have to be eliminated or determined. In [78] narrow bandwidth wavelength filters with FWHM of 3 nm are placed in front of the red and green LED causing a sufficiently long coherence length to assume $C_k(x, y) \approx 1$ within the field of view. However, this introduces constraints towards the maximum allowed structure depth of the measuring object, since the fringe contrast is decreasing with increasing distance to the phase balance point of zero OPLD. The offset intensity distribution in the reference arm $B_k(x, y)$ is received by calibration measurements with blocked measurement arm. It is assumed that the intensity distributions of the imaged measuring object in all three color channels in the absence of interference are proportional to each other, linked by a matrix of constant coefficients $D_k(x, y)$.

$$A_k(x, y) = D_k(x, y) I_{blue}(x, y) \tag{4.3}$$

The coefficients of $D_k(x, y)$ are also determined in a calibration measurement using an arbitrary measuring object and blocking the reference light path [78]. Employing the assumption considering the constant degree of coherence $C_k(x, y) = 1$ and identifying $A_k(x, y)$, $B_k(x, y)$ by the reference measurements and rescaling of the blue object image, the wrapped surface height $h_k(x, y)$ is retrieved from equation 4.1 for the red and green color channel, respectively using the inverse cosine function. The phase corresponding to the retrieved surface height is indeterminate to an integer multiple of 2π and also the sign of the height function is lost due to the symmetry of the cosine function. Therefore, the resulting unambiguity interval is limited to $[0, \pi]$. To restore the sign information and unwrap the surface height the combination of the phase shifted height profiles is employed. The phase evolution of the corresponding surface height $h_2(x, y)$ is rescaled to match that of $h_1(x, y)$. Due to the unambiguity in the phase information, the phase evolution rescaling is fringe order specific. If the surface heights are correctly matched within the unambiguity range of one fringe order, they should only differ by the known adjusted phase shift ϕ_k introduced by the oscillating reference mirror during the pulse gap. In [78] the rescaling procedure of the phase evolution is described in detail and a fringe order dependent optimization problem is found assigning the fringe order of each pixel within the field of view to the extended unambiguity range of the exact fraction method [42, 56]. After solving the optimization problem a fringe order n is assigned to each pixel and stored in the matrix $F(x, y)$. Also, the wrapped height value $h_1(x, y)$ as well as the wrapped fringe order specific rescaled value of the second wavelength height profile $\tilde{h}_1(x, y, n)$ is determined for each pixel. The phase offset ϕ_k between the red and green interferogram is chosen sufficiently small such that the difference of the original and rescaled height profile divided by the phase offset is a feasible approximation of the difference quotient of the height profiles. Thus, it can be used to restore the sign information of phase evolution in the wrapped height profile. Finally the unwrapped surface topography is retrieved by summing the sign corrected height values and their corresponding fringe order offsets. Simulation results of the parameter identification based phase retrieval procedure are presented in [78]. Mandatory assumptions influencing the performance of the algorithm when applied to experimental measurement data consider

the precision of the adjusted path length difference $\phi_k \lambda_k/(4\pi)$ during the pulse gap, the intensity scaling between color channels by equation (4.3) and the influence of coherence and dispersion on the interference patterns. An experiment varying the pulse gap between the red and green LED and measuring the corresponding phase shift employing a stroboscopic interferometric method and carrier fringes for Fourier transformation based lock-in phase retrieval is presented in [78]. The results presented there indicate that the oscillating coil driving the reference mirror is applicable to create a phase shift with a standard deviation of $\mathrm{std}(e_{h_1(x,y)}) \approx 0.8\,\mathrm{nm}$, which would be feasible for the parameter identification algorithm. However, a similar experiment with a modified oscillating coil actor in [79] showed a standard deviation of $\mathrm{std}(e_{h_1(x,y)}) \approx 1.8\,\mathrm{nm}$ and worse results are observed if unfavorable settings are chosen for the driving voltage. Replacing the oscillating coil with a piezo actuator might yield higher precision and better repeatability. The feasibility of the intensity scaling of the color channels employing the proportionality matrix $D_k(x, y)$ from equation (4.3) to retrieve the pixel specific intensity offset distribution of the red and green interferogram in the measurement path enabling the measurement of inhomogeneous surfaces is evaluated by measurements of 100 images illuminated by the pulsed LEDs [78]. The results indicate that the pulsed LED intensity varies up to $\pm 3\%$ between images which is a sufficiently small deviation. Experimental consideration of chromatic aberration effects showed that the longitudinal chromatic aberration in the Linnik interferometer introduces an additional wavelength dependent unknown phase offset $\Delta\phi_{k,\mathrm{dis}}$ [78]. The measured phase offset $\Delta\phi_{k,\mathrm{dis}}$ corresponds to a height difference of $\Delta h_{k,\mathrm{dis}} > \lambda_k/4$ and thus, can not be unambiguously compensated. Therefore, the constraint of the known adjustable phase shift between the red and green LED interferogram is not fulfilled. The dispersion related offset $\Delta\phi_{k,\mathrm{dis}}$ in the zero phase crossing points of the red and green interferogram is much bigger than the phase shift assigned by the actor oscillation and causes erroneous fringe order estimation. Topography measurements based on experimental data of the Linnik interferometer are therefore not possible. The details considering the experiments and the theory of phase retrieval summarized in this section are available in [78]. Important results are:

- The characteristics of the oscillating coil, driving the reference mirror movement and its feasibility to adjust a precise, repeatable phase shift between the LED pulses with nm precision [78].

- The potential of the blue microscopic image to yield a good estimation of the measurement path intensity distribution of the red and green interferogram with a deviation smaller $\pm 3\%$ [78].

- The strong influence of longitudinal chromatic aberration [78].

4.2 RGB-Michelson-Interferometer for quadrature based phase retrieval

The employed Michelson type interferometer is schematically depicted in figure 4.3 and illustrated by a photograph in 4.4. A comprised description of related research articles as well as a detailed explanation of the employed phase retrieval procedure and experimental results are presented in [11, 79]. The illumination path contains three LEDs of red, green and blue color respectively. The light of each LED is collimated by an aspheric lens

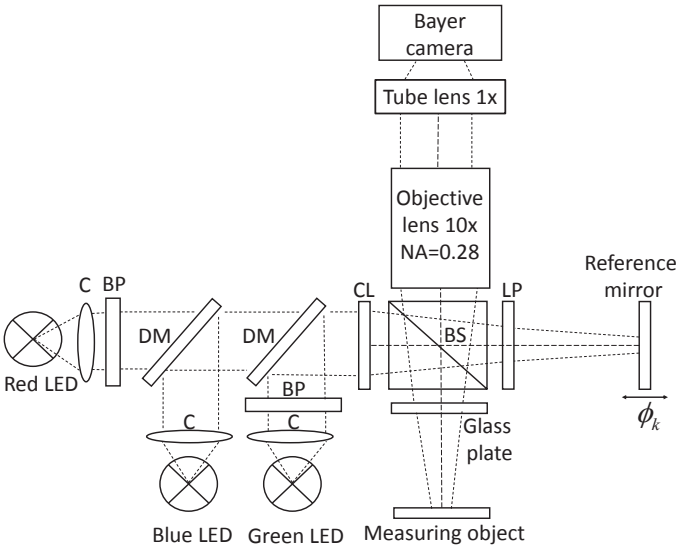

Figure 4.3: Schematic drawing of the Michelson interferometer with RGB illumination and oscillating reference mirror, bandpass filter (BP), dichroic mirror (DM), collimator (C), beam splitter (BS), condenser lens (CL), and long pass filter (LP).

(C). Interferometric bandpass filters (BP) may be placed in front of the red and green LED, which illuminate the interference images, to narrow the spectral composition of the emitted light and thus increase the coherence length and reduce crosstalk interactions. The LED light is combined and aligned on the optical axis employing dichroic mirrors (DM). A condenser lens (CL), with NA = 0.16 and a nominal focus length of 40 mm may be placed in front of the beam splitter, such that its focal point aligns with that of the microscope objective and more light is available in the field of view. A 50/50

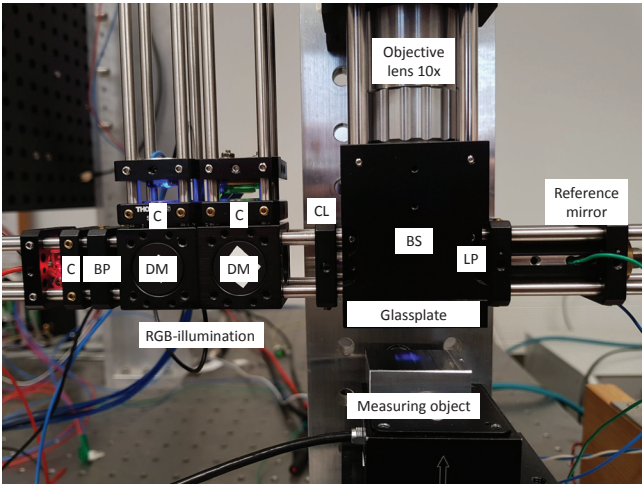

Figure 4.4: Photography of the employed Michelson interferometer setup.

beam splitter (BS), separates the incoming light into the measurement and reference path. In front of the reference path a color glass long pass filter (LP) is placed, absorbing the blue light and thus, suppressing interference in the blue color channel. Red and green light are transmitted to the oscillating reference mirror in the reference path. This consists of an oscillating coil with a polished fragment of a silicon wafer mounted on top. To compensate for the optical path length difference introduced by the long pass filter, a compensation glass plate is placed in the measurement path. The interfering red and green light from both interferometer arms, as well as the microscopic image of the object intensity distribution in the blue color channel are imaged by a NA = 0.28, 10× microscope objective and corresponding 1× tube lens on a Bayer pattern CMOS camera for image recording. The chip size is $11.26\,\mathrm{mm} \times 11.26\,\mathrm{mm}$ containing 2048×2048 pixels, resulting in a pixel pitch of 5.5 µm. The camera frame rate is set to 10 frames per second (fps) in dual shot mode, issuing the camera to record two images after receiving an external trigger signal. Therefore, every 100 ms two images with an exposure time of approximately 10 ms and an exposure gap of $\Delta\tau_{\mathrm{exp}} < 80\,\mu\mathrm{s}$ are recorded. The pulse width of the red and green LED is in the range of $\tau_r,\ \tau_g \in [1\,\mu\mathrm{s}, \cdots, 5\,\mu\mathrm{s}]$ and the pulses are synchronized with the exposure gap. The width of the pulse gaps $\Delta\tau_{\mathrm{exp}} < \Delta\tau_r < 100\,\mu\mathrm{s}$ and $\Delta\tau_{\mathrm{exp}} < \Delta\tau_g < 100\,\mu\mathrm{s}$ for the respective color LEDs are chosen greater than that of the exposure gap, but as small as possible to yield a short data acquisition time. This ensures illumination in both recorded camera frames and limits the maximum effective data acquisition time to $\approx 100\,\mu\mathrm{s}$. A timing diagram illustrating the pulse synchronization is depicted in figure 4.5. The relation between the pulse gaps $\Delta\tau_r/\Delta\tau_g$ is adjusted to

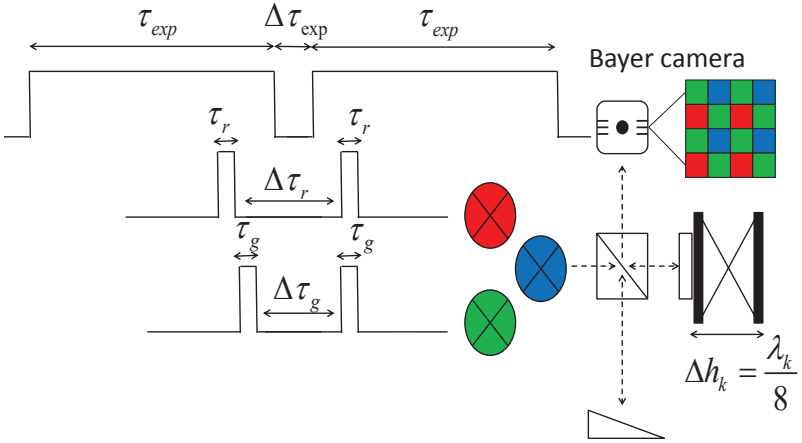

Figure 4.5: Timing diagram visualizing the synchronization of the RG LED pulse timing with respect to the camera exposure gap $\Delta\tau_{\text{exp}}$ [79].

match the wavelength relation λ_1/λ_2. Assuming an approximately linear movement of the reference path actuator during the short exposure gap, the adjustment of the pulse gap ratio to the wavelength ratio ensures that the quadrature condition is achieved in both color channels simultaneously. The oscillation amplitude of the reference mirror is adjusted such, that the recorded images of index $m \in \{1,2\}$, in the k-th color channel $k \in \{1,2\}$ with $\lambda_1 \approx 632\,\text{nm}$ and $\lambda_2 \approx 532\,\text{nm}$ are in quadrature. Thus, the phase difference between the recorded interferometric images is $\Delta\phi_{21,k} = |\phi_{2k} - \phi_{1k}| = \pi/2$. The m-th recorded interferogram, in the k-th wavelength channel is described by the two beam interference equation Eq. (4.4) [78,110].

$$\begin{aligned} I_{mk}(x,y) =& A_k(x,y) + B_k(x,y) \\ &+ 2\sqrt{A_k(x,y)B_k(x,y)}|C_k(x,y,h_k)|\cos\left(\frac{4\pi}{\lambda_k}\left(h_k(x,y) + e_{mk}(x,y)\right) + \phi_{mk}\right) \end{aligned} \tag{4.4}$$

In Eq. (4.4), x and y denote the pixel index, $I_{mk}(x,y)$ denotes the m-th recorded interferogram of the k-th color channel, $A_k(x,y)$ and $B_k(x,y)$ describe the intensity offset distribution in the measurement path and reference path, respectively, $C_k(x,y,h_k)$ represents the complex degree of coherence, λ_k denotes the wavelength, $h_k(x,y)$ is the wrapped surface height and ϕ_{mk} is the known, adjustable phase offset between the m-th and (m+1)-th interferogram applied by the reference mirror movement. Equation (4.4) differs from equation (4.1) by considering the recording of two consecutive images with

index m. The adjusted optical path length difference $\Delta h_k = \frac{\phi_{2k}-\phi_{1k}}{4\pi}\lambda_k$ occurring during the short pulse gap is adjusted to be $\lambda_k/8$. The optical path length difference due to environmental perturbations is expected to be small compared to the intended phase shift $e_{mk}(x,y) << \lambda_k/8$ and is thus assumed in the single digit nm range. The offset intensity distributions $A_k(x,y)$, $B_k(x,y)$ as well as $C_k(x,y,h_k)$ the complex degree of coherence are assumed to be neglectably affected by the optical path length difference between the quadrature images and are therefore independent of the image index [79]. The microscopic image in the blue color channel is described by Eq. (4.2). Due to the color glass filter in front of the reference arm the blue light is not reflected from the reference mirror and just the offset intensity distribution of the object image is observed in the blue color channel. To apply the quadrature based phase retrieval, the intensity distribution $B_k(x,y)$ is identified by calibration measurements with blocked measurement arm. The intensity distribution $A_k(x,y)$ is determined by rescaling of the microscopic image $A_k(x,y) = D_k(x,y)I_{blue}(x,y)$ as described in equation (4.3) for the Linnik interferometer. The coefficients of the scaling matrix $D_k(x,y)$ are identified by calibration measurements with blocked reference path [78,79]. The the pixel specific scaling matrix $D_k(x,y)$ compensates for inhomogeneities in the illumination and improves results on structured measurement surfaces. However, the scaling matrix being specifically dependent on the measuring object structure requires to repeat the calibration measurement for determination of $D_k(x,y)$ prior to each measurement on a different measuring object. Thus, it is not applicable if the measuring object is in motion, since the surface structure during the calibration would not coincide with the surface structure during measurement. If measuring objects in motion are considered, the scaling matrix is replaced by a scalar $\overline{D}_k$, which is the mean value of the intensity distribution matrix. The intensity distribution scaling still is pixel specific, due to the use of $A_{\text{blue}}(x,y)$, but the scaling factor is constant throughout the field of view. A detailed discussion of the intensity distribution scaling is presented in section 4.4. Since the interferometric images $I_{1k}(x,y)$, $I_{2k}(x,y)$ are in quadrature due to the adjusted $\pi/2$ phase shift employing equation (4.4) and subtracting the identified offset intensities, yielding $\tilde{I}_{mk}(x,y)$, the following equation is found for phase retrieval.

$$\begin{aligned} \frac{\tilde{I}_{2k}(x,y)}{\tilde{I}_{1k}(x,y)} &= \frac{\sin\left(\frac{4\pi}{\lambda_k}\left(h_k(x,y)+e_{2k}(x,y)\right)\right)}{\cos\left(\frac{4\pi}{\lambda_k}\left(h_k(x,y)+e_{1k}(x,y)\right)\right)} \\ h_k(x,y)+e_{12k}(x,y) &= \tan^{-1}\left(\frac{\tilde{I}_{2k}(x,y)}{\tilde{I}_{1k}(x,y)}\right)\frac{\lambda_k}{4\pi} \end{aligned} \tag{4.5}$$

The relation between the phase detuning errors $e_{mk}(x,y)$ and the resulting deviation in the retrieved surface height $e_{12k}(x,y)$ is elaborated in [11, 79]. Due to the short image acquisition time of $\approx 100\,\mu s$, the measurement deviation $e_{mk}(x,y)$ is expected to be smaller than 1 nm for mechanical disturbances up to a velocity of $v_d = 10\,\mu m/s$ and is therefore neglected. Thus, equation (4.5) is employed to directly retrieve the wrapped surface height $h_k(x,y)$. From this also the wrapped phase values of the respective color channels

are retrieved, which are indeterminate with respect to an integer multiple of 2π.

$$\theta_k(x,y) = 4\pi \frac{h_k(x,y)}{\lambda_k} \tag{4.6}$$

The surface unwrapping is performed employing a 2D phase-unwrapping algorithm following a noncontinuous path, based on sorting by reliability [167]. References [78, 79] contain more detailed information concerning the rescaling of the microscopic image, the synchronization of the LED pulses to the exposure gap and the adjustment and repeatability of the actor induced phase shift for quadrature evaluation. In reference [11, 79] the feasibility of the quadrature based phase retrieval approach for precise topography measurements is discussed, showing results from different measurement standards. The influence of imperfections in the actor movement and phase noise on the topography results are considered in [79]. The feasibility of the retrieved topography phase for the application of exact fraction based unambiguity range extension and the robustness of the Michelson type interferometer with pulsed LED illumination to mechanical vibration perturbations are also considered in [79]. Reference [11] shows the applicability of the setup for surface roughness measurements and its capability to measure the topography of objects in lateral motion. Important results are:

- The standard deviation in the $\pi/2$ quadrature phase shift due to imperfections of the oscillating coil actor movement is $\approx 2\,\text{nm}$ and dependent on the driving voltage and frequency. Replacing the oscillating coil by a more stable piezo actuator might benefit the measurement repeatability [79].

- The standard deviation in the topography measurements due to signal noise is expected to be in the range of $\text{std}(e_{h_k(x,y)}) \in [3\,\text{nm}, 7\,\text{nm}]$ depending on the reflectivity of the measuring object and the corresponding signal to noise ratio of the recorded interference images [79].

- Unambiguity range extension employing the longer synthetic wavelength is possible, however, the application of exact fraction based approaches for further analytic unambiguity extension does not yield feasible results since it requires less phase noise $\text{std}(e_{h_k(x,y)}) \overset{!}{<} 0.5\lambda_k/100$ [79].

- Mechanical vibrations in axial direction up to a velocity of $v_d = 10\,\mu\text{m/s}$ cause a neglectable topography error $e_{h_k(x,y)} \approx 1\,\text{nm}$ due to the short data acquisition time of $\approx 100\,\mu\text{s}$, which is dependent on the camera's exposure gap $\Delta\tau_{\text{exp}}$ [79].

- The quadrature based RGB-interferometer is applicable for surface roughness measurements of a superfine roughness standard with nominal $R_a = 25\,\text{nm}$ and $R_z = 150\,\text{nm}$. An areal surface roughness measurement obtained from this standard in lateral motion, moving at a velocity of $v = 5\,\text{mm/s}$, shows good agreement with the results obtained from a stylus instrument and point wise measuring laser

interferometer. This demonstrates the capability of the quadrature based RGB-interferometer to measure objects in lateral motion. The height data rate of the RGB-interferometer is much higher than that of the compared sensors [11].

- The interferometric measurement results can be employed to reference a Hartmann-Schack (HS) wavefront sensor. Using the surface height information obtained from the HS sensor the phase ambiguity of the interferometric measurement may be resolved without an algebraic unwrapping procedure. The combination of surface height information for fringe order retrieval is successfully demonstrated for a tilted, plane measuring object [11].

4.3 Dispersion in the Michelson interferometer with pulsed RGB illumination

In multicolor interferometry, the influence of chromatic dispersion effects on the interferogram has to be considered. Longitudinal chromatic aberration may introduce a wavelength dependent phase offset, due to the different propagation velocity of the employed wavelengths in dispersive media. This causes the position of the phase balance point to vary for the corresponding fringe patterns of different illumination colors. The microscope objective used in the Michelson setup displayed in figure 4.3 is apochromatic and therefore, its focus distance should show a minor dependence of the wavelength. However, the beam splitter cube, the long pass filter in the reference path and the compensation glass in the measurement path are dispersive elements, which will introduce chromatic aberration. In reference [78], the influence of longitudinal chromatic aberration on the color specific correlograms in the Linnik interferometer is discussed. The results presented in [78] indicate that the path length difference induced by the long pass filter (LP) is not fully compensated by the compensation glass plate of same thickness, and that the combination of these elements is the dominant source of dispersion in the Linnik interferometer. Comparing the longitudinal chromatic aberration in the setup with and without the long pass filter and the compensation glass, these elements introduced a path length difference between the phase balance points of red and green illumination of $\approx 6730\,\mathrm{nm}$. Since no information about the material composition of the color glass long pass filter is available a more feasible compensation than given by the compensation glass of same thickness is not yet found, and the same combination of these dispersive elements is employed in the Michelson interferometer setup. However, since the quadrature based phase retrieval procedure employed in this setup is robust against these dispersion influences, the presence of longitudinal chromatic aberration causes minor problems. To characterize the influence of dispersion effects in the Michelson interferometer, the experiment described in reference [78] is repeated. No bandpass filters are placed in front of the red and green LED, to ensure confinement of the correlograms by a clear envelope, due to the rather broad illumination bandwidth. The envelopes maximum position indicates the phase balance point

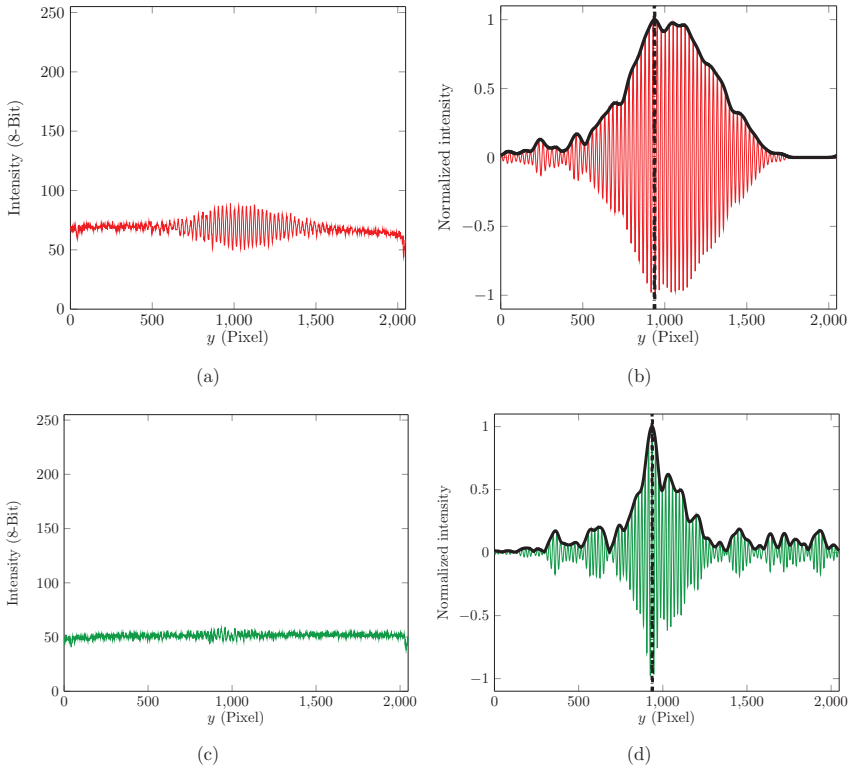

Figure 4.6: Long pass filter and compensation glass removed: a) Correlogram in the red color channel, b) Frequency filtered correlogram with envelope in the red color channel, envelope maximum (dashed line), c) Correlogram in the green color channel, d) Frequency filtered correlogram with envelope in the green color channel, envelope maximum (dash-dotted line).

of the respective wavelength, where the path length of measurement and reference arm are balanced and thus the highest interference contrast occurs. A strongly tilted mirror is used as the measuring object, emulating a depth scan along one dimension of the camera chip. The strong difference in the inclination between the beams in the measurement and reference arm may cause additional dispersion effects. The measurement is conducted with and without the long pass filter and compensation glass. The red and green illumination are turned on separately, to preclude influences of color crosstalk. To determine

the envelopes maximum position the recorded interference signals are bandpass filtered in the frequency domain, to eliminate signal noise and to receive a smooth envelope from the analytic signal. Figure 4.6 a) and c) show the recorded correlogram in the red and green color channel without the long pass filter and compensation glass. In figure 4.6 b) and d) the frequency filtered correlograms with the corresponding envelope are depicted. The envelopes maximum position in the red color channel is indicated by a dashed line, in the green color channel its indicated by a dash-dotted line. Figure 4.6 shows, that

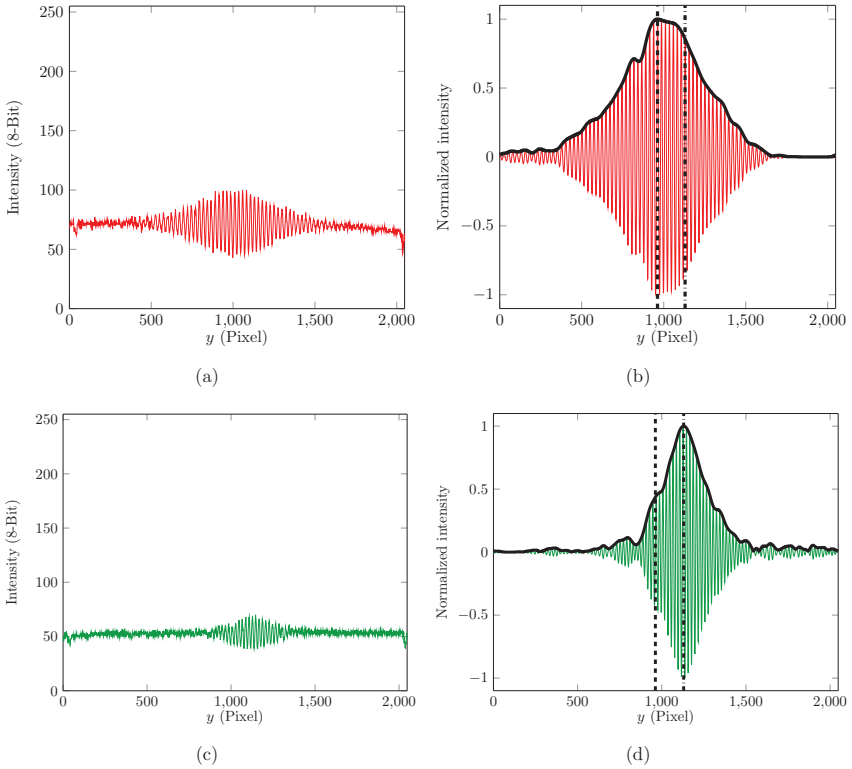

Figure 4.7: Long pass filter and compensation glass removed, glass plate inserted in the reference path: a) Correlogram in the red color channel, b) Frequency filtered correlogram with envelope in the red color channel, envelope maximum (dashed line), c) Correlogram in the green color channel, d) Frequency filtered correlogram with envelope in the green color channel, envelope maximum (dash-dotted line).

although the longitudinal chromatic aberration in the interferometer is small in absence of the color glass filter in the reference and the compensation glass in the measurement path, the contrast or modulation depth of the interferograms is low, especially in the green color channel. Also employing no focusing lens in the illumination path, but only collimating lenses in front of the respective LEDs the recorded intensity is low too. The low interference contrast indicates an asymmetric form of the beam splitter cube or an infeasible alignment of this component. The phase balance point does not align with the focal position of the microscope objective causing the low interference contrast.

Considering the low interference contrast of the recorded interferograms in figure 4.6, there is a strong influence of the signal noise on the retrieved envelope form. Therefore, this measurement was repeated employing a continuous illumination in the red and green color channel and using an expanded camera exposure time to achieve a better signal to noise ratio. The measurement results with continuous illumination yield similar results, showing a small longitudinal aberration, but also very low interference contrast. The images recorded with continuous illumination also show a significant misalignment of the phase balance point and the focus position of the microscope objective. To identify if either the measurement or reference arm has a longer light path through the glass of the beam splitter cube, thin glass plates of $\approx 0.15\,\mathrm{mm}$ thickness are inserted in the respective light path and the contrast in the interferogram is evaluated. Figure 4.7 a) and c) show the recorded correlogram in the red and green color channel without the long pass filter and compensation glass, but one of the thin glass plates inserted in the reference path. In figure 4.7 b) and d) the frequency filtered correlograms with the corresponding envelope are depicted. The envelopes maximum position in the red color channel is indicated by a dashed line, in the green color channel its indicated by a dash-dotted line. Comparing figure 4.6 and 4.7 shows an increase in the interference contrast, but also an increase in the longitudinal chromatic aberration error as indicated by the distance between the envelope maximum positions. If glass plates are added to the measurement path the interference contrast decreases. This indicates that the distance the light propagates through glass is longer in the measurement path, probably due to an asymmetric form of the beam splitter cube like different edge lengths or improper alignment.

In figure 4.8 the influence of the condenser lens in the illumination path on the interferograms is considered. Figure 4.8 a) and b) show the recorded correlogram in the red and green color channel without the long pass filter and compensation glass, but the condenser lens inserted in the illumination path. Comparing the correlograms depicted in figure 4.8 to figure 4.6 or 4.7 shows a strong increase in offset intensity caused by the condenser lens. However, the interference contrast remains low, since the phase balance point and the microscope objective's focus point differ. Also the correlograms appear to be degenerated. This may be an influence of the incoherent illumination with the LED. Employing the condenser lens the extended LED emitter is imaged on the measuring object surface and the incoherent light from different emitter areas is superposed. This effect also occurs in case of illumination with collimated light, since the LED is a spatially

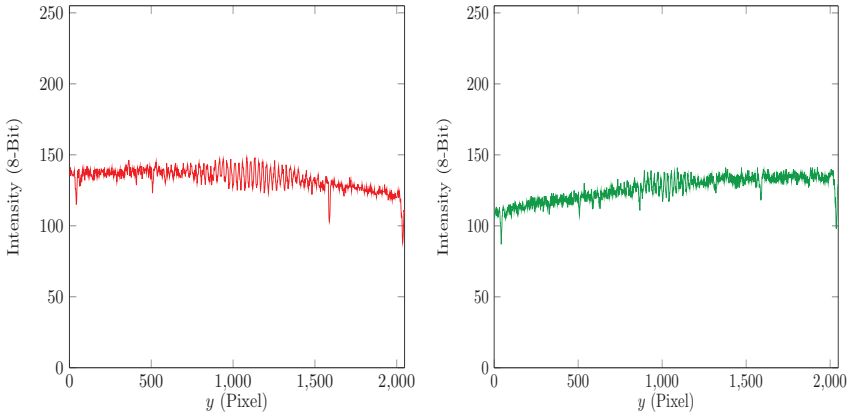

Figure 4.8: Long pass filter and compensation glass removed, condenser lens inserted in the illumination path: a) Correlogram in the red color channel, b) Correlogram in the green color channel.

incoherent source of illumination, but by focusing the light a more extended area of the emitter is imaged on a smaller area on the measuring object, amplifying the influence. Due to this, the correlogram envelope shaped by the temporal incoherence in dependence of the LED bandwidth in case of collimated illumination may be stronger affected by the spatial incoherence of the illumination source.

Figure 4.9 shows the correlograms and longitudinal chromatic aberration error of the setup, with inserted color glass filter (LP), compensation glass and condenser lens (CL). Comparing figure 4.9 and 4.6 shows a strong increase in the interference contrast, the offset intensity and the longitudinal chromatic aberration. The longitudinal chromatic aberration error introduced by the color glass filter and the corresponding compensation glass plate corresponds to an optical path length difference between the phase balance points of red and green illumination of $\approx 6600\,\mathrm{nm}$, determined by counting the fringes in figure 4.9 b) and d). Considering the uncertainty of the fringe counting approach, which is $\approx \lambda/2$, the result is in good agreement with the results in reference [78], where the same combination of filter elements is employed. In an ideal Michelson interferometer, the phase balance point and the focus of the microscope objective would align and the maximum interference contrast would occur for the case of minimal longitudinal aberration. However, the employed setup shows a shift between the phase balance point and the microscope objective's focus, caused by the beam splitter cube dimensions or its alignment as the results of figure 4.6 and 4.7 indicate. The optical path length difference

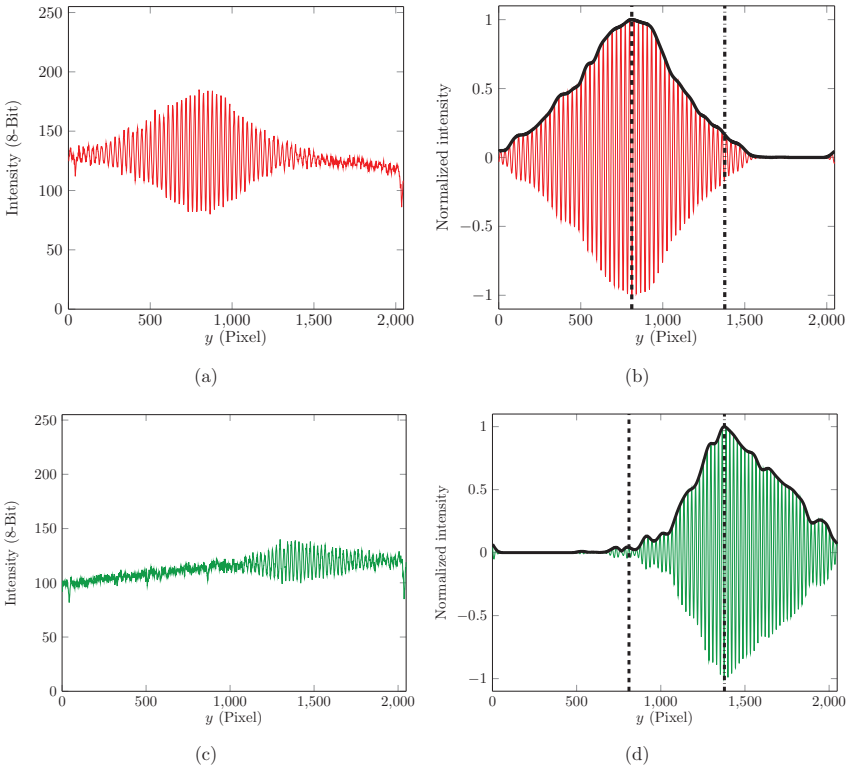

Figure 4.9: Long pass filter, compensation glass and condenser lens inserted: a) Correlogram in the red color channel, b) Frequency filtered correlogram with envelope in the red color channel, envelope maximum (dashed line), c) Correlogram in the green color channel, d) Frequency filtered correlogram with envelope in the green color channel, envelope maximum (dash-dotted line).

between the compensation glass plate in the measurement and the color glass filter in the reference path apparently partially compensates the distance between the phase balance point and the microscope objective focus, thus increasing the interference contrast while introducing an increase in the longitudinal chromatic aberration as depicted in figure 4.9. Therefore, the imbalance of the interferometer in its basic configuration without the additional dispersive elements actually benefits the performance of the setup in the configuration with applied long pass filter in the reference path. However, to receive a

more reproducible performance of the instrument, the interferometer should be balanced in its basic configuration and based on the information about the dispersion induced path length difference caused by the filter and compensation glass plate the proper thickness of the compensation glass should be found. To do so the beam splitter cube needs to be realigned or exchanged until a decent interference contrast appears in the configuration of figure 4.6. Than the color glass filter is inserted in the reference arm and compensation glasses of varying thickness are inserted in the measurement path until the interference contrast is feasible. The required thickness of the compensation glass is most probably not commercially available and will need to be specifically fabricated.

4.4 Offset intensity distribution retrieval from the microscopic image

Section 4.2 introduces the quadrature based phase retrieval approach for topography measurements with the RGB interferometer [79]. An innovative feature of the proposed algorithm is the application of a microscopic image of the measuring surface, recorded in the blue color channel, to determine the object intensity distribution of the interferograms. The algebraic expression of the intensity distribution scaling is a simple multiplication introduced in equation (4.3). The mandatory assumption for successful application of this procedure is that in absence of interference the intensity distributions of the imaged measuring object in all three color channels are proportional to each other, linked by constant coefficients. These coefficients may than be determined by calibration measurements. They are dependent on the LED illumination intensity. Therefore, if the pulse width τ_r, τ_g or the LEDs supply voltage is changed, the matrix coefficients of $D_{mk}(x, y)$ require new calibration. In reference [78], the feasibility of the intensity distribution rescaling from the blue to the red color channel is demonstrated by experimental results. Comparing the current experimental setup to that in reference [78], there are major differences considering the used LEDs, their pulse timing and the recording device. Therefore, the experiment presented in [78] is repeated, with minor optimizations, to demonstrate, that the ratio of the intensity distribution between the pulsed LEDs and the continuously illuminated blue LED is constant over multiple images. Since the red and green LED are pulsed, it can occur that their emitted intensity varies and the ratio between their intensity and that of the constantly illuminated blue LED might not be constant over multiple recorded images. To check this, a plane mirror is chosen as the measuring object and a measurement is performed, for which the reference arm of the interferometer is blocked and the camera records the object intensity distribution in the m-th frame $m \in \{1, 2\}$ of the i-th dual shot image $i \in \mathbb{N}$ of the red, green and blue LED light $A_{m1}(x, y, i)$, $A_{m2}(x, y, i)$ and $A_{\mathrm{m,blue}}(x, y, i)$, reflected from the measuring object. The camera is running in dual shot mode as introduced in section 4.2 and thus each dual shot image consists of two separate frames illuminated by the m-th pulse of the red and green LED respectively. Referring

to equation (4.3) the scaling matrix $D_{mk}(x, y)$ is determined based on the first recorded image pair.

$$\begin{aligned} D_{mk}(x, y) &= \frac{A_{mk}(x, y, 1)}{A_{\mathrm{m,blue}}(x, y, 1)} \\ \overline{D}_{mk} &= \frac{1}{N_x N_y} \sum_{x=1}^{N_x} \sum_{y=1}^{N_y} D_{mk}(x, y) \end{aligned} \tag{4.7}$$

Based on the scaling matrix with N_x columns and N_y rows the corresponding scalar scaling factor $\overline{D}_{mk}$ is determined as shown in equation (4.7). The intensity distribution deviation $\Delta A_{mk}(x, y, i) = A_{mk}(x, y, i) - \overline{D}_{mk} \cdot A_{\mathrm{m,blue}}(x, y, i)$ is determined for $i \in [1, \cdots, 50]$ images. For the purpose of visualization the mean value of the respective intensity distributions $\overline{A}_{mk}(i)$ and deviations $\overline{\Delta A}_{mk}(i)$ are displayed in figure 4.10. The results presented in

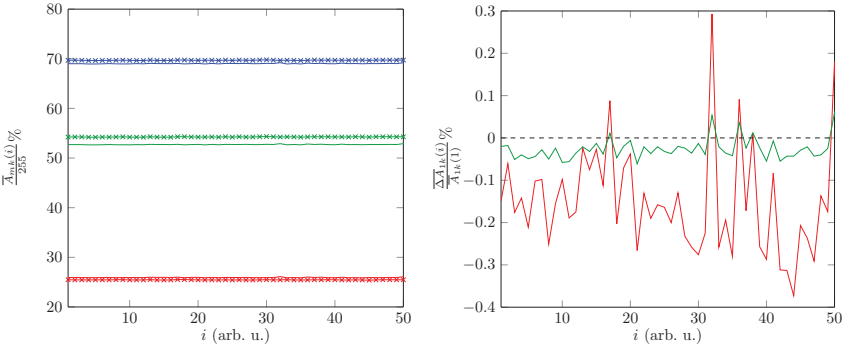

(a) (b)

Figure 4.10: a) Relative mean intensity distribution $\overline{A}_{mk}(i)/255$ in the i-th recorded 8-Bit object image for the respective color channels and LED pulses. First LED pulse $m = 1$ RGB (solid line), second LED pulse $m = 2$ RGB (asterix line). b) Relative mean intensity distribution deviation $\overline{\Delta A}_{1k}(i)/\overline{A}_{1k}(1)$ in the i-th recorded image for the first pulse $m = 1$.

figure 4.10 a) indicate, that the consecutive LED pulses of the color LEDs as well as the recorded intensity of the continuously illuminated blue LED in the m-th frame of the i-th dual shot image are different. In case of the red and green pulsed LEDs the difference in the mean intensity distribution between the recording frames may be related to a difference in the pulse intensity as well as an unintended overlap of the LED's pulse width τ_r, τ_g with the exposure gap interval $\Delta\tau_{\mathrm{exp}}$. The alignment of the LED pulse gaps to the camera exposure gap is done manually and it is not precluded that a small interval of the LED pulse coincides with the exposure gap. The difference in the mean intensity

distribution in the color channel of the continuously illuminated blue LED is probably caused by a slightly different total exposure time of the respective frames in the dual shot image. However, the relative deviation in the mean intensity distribution between the first $m = 1$ and second $m = 2$ frame is $< 3\%$. Figure 4.10 b) shows the relative, mean intensity distribution deviation for the red and green LED's first pulse. This is an indicator for the stability of the intensity distribution ratio over multiple images. The presented results show, that the mean intensity variation in the m-th frame for all three colors is small. Indicating that the intensity distribution scaling $D_{mk}(x, y)$ as well as $\overline{D}_{mk}$ determined from the first dual shot image $i = 1$ is feasible to rescale the intensity distribution in consecutive images, and thus may be determined in an a priori calibration measurement. In terms of the relative mean intensity distribution deviation $\overline{\Delta A}_{1k}(i)/\overline{A}_{1k}(1)$ presented in figure 4.10 a remarkable improvement compared to the previous experiment presented in [78] is achieved. This is due to the use of an extra capacitor to smooth the blue LED's supply voltage, removing a ripple which caused higher deviations between consecutive images. If measurements on moving objects are performed, the blue LED requires pulsing as well to provide pixel specific information of the measuring object surface, which is not blurred by motion during high exposure times. To demonstrate, that pulsing of the blue LED has no consequence for the applicability of the intensity distribution rescaling using $D_{mk}(x, y)$ or $\overline{D}_{mk}$ the intensity distribution recording is repeated, pulsing the red and the blue LED. The results for the relative mean intensity distribution and the relative mean intensity distribution deviation are presented in figure 4.11 a) and b), respectively. Figure

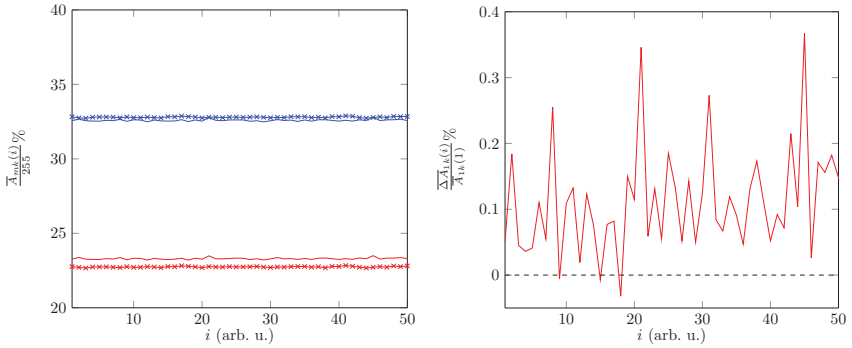

(a) (b)

Figure 4.11: a) Relative mean intensity distribution $\overline{A}_{mk}(i)/255$ in the i-th recorded 8-Bit object image for the respective color channels and LED pulses. First LED pulse $m = 1$ RB (solid line), second LED pulse $m = 2$ RB (asterix line). b) Relative mean intensity distribution deviation $\overline{\Delta A}_{1k}(i)/\overline{A}_{1k}(1)$ in the i-th recorded image for the first pulse $m = 1$.

4.11 a) shows that pulsing of the blue LED, results in an overall lower intensity in the

blue color channel. Besides that, the relative deviation in the mean intensity distribution between the first $m = 1$ and second $m = 2$ frame is almost unaffected. Comparing the relative mean intensity distribution deviation of the rescaled red intensity distribution in figure 4.11 b) to that depicted in figure 4.10 b), where the blue LED is continuously illuminated, shows that the magnitude of the deviation is very similar. This leads to the conclusion, that pulsing of the blue LED for recording of the microscopic object image has negligible influence on the intensity distribution determination in the red and green color channel. Therefore, the blue LED may be employed in pulsed or continuous illumination mode. The continuous illumination yields the advantage of higher intensity in the blue color channel, while pulsing of the blue LED enables the determination of the pixel specific intensity distribution on moving specimens.

The results presented in figure 4.10 and 4.11 demonstrate, that the offset intensity distribution retrieval from the microscopic image based on an a priori determined scaling factor is possible, since the ratio between the intensity distribution in the respective color channels, in the m-th frame of the dual shot image, is almost constant considering consecutively recorded images. In the upcoming part of this section the advantages and disadvantages employing either the matrix based rescaling $D_{mk}(x, y)$ or the scalar rescaling $\overline{D}_{mk}$ are discussed. In terms of intensity distribution deviation on a plane surface, like the tilted mirror considered above, there is no remarkable difference between these approaches. Also it is discussed if the additional effort to determine the scaling factor $D_{mk}(x, y)$ or $\overline{D}_{mk}$ for the m-th recorded frame in the dual shot image separately has a remarkable impact on the retrieved topography.

Considering structured measuring surfaces, featuring edges and differently tilted surface areas, the intensity distribution in the object image will be inhomogeneous. Also the illumination itself might be partially inhomogeneous. Diffraction and dispersion effects like longitudinal chromatic aberration may have a wavelength dependent influence on the object intensity distribution. As a result of this the ratio between the intensity distributions in the respective color channels is not perfectly constant over the field of view, but varies at specific surface sections. To illustrate this the rectangular structure of the RS-M standard [168] with a lateral periodicity of 80 µm and a nominal structure depth of 90 nm is considered. The structure depth is small enough that there are no differences expected in the object intensity reflected from the upper and lower plateau of the structure. However, at the edges of the structure diffraction occurs and due to the longitudinal chromatic aberration of the imaging system described in detail in section 4.3, the image may only be focused for one wavelength at a time, causing blur in the images of the other color channels. Figure 4.12 depicts the object intensity distribution on the RS-M standard in the respective color channels for red, green and blue illumination from left to right. The object is focused with respect to the green illumination. This is visible in figure 4.12 by the edges of the rectangular structure being sharp lines in the green image, while expanded and blurred in the red and blue image. This results in inhomogeneities of the intensity scaling close to the edges, which influences the entries of $D_{mk}(x, y)$ but has almost no impact on

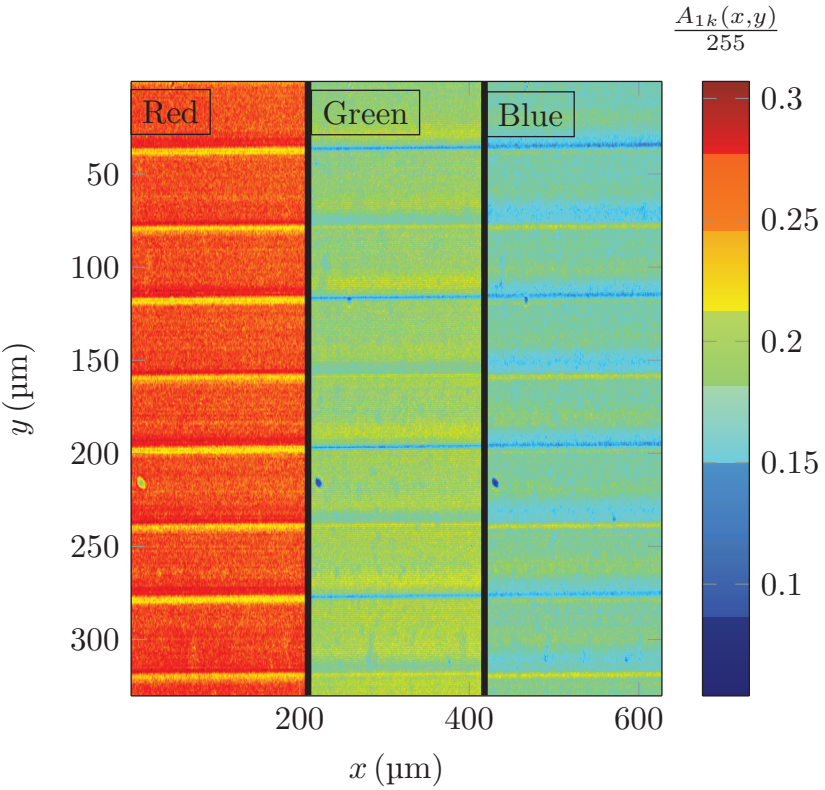

Figure 4.12: RGB object intensity distribution $A_{11}(x, y)$, $A_{12}(x, y)$ and $A_{1,\text{blue}}(x, y)$ (from left to right) on the surface section of the RSM standard with nominal periodicity of 80 µm.

$\overline{D}_{mk}$. To evaluate the impact of the employed method for intensity distribution rescaling, the topography of the RS-M surface depicted in figure 4.12 is retrieved employing the quadrature phase retrieval approach introduced in section 4.2. Thereby, the object image intensity in the red and green color channel will be retrieved by rescaling of the blue object image using the matrix $D_{mk}(x, y)$ or the scalar $\overline{D}_{mk}$, respectively. Figure 4.13 a) shows the topography of the RS-M standard retrieved from the interferograms recorded in the red color channel employing the intensity distribution rescaling matrix $D_{1k}(x, y)$, for intensity distribution scaling in both frames. Figure 4.13 b) shows a section of the

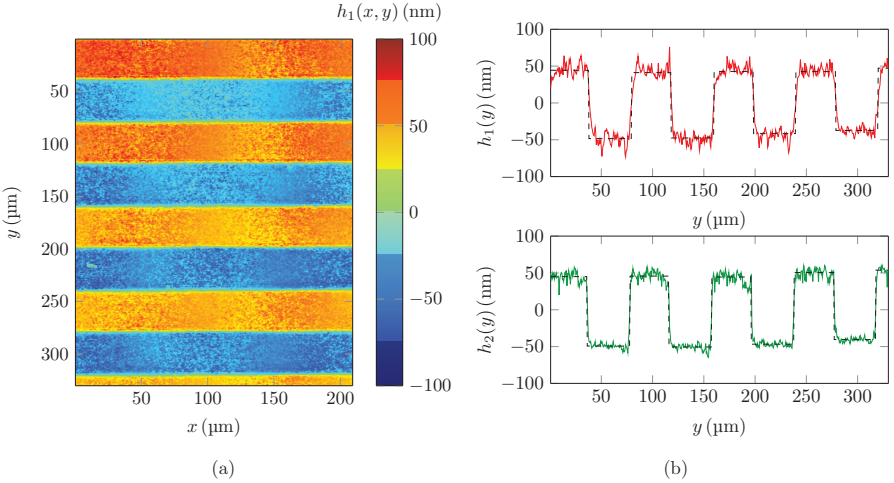

Figure 4.13: a) Surface topography of the RS-M standard with 80 µm periodicity and 90 nm nominal structure depth retrieved from the red color channel interferogram using matrix rescaling $D_{1k}(x, y)$. b) Profile of the RS-M topography along the rectangular structure at $x = 27.5$ µm for the red color channel $h_1(y)$ and green color channel $h_2(y)$ using matrix rescaling $D_{1k}(x, y)$.

measured topography along the rectangular structure of the RS-M standard retrieved from the interferograms in the red and green color channel respectively. Figure 4.13 a) shows that the edges of the rectangular structure are not perfectly sharp, but low pass filtered by the limited lateral resolution of the microscope objective and also slightly blurred by the defocusing as expected, comparing the topography to the object image in figure 4.12. The topography sections in figure 4.13 b) show a mean structure depth of 87 nm with a standard deviation $\mathrm{std}(e_{h_1(y)}) = 6.95$ nm for the topography retrieved from the red color channel $h_1(y)$ and a mean structure depth of 94 nm with a standard deviation $\mathrm{std}(e_{h_2(y)}) = 5.43$ nm for the topography retrieved from the green color channel $h_2(y)$. The standard deviation is determined with respect to the median filtered structure indicated by the dashed black line. These results are in good agreement with those presented in [79], which are also generated employing the matrix rescaling.

The topography of the RS-M standard retrieved from the interferograms recorded in the red and green color channel employing the scalar intensity distribution rescaling $\overline{D}_{1k}$, for intensity distribution scaling in both frames are presented in figure 4.14. Figure 4.14 a) shows the topography of the RS-M standard retrieved from the interferograms recorded in the red color channel employing the scalar intensity distribution rescaling $\overline{D}_{1k}$, for in-

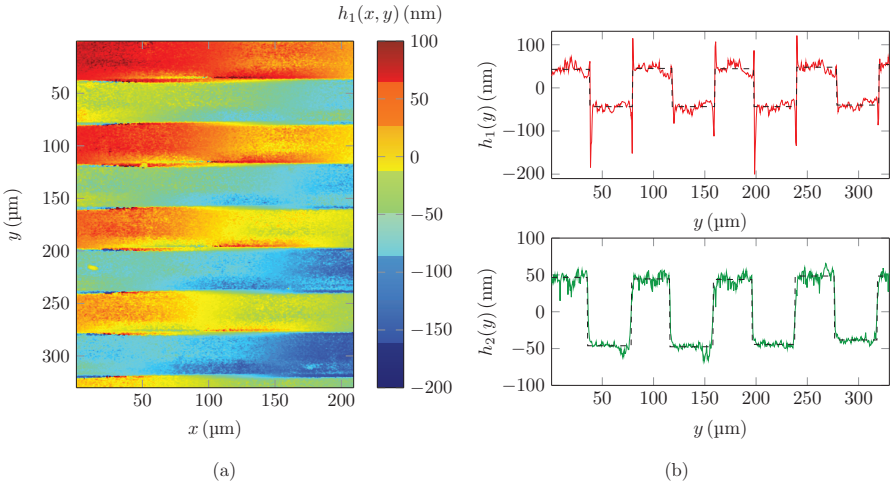

Figure 4.14: a) Surface topography of the RS-M standard with 80 µm periodicity and 90 nm nominal structure depth retrieved from the red color channel interferogram using scalar rescaling $\overline{D}_{1k}$. b) Profile of the RS-M topography along the rectangular structure at $x = 27.5$ µm for the red color channel $h_1(y)$ and green color channel $h_2(y)$ using scalar rescaling $\overline{D}_{1k}$.

tensity distribution scaling in both frames. Figure 4.14 b) shows a profile of the measured topography along the rectangular structure of the RS-M standard retrieved from the interferograms in the red and green color channel respectively. Comparing figure 4.14 a) and 4.13 a) reveals that in figure 4.14 a) the edges of the rectangular structure are distorted by over- and undershooting similar to the batwing effect. Using the scalar intensity distribution rescaling, the local variations in the intensity ratio of the red and blue object image from figure 4.12, which especially occur at the blurred edges, are not considered. The numerical aperture of the employed 10× microscope objective is NA = 0.28 referring to an airy disc diameter of $d_{\min} \approx 1.22\lambda/\mathrm{NA}$, which limits the resolution due to diffraction [110]. Employing the red LED for illumination, the resolution limit is $d_{\min}/2 \approx 1.4$ µm. At the edges of the RS-M structure the airy disc overlaps with the top and bottom level of the plateaus and the intensity values recorded there are a mixture from both levels including interference of both components. Figure 4.15 shows the consecutively recorded interference images of a dual shot recording in the red color channel. Considering the intensity at the edges in the left and right image, shows that the mixed intensity values there do not show the quadrature pattern observed at the plateaus. Therefore, deviations in phase retrieval are stronger and more likely in the vicinity of the edges. The stronger deviations

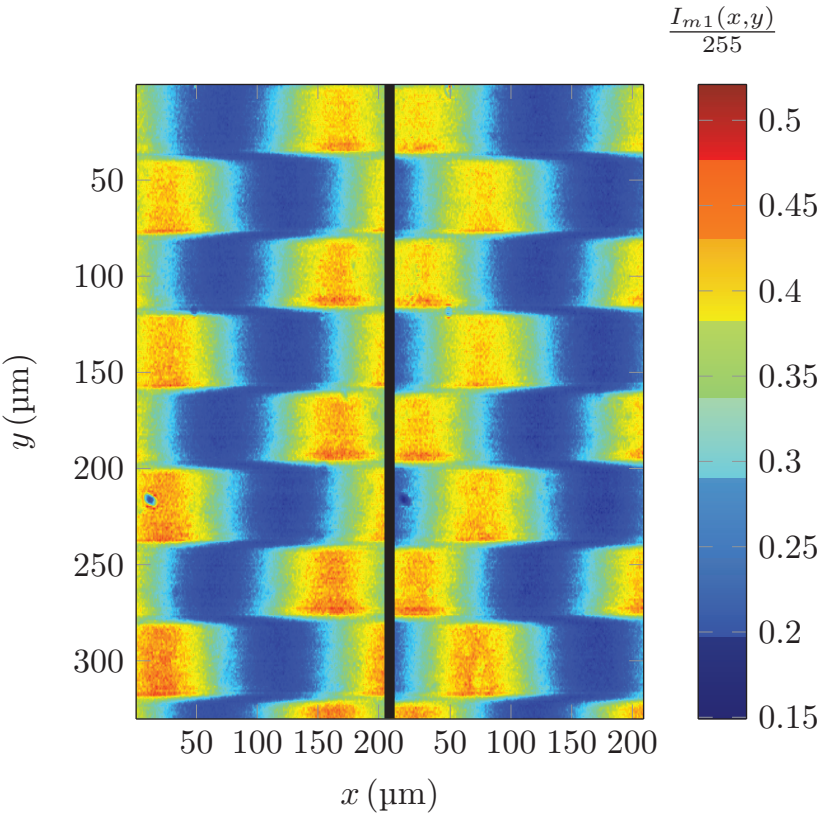

Figure 4.15: Dual shot pair of interference images in quadrature, recorded in the red color channel, employed for phase retrieval of the topography in figure 4.14. The black vertical line separates the first recorded image on the left side from the second recorded image on the right side.

at the edges in the red color channel are clearly visible in the sectional view in figure 4.14 b). However, the influence of the scalar intensity distribution rescaling on the green color channel topography is less remarkable, which is reasonable since the green image is focused and has higher overall intensity reducing the influence and occurrence of invalid phase values at the edges. The profiles in figure 4.14 b) show a mean structure depth of 89 nm with a standard deviation $\mathrm{std}(e_{h_1(y)}) = 8.52\,\mathrm{nm}$ for the topography retrieved

from the red color channel $h_1(y)$ and a mean structure depth of 90 nm with a standard deviation $\mathrm{std}(e_{h_2(y)}) = 5.89\,\mathrm{nm}$ for the topography retrieved from the green color channel $h_2(y)$. Comparing these characteristics to the matrix based intensity distribution rescaling approach, there is an improvement in the precise determination of the mean structure depth, while the standard deviation is increased, especially in the red color channel. This is plausible, since the scalar intensity distribution rescaling works well on the extended plateau surfaces and causes higher deviations at the edges. In figure 4.16 the topogra-

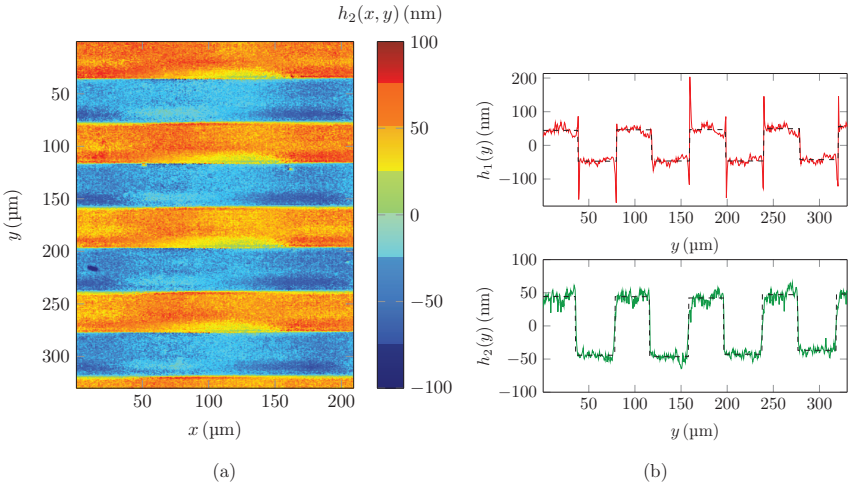

Figure 4.16: a) Surface topography of the RS-M standard with 80 µm periodicity and 90 nm nominal structure depth retrieved from the green color channel interferogram using specific scalar rescaling $\overline{D}_{mk}$. b) Profile of the RS-M topography along the rectangular structure at $x = 27.5\,\mu\mathrm{m}$ for the red color channel $h_1(y)$ and green color channel $h_2(y)$ using specific scalar rescaling $\overline{D}_{mk}$.

phy retrieved by employing specific scalar rescaling factors $\overline{D}_{mk}$ in the m-th frame of the dual shot image is presented. Defining a specific rescaling scalar $\overline{D}_{mk}$ for each of the two frames should compensate the intensity difference between the light pulses shown in figure 4.10 a), and therefore, should improve the object intensity distribution determination in the respective interferograms. Figure 4.16 a) shows the topography of the RS-M standard retrieved from the interferograms recorded in the green color channel employing the scalar intensity distribution rescaling $\overline{D}_{mk}$, for separate intensity distribution scaling in the respective frames. Comparing figure 4.16 a) and 4.14 a) shows that the over- and undershoot deviations observed in the topography of the red color channel retrieved with scalar intensity distribution rescaling occur far less in the topography retrieved from the

green color channel with scalar intensity distribution rescaling. This is due to the green image being focused and having higher overall intensity, such that less deviations occur at the edges. The topography sections in figure 4.16 b) show a mean structure depth of 94 nm with a standard deviation $\mathrm{std}(e_{h_1(y)}) = 8.08\,\mathrm{nm}$ for the topography retrieved from the red color channel $h_1(y)$ and a mean structure depth of 87 nm with a standard deviation $\mathrm{std}(e_{h_2(y)}) = 6.2\,\mathrm{nm}$ for the topography retrieved from the green color channel $h_2(y)$. In terms of the retrieved mean structure depth, the deviation to the nominal structure depth is increased compared to the case of employing the same scalar rescaling factor in both frames depicted in figure 4.14, while the standard deviation is similar. However, considering the impact of imperfections of the actor movement on the measuring results, discussed in [79], the deviations between the retrieved topography employing $\overline{D}_{1k}$ in both frames or $\overline{D}_{mk}$ in the m-th frame are not significant. The characteristic topography parameters retrieved from the depicted surface sections in figure 4.13 b), 4.16 b) and 4.14 b) are summarized in table 4.4. The conclusion of this section is, that all three considered

Table 4.1: Comparison of the measured structure depth and standard deviation at the RS-M standard for different methods of object image intensity determination in the respective color channels. The standard deviation is determined with respect to the median filtered structure indicated by the dashed black line in the figures.

	Depth $h_1(y)$	Depth $h_2(y)$	$\mathrm{std}(e_{h_1(y)})$	$\mathrm{std}(e_{h_2(y)})$
Nominal value:	90 nm	90 nm		
Matrix rescaling $D_{mk}(x, y)$:	87 nm	94 nm	6.95 nm	5.43 nm
Scalar rescaling $\overline{D}_{1k}$:	89 nm	90 nm	8.52 nm	5.89 nm
Specific scalar rescaling $\overline{D}_{mk}$:	94 nm	87 nm	8.08 nm	6.2 nm

methods of offset intensity distribution retrieval from the microscopic image yield comparable topography results on a structured surface, while showing even less differences on plane measuring objects. When objects in motion are considered, the matrix rescaling approach is not applicable, since it considers the specific surface structure recorded during the reference measurement, which will not align to consecutively recorded images on a moving measuring object. Therefore, employing the simple approach of scalar rescaling based on the rescaling factor $\overline{D}_{1k}$ determined from a calibration measurement with blocked reference path evaluating the first recorded frame of the dual shot image is most convenient. This method is employed in [11] for measurement of the superfine roughness standard in motion. Comparison of figure 4.14 and 4.16 with respect to the red and green color channel implies, that illumination intensity and focusing have a stronger influence on the quality of the retrieved topography than the algorithm employed for compensation of the offset intensity distribution in the recorded interferograms. The standard deviation in retrieved surface height values and deviations at the edges of the rectangular structure are smaller in the green color channel, which compared to the red color channel is better focused on the object surface and has higher illumination intensity.

4.5 Crosstalk correction

The color channels of a Bayer pattern camera usually show an overlapping sensitivity in their spectral range. Therefore, using broad band illumination sources like color LEDs results in color crosstalk. Also, the Demosaicing or De-Bayering reconstructing the full resolution color images from the incomplete RGB-samples may introduce artificial crosstalk effects. These color crosstalk errors may disturb the phase retrieval. Color crosstalk is omitted or reduced by the usage of three chip cameras with narrow bandwidth color filters and narrow bandwidth light sources [101] or spatial separation of the respective color interferograms [169]. These attempts require the use of a special recording device or special light sources. Narrow bandpass filtering can be applied to the illuminating LEDs, to reduce crosstalk interaction, but will strongly reduce the intensity. An alternative is given by algorithmic crosstalk correction commonly applied in RGB fringe-projection profilometry [170–172]. Assuming an approximately linear crosstalk behavior, a 3×3 matrix of coupling coefficients is identified by calibration measurements. The coupling coefficients describe to what extend light of wavelength λ_k will influence the recording in each color channel. Using this approach the crosstalk corrected images $\tilde{R}$, $\tilde{G}$, $\tilde{B}$ result

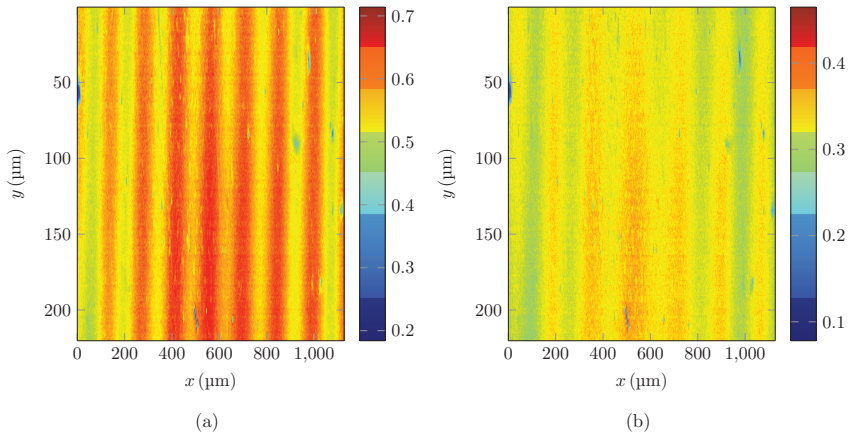

Figure 4.17: a) Microscopic image intensity distribution $A_{1,\mathrm{blue}}(x, y)/255$ in the blue color channel with color crosstalk from red and green illumination, b) Microscopic image intensity distribution $\tilde{A}_{1,\mathrm{blue}}(x, y)/255$ in the blue color channel after crosstalk correction employing equation (4.9).

by multiplication of the coupling coefficient matrix with the recorded images R, G, B as

described in equation (4.8).

$$\begin{bmatrix} \tilde{R} \\ \tilde{G} \\ \tilde{B} \end{bmatrix} = \begin{bmatrix} 1 & -C_{\mathrm{gr}} & -C_{\mathrm{br}} \\ -C_{\mathrm{rg}} & 1 & -C_{\mathrm{bg}} \\ -C_{\mathrm{rb}} & -C_{\mathrm{gb}} & 1 \end{bmatrix} \cdot \begin{bmatrix} R \\ G \\ B \end{bmatrix} \tag{4.8}$$

To identify the coupling coefficients, a calibration measurement is performed. A plane mirror is chosen as the measuring object and the reference arm of the interferometer is blocked to preclude the influence of interference fringes during the calibration routine. The RGB LEDs are illuminated one at a time and the corresponding color images are recorded. This is repeated for different pulse widths and supply voltages and therefore, different intensities of the illuminating LEDs to investigate the linearity of the color crosstalk. For each respective illumination color, the ratio between the intensity in the corresponding color channel and the crosstalk intensity in the neighboring color channels is determined, yielding the coupling coefficients. To demonstrate the functionality of the cross talk correction and its impact on the quadrature phase retrieval, a plane mirror is considered as the measuring object. Interference images are recorded in the red and green color channel and the microscopic image in the blue channel, as introduced in section 4.2. The calibration measurements yield the crosstalk correction coefficients in equation (4.9).

$$\begin{bmatrix} \tilde{R} \\ \tilde{G} \\ \tilde{B} \end{bmatrix} = \begin{bmatrix} 1 & -0.0783 & -0.0615 \\ -0.1522 & 1 & -0.1863 \\ -0.0915 & -0.3304 & 1 \end{bmatrix} \cdot \begin{bmatrix} R \\ G \\ B \end{bmatrix} \tag{4.9}$$

Figure 4.17 a) shows the intensity distribution in the blue color channel without crosstalk correction. Apparently the intensity distribution of the microscopic picture in the blue color channel is distorted by the fringes from the red and green interferograms. Applying the crosstalk correction with the coefficients from equation (4.9) yields the intensity distribution depicted in figure 4.17 b). In the crosstalk corrected image the modulation depth of the disturbing fringes is decreased. For better comparison, a single line of the intensity distributions $A_{1,\mathrm{blue}}(x)$ and $\tilde{A}_{1,\mathrm{blue}}(x)$ from figure 4.17 a) and b) is plotted in figure 4.18 a). The impact of the crosstalk correction is clearly visible there. To evaluate the influence of the color crosstalk on the quadrature phase retrieval with scalar intensity distribution rescaling, the mirror topography is retrieved from the crosstalk distorted images and the crosstalk corrected images. An ideal plane is subtracted from the reconstructed mirror surface and the deviation of the measured topography to the ideal plane $e_{h_2(x)}, e_{\tilde{h}_2(x)}$ is compared for both cases. Figure 4.18 b) shows the deviation of the ideal plane for the line sections depicted in figure 4.18 a). Although the crosstalk reduction is clearly visible in figure 4.18 a) it has no remarkable influence on the topography quality. The deviation from the assumed ideal mirror surface is not significantly decreased by the crosstalk correction. The benefit of the crosstalk correction is higher, when the matrix method from section 4.4 is employed for intensity distribution rescaling, since the disturbing fringes also affect the matrix coefficients. However, as figure 4.17 and 4.18 a) demonstrate, the crosstalk correction based on equation (4.8) reduces the crosstalk error. The processing

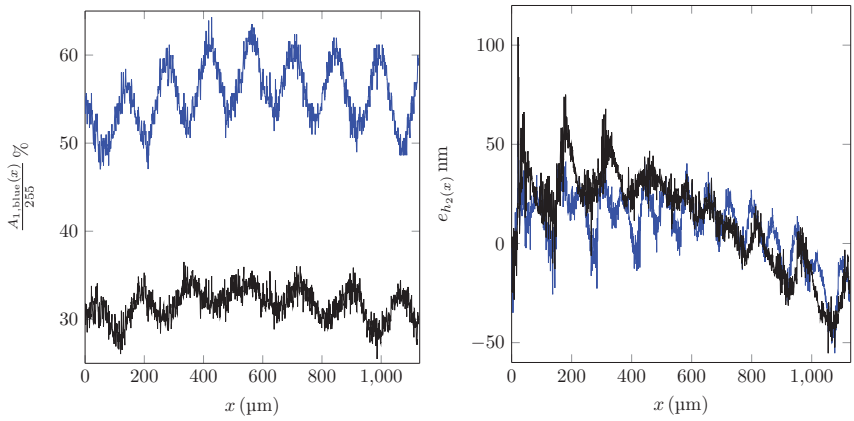

Figure 4.18: a) Section of figure 4.17 a) blue image with color crosstalk $A_{1,\mathrm{blue}}(x)$ (blue line), section of figure 4.17 b) blue image after crosstalk correction $\tilde{A}_{1,\mathrm{blue}}(x)$ (black line) at $y = 110\,\mu\mathrm{m}$. b) Deviation of the retrieved mirror surface topography from an ideal plane, quadrature phase retrieval without crosstalk correction $e_{h_2(x)}$ (blue line), quadrature phase retrieval with crosstalk correction $e_{\tilde{h}_2(x)}$ (black line) at $y = 110\,\mu\mathrm{m}$.

capacity required for the crosstalk correction is that of a simple matrix multiplication. It is easy to implement and yields plausible results in the images intensity distribution.

4.6 Measuring objects in lateral motion

The dimensions of the employed camera chip constrict the field of view on the measuring object to a 1.126 mm × 1.126 mm rectangular area. To receive topography information of an extended surface area stitching of consecutive topography measurements with the object in lateral motion is performed. The interferometric setup employed offers a high robustness to environmental perturbations due to its short acquisition time [79] and is capable to measure the surface of objects in motion. Reference [11] presents the capability of the setup to measure a superfine roughness standard in motion. The application of surface roughness filters removes offset, tilt and waviness from the topography and simplifies the stitching procedure. The numerical aperture of the employed 10× microscope objective is NA = 0.28 referring to an airy disc diameter of $d_{\mathrm{min}} \approx 1.22\lambda/\mathrm{NA}$, that limits the resolution due to diffraction [110]. Employing the red LED for illumination, the res-

olution limit is $d_{\min}/2 \approx 1.4\,\mu m$. The effective image acquisition time, due to the pulsing of the LEDs is $\approx 100\,\mu s$. Since a lateral displacement $< d_{\min}/2$ could not be resolved it should have neglectable influence on the surface phase retrieval. Thus, a lateral movement with the velocity $v \leq 14\,mm/s$ should negligibly affect the topography measurement. For the experimental results presented in this section a lateral velocity of $v = 5\,mm/s$ and $v = 10\,mm/s$ is chosen. The camera frame rate in the dual shot mode is 10 FPS, enabling the recording of one pair of interference images in quadrature every 100 ms. The retrieved topographies are laterally shifted by 0.5 mm or 1.0 mm to each other in the direction of scanning axis movement and will overlap on a length of 0.626 mm or 0.126 mm respectively. During each dual shot recording of the camera, the red and blue LED are pulsed. Pulsing of the blue LED and application of the scalar rescaling technique discussed in section 4.4 is applied to record the intensity distribution in the measurement arm without motion blur. Two interference images in quadrature are recorded in the red color channel and the object intensity distribution is recorded in the blue color channel. Employing the quadrature based phase retrieval introduced in section 4.2 the corresponding surface topographies result. Figure 4.19 shows five consecutively retrieved topography results on

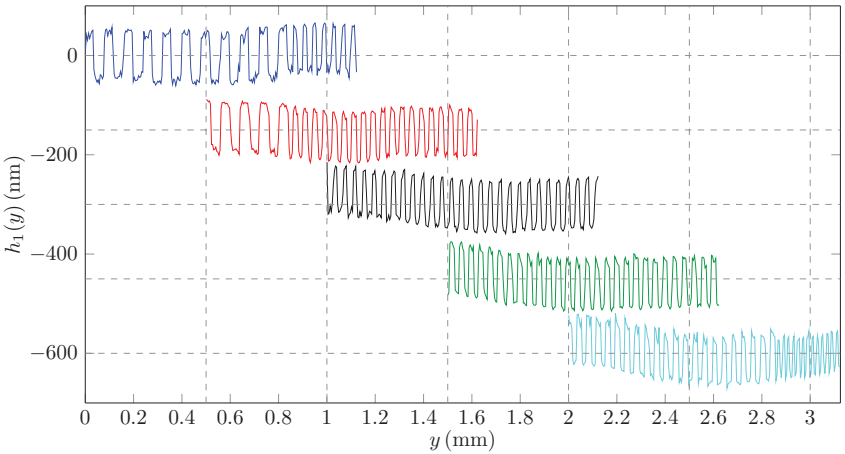

Figure 4.19: Consecutively recorded topography sections of the RS-M standard, covering 80 µm to 20 µm periodicity. The scanning velocity in axial direction is $v = 5\,mm/s$ and dual shot image recording is set to 10 FPS.

a RS-M standard with 90 nm nominal structure depth [168] for a scanning velocity of $v = 5\,mm/s$. The individual surface sections are each recorded with the low data acquisition time of $< 100\,\mu s$. However, there is a 100 ms interval between the consecutive surface section recordings. Therefore, the combined measurement result does not yield the perturbation robustness of the single topography sections. Environmental changes, vibration

or phase detuning of the actuator may influence the combined topography result. Since the RS-M standard is moved relatively to the interferometer and is not perfectly aligned, the surface tilt will result in increasing defocusing. Considering the results presented in figure 4.19 a waviness is observed superposed to the RS-M structure. This deviation might be related to increasingly inhomogeneous illumination by defocusing during motion or phase detuning of the actuator between measurements. The amplitude of the waviness is $< 100\,\mathrm{nm}$ distributed on a lateral surface section in the mm range. Thus, it could stem from a fabrication uncertainty or be related to wobble of the scanning axis. For the surface roughness measurements in reference [11], these deviations are not important, since they are completely extinct by the roughness filter. Figure 4.20 shows the stitched

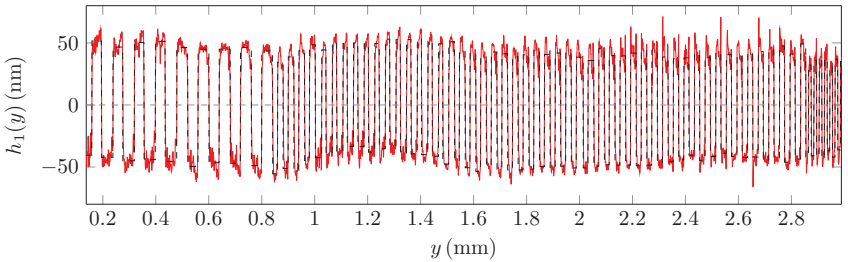

Figure 4.20: Stitched RS-M profile based on the topography sections in figure 4.19 after removing the waviness (red line), median level plateaus for determination of the structure depth (black dashed line). The mean structure depth is $\approx 87\,\mathrm{nm}$ with a standard deviation of $\mathrm{std}(e_{h_1(y)}) = 12\,\mathrm{nm}$ considering the difference to the median plateau levels.

surface topography based on the surface sections from figure 4.19. The well known overlap of the surface sections is used to directly stitch them together at the designated lateral positions. A short median filter is applied to suppress noise in the topography sections. The stitched surface profile is low pass filtered to determine the waviness and subtract it. The retrieved topography shows a mean structure depth of $\approx 87\,\mathrm{nm}$ with a standard deviation of $\mathrm{std}(e_{h_1(y)}) = 12\,\mathrm{nm}$ considering the difference to the median plateau levels. The mean structure depth is determined by separating the upper and lower plateaus of the rectangular structure and determining the median value of each respective plateau (e.g. 4.20 black dashed line). Then a vector containing the step height between the median values of the consecutive plateaus is determined and its mean value is referred to as the mean structure depth in this section. As discussed in section 4.4 there are over- and undershooting effects observed at the structures edges.

The measurements are repeated at a higher lateral scanning speed of $v = 10\,\mathrm{mm/s}$. The consecutively recorded topography sections of the RS-M standard covering 80 µm to 40 µm periodicity are depicted in figure 4.21. Three topography sections cover a comparably large field of view due to the smaller overlap. Figure 4.22 shows the stitched and filtered

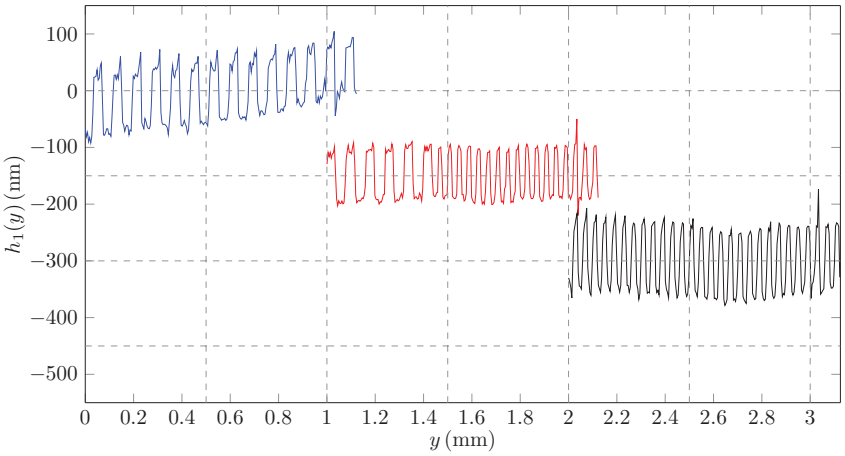

Figure 4.21: Consecutively recorded topography sections of the RS-M standard, covering 80 µm to 40 µm periodicity. The scanning velocity in axial direction is $v = 10\,\mathrm{mm/s}$ and dual shot image recording is set to 10 FPS.

topography results at $v = 10\,\mathrm{mm/s}$ scanning velocity. Comparing figure 4.20 and 4.22

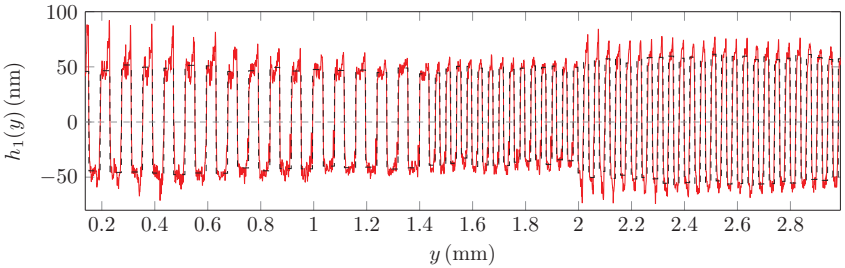

Figure 4.22: Stitched RS-M profile based on the topography sections in figure 4.21 after removing the waviness (red line), median level plateaus for determination of the structure depth (black dashed line). The mean structure depth is $\approx 99\,\mathrm{nm}$ with a standard deviation of $\mathrm{std}(e_{h_1(y)}) = 16\,\mathrm{nm}$ considering the difference to the median plateau levels.

indicates, that the RS-M structure is resolved and retrieved for both measuring velocities successfully. At higher speed of $v = 10\,\mathrm{mm/s}$, the standard deviation is increased as well as over- and undershooting at the edges. This is plausible, since the surface is moving

by almost half an airy disc diameter between the recording of the images in quadrature. Thus, the edge position is slightly different in the second picture and the area of invalid phase values due to overlapping of the airy disc with the edge in the respective images is overlapping too, such that it broadens. Additionally, the structure depth in the third topography section of figure 4.21 is significantly higher than the nominal structure depth. This might be caused by defocusing or phase detuning in the recording of the third quadrature image pair.

Figure 4.23 depicts a topography measurement of the RS-M standard recorded with the fiber coupled interferometric point sensor introduced in chapter 3. As for the topography measurements of the quadrature phase retrieval based Michelson interferometer in figure 4.20 and 4.22 the waviness and tilt of the original topography measurement is reduced employing the same filter. At a scanning speed of $v = 0.6\,\mathrm{mm/s}$, the point sensor re-

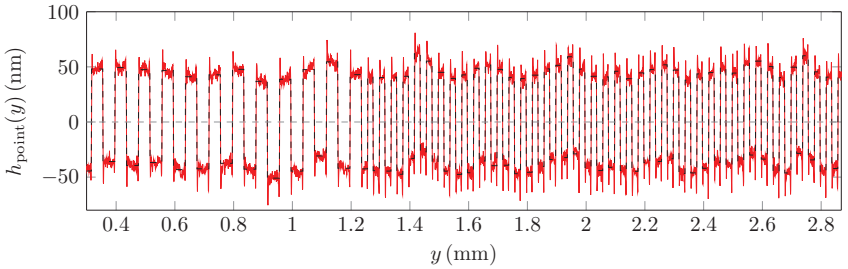

Figure 4.23: RS-M profile measured with the fiber coupled interferometric point sensor introduced in chapter 3 after removing the waviness (red line), using a scanning velocity of $v = 0.6\,\mathrm{mm/s}$, a sampling rate of $f_s = 1\,\mathrm{kHz}$ and a wavelength of $\lambda_{\mathrm{point}} = 1310\,\mathrm{nm}$, median level plateaus for determination of the structure depth (black dashed line). The mean structure depth is $\approx 87\,\mathrm{nm}$ with a standard deviation of $\mathrm{std}(e_{h_{\mathrm{point}}(y)}) = 10\,\mathrm{nm}$ considering the difference to the median plateau levels.

trieves the RS-M surface with a structure depth of $\approx 87\,\mathrm{nm}$ and a standard deviation of $\mathrm{std}(e_{h_{\mathrm{point}}(y)}) = 10\,\mathrm{nm}$ considering the difference to the median plateau levels. This is comparable to the characteristics of the Michelson interferometer. However, the quadrature based RGB-interferometer conducts areal measurement at a higher scanning speed and thus, provides a far higher data rate. A small waviness is also observed in the measurement results of the point sensor. It may be related to environmental perturbations during the extended recording time of this sensor or due to mechanical vibrations introduced by the scanning axis.

The results presented in this section together with those in [11, 79], show the capability of the RGB-Michelson interferometer to yield feasible topography results on structured surfaces in motion.

Chapter 5

Conclusion and future work

The theoretical part of this dissertation in chapter 2 serves as a compendium for the application of the non-uniform wave model to describe wave propagation and interference effects in dissipative media. A common issue in the derivation of Fresnel's coefficients and Snell's law at attenuating interfaces is solved by unraveling the commonly confused wave vector notations in the uniform and non-uniform wave model [128]. The theory of two beam interference is outlined considering wave propagation in dissipative media and employing the non-uniform wave model. This covers the derivation of the two beam interference equation (2.79), the complex non-uniform poynting vector (2.88) and a detailed analytical study of energy conservation in a common path interferometer 2.11.3. To the best knowledge of the author there is no textbook or manuscript available covering the aforementioned in comparative detail. Thus, the theoretical part of this thesis provides a original foundation for teaching wave propagation in dissipative media at undergraduate or postgraduate level. The mayor results of this chapter are:

- A comparative analysis of the uniform and non-uniform wave model including the commonly employed notations.
- The derivation of the dispersion relation for the non-uniform plane wave indicating the difference between the intrinsic and effective propagation constants.
- The derivation of Snell's law in dissipative media indicating the limitation of the uniform wave model to non-dissipative media.
- The derivation of Fresnel coefficients for the interface between attenuating media in phase-attenuation vector notation, which allows to describe the propagation characteristics of the wave fronts and the planes of constant amplitude in dependence of the real valued effective propagation constants omitting the use of complex angles.
- The derivation of the complex poynting vector of the non-uniform wave and the two beam interference equation for dissipative media showing that energy is only

transported in the direction of wavefront propagation described by the real valued effective propagation constant of phase evolution.

- The derivation of energy conservation at the reference plane of a common path interferometer covering dissipative and non-dissipative media. The presented results indicate that the non-uniform wave model is not only a valid solution to Maxwell's equations, but employing the effective propagation constants also complies to the law of energy conservation. The combination of equation (2.99) and (2.100) indicating the phase coupling of the pairs of interfering waves propagating to the detector and the measuring object, respectively, enables the determination of the intensity distribution at the measuring object based on the intensity recorded at the detector. This could be employed to establish a feedback loop in lithography applications, which mostly rely on ex situ process control [173, 174].

The introduction in chapter 1 provides a general survey regarding the state of the art in interferometric surface metrology and specifically elaborates on point wise measuring interferometers with optical path length modulation and areal low coherence interferometers for surface phase retrieval. Chapter 3 focuses on topography retrieval employing a fiber coupled dual wavelength common path laser interferometer with periodical optical path length modulation. The basic concept of the fiber coupled interferometric sensor is introduced and significant results considering its measuring characteristics and applicability for topography measurements are presented:

- The reference plane inside the interferometric probe is experimentally identified, exploiting the wavelength dependence of the measured optical path length difference. The employed experiment also yields information about the wavelength stability in the vicinity of temperature changes and could be used to conduct absolute height measurements.

- Recording the depth response of the fiber coupled probe shows its confocal characteristics. The confocal behavior is caused by the small fiber core diameter, which acts as a pinhole in the measurement and reference path. An interferometric fiber coupled low aperture probe is designed employing transfer matrices to establish a reference interferometer system for focus tracking. This enables the dynamic repositioning of the high aperture probe with respect to the measuring object surface without loss in height resolution. The employed low aperture probe shows a depth of field of $\approx 20\,\mathrm{mm}$.

- An analytical derivation of fast surface phase retrieval algorithms based on time discrete Hilbert filters is presented. Pointing out systematic deviations related to these filters and proposing feasible measures to reduce them by spatially equidistant resampling of the temporally equidistant input data.

- The capability of the high aperture probe with focus tracking, to measure expanded curved or tilted surface areas while maintaining the focus position is demonstrated by experimental results. The topography is feasibly retrieved on multiple square mm surface areas of a sinusoidal standard and a plano-convex lens.
- An analytical algorithm for unambiguity range extension in multicolor interference systems based on the exact fraction method is modified to be applicable in measurement applications. The successful extension of the unambiguity range is demonstrated with experimental results and implications of edge effects like the batwing effect are discussed.
- The fiber coupled point sensor is feasible to measure the structure of rough surfaces despite employing long coherent illumination, since the speckle patterns do not pass through the small aperture of the fiber core pinhole. Roughness standards of various R_a values in the range of $R_a \in [25\,\text{nm}, 1500\,\text{nm}]$ are measured by the sensor abiding to the appropriate ISO standards.

As implied by the results presented above, the research dedicated to further development of the fiber coupled interferometric point sensor yields an original miniaturized measurement system. It enables 3D-topography retrieval in an extended measurement volume with dynamic focus tracking due to the implementation on a real time system, and thus is feasible for form and surface measurements of sophisticated 3D-objects.

Chapter 4 introduces two novel methods for perturbation resistant surface phase retrieval in RGB-interferometry without the use of carrier fringes or polarizing interferometry. A sophisticated technique for surface phase retrieval employing a parameter identification approach is proposed. However, experimental results demonstrate the high sensitivity of this approach to dispersion effects, precluding the retrieval of feasible topography result applying this method. The other proposed method employs precise synchronization of LED pulses to the camera exposure gap and the actuator movement in the reference path to record interference images in quadrature. Also a microscopical image is recorded to determine the offset intensity distribution. Using the recorded images a simple quadrature phase retrieval algorithm is employed, which yields feasible topography results:

- The adjustability of a phase shift between two consecutive recorded interference images employing the synchronization of the LED pulses to the actuator movement is demonstrated to yield nm precision.
- The intensity distribution rescaling between microscopic images recorded in separate color channels is successfully performed by either a matrix or scalar assuming a linear behavior. The advantages and disadvantages of using the matrix or scalar rescaling are discussed considering phase retrieval at an RS-M standard. The experimental results indicate that the scalar rescaling is more advantageous to employ for measuring objects in motion.

- The standard deviation in topography measurement results retrieved by the quadrature method are determined to be in the range of $\mathrm{std}(e_{h_k(x,y)}) \in [3\,\mathrm{nm}, 7\,\mathrm{nm}]$ depending on the reflectivity of the measuring object and the corresponding signal to noise ratio of the recorded interference images.
- Employing the retrieved phase information of the red and green interference images respectively, the longer synthetic wavelength is employed to increase the unambiguity range of the topography measurement. However, the phase noise associated with the quadrature phase retrieval precludes the application of analytic unambiguity range extensions based on the exact fraction method.
- The perturbation resistance of the measurement system to mechanical vibrations in axial direction is demonstrated. Mechanical vibrations in axial direction up to a velocity of $v_d = 10\,\mu\mathrm{m/s}$ have negligible impact on the retrieved topography results.
- An extensive study of the dispersion effects in the Michelson interferometer indicates misalignment in the interferometer and demonstrates that the long pass filter in the reference arm is not feasibly compensated by a glass plate of same thickness in the measuring arm. Correcting the misalignment and employing adapted compensation plates might improve signal quality in the recorded interference images.
- An algebraic method for crosstalk error corrections in fringe-projection systems is applied to the recorded interference images and yields feasible results.
- The very short data acquisition time of the proposed RGB-interferometer, which is smaller 100 µs, enables its high perturbation resistance to mechanical vibrations and also the measurement of objects in motion. Successful surface phase retrieval is demonstrated on a superfine roughness standard and a resolution standard, which move with a velocity of $v = 5\,\mathrm{mm/s}$ or even $v = 10\,\mathrm{mm/s}$. By stitching together multiple topographies retrieved from the moving objects, extended surface areas of the standards are retrieved.

The proposed interferometric measurement system employing pulsed RGB-illumination and quadrature phase retrieval is an original addition to existing single shot techniques for surface phase retrieval. It features a straight forward design and does not depend on polarizing interferometry or carrier fringes. A minor draw back is the comparable high influence of noise and phase detuning on the 2-step quadrature phase retrieval algorithm. Yet, to the best knowledge of the author, currently there is no other interferometric system available, which achieves a comparable low data acquisition time without employing carrier fringes or polarizing interferometry. The limitation of the frame rate to 10 fps and the pulse gap of $\approx 100\,\mu\mathrm{s}$ are related to the employed camera and may be further reduced by change of the hardware. The same accounts for the pulse width of the LEDs. The capability of the proposed method, to measure objects in lateral motion with high robustness to vibrations as demonstrated by experimental results addresses the needs of inline quality control.

The advances presented in characterization and applicability of the fiber coupled interferometric point sensor establish the basis for further developments. In successive work [1, 45, 47, 72, 155] a novel probe head for the fiber coupled interferometric sensor is introduced. The mechanical oscillation of the piezo actuated bending beam is replaced by the actuation of a reference mirror in a miniaturized Michelson interferometer probe. This enables higher oscillation frequencies up to 58 KHz and therefore, a much higher data rate and measurement speed of the system. The principle of the miniaturized fiber coupled laser interferometer is also employed to implement nm precise motion control of a rotation axis, to compensate imperfections of the axis movement [175]. The miniaturized fiber coupled design of the interferometric probe and its high adaptability to specific measurement requirements as well as the robust phase evaluation by the lock-in method or the very high data rate accessible employing time discrete Hilbert filters motivate its continuing development and application. In the mentioned ongoing projects and probably also in future work, the potential and capabilities of the point sensor and the corresponding phase retrieval techniques will be harnessed and extended.

The presented RGB-interferometer with pulsed LED illumination and quadrature based phase retrieval represents a fast, perturbation resistant and affordable method for areal surface measurement. An obstacle in the reported results [11, 79] are influences of phase detuning errors due to imperfections in the actuator movement in the reference light path. Therefore, replacing the oscillation coil actuator by a more stable actuator could increase the system performance. Another common issue of the RGB-interferometer is the ambiguity in the phase retrieval, which requires phase unwrapping if the surface height difference in the field of view extends $\pm\lambda_k/4$. In reference [11] the potential use of topography measurements obtained from a wavefront sensor to determine the interferometric fringe orders in the field of view is discussed. This method may be pursued in future work, to resolve the phase ambiguity without employing an algebraic unwrapping procedure. It requires careful referencing of the wavefront sensor, to ensure that the topography results obtained from the individual sensors align within the unambiguity range of the interferometer. The interferometer shows feasible topography measurement results, even when measuring in the vicinity of mechanical vibrations or a laterally moving object. Stitching algorithms may be employed to reconstruct an extended surface area scanned by the interferometer on structured objects besides rough surfaces. Since stitching of multiple consecutively recorded topographies of a superfine roughness standard yielded convincing results [11] due to the applied roughness filter removing potential drifts or height offsets between measurements, the capability of the sensor to measure rough surfaces employing its extended unambiguity range might be considered. This manuscript presents a detailed study of dispersion influences, like longitudinal chromatic aberration in the Michelson interferometer. Correction of the outlined alignment issues and improving the path length difference compensation of the employed long pass filter in the reference arm might result in a better interference contrast, improving the signal to noise ratio and the standard deviation in height measurements. The microscope objectives used throughout this study are not designed for the insertion of several millimeters or centimeters of glass into the

focusing beam path. Therefore, improvements are to be expected if specially designed objectives are used.

Appendix

Staschenko identity of the time averaged poynting vector in real field expression using complex konjugate fields

$$
\begin{aligned}
&\frac{1}{T}\int_{t-\frac{T}{2}}^{t+\frac{T}{2}} \left(\vec{E}(\vec{r},t)\cdot\Re\left\{\underline{\vec{E}}(\vec{r},t)\cdot e^{j\gamma_\eta}\right\}\right)dt \\
=&\frac{1}{4}e^{-2\mathrm{b}(\vec{r})}\frac{1}{T}\int_{t-\frac{T}{2}}^{t+\frac{T}{2}} \left[\left(\underline{\vec{E}}_{01}e^{j\phi_1}+\underline{\vec{E}}_{02}e^{j\phi_2}\right)e^{j\mathrm{a}(\vec{r},t)}+\left(\underline{\vec{E}}^*_{01}e^{-j\phi_1}+\underline{\vec{E}}^*_{02}e^{-j\phi_2}\right)e^{-j\mathrm{a}(\vec{r},t)}\right] \\
&\cdot\left[\left(\underline{\vec{E}}_{01}e^{j\phi_1}+\underline{\vec{E}}_{02}e^{j\phi_2}\right)e^{j\mathrm{a}(\vec{r},t)}e^{j\gamma_\eta}+\left(\underline{\vec{E}}^*_{01}e^{-j\phi_1}+\underline{\vec{E}}^*_{02}e^{-j\phi_2}\right)e^{-j\mathrm{a}(\vec{r},t)}e^{-j\gamma_\eta}\right]dt \\
=&\frac{1}{4}e^{-2\mathrm{b}(\vec{r})}\Bigg[\frac{1}{T}\int_{t-\frac{T}{2}}^{t+\frac{T}{2}} \left(\underline{\vec{E}}_{01}e^{j\phi_1}+\underline{\vec{E}}_{02}e^{j\phi_2}\right)e^{2j\mathrm{a}(\vec{r},t)}e^{j\gamma_\eta} \\
&+\left(\underline{\vec{E}}^*_{01}e^{-j\phi_1}+\underline{\vec{E}}^*_{02}e^{-j\phi_2}\right)e^{-2j\mathrm{a}(\vec{r},t)}e^{-j\gamma_\eta} \\
&+\left(\underline{\vec{E}}_{01}e^{j\phi_1}+\underline{\vec{E}}_{02}e^{j\phi_2}\right)\cdot\left(\underline{\vec{E}}_{01}e^{-j\phi_1}+\underline{\vec{E}}_{02}e^{-j\phi_2}\right)e^{j\gamma_\eta} \\
&+\left(\underline{\vec{E}}_{01}e^{j\phi_1}+\underline{\vec{E}}_{02}e^{j\phi_2}\right)\cdot\left(\underline{\vec{E}}_{01}e^{-j\phi_1}+\underline{\vec{E}}_{02}e^{-j\phi_2}\right)e^{-j\gamma_\eta}\Bigg]dt \\
=&\frac{1}{4}e^{-2\mathrm{b}(\vec{r})}\Big[\left(E_{01}^2+E_{02}^2+E_{01}E_{02}\cos(\theta)e^{j(\phi_1-\phi_2)}+E_{01}E_{02}\cos(\theta)e^{-j(\phi_1-\phi_2)}\right)\cdot e^{j\gamma_\eta} \\
&+\left(E_{01}^2+E_{02}^2+E_{01}E_{02}\cos(\theta)e^{j(\phi_1-\phi_2)}+E_{01}E_{02}\cos(\theta)e^{-j(\phi_1-\phi_2)}\right)\cdot e^{-j\gamma_\eta}\Big] \\
=&\frac{1}{4}e^{-2\mathrm{b}(\vec{r})}\Big[\left(E_{01}^2+E_{02}^2+2E_{01}E_{02}\cos(\theta)\cos(\phi_1-\phi_2)\right)\cdot e^{j\gamma_\eta} \\
&+\left(E_{01}^2+E_{02}^2+2E_{01}E_{02}\cos(\theta)\cos(\phi_1-\phi_2)\right)\cdot e^{-j\gamma_\eta}\Big] \\
=&\frac{1}{2}e^{-2\mathrm{b}(\vec{r})}\left(E_{01}^2+E_{02}^2+2E_{01}E_{02}\cos(\theta)\cos(\phi_1-\phi_2)\right)\cos(\gamma_\eta)
\end{aligned}
\tag{5.1}
$$

The conclusion drawn from equation (5.1) is, that if $\gamma_\eta \neq 0$ the result does only change in the cosine term $\cos(\gamma_\eta)$. Thus the Staschenko identity equation (5.2) results.

$$
\begin{aligned}
&\frac{1}{T}\int_{t-\frac{T}{2}}^{t+\frac{T}{2}} \left(\vec{E}(\vec{r},t)\cdot\Re\left\{\underline{\vec{E}}(\vec{r},t)\cdot e^{j\gamma_\eta}\right\}\right)dt \\
=&\cos(\gamma_\eta)\frac{1}{T}\int_{t-\frac{T}{2}}^{t+\frac{T}{2}} \left(\vec{E}(\vec{r},t)\cdot\vec{E}(\vec{r},t)\right)dt
\end{aligned}
\tag{5.2}
$$

This identity is the exclusive and original work of the author and first published in this dissertation. It was derived, as presented above, to determine the Poynting vector in

the non-uniform wave model employing real electric field vectors in the time domain. Euler's formula describes the relation between a complex exponential function and the trigonometric functions. In general, the real part of a complex number may be expressed as half the sum of itself with its complex conjugate. This approach is employed in the beginning of equation (5.1) and finally yields the identity in equation (5.2). Besides its application in the derivation of the Poynting vector in real field expression, the identity generally states that the integral over a full period of the real part of a phasor multiplied with the real part of a phase shifted version of itself may be simplified to the integral over the phasor's squared real part multiplied with the cosine of the additional phase shift.

I dedicate this identity to Stanislav Tereschenko in acknowledgement for his great support and patience in teaching me and other former colleagues how to program stuff in C, C++ and Python while pursuing his own time intensive scholarly work.

List of Publications

- [11] Schake M., and Lehmann P., "Double pulse led illumination for phase detection in rgb-interferometry," *Proc.SPIE* 11056, 176-187 (2019).
- [38] Knell H., Schake M., Schulz M., and Lehmann P.,"Interferometric sensors based on sinusoidal optical path length modulation," *Proc.SPIE* 9132 (2014).
- [40] Lehmann P., Tereschenko S., Schulz M., Schake M., and Riebeling J., "Robust interferometric sensors based on sinusoidal phase modulation," *European Optical Society Annual Meeting (EOSAM) 2016, Berlin* 26-30 September 2016 (2016).
- [41] Schake M., Schulz M., and Lehmann P., "High-resolution fiber-coupled interferometric point sensor for micro- and nano-metrology, "*tm - Technisches Messen* 82(7-8), 367-376 (2015).
- [42] Schake M. and Lehmann P., "Anwendungsorientiertes Verfahren zur Eindeutigkeits-Bereichserweiterung eines fasergekoppelten Zweiwellenlängen-Interferometers," *tm - Technisches Messen* 83(4), 192 - 200 (2016).
- [78] Schake M. and Lehmann P.,"Perturbation resistant rgb-interferometry with pulsed led illumination," *Proc.SPIE* 10678(1067805) (2018).
- [79] Schake M. and Lehmann P., "Quadrature-based interferometry using pulsed rgb illumination," *Opt. Express* 27(11), 16329 - 16343 (2019).
- [128] Schake M. C., "Comparison of recent results for the determination of effective propagation constants at attenuating interfaces," *European Journal of Physics* 39(1), 015302 (2017).
- [155] Hagemeier S., Schake M., and Lehmann P., "Sensor characterization by comparative measurements using a multi-sensor measuring system," *Journal of Sensors and Sensor Systems* 8(1), 111 - 121 (2019).

Nomenclature

Symbols

$\vec{a},\ \vec{b},\ \vec{c}$	Arbitrary vectors $\in \mathbb{R}^3$.
$A,\ \tilde{A}$	Integration area.
$\tilde{A}_{1,\text{blue}}$	Intensity distribution in the blue color channel after crosstalk correction.
$\overline{AD},\ \overline{BD},\ \overline{CD},\ \overline{P_1P_2}$	Distance between the respective planes $A,\ B,\ C,\ D$ and points $P_1,\ P_2$.
$A_k(x, y)$	Offset intensity distribution of the measurement path for the k-th wavelength.
α_{0m}	Real part of the intrinsic propagation constant in the m-th medium.
$\vec{\alpha}_m$	Real part of the effective propagation constants in the m-th medium.
$\alpha(t), A(\omega)$	In section 2.12 arbitrary signal in the time domain and its Fourier transform in the frequency domain.
$\mathrm{a}(\vec{r}, t)$	Time and position dependent phase evolution, indicating the planes of constant phase.
$1''$	Arcsecond $1'' = \pi/64800\,\text{rad}$
β_{0m}	Imaginary part of the intrinsic propagation constants in the m-th medium.
$\vec{\beta}_m$	Imaginary part of the effective propagation constants in the m-th medium.
$B_k(x, y)$	Offset intensity distribution of the reference path for the k-th wavelength.
$\vec{B}^{(m)} = \sum \vec{B}_m$	Sum of the magnetic flux density components in the m-th medium.
$\vec{B}_m$	Magnetic flux density vector in the m-th medium.

$\mathrm{b}(\vec{r})$	Position dependent attenuation, indicating the planes of constant amplitude.
c	Light velocity in matter.
c_0	Light velocity in vacuum.
$\chi^{''}$	Imaginary part of the complex susceptibility in the frequency domain.
$\chi^{'}$	Real part of the complex susceptibility in the frequency domain.
$\underline{\chi}(\omega)$	Complex susceptibility in the frequency domain.
$\chi(t)$	Susceptibility.
$C_k(x, y, h_k)$	Complex degree of coherence for the k-th wavelength.
$c_m^{'},\ c_{m+1}$	Offset of the coordinate system's origin.
D	Abbreviation for the common denominator in section 2.11.3.
$\Delta A_{mk}(x, y, i)$	Intensity distribution deviation of the i-th dual shot image for the k-th wavelength and m-th LED pulse.
Δf	Frequency resolution in the discrete spectral domain.
$\Delta h_k,\ \Delta\phi_{21,k}$	In chapter 4, adjusted OPLD or phase difference $\Delta h_k = \frac{\phi_{2k}-\phi_{1k}}{4\pi}\lambda_k$ between two consecutively recorded interferograms.
$\Delta\lambda_k$	Change in the wavelength of index k.
$\Delta\acute{\phi}_k(n)$	Change in the phase evolution of the k-th wavelength between two consecutive sample points.
$\Delta\acute{\Phi}(n)$	Change in the phase evolution of the synthetic wavelength between two consecutive sample points.
$\Delta\phi$	Phase difference.
$\Delta\phi_{k,\mathrm{dis}},\ \Delta h_{k,\mathrm{dis}}$	In chapter 4, unknown additional phase or height offset due to dispersion effects.
Δs	Spatially equidistant sample interval.
ΔT	Temperature change in Kelvin
Δt	Sample interval in the time domain.

$\delta(t-\tau), \delta(\omega-\acute{\omega})$	Dirac-Function also referred to as Delta-Distribution in the time or frequency domain.
$\Delta\tau_{\text{exp}}$	Exposure gap of the employed camera.
$\Delta\tau_r,\ \Delta\tau_g$	Pulse gap between consecutive LED pulses.
$\Delta x_{\text{opt}},\ \Delta x_{\text{ref}}$	Lateral sampling interval.
Δz_{Thr}	Threshold value of the OPLD change for focus tracking.
$\Delta z_k(\phi_k(t), \lambda_k(t))$	Change in the optical path length difference caused by mechanical motion or a change in k-th wavelength.
$\overline{D}_k,\ \overline{D}_{mk}$	Intensity distribution rescaling scalar for the k-th wavelength and m-th LED pulse.
$D_k(x,y),\ D_{mk}(x,y)$	Intensity distribution rescaling matrix.
$\vec{D}^{(m)} = \sum \vec{D}_m$	Sum of the electric flux density components in the m-th medium.
$\vec{D}_m$	Electric flux density vector in the m-th medium.
d_{min}	Minimal expected Airy disc diameter.
$\vec{D}(t)$	Time domain representation of the electric flux density.
$\underline{\vec{E}}_{00m},\ \underline{\vec{E}}_{01m},\ \underline{\vec{E}}_{02m}$	Electric field's complex amplitude (Jones vector) of a temporally and spatially coherent interfering pair of waves.
$\underline{\vec{E}}_{0m}$	In section 2.1-2.9 Jones vector of the electric field in the m-th medium, in section 2.11.3 complex electric field vector in the m-th medium.
$e_{12k}(x,y)$	Deviation in the retrieved surface height due to phase detuning and other perturbations.
$\vec{E}_{1m}(\vec{r},t),\ \vec{E}_{2m}(\vec{r},t)$	Electric fields of a temporally and spatially coherent interfering pair of waves.
$e_{h_k(x,y)}$	Deviation between the measured surface height and the expected surface height.
$\left(\frac{E_{(m+1)}}{E_m}\right)_{\parallel}$	Transmission coefficient of a TM-polarized uniform wave in loss free media.
$\left(\frac{E_{(m+1)}}{E_m}\right)_{\perp}$	Transmission coefficient of a TE-polarized uniform wave in loss free media.

$\left(\frac{E_m^{'}}{E_m}\right)_{\parallel}$	Reflection coefficient of a TM-polarized uniform wave in loss free media.
$\left(\frac{E_m^{'}}{E_m}\right)_{\perp}$	Reflection coefficient of a TE-polarized uniform wave in loss free media.
$\underline{\vec{E}}_m$	Phasor representation of the electric field vector in the m-th medium.
$\vec{E}^{(m)} = \sum \vec{E}_m$	Sum of the electric field components in the m-th medium.
$\vec{E}_m$	Electric field vector in the m-th medium.
$\underline{E}_{\text{mea}},\ \underline{E}_{\text{ref}}$	Electric field in the measurement and reference path of the confocal interferometer.
$e_{mk}(x, y)$	OPLD due to environmental perturbations.
$\underline{\vec{E}}_{pm}$	Phasor representation of the TM-polarized electric field vector in the m-th medium.
ϵ_0	Electric permittivity in vacuum.
$\epsilon_m^{''}$	Imaginary part of the electric permittivity in the m-th medium.
$\epsilon_m^{'}$	Real part of the electric permittivity in the m-th medium.
ϵ_m	Real valued electric permittivity in the m-th medium $\epsilon_m = \epsilon_0 \epsilon_m^{'}$.
$\underline{\epsilon}_m$	Complex electric permittivity in the m-th medium $\underline{\epsilon}_m = \epsilon_0 \left(\epsilon_m^{'} + j\epsilon_m^{''}\right)$.
$\underline{\vec{E}}_{sm}$	Phasor representation of the TE-polarized electric field vector in the m-th medium.
$\vec{E}(t)$	Time domain representation of the electric field.
$\underline{\eta}_m = \sqrt{\frac{\underline{\epsilon}_m}{\mu_m}}$	Complex intrinsic impedance in the m-th medium.
$E_{xm},\ E_{ym},\ E_{zm}$	Polarization related absolute values of the Jones vector of the electromagnetic wave in the m-th medium.
f_0	Oscillation frequency.
$\mathbb{F}\{f(t)\}$	Operator to yield the Fourier transform of the time domain function $f(t)$.
$f_{\max}$	Maximum frequency considering the Nyquist-Shannon theorem.

f_s	Sample frequency.
$F(x, y)$	Fringe order map.
$\overline{\boldsymbol{\gamma}}$	$\overline{\boldsymbol{\gamma}} = \boldsymbol{\alpha} + j\boldsymbol{\beta}$, $\overline{\boldsymbol{\gamma}} = -j\vec{\underline{k}}_m^{(\mathrm{nu})}$ complex non-uniform propagation vector in [135] p. 321
$\gamma_{\eta m}$	Angle enclosed by α_{0m} and β_{0m} in the complex plane in the m-th medium.
$\underline{G}(k)$	Discrete Hilbert filter in the frequency domain.
$g(m)$	Discrete Hilbert filter of index m in the time domain.
$\underline{G}(\omega)$	Transfer function in the frequency domain.
$g(t)$	Transfer function in the time domain.
$\underline{G}(z)$	Transfer function in the z-plane.
$\vec{\underline{H}}_{0m}$	Jones vector of the magnetic field in the m-th medium.
$\tilde{h}_k(x, y, n)$	Fringe order specific rescaled surface height.
$h_k(x, y)$	Retrieved surface height for the k-th wavelength.
$\left(\frac{\underline{H}_{m+1}}{\underline{H}_m}\right)_{\parallel}$	Transmission coefficient of a TM-polarized non-uniform wave in lossy media.
$\left(\frac{\underline{H}'_m}{\underline{H}_m}\right)_{\parallel}$	Reflection coefficient of a TM-polarized non-uniform wave in lossy media.
$\vec{\underline{H}}_m$	Phasor representation of the magnetic field vector in the m-th medium.
$\vec{H}^{(m)} = \sum \vec{H}_m$	Sum of the magnetic field components in the m-th medium.
$\vec{H}_m$	Magnetic field vector in the m-th medium.
$\underline{H}_{m_0}$	Complex spectral component of the Fourier transformed signal at index m_0.
$\tilde{h}_n$	Sampled signal with $\pi/2$ phase shift.
h_n	Sampled signal.
$\underline{H}(\omega)$	Arbitrary signal in the frequency domain.

$h(t)$	Arbitrary signal in the time domain.
$I_{1k},\ I_{2k}$	Energy flux density or intensity in the measurement or reference path, respectively, recorded in the k-th wavelength channel.
$I_{blue}(x,y),\ A_{blue}(x,y)$	Offset intensity distribution of the microscopic image in the blue color channel.
$I(\Delta z)$	Intensity distribution of the depth response.
$I_k(x,y),\ I_{mk}(x,y)$	Intensity of the interferogram of the k-th wavelength channel and m-th LED pulse.
$I_k(t)$	Energy flux density or intensity in the k-th wavelength channel.
I_m	Irradiance also referred to as radiant flux density, energy flux density or intensity in the m-th medium.
$I_m^{(\mathrm{uf})}$	Energy flux density or intensity considering a uniform wave vector in the m-th medium.
$\tilde{I}_{mk}(x,y)$	Interferogram after removing the offset intensity distribution.
$\Im\{\underline{Z}\}$	Operator to yield the imaginary part of a complex number $\underline{Z}$.
j	Imaginary unit $j^2=-1$.
$\vec{\underline{k}}_m$	Complex uniform wave vector in the m-th medium.
$\vec{\underline{k}}_m^{(\mathrm{nu})}$	Complex non-uniform wave vector in the m-th medium.
l	Evaluation length.
Λ	Synthetic wavelength.
λ	Wavelength of light.
λ_0	Center wavelength
λ_c	Cut off wavelength.
λ_k	Wavelength of index k.
$\lambda_{k\mathrm{eff}}$	Effective wavelength.
l_t	Lateral testing interval.
m_0	Index of the frequency chosen for the lock-in phase retrieval.

$\underline{\vec{M}}_m,\ \underline{\vec{M}}_{m+1}$	Complex propagation vectors of the coupled interference pairs in the m-th and $(m+1)$-th medium employed for the demonstration of energy conservation.
μ_0	Magnetic permeability in vacuum.
$\mu_m^{''}$	Imaginary part of the magnetic permeability in the m-th medium.
$\mu_m^{'}$	Real part of the magnetic permeability in the m-th medium.
μ_m	Real valued magnetic permeability in the m-th medium $\mu_m = \mu_0 \mu_m^{'}$.
n	In chapter 4, index of the fringe order.
n	Sample index.
N, M	Total number of samples.
$\vec{\nabla}$	Nabla-operator.
n_m	Refractive index of the m-th medium.
$N_{\Delta s}$	Absolute number of spatially equidistant sample points.
$n_{\Delta s},\ \tilde{n}_{\Delta s}$	Sample index of spatially equidistant sample points before and after interpolation.
$N_x,\ N_y$	Row and column count of a matrix.
ω_0	Angular frequency.
$\omega_{\max}$	Maximum angular frequency $2\pi f_{\max}$ considering the Nyquist-Shannon theorem.
$p_{\mathrm{GRIN}},\ l_{\mathrm{GRIN}},\ d_{\mathrm{GRIN}}$	Pitch, length and diameter of GRIN lenses.
Φ	Phase evolution corresponding to the synthetic wavelength.
$\phi_{1m},\ \phi_{2m}$	Phase offset of a temporally and spatially coherent interfering pair of waves.
ϕ_k	Phase evolution corresponding to the k-th wavelength.
$\phi_k,\ \phi_{mk}$	In chapter 4, constant adjustable phase offset between consecutively recorded interference images for the k-th wavelength and m-th LED pulse.
ϕ_{k0}	Phase offset at the first sample point.

$\acute{\phi}_k(n)$	Discrete sampled phase evolution of the k-th wavelength after subtraction of the phase offset.
$\Phi_{R^m_{m+1}},\ \Phi_{T^m_{m+1}},\ \Phi_{T^{m+1}_m}$	Real valued phase coefficient of reflection or transmission in Euler notation.
$\phi_{xm},\ \phi_{ym},\ \phi_{zm}$	Polarization related phase offset in the Jones vector's exponent of the electromagnetic wave in the m-th medium.
$\vec{P}_m$	Electric polarization vector in the m-th medium.
$P(\theta_e)$	Pupil function of the confocal interferometer.
Q	Electric charge.
$\hat{\underline{R}},\ \underline{R},\ \tilde{\underline{R}}$	Differently parametrized energy transfer by absorption and radiation, considering propagation through an attenuating interface.
$\vec{r}$	Position vector in a cartesian coordinate system.
R_a	The average roughness (Mittenrauwert) is the arithmetic mean of the absolute values of the sampled roughness profile (ISO 4287).
$\Re\{\underline{Z}\}$	Operator to yield the real part of a complex number $\underline{Z}$.
$\tilde{R},\ \tilde{G},\ \tilde{B}$	Crosstalk corrected images in the respective color channels.
$R,\ G,\ B$	Recorded images in the respective color channels.
ρ	Electric charge density.
ρ_m	Angle enclosed between the direction vectors of the effective propagation constants considering coplanar propagation.
$R^m_{m+1},\ T^m_{m+1},\ T^{m+1}_m$	Real valued amplitude coefficient of reflection or transmission in Euler notation.
$R^m_{m+1}e^{j\Phi_{R^m_{m+1}}}$	Euler notation of the complex reflection coefficient considering propagation from the m-th to the $(m+1)$-th medium.
$\vec{r}_\parallel$	Position vector lying inside the boundary surface in a cartesian coordinate system.
R_z	The average maximum height (Rautiefe) is the arithmetic mean of the maximum heights of the considered measuring sections (ISO 4287).
$S,\ \tilde{S}$	Integration path.

σ	Standard deviation of a random distribution.
σ_m	Electric conductivity of the m-th medium.
sign()	Sign function.
$\underline{\vec{S}}_m(\vec{r},t)$	Complex poynting vector in the m-th medium.
$\vec{S}_m(\vec{r},t)$	Poynting vector in the m-th medium.
$\vec{S}_m^{(\mathrm{uf})}(\vec{r},t)$	Poynting vector considering a uniform wave vector in the m-th medium.
T	Periodic time, connected to the angular frequency $\omega_0 = 2\pi/T$.
t	Variable of time.
$T_1,\ T_2$	Temperature at different points in time in Kelvin.
τ_{exp}	Exposure time of the employed camera.
$\tau_r,\ \tau_g$	Pulse width of the LED pulses.
θ	Angle enclosed between two arbitrary vectors $\vec{\alpha},\ \vec{\beta}\ \in \mathbb{R}^3$.
$\theta_e,\ \theta_{max}$	Angle of incidence and maximum angle of incidence.
$\theta_k(x,y)$	Surface phase retrieved by the RBG-quadrature method.
θ_m	Angle enclosed between the direction vector of the uniform wave and a vector normal to the interface.
$\underline{\theta}_m$	Complex angle enclosed between the complex direction vector of the non-uniform wave in complex angle notation and a vector normal to the interface.
$\theta(t)$	In section 2.12 step function in the time domain.
$T_{m+1}^{m} e^{j\Phi_{T_{m+1}^{m}}}$	Euler notation of the complex transmission coefficient considering propagation from the m-th to the $(m+1)$-th medium.
$T_{m}^{m+1} e^{j\Phi_{T_{m}^{m+1}}}$	Euler notation of the complex transmission coefficient considering propagation from the $(m+1)$-th to the m-th medium.
$\vec{u}_1,\ \vec{u}_2,\ \vec{u}_3$	Unit vectors of a right handed cartesian coordinate system.
$\vec{u}_A$	Unit vector normal to surface A.
$\vec{u}_{bs}$	Unit direction vector normal to the boundary surface between two media

$\vec{u}^{1}_{E_m},\ \vec{u}^{2}_{E_m}$	Unit direction vectors of the electric field components.
$\vec{u}_{H_m}$	Unit direction vector of the magnetic field.
$\underline{\vec{u}}^{\text{uni}}_{km}$	Complex unit direction vector of the non-uniform wave in complex angle notation in the m-th medium.
$\vec{u}_{km}$	Unit direction vector of the uniform wave in the m-th medium.
V	Integration volume.
v	Velocity
ξ_m	Angle enclosed between the attenuation vector $\vec{\beta}_m$ and a vector normal to the boundary surface.
$x(t) \circ\!\!-\!\!\bullet \underline{X}(\omega)$	Arbitrary transformation pair of a time-frequency domain transformation.
$\left[\begin{array}{ccc} x & y & z \end{array}\right]^{\mathrm{T}}$	Position vector in a cartesian coordinate system.
$\hat{z}$	Oscillation amplitude.
z_0	Constant optical path length offset common for the measurement and reference path.
$z_A(n\Delta t)$	Reconstructed actuator movement based on discrete Hilbert filtering.
$z_k(\phi_k(t), \lambda_k(t))$	Absolute optical path length difference in the k-th wavelength channel.
$z(t),\ z(x,y)$	Optical path length difference between the reference and measurement plane in the interferometer, which is proportional to the recreated 3D-topography.

Abbreviations

3D	Three dimensional
ARM	Advanced RISC Machine
BP	Band pass
BS	Beam splitter

C	Collimating lens
CCD	Charge-coupled device
CL	Condenser lens
CMOS	Complementary metal-oxide-semiconductor
CSI	Coherence scanning interferometry
DFB	Distributed feedback
DFT	Discrete Fourier transform
DM	Dichroic mirror
DOF	Depth of field
DSP	Digital signal processor
EOM	Electro-optic modulator
ESPI	Electronic speckle pattern interferometer
FIR	Finite impulse response
FPGA	Field programmable gate array
FPS	Frames per second
FWHM	Full width at half maximum
GRIN	Gradient index
HS	Hartmann-Shack
HWR	Height-to-wavelength-ratio
IIR	Infinite impulse response
ISO	International Organization for Standardization
Laser	Light amplification by stimulated emission
LD	Laser diode
LED	Light emitting diode
LMF	Local model fitting
LP	Long pass

NA	Numerical aperture
OCT	Optical coherence tomography
OPLD	Optical path length difference
PD	Photo diode
PSI	Phase shifting interferometry
RGB	Red, green, blue
RISC	Reduced instruction set computing
RS	Resolution standard
SI	Spectral interferometry
SIM	Structured illumination microscope
STED	Stimulated emission depletion
SWLI	Scanning White light interferometry
TE	Transverse electric
TM	Transverse magnetic
WDM	Wavelength division multiplexer

Bibliography

[1] Hagemeier S. and Lehmann P., "Multisensor-Messsystem zur Messung von Mikro- und Nanotopographien," *tm - Technisches Messen* **84**(S1), 2–12. (2017).

[2] Vorburger T., Rhee H. G., Renegar T. B., Song J. F., and Zheng A., "Comparison of optical and stylus methods for measurement of surface texture," *Int. J. Adv. Manuf.* **33**, 110–118 (2007).

[3] Padilla M., Servin M., and Garnica G., "Fourier analysis of rgb fringe-projection profilometry and robust phase-demodulation methods against crosstalk distortion," *Opt. Express* **24**(14), 15417–15428 (2016).

[4] Dai X., Shao X., Li L., Liu C., Dai M., Yun H., and Yang F., "Shape measurement with modified phase-shift lateral shearing interferometry illumination and radial basis function," *Appl. Opt.* **56**(21), 5954–5960 (2017).

[5] Zhang Z., Towers D. P., and Towers C. E., "Snapshot color fringe projection for absolute three-dimensional metrology of video sequences," *Appl. Opt.* **49**(31), 5947–5953 (2010).

[6] Hausotte T., Gröschl A., and Schaude J., "High-speed focal-distance-modulated fiber-coupled confocal sensor for coordinate measuring systems," *Appl. Opt.* **57**(14), 3907–3914 (2018).

[7] Ni H., Zou L., Guo Q., and Ding X., "Lateral resolution enhancement of confocal microscopy based on structured detection method with spatial light modulator," *Opt. Express* **25**(3), 2872–2882 (2017).

[8] Rittweger E., Han K. Y., Irvine S. E., Eggeling C., and Hell S. W., "Sted microscopy reveals crystal colour centres with nanometric resolution," *Nat Photon* **3**(3), 144–147 (2009).

[9] Vorburger T., "Optical methods of surface measurement." Online material (NIST) Measurement Science and Standards in Forensic Firearms Analysis (2012).

[10] Furukawa Y., Takaie Y., Maeda Y., Ohsaki Y., Takeuchi S., and Hasegawa M., "Development of one-shot aspheric measurement system with a shack–hartmann sensor," *Appl. Opt.* **55**(29), 8138–8144 (2016).

[11] Schake M. and Lehmann P., "Double pulse LED illumination for phase detection in RGB-interferometry," *Proc.SPIE* **11056**, 176–187 (2019).

[12] Schäfer B. and Mann K., "Investigation of the propagation characteristics of excimer lasers using a hartmann-shack sensor," *Review of Scientific Instruments* **71**(7), 2663–2668 (2000).

[13] Schäfer B. and Mann K., "Determination of beam parameters and coherence properties of laser radiation by use of an extended hartmann-shack wave-front sensor," *Appl. Opt.* **41**(15), 2809–2817 (2002).

[14] Schäfer B., Lübbecke M., and Mann K., "Hartmann-shack wave front measurements for real time determination of laser beam propagation parameters," *Review of Scientific Instruments* **77**(5), 053103 (2006).

[15] Schnars U. and Jüptner W., [*Digital holography: digital hologram recording, numerical reconstruction, and related techniques*], Springer, Berlin (2005).

[16] Zhu Y., Vaillant J., François M., Montay G., and Bruyant A., "Co-axis digital holography based on sinusoidal phase modulation using generalized lock-in detection," *Appl. Opt.* **56**(13), 97–104 (2017).

[17] Khare K., Ali P. T. S., and Joseph J., "Single shot high resolution digital holography," *Opt. Express* **21**(3), 2581–2591 (2013).

[18] Khare K., Ali P. T. S., Singh M., and Joseph J., "Single shot high resolution digital holographic imaging," in [*Classical Optics 2014*], paper CM3D.3, Optical Society of America (2014).

[19] Li J., Niu H., and Niu Y. X., "Laser feedback interferometry and applications: a review," *Optical Engineering* **56**(5), 1–20 (2017).

[20] Taimre T., Nikolić M., Bertling K., Lim Y. L., Bosch T., and Rakić A. D., "Laser feedback interferometry: a tutorial on the self-mixing effect for coherent sensing," *Adv. Opt. Photon.* **7**(3), 570–631 (2015).

[21] Herbert J., Bertling K., Taimre T., Rakić A. D., and Wilson S., "Surface roughness characterisation using optical feedback interferometry," *Electronics Letters* **53**(4), 268–270 (2017).

[22] Arriaga A. L., Bony F., and Bosch T., "Speckle-insensitive fringe detection method based on hilbert transform for self-mixing interferometry," *Appl. Opt.* **53**(30), 6954–6962 (2014).

[23] Birgitta B., *Dual Comb Spectroscopy*, PhD thesis, Ludwig-Maximilians-Universität München (2011).

[24] Shao L. and Gorman J. J., "Pulsed laser interferometry with sub-picometer resolution using quadrature detection," *Opt. Express* **24**(15), 17459–17469 (2016).

[25] Jin J., Maeng S., Park J., Kim J.-A., and Kim J. W., "Fizeau-type interferometric probe to measure geometrical thickness of silicon wafers," *Opt. Express* **22**(19), 23427–23432 (2014).

[26] Lee J., Han S., Lee K., Bae E., Kim S., Lee S., Kim S.-W., and Kim Y.-J., "Absolute distance measurement by dual-comb interferometry with adjustable synthetic wavelength," *Measurement Science and Technology* **24**(4), 045201 (2013).

[27] Durán V., Tainta S., and Torres-Company V., "Ultrafast electrooptic dual-comb interferometry," *Opt. Express* **23**(23), 30557–30569 (2015).

[28] Malacara D., [*Optical shop testing*], Wiley series in pure and applied optics, John Wiley & Sons, Inc., Hoboken and NJ, 3. ed. (2007).

[29] Rodriguez-Zurita G., Toto-Arellano N., Meneses-Fabian C., and Vazquez-Castillo J. F., "Lateral and rotational shearing phase-shifting interferometry with phase-grating multiplexing," in [*Conference on Lasers and Electro-Optics/Pacific Rim 2009*], 1–2, Optical Society of America (2009).

[30] Ling T., Yang Y., Yue X., Liu D., Ma Y., Bai J., and Wang K., "Common-path and compact wavefront diagnosis system based on cross grating lateral shearing interferometer," *Appl. Opt.* **53**(30), 7144–7152 (2014).

[31] Xia J., Chen Z., Sun H., Liang P.-Y., and Ding J., "Generalized phase-shifting for three-wave shearing interferometry," *Appl. Opt.* **55**(11), 2843–2847 (2016).

[32] Statsenko T., Chatziioannou V., Moore T., and Kausel W., "Methods of phase reconstruction for time-averaging electronic speckle pattern interferometry," *Appl. Opt.* **55**(8), 1913–1919 (2016).

[33] Statsenko T., Chatziioannou V., Moore T., and Kausel W., "Deformation reconstruction by means of surface optimization. part i: Time-averaged electronic speckle pattern interferometry," *Appl. Opt.* **56**(3), 654–661 (2017).

[34] Wu S., Zhu L., Pan S., and Yang L., "Spatiotemporal three-dimensional phase unwrapping in digital speckle pattern interferometry," *Opt. Lett.* **41**(5), 1050–1053 (2016).

[35] Rodríguez-Zurita G., García-Arellano A., Toto-Arellano N. I., Flores-Muñoz V. H., Pastrana-Sánchez R., Robledo-Sánchez C., Martínez-Bravo O., Vásquez-Pasmiño

N., and Costa-Vera. C., "One–shot phase stepping with a pulsed laser and modulation of polarization: application to speckle interferometry," *Opt. Express* **23**(18), 23414–23427 (2015).

[36] Passos M. H. M., Lemos M. R., Almeida S. R., Balthazar W. F., da Silva L., and Huguenin J. A. O., "Speckle patterns produced by an optical vortex and its application to surface roughness measurements," *Appl. Opt.* **56**(2), 330–335 (2017).

[37] Depiereux F., Lehmann P., Pfeifer T., and Schmitt R., "Fiber-optical sensor with miniaturized probe head and nanometer accuracy based on spatially modulated low-coherence interferogram analysis," *Applied optics* **46**(17), 3425–3431 (2007).

[38] Knell H., Schake M., Schulz M., and Lehmann P., "Interferometric sensors based on sinusoidal optical path length modulation," *Proc.SPIE* **9132** (2014).

[39] Lehmann P., Schulz M., and Niehues J., "Fiber optic interferometric sensor based on mechanical oscillation," *Proc.SPIE* **7389** (2009).

[40] Lehmann P., Tereschenko S., Schulz M., Schake M., and Riebeling J., "Robust interferometric sensors based on sinusoidal phase modulation," *European Optical Society Annual Meeting (EOSAM) 2016, Berlin 26-30 September 2016* (2016).

[41] Schake M., Schulz M., and Lehmann P., "High-resolution fiber-coupled interferometric point sensor for micro- and nano-metrology," *tm - Technisches Messen* **82**(7-8), 367–376 (2015).

[42] Schake M. and Lehmann P., "Anwendungsorientiertes Verfahren zur Eindeutigkeitsbereichserweiterung eines fasergekoppelten Zweiwellenlängen-Interferometers," *tm - Technisches Messen* **83**(4), 192–200 (2016).

[43] Schulz M., Lehmann P., and Niehues J., "Fiber optical interferometric sensor based on a piezo-driven oscillation," *Proc.SPIE* **7790** (2010).

[44] Schulz M. and Lehmann P., "Measurement of distance changes using a fibre-coupled common-path interferometer with mechanical path length modulation," *Measurement Science and Technology* **24**(6), 065202 (2013).

[45] Schulz M. and Lehmann P., "Fiber-coupled interferometric sensor for high-speed measurement of optical surfaces," *Optimess 2015, 6thInternational Conference on Optical Measurement Techniques for Structures & Systems* (2015).

[46] Schulz M., *Interferometrisch messender faseroptischer Sensor mit mechanisch oszillierender Sonde*, PhD thesis, Universität Kassel (2015).

[47] Schulz M. and Lehmann P., "Fasergekoppelter High-Speed-Sensor zum Messen optischer Funktionsflächen," *18. GMA/ITG-Fachtagung Sensoren und Messsysteme 2016* , 411–417 (2016).

[48] Bosbach C., Pfeifer T., and Depiereux F., "Neue Konzepte für ein faserbasiertes Messsystem zur absoluten Abstandsmessung (new concepts for a fiber based system for absolute distance measurements)," *tm – Technisches Messen* **70**(2), 85–92 (2018).

[49] Schmitt R., Pfeifer T., Depiereux F., and König N., "Novel fiber-optical interferometer with miniaturized probe for in-hole measurements," *Optoelectronics Letters* **4**(2), 140–142 (2008).

[50] Schmitt R., König N., Mallmann G. F., and Depiereux F., "Fiber-optical measurement of form deviations of rotation-symmetric parts," *Measurement* **43**(5), 714–718 (2010).

[51] Jennewein H., Gottschling H., and Tschudi T., "Absolute Distanzmessung mit einem faseroptischen Interferometer (absolute distance measurements with a fiber optic interferometer)," *tm - Technisches Messen* **67**(10/2000), 410 (2000).

[52] Kulkarni A. A., Bhattacharya S., and Prabhakar A., "All-fiber interferometry: design and analysis," *Appl. Opt.* **50**(22), 4450–4456 (2011).

[53] Muralidharan B., Wang T., and Milner T., "Reduced speckle in swept source optical coherence tomography by using high numerical aperture fibers," in [*Optics in the Life Sciences Congress*], BoM4A.2, Optical Society of America (2017).

[54] Nakata T. and Watanabe M., "Ultracompact and highly sensitive common-path phase-shifting interferometer using photonic crystal polarizers as a reference mirror and a phase shifter," *Appl. Opt.* **48**(7), 1322–1327 (2009).

[55] Xiong J., Zhong L., Liu S., Qiu X., Zhou Y., Tian J., and Lu X., "Improved phase retrieval method of dual-wavelength interferometry based on a shorter synthetic-wavelength," *Opt. Express* **25**(7), 7181–7191 (2017).

[56] de Groot P. J., "Extending the unambiguous range of two-color interferometers," *Appl. Opt.* **33**(25), 5948–5953 (1994).

[57] Sharma S., Eiswirt P., and Petter J., "Electro optic sensor for high precision absolute distance measurement using multiwavelength interferometry," *Opt. Express* **26**(3), 3443–3451 (2018).

[58] Falaggis K., Towers D. P., and Towers C. E., "Method of excess fractions with application to absolute distance metrology: theoretical analysis," *Appl. Opt.* **50**(28), 5484–5498 (2011).

[59] Falaggis K., Towers D. P., and Towers C. E., "Method of excess fractions with application to absolute distance metrology: analytical solution," *Appl. Opt.* **52**(23), 5758–5765 (2013).

[60] Falaggis K., Towers D. P., and Towers C. E., "Algebraic solution for phase unwrapping problems in multiwavelength interferometry," *Appl. Opt.* **53**(17), 3737–3747 (2014).

[61] Decker J. E., Miles J. R., Madej A. A., Siemsen R. F., Siemsen K. J., Bonth S. d., Bustraan K., Temple S., and Pekelsky J. R., "Increasing the range of unambiguity in step-height measurement with multiple-wavelength interferometry—application to absolute long gauge block measurement," *Appl. Opt.* **42**(28), 5670–5678 (2003).

[62] Koyama N., "A method of step height measurement within the unambiguous range of two laser wavelengths interferometer," *Optik - International Journal for Light and Electron Optics* **126**(3), 313–316 (2015).

[63] Yang C., Wax A., Dasari R. R., and Feld M. S., "2π ambiguity-free optical distance measurement with subnanometer precision with a novel phase-crossing low-coherence interferometer," *Opt. Lett.* **27**(2), 77–79 (2002).

[64] Chand M., Mehta A., Sharma R., Ojha V. N., and Chaudhary K. P., "Roughness measurement using optical profiler with self-reference laser and stylus instrument — a comparative study," *NISCAIR-CSIR, India* **49**(5), 335–339 (2011).

[65] Caber P. J., "Interferometric profiler for rough surfaces," *Appl. Opt.* **32**(19), 3438–3441 (1993).

[66] Kim N., Lee S. W., I Y., and Pahk H.-J., "Accurate roughness measurement using a method for evaluation and interpolation of the validity of height data from a scanning white-light interferometer," *Curr. Opt. Photon.* **1**(6), 604–612 (2017).

[67] Bodendorfer T. and Koch A. W., "Kombinierte Ebenheits- und Rauheitsmessung mittels Speckle-Interferometrie," *DGaO Proceedings* **ISSN 1614-8436** (2011).

[68] Bodendorfer T., Mayinger P., and Koch A. W., "Influence of surface structure on shape and roughness measurement using two-wavelength speckle interferometry," *Proc.SPIE* **8789** (2013).

[69] Sasaki O. and Okazaki H., "Sinusoidal phase modulating interferometry for surface profile measurement," *Appl. Opt.* **25**(18), 3137–3140 (1986).

[70] Kawata Y., Hyashi K., and Aoto T., "Two-wavelength interferometer based on sinusoidal phase modulation with an acetylene stabilized laser and a second harmonic generation," *Opt. Express* **23**(12), 16024–16034 (2015).

[71] Minoni U., Sardini E., Gelmini E., Docchio F., and Marioli D., "A high-frequency sinusoidal phase-modulation interferometer using an electro-optic modulator: Development and evaluation," *AIP Review of Scientific Instruments* **62**(11), 2579–2583 (1991).

[72] Hagemeier S., Tereschenko S., and Lehmann P., "High-speed laser interferometric distance sensor with reference mirror oscillating at ultrasonic frequencies," *tm - Technisches Messen* **86**(3), 164–174 (2019).

[73] Zhu Y., Vaillant J., Montay G., and Bruyant A., "Generalized lock-in detection applied to lens-less digital holographic interferometry," in [*Imaging and Applied Optics 2016*], DTh3C.3, Optical Society of America (2016).

[74] Duan F., Huang T., Jiang J., Fu X., and Ma L., "Simple lock-in detection technique utilizing multiple harmonics for digital pgc demodulators," *Appl. Opt.* **56**(16), 4807–4813 (2017).

[75] Estrada J. C., Servin M., and Quiroga J. A., "Easy and straightforward construction of wideband phase-shifting algorithms for interferometry," *Opt. Lett.* **34**(4), 413–415 (2009).

[76] Magalhaes P. A. A., Neto P. S., and de Barcellos C. S., "Phase shifting technique using generalization of carre algorithm with many images," *Optical Review* **16**(4), 432–441 (2009).

[77] Tian C. and Liu S., "Two-frame phase-shifting interferometry for testing optical surfaces," *Opt. Express* **24**(16), 18695–18708 (2016).

[78] Schake M. and Lehmann P., "Perturbation resistant rgb-interferometry with pulsed led illumination," *Proc.SPIE* **10678**(1067805) (2018).

[79] Schake M. and Lehmann P., "Quadrature-based interferometry using pulsed rgb illumination," *Opt. Express* **27**(11), 16329–16343 (2019).

[80] de Boer J. F., Leitgeb R., and Wojtkowski M., "Twenty-five years of optical coherence tomography: the paradigm shift in sensitivity and speed provided by fourier domain oct," *Biomed. Opt. Express* **8**(7), 3248–3280 (2017).

[81] Deck L. and de Groot P., "High-speed noncontact profiler based on scanning white-light interferometry," *Appl. Opt.* **33**(31), 7334–7338 (1994).

[82] de Groot P., de Lega X. C., Kramer J., and Turzhitsky M., "Determination of fringe order in white-light interference microscopy," *Appl. Opt.* **41**(22), 4571–4578 (2002).

[83] Lehmann P., "Vertical scanning white-light interference microscopy on curved microstructures," *Opt. Lett.* **35**(11), 1768–1770 (2010).

[84] Pförtner A. and Schwider J., "Dispersion error in white-light linnik interferometers and its implications for evaluation procedures," *Appl. Opt.* **40**(34), 6223–6228 (2001).

[85] Takeda M., Ina H., and Kobayashi S., "Fourier-transform method of fringe-pattern analysis for computer-based topography and interferometry," *J. Opt. Soc. Am.* **72**(1), 156–160 (1982).

[86] Pawłowski M. E., Sakano Y., Miyamoto Y., and Takeda M., "Phase-crossing algorithm for white-light fringes analysis," *Optics Communications* **260**(1), 68–72 (2006).

[87] Xie W., Lehmann P., Niehues J., and Tereschenko S., "Signal modeling in low coherence interference microscopy on example of rectangular grating," *Opt. Express* **24**(13), 14283–14300 (2016).

[88] Dong J., Lu R., Li Y., and Wu K., "Automated determination of best focus and minimization of optical path difference in linnik white light interferometry," *Appl. Opt.* **50**(30), 5861–5871 (2011).

[89] Pavliček P. and Hýbl O., "White-light interferometry on rough surfaces—measurement uncertainty caused by noise," *Appl. Opt.* **51**(4), 465–473 (2012).

[90] Yoshino H., Kaminski P. M., Smith R., Walls J. M., and Mansfield D., "Refractive index determination by coherence scanning interferometry," *Appl. Opt.* **55**(15), 4253–4260 (2016).

[91] Tereschenko S., Lehmann P., Zellmer L., and Brueckner-Foit A., "Passive vibration compensation in scanning white-light interferometry," *Appl. Opt.* **55**(23), 6172–6182 (2016).

[92] Park H. M., Jung H. W., and Joo K.-N., "Dual low coherence scanning interferometry for rapid large step height and thickness measurements," *Opt. Express* **24**(25), 28625–28632 (2016).

[93] Pavlíček P. and Häusler G., "White-light interferometer with dispersion: an accurate fiber-optic sensor for the measurement of distance," *Appl. Opt.* **44**(15), 2978–2983 (2005).

[94] Papastathopoulos E., Körner K., and Osten W., "Chromatic confocal spectral interferometry," *Appl. Opt.* **45**(32), 8244–8252 (2006).

[95] Kassamakov I., Tureanu A., Heikkinen V., and Hæggström E., "Transfer standard for traceable dynamic calibration of stroboscopic scanning white light interferometer," *Appl. Opt.* **56**(9), 2483–2488 (2017).

[96] Kitagawa K., "Multi-wavelength single-shot interferometry," in [*2009 International Symposium on Optomechatronic Technologies*], 34–39 (2009).

[97] Kitagawa K., "Fast surface profiling by multi-wavelength single-shot interferometry," *International Journal of Optomechatronics* **4**(2), 136–156 (2010).

[98] Kitagawa K., "Multiwavelength single-shot interferometry without carrier fringe introduction," *Proc.SPIE* **8000** (2011).

[99] Kitagawa K., "Single-shot surface profiling by multiwavelength interferometry without carrier fringe introduction," *Journal of Electronic Imaging* **21**(2), 1 – 10 – 10 (2012).

[100] Srivastava V., Inam M., Kumar R., and Mehta D. S., "Single shot white light interference microscopy for 3d surface profilometry using single chip color camera," *J. Opt. Soc. Korea* **20**(6), 784–793 (2016).

[101] Pförtner A. and Schwider J., "Red-green-blue interferometer for the metrology of discontinuous structures," *Appl. Opt.* **42**(4), 667–673 (2003).

[102] Koliopoulos C. L., "Simultaneous phase-shift interferometer," *Proc.SPIE* **1531** (1992).

[103] Millerd J. E., Brock N. J., Hayes J. B., North-Morris M. B., Novak M., and Wyant J. C., "Pixelated phase-mask dynamic interferometer," *Proc.SPIE* **5531** (2004).

[104] Safrani A. and Abdulhalim I., "High-speed 3d imaging using two-wavelength parallel-phase-shift interferometry," *Opt. Lett.* **40**(20), 4651–4654 (2015).

[105] Tian X., Tu X., Zhang J., Spires O., Brock N., Pau S., and Liang R., "Snapshot multi-wavelength interference microscope," *Opt. Express* **26**(14), 18279–18291 (2018).

[106] Ma S., Quan C., Zhu R., Tay C. J., and Chen L., "Surface profile measurement in white-light scanning interferometry using a three-chip color ccd," *Appl. Opt.* **50**(15), 2246–2254 (2011).

[107] Buchta Z., Mikel B., Lazar J., and Číp O., "White-light fringe detection based on a novel light source and colour ccd camera," *Measurement Science and Technology* **22**(9), 094031 (2011).

[108] Zhu P. and Wang K., "Single-shot two-dimensional surface measurement based on spectrally resolved white-light interferometry," *Appl. Opt.* **51**(21), 4971–4975 (2012).

[109] Klaus L. and Gebhard O., [*Band 2 Relativistische Physik - von der Elektrizität zur Optik*], De Gruyter, Berlin and Boston (2015).

[110] Born M. and Wolf E., [*Principles of Optics*], Pergamon, 7. ed. (1999).

[111] Hecht E., [*Optik*], Oldenbourg Verlag, 5. ed. (2009).

[112] Jackson J. D., [*Klassische Elektrodynamik*], De Gruyter, 4. ed. (2006).

[113] van Keuren E. R., "Refractive index measurement using total internal reflection," *American Journal of Physics* **73**(7), 611–614 (2005).

[114] Stratton J., [*Electromagnetic Theory*], McGraw-Hill, New York (1941).

[115] Canning F. X., "Corrected fresnel coefficients for lossy materials," in [*2011 IEEE International Symposium on Antennas and Propagation (APSURSI)*], 2123–2126 (2011).

[116] Canning F. X., "Reply," *IEEE Antennas and Propagation Magazine* **Vol. 53.**(No. 4), 165–168 (2011).

[117] Canning F. X., "On fresnel coefficients for transmission into a lossy medium," in [*2015 International Conference on Electromagnetics in Advanced Applications (ICEAA)*], 165–168 (2015).

[118] Pereyra P. and Robledo-Martinez A., "On the equivalence of the summation and transfer-matrix methods in wave propagation through multilayers of lossless and lossy media," *European Journal of Physics* **30**(2), 393 (2009).

[119] Petrova-Mayor A. and Gimbal S., "Advanced lab on fresnel equations," *American Journal of Physics* **83**(11), 935–941 (2015).

[120] Ramakrishna S. A. and Armour A. D., "Propagating and evanescent waves in absorbing media," *American Journal of Physics* **71**(6), 562–567 (2003).

[121] Vitela J. E., "Electromagnetic waves in dissipative media revisited," *American Journal of Physics* **72**(3), 393–403 (2004).

[122] Aieta F., Genevet P., Yu N., Kats M. A., Gaburro Z., and Capasso F., "Out-of-plane reflection and refraction of light by anisotropic optical antenna metasurfaces with phase discontinuities," *Nano Letters* **12**(3), 1702–1706 (2012).

[123] Aieta F., Kabiri A., Genevet P., Yu N., Kats M. A., Gaburro Z., and Capasso F., "Reflection and refraction of light from metasurfaces with phase discontinuities," *Journal of Nanophotonics* **6**(1), 1–9 (2012).

[124] Yu N., Genevet P., Kats M. A., Aieta F., Tetienne J.-P., Capasso F., and Gaburro Z., "Light propagation with phase discontinuities: Generalized laws of reflection and refraction," *Science* **334**(6054), 333–337 (2011).

[125] Yu N. and Capasso F., "Flat optics with designer metasurfaces," *Nature materials* **13**(2), 139–150 (2014).

[126] Dupertuis M. A., Proctor M., and Acklin B., "Generalization of complex snell–descartes and fresnel laws," *J. Opt. Soc. Am. A* **11**(3), 1159–1166 (1994).

[127] Roy J. E., "New results for the effective propagation constants of nonuniform plane waves at the planar interface of two lossy media," *IEEE Transactions on Antennas and Propagation* **Vol. 51**(No. 6), 1206–1215 (2003).

[128] Schake M. C., "Comparison of recent results for the determination of effective propagation constants at attenuating interfaces," *European Journal of Physics* **39**(1), 015302 (2017).

[129] Demtröder W., [*Experimentalphysik 2*], Springer Spektrum Verlag, 6. ed. (2013).

[130] Pedrotti F., [*Optik für Ingenieure*], Springer Verlag, 3. ed. (2002).

[131] Reider G. A., [*Photonik eine Einführung in die Grundlagen*], Springer Verlag, 3. ed. (2012).

[132] Schiffner G., [*Optische Nachrichtentechnik*], Teubner Verlag, 1. ed. (2005).

[133] Suter D. and Uhrig G. S., "Physik iii - Optik." Tu-Dortmund online lecture (2011).

[134] Weber R., [*Physik Teil I: Klassische Physik- Experimentelle und theoretische Grundlagen*], Teubner Verlag, 1. ed. (2007).

[135] Adler R. B., Chu L. J., and Robert M. F., [*Electromagnetic Energy Transmission and Radiation: Plane Waves in Dissipative Media*], Wiley, New York (1960).

[136] Lorrain P., Corson D. R., and Lorrain F., [*Elektromagnetische Felder und Wellen*], De Gruyter, Berlin (1995).

[137] Balanis C. A., [*Advanced Engineering Electromagnetics*], Wiley, New York (1989).

[138] Staelin D., *Electromagnetics and Applications*, PhD thesis, Massachusetts Institute of Technology (2009).

[139] Klingshirn C. F., [*Semiconductor Optics*], Springer Verlag, 4. ed. (2001).

[140] Besieris I. M., "Comment on the corrected fresnel coefficients for lossy materials," *IEEE Antennas and Propagation Magazine* **Vol. 53**(No. 4), 161–164 (2011).

[141] Mangini F. and Frezza F., "Analysis of the electromagnetic reflection and transmission through a stratified lossy medium of an elliptically polarized plane wave," *Mathematics and Mechanics of Complex Systems* **4**(2) (2016).

[142] David M. P., [*Microwave Engineering*], Wiley Verlag, 4. ed. (2012).

[143] Hayt W. H. and Buck J. A., [*Engineering Electromagnetics*], Mc Graw hill, 6. ed. (2001).

[144] Landau L. D. and Lifshitz E. M., [*Electrodynamics of Continuous Media*], Pergamon Press, 1. ed. (1960).

[145] Yuffa A. J. and Scales J. A., "Linear response laws and causality in electrodynamics," *IOP Publishing Eur. J. Phys.* **33**(6), 1635–1650 (2012).

[146] Fritzsche K., [*Grundkurs Funktionentheorie*], Springer Spektrum Verlag, 1. ed. (2009).

[147] Wooten F., [*Optical properties of solids*], Academic Press Inc., 1. ed. (1972).

[148] Gold B., Oppenheim A., and Rader C. M., "Theory and implementation of the discrete hilbert transformator," in [*Symposium on Computer processing in Communications*], 235–250, Polytechnic Institute of Brooklyn (1969).

[149] Waiss S. M. K., *Design and control of a laser cooling system for wavelength stabilization of a monochromatic light source*, Master's thesis, Universität Kassel (2015).

[150] GRINTECH GmbH, "Grin rod lenses – numerical aperture 0.5: Gradient index lenses for fiber coupling and beam shaping of laser diodes." Online datasheet (2018).

[151] Xie W., *Transfer characteristics of white light interferometers and confocal microscopes*, PhD thesis, Universität Kassel (2017).

[152] Dabbs T. and Glass M., "Single-mode fibers used as confocal microscope pinholes," *Appl. Opt.* **31**(6), 705–706 (1992).

[153] Dabbs T. and Glass M., "Fiber-optic confocal microscope: Focon," *Appl. Opt.* **31**(16), 3030–3035 (1992).

[154] Kimura S. and Wilson T., "Confocal scanning optical microscope using single-mode fiber for signal detection," *Appl. Opt.* **30**(16), 2143–2150 (1991).

[155] Hagemeier S., Schake M., and Lehmann P., "Sensor characterization by comparative measurements using a multi-sensor measuring system," *Journal of Sensors and Sensor Systems* **8**(1), 111–121 (2019).

[156] Jung W., Benalcazar W. A., Ahmad A., Sharma U., Tu H., and Boppart S. A., "Numerical analysis of gradient index lens-based optical coherence tomography imaging probes," *Journal of Biomedical Optics* **15**(6), 1–10 (2010).

[157] Knell H., *Interferometrische Sensoren mit Modulation der optischen Weglänge für die Fertigungsmesstechnik*, PhD thesis, Universität Kassel, Kassel (2016).

[158] Fechner T., "Laufzeitkosten in c." Online Seminar Universität Hamburg (2013).

[159] Klakow D., "Grundlagen der Signalverarbeitung." Online material Universität des Saarlandes (2013).

[160] Vogel P., [*Systemtheorie ohne Ballast: Zeitdiskrete LTI-Systeme*], Springer-Verlag (2011).

[161] Tereschenko S., *Digitale Analyse periodischer und transienter Messsignale anhand von Beispielen aus der optischen Präzisionsmesstechnik*, PhD thesis, Universität Kassel (2018).

[162] Hausotte T., "Personal correspondence," (2019).

[163] Leach R., [*Abbe Error/Offset*], 1–4, Springer Berlin Heidelberg, Berlin, Heidelberg (2014).

[164] International Organization for Standardisation, "ISO 4287 (1997) geometrical product specifications (GPS) – surface texture: profile method-terms, definitions and surface texture parameters.," (1997).

[165] International Organization for Standardization, "ISO 11562 (1997) geometrical product specifications (GPS) – surface texture: Profile method – metrological characteristics of phase correct filters.," (1997).

[166] HALLE Präzisions-Kalibriernormale GmbH, "Kalibriernormale für Tastschnittgeräte entsprechend PTB-Normalen: Raunormale." Online datasheet Nr.: 6.2 (2014).

[167] Herráez M. A., Burton D. R., Lalor M. J., and Gdeisat M. A., "Fast two-dimensional phase-unwrapping algorithm based on sorting by reliability following a noncontinuous path," *Appl. Opt.* **41**(35), 7437–7444 (2002).

[168] SiMETRICS GmbH, "Resolution standard type RS-M." Online datasheet (2009).

[169] Butola A., Ahmad A., Dubey V., Singh V., Joshi T., Senthilkumaran P., and Mehta D. S., "Quantitative phase imaging using spectrally resolved white light interferometry," *Proc.SPIE* **10414** (2017).

[170] Huang P. S., Hu Q., Jin F., and Chiang F.-P., "Color-encoded digital fringe projection technique for high-speed 3-d surface contouring," *Optical Engineering* **38**(6), 1065–1071 (1999).

[171] Padilla M., Servin M., and Garnica G., "Fourier analysis of rgb fringe-projection profilometry and robust phase-demodulation methods against crosstalk distortion," *Opt. Express* **24**(14), 15417–15428 (2016).

[172] Zhang Z., Towers C. E., and Towers D. P., "Time efficient color fringe projection system for 3d shape and color using optimum 3-frequency selection," *Opt. Express* **14**(14), 6444–6455 (2006).

[173] Dey R. K. and Cui B., "Electron beam lithography with feedback using in situ self-developed resist.," *Nanoscale research letters* **9**(184) (2014).

[174] Kiani A., Venkatakrishnan K., Tan B., and Venkataramanan V., "Maskless lithography using silicon oxide etch-stop layer induced by megahertz repetition femtosecond laser pulses," *Opt. Express* **19**(11), 10834–10842 (2011).

[175] Laubach S., Ehret G., Riebling J., and Lehmann P., "Combination of a fast white-light interferometer with a phase shifting interferometric line sensor for form measurements of precision components," *Proc.SPIE* **10329** (2017).

This manuscript provides a compendium for the application of the non-uniform wave model to standard problems of two beam interference and addresses common educational issues associated with wave propagation at attenuating interfaces. It also reports scientific advances in interferometric applications focusing on an interferometric point sensor with optical path length modulation and an areal measuring RGB-interferometer for fast topography measurements in the sub millisecond regime.

ISBN 978-3-7376-0840-4